Theory-based integrated modelling of impurity transport in tokamaks

Daniel Fajardo

SIGILL·UNIVERSITAT·LUDOVIC·MAXIM·

München 2024

Theory-based integrated modelling of impurity transport in tokamaks

Dissertation zur Erlangung des akademischen Grades eines
Doktors der Naturwissenschaften (Dr. rer. nat.)
an der Fakultät für Physik der Ludwig–Maximilians–Universität
München

durchgeführt am
Max-Planck-Institut für Plasmaphysik

vorgelegt von
Daniel Fajardo
geboren am 18. September 1996 in Medellín, Colombia

München, den 16.09.2024

Erstgutachter: Prof. Dr. Hartmut Zohm
Zweitgutachter: Dr. habil. Yann Camenen
Tag der mündlichen Prüfung: 24.10.2024

A Mechitas

Zusammenfassung

Verunreinigungen spielen eine entscheidende Rolle bei der Kombination eines heißen Plasmazentrums mit einem kalten Plasmarand, die beide Voraussetzungen für den Betrieb eines Kernfusionsreaktors sind. Verunreinigungen können das Plasmazentrum abkühlen und den Brennstoff verdünnen. Dies setzt strenge Grenzen für die tolerierbaren Verunreinigungskonzentrationen, um thermonukleare Bedingungen aufrechtzuerhalten oder sogar für die Stabilität der Plasmaentladung selbst. Gleichzeitig sind gezielt eingebrachte Verunreinigungen unerlässlich, um die überschüssige Wärme in einer Fusionsanlage abzuführen, bevor sie die Reaktorwände erreicht.

Diese Arbeit konzentriert sich auf die prädiktive Modellierung von Tokamaks mit besonderem Schwerpunkt auf der selbstkonsistenten Wechselwirkung zwischen Verunreinigungen und dem Plasma, wobei physikalisch basierte Modelle für den Teilchen- und Wärmetransport verwendet werden. Zu diesem Zweck wird ein integriertes Modell eingeführt, das Verunreinigungen und deren Strahlung einschließt. Dieses kombiniert alle derzeit bekannten Elemente der lokalen Theorie des quasilinearen turbulenten und stoßbehafteten Verunreinigungstransports.

Es wird ein analytisches Modell eingeführt, das die Auswirkungen der toroidalen Plasmarotation auf den stoßbehafteten Transport von Verunreinigungen beschreibt. Diese Effekte sind entscheidend für die Beschreibung des Verhaltens schwerer Verunreinigungen, und es wird gezeigt, dass das Modell im Vergleich zu vollständigeren Codes genau ist, sich aber besser für schnelle Anwendungen eignet.

Der Modellierungsablauf wird anhand von experimentellen Daten aus einer Vielzahl von Plasmen in ASDEX Upgrade validiert. Es wird gezeigt, dass das integrierte Modell in der Lage ist, Messungen der Plasmaprofile, der Verunreinigungsdichten und der abgestrahlten Leistungen von Entladungen im Low-Confinement-Regime in Simulationen über den gesamten Plasmaradius bei verschiedenen Plasmaströmen und Kombinationen von Plasmaheizungen zu reproduzieren. Darüber hinaus wird die Kontrolle der Anreicherung schwerer Verunreinigungen durch zentrale Wellenheizung für eine Reihe von Entladungen im High-Confinement-Regime mit dominanter Neutralstrahlheizung untersucht. Es wird gezeigt, dass der Modellierungsablauf die experimentell beobachtete Abflachung der Wolframdichte im Plasmazentrum bei zunehmender Wellenheizleistung quantitativ reproduziert, und die physikalischen Grundlagen dieser wichtigen experimentellen Technik werden analysiert.

Mit dem validierten Modellierungsablaufs wird eine prädiktive Analyse der Wechselwirkung zwischen der Wolframstrahlung, der zur Aufrechterhaltung des Betriebs im High-Confinement-Regime erforderlichen Zusatzheizleistung und der Fusionsleistung im zukünftigen ITER-Reaktor vorgestellt. Die Anwendung von physikalisch basierten Transportmodellen und die gekoppelte Entwicklung des Plasmas mit den Verunreinigungen tragen zu einem besseren Verständnis des Betriebsbereichs bei.

Abstract

Impurities play a critical role in the integration of a hot plasma core with a cold plasma edge, which are both requirements for the viable operation of a nuclear fusion reactor. Impurities can cool down the plasma core and dilute the fuel. This sets stringent limits on the tolerable impurity concentrations in order to sustain thermonuclear conditions or even for the survival of the plasma itself. At the same time, purposefully-injected impurities will be essential to dissipate the excess heat in a fusion device before it reaches the reactor walls.

This thesis focuses on the predictive modelling of tokamaks with particular emphasis on the self-consistent interaction between impurities and the background plasma, using physics-based models to describe the transport of particles and heat.

For this purpose, an integrated modelling framework including impurities and their radiation is introduced. It combines all presently known theoretical elements in the local description of quasi-linear turbulent and collisional impurity transport.

An analytical model which describes the effects of toroidal plasma rotation on the collisional transport of impurities is introduced. These effects are crucial to describe the behavior of heavy impurities, and the model is shown to be accurate with respect to more complete codes but better suited for fast applications.

The workflow is validated against experimental data from a variety of plasmas in the ASDEX Upgrade tokamak. It is demonstrated that the modelling framework is able to reproduce measurements of the main plasma profiles, the impurity densities, and the radiated powers of low-confinement regime discharges in full-radius simulations at different plasma currents and heating power mixtures, as well as of a discharge with impurity seeding and a large radiated power fraction. Furthermore, the control of heavy impurity accumulation with central wave heating is investigated for a set of high-confinement regime discharges with dominant neutral beam heating. The workflow is shown to quantitatively reproduce the experimentally-observed reduction of core tungsten peaking at increasing wave heating power, and the physics behind this important experimental technique is analyzed.

Having validated the modelling workflow with impurities, a predictive study of the high power and full current baseline scenario of the future ITER reactor is presented. The analysis specifically investigates the interplay among the tungsten edge concentration, transport and radiation, the auxiliary heating power required to sustain the high confinement regime and the quality of the plasma confinement and the consequent fusion performance. The application of physics-based transport models and the coupled evolution of the main plasma and the impurities are shown to contribute to a more solid definition of the domain of operational conditions which allow the achievement of the main ITER targets.

Contents

Chapter 1

Introduction

Nuclear fusion is the process that powers the stars, including our Sun, and consequently it is the fundamental energy source for life on Earth. Harnessing fusion power in a controlled and efficient way would provide humanity a clean, practically inexhaustible, safe and geographically available energy source. This would contribute to the solution of two crucial, coupled problems: supplying the increasing energy demands of an ever-growing and industrializing world population, and doing so without the emission of greenhouse gases to alleviate climate change. Over the decades since the start of fusion research, an incomplete understanding of the rich physics involved in fusion plasmas and numerous technological challenges have impeded achieving a net energy gain from fusion, but substantial progress has been and is currently being made. The promising implications for humanity and the complex physics involved make fusion energy an exciting and interesting research field.

1.1 Nuclear fusion and plasma physics

Fusing positively-charged atomic nuclei requires vast amounts of energy, sufficient to overcome the long-range electromagnetic repulsion between them, such that short-range nuclear forces bind them. The necessary kinetic energy of these nuclei, $E \sim 10$ keV, translates to extreme fuel temperatures, $T = E/k_\mathrm{B} \sim 10^8$ K (where k_B is Boltzmann's constant), at which matter only exists in the plasma state. This is the basis for most challenges in controlled fusion: hot plasmas must be confined away from reactor walls to avoid damaging the device and sustain the right conditions for fusion reactions to occur. In Magnetic Confinement Fusion (MCF), magnetic field configurations are used to trap the charged particles that constitute the plasma.

1.1.1 The D–T reaction

The most viable fusion reaction for controlled energy generation is the one between deuterium ($\mathrm{D} = {}^2_1\mathrm{H}$) and tritium ($\mathrm{T} = {}^3_1\mathrm{H}$), two heavier isotopes of hydrogen (${}^1_1\mathrm{H}$), because it has the highest cross section and reactivity at lower temperatures [1]. The 17.6 MeV of energy produced per D–T reaction are carried by an alpha particle (which is a helium-4 nucleus) and an energetic neutron, in 1/5–4/5 fractions:

$$\mathrm{D} + \mathrm{T} \longrightarrow {}^4_2\mathrm{He}^{2+}\ (3.5\ \mathrm{MeV}) + {}^1_0\mathrm{n}\ (14.1\ \mathrm{MeV}). \tag{1.1}$$

The neutrons are unaffected by the magnetic field, escape the plasma and subsequently deposit their kinetic energy to the walls of the reactor, producing the heat for electricity generation or its use in heat-intensive industrial applications. The charged alpha particles remain confined in the plasma and contribute to its heating.

The high energy density of its fuels is one of the main advantages of fusion energy, typically needing only a few grams at any given moment for nominal operation. For reference, chemical reactions release around 1 eV per reaction, compared to 17.6 MeV per D–T reaction. Deuterium is easily obtainable from seawater, however tritium has a half-life of 12.4 years and is therefore not present in nature. It has to be produced in a process called tritium breeding, which is currently planned to be first tested in a real fusion environment in ITER [2,3], an experimental reactor currently under construction in France. The neutrons generated in the D–T process react with lithium (abundant in Earth's crust) placed in the walls of the device, breeding the tritium during operation of the MCF device (however sufficient availability of this isotope for start-up of future reactors remains a challenge [4]). Present-day experimental devices typically operate with deuterium, hydrogen or helium plasmas, with the exception of a few dedicated campaigns with tritium aimed at generating fusion power performed at the JET and TFTR devices [5–8].

1.1.2 Charged particle motion in electromagnetic fields

The principle behind MCF is that, due to the Lorentz force, charged particles follow helical trajectories in the presence of a magnetic field **B**, with free motion along the field lines and gyromotion around them. This motion is characterized by the cyclotron frequency and Larmor radius (also called gyro-frequency and gyro-radius),

$$\omega_c = \frac{|Ze|B}{m}, \qquad \rho_L = \frac{v_\perp}{\omega_c} = \frac{m v_\perp}{|Ze|B}, \tag{1.2}$$

respectively. Here, Ze is the charge of the particle, m is its mass and $v_\perp$ is the velocity component perpendicular to **B**. A particle will be confined in the perpendicular direction if its Larmor radius is much smaller than the size of the device. This is a fundamental condition for a *magnetized* plasma, and it leads to strongly anisotropic dynamics in the directions parallel and perpendicular to the magnetic field.

The motion of the guiding center of the gyrating particles can be affected by different mechanisms, leading to *drifts*, i.e. motion perpendicular to the magnetic field. Particle drifts are generated by forces, where the $\mathbf{E} \times \mathbf{B}$ drift (caused by an electric field $\mathbf{E} \perp \mathbf{B}$) is a particularly relevant case in fusion plasmas, and inhomogeneous magnetic fields that lead to the ∇B (grad-B) and curvature drifts [9]. Likewise, collective effects can lead to average plasma flows perpendicular to **B**, with the relevant example of the diamagnetic drift, caused by pressure gradients.

1.1.3 Power balance in a fusion device

In order to achieve thermonuclear conditions, both external and intrinsic heating mechanisms are typically present in a fusion plasma. In stationary operation, the total heating power (P_heat) must balance the plasma energy losses (P_loss), or explicitly

$$P_\text{heat} = P_\text{loss} \quad \longrightarrow \quad P_\text{aux} + P_\alpha + P_\text{ohm} = P_\text{transp} + P_\text{rad}. \tag{1.3}$$

The external heating systems that generate the auxiliary power P_{aux} are briefly discussed in section 1.2.2, along with the intrinsic self-heating alpha power P_α and the Ohmic heating P_{ohm} (present if there is a loop voltage around the plasma). The power losses are due to radial heat transport and processes that radiate energy away from the plasma, leading to the P_{transp} and P_{rad} terms respectively. Transient events, such as Edge-Localized Modes (ELMs) and other magnetohydrodynamic (MHD) activity, can cause additional losses of particles and energy [10, 11].

The ability of a fusion plasma to retain its energy is quantified by the *energy confinement time*, formally defined as the e-folding relaxation time of the thermal energy stored in the plasma (W_{th}) due to losses,

$$\tau_{\mathrm{E}} = \frac{W_{\mathrm{th}}}{P_{\mathrm{loss}}}, \qquad W_{\mathrm{th}} = \frac{3}{2}\int_V p\,\mathrm{d}V, \tag{1.4}$$

where p is the total plasma pressure and V is the confined plasma volume. A high τ_{E} is naturally desired for a better fusion performance, since it is a measure of the efficiency of energy insulation in the plasma.

An ideal operational regime for a fusion device is *ignition*, where the alpha heating produced by the fusion reactions is able to compensate the energy losses and maintain thermonuclear conditions by itself, rendering auxiliary heating unnecessary. Ignition can be achieved when the *triple product* of density (n), temperature (T) and confinement time exceeds a specific threshold [12], so the value of $nT\tau_{\mathrm{E}}$ serves as a figure of merit for the performance of a fusion device.

Full ignition is however not a strict requirement for viable energy generation, as long as the power generated through fusion reactions, P_{fus}, is significantly larger than the power invested for operation through auxiliary heating. This is quantified by the *fusion power multiplication factor*, defined as $Q_{\mathrm{fus}} = P_{\mathrm{fus}}/P_{\mathrm{aux}}$. Considering unavoidable inefficiencies in power plant systems, commercial operation is expected to require $Q_{\mathrm{fus}} \gg 1$ [13]. Break-even at $Q_{\mathrm{fus}} = 1$ has so far not been achieved in MCF, with a record of $Q_{\mathrm{fus}} \approx 0.64$ set by the Joint European Torus (JET) [14]. Recently, laser fusion experiments have demonstrated $Q_{\mathrm{fus}} > 1$ in nanosecond implosions [15, 16], producing 3.15 MJ of fusion energy in December 2022. The current fusion energy record is JET's 69 MJ [17], set in its final campaign in December 2023.

The goal of next-generation fusion devices like ITER and SPARC is to demonstrate the feasibility of nuclear fusion for energy generation, in the former case by achieving $Q_{\mathrm{fus}} = 10$, producing 500 MW of fusion power from 50 MW of input heating power [18], and in the latter by reaching $Q_{\mathrm{fus}} > 2$ [19] with $P_{\mathrm{aux}} = 25$ MW.

1.2 The tokamak

In order to avoid end losses during the motion of the charged particles along the magnetic field lines, a toroidal geometry is typically used for the plasma. However, a purely toroidal magnetic field B_φ cannot provide stable confinement, due to the drifts caused by its inherent $1/R$ dependence (where R is the major radius coordinate of the torus) which lead to a fast loss of the plasma particles. A helical magnetic field that connects the High Field Side (HFS) and Low Field Side (LFS) of the device, compensating the outward drift of particles, is therefore necessary. The two leading MCF concepts, the *tokamak* and the *stellarator*, differ in the way they generate such a field. In tokamaks, a poloidal field component B_θ is produced by a toroidal current that is induced in the plasma, maintaining a 2D axisymmetric configuration. In stellarators, a non-axisymmetric magnetic topology is generated, typically employing complex 3D coils, without the need for a plasma current. The main advantages of stellarators are an intrinsic steady-state operation and the avoidance of current-driven instabilities. However, tokamaks have demonstrated superior plasma confinement so far. The work of this thesis focuses on tokamaks, in particular modelling ASDEX Upgrade (AUG) experiments and predicting ITER plasmas.

1.2.1 Magnetic configuration

Tokamaks employ an array of coil systems to provide the confining magnetic field. The B_φ component is generated by toroidal field coils, while the plasma current I_p that produces the B_θ component is driven into the plasma by a central solenoid, which acts as the primary winding of a transformer whose secondary winding is the (conducting) plasma itself [20]. This inherently requires a transient state, leading to a pulsed operation of tokamaks. Advanced scenarios with high non-inductive current fractions are being developed for stationary operation [21], profiting from current drive by external heating methods and the intrinsic *bootstrap* current (j_{bs}) generated by pressure gradients and the toroidicity of the system [22]. An additional vertical field, necessary for plasma positioning and shaping, is produced by vertical field coils. This magnetic configuration is shown in figure 1.1(a). Finally, smaller in-vessel coils are used to correct field deviations and mitigate plasma instabilities [23].

A plasma equilibrium is reached when the compression force due to the magnetic field and the current density $\mathbf{j}$ balances the expansion due to the pressure gradient,

$$\nabla p = \mathbf{j} \times \mathbf{B}. \tag{1.5}$$

In equilibrium, the axisymmetry of the tokamak guarantees the existence of nested magnetic flux surfaces traced by non-closing field lines [24], where the pressure is constant. This motivates the use of *flux coordinates* (ψ, θ, φ), where the radial coordinate is given by regions of constant poloidal magnetic flux ψ and the angular coordinates are given by the poloidal and toroidal directions (θ, φ) respectively. In these coordinates, the magnetic field and current density take the useful form

$$\mathbf{B} = I\nabla\varphi + \nabla\varphi \times \nabla\psi, \quad \mu_0\,\mathbf{j} = R^2\,\nabla\cdot(R^{-2}\nabla\psi)\nabla\varphi + \nabla I \times \nabla\varphi\,, \tag{1.6}$$

where $I(\psi) = RB_\varphi$ is a flux function, i.e. only a function of ψ. The helicity of the magnetic field is characterized by the *safety factor* q, which measures the number of turns $\mathbf{B}$ takes in the toroidal direction per turn in the poloidal direction, such that

$$q = \frac{1}{2\pi}\oint \frac{\mathbf{B}\cdot\nabla\varphi}{\mathbf{B}\cdot\nabla\theta}\,\mathrm{d}\theta, \tag{1.7}$$

integrating along field lines in one poloidal turn. It increases with B_φ and decreases with I_p, and its name stems from the fact that it is an important parameter for MHD stability, where in particular $q > 2$ at the edge is required [25]. The field components can be related in a simple way for circular flux surfaces as $B_\varphi/B_\theta \approx q/\epsilon$. The local inverse aspect ratio ϵ is defined as the ratio between the minor radius,

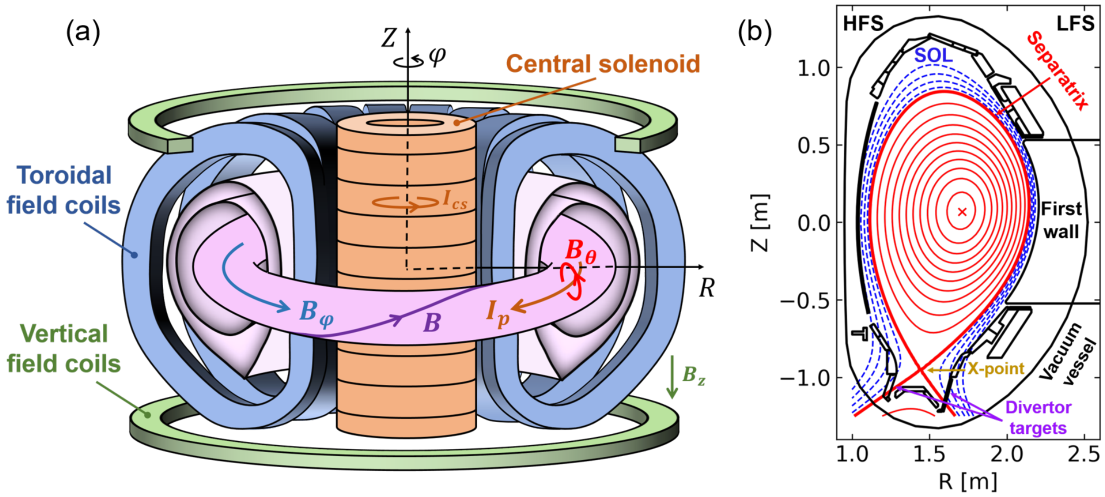

Figure 1.1: (a) Schematic representation of a tokamak. (b) Magnetic equilibrium in the divertor configuration, from a poloidal cross section of an AUG discharge.

$r = (R_{\max} - R_{\min})/2$ at each flux surface, and the major radius at the magnetic axis, R_0. In conventional tokamaks with $\epsilon/q \ll 1$, this leads to $B_\varphi \gg B_\theta$.

A final important element of the magnetic geometry of a tokamak is the plasma boundary. Two main configurations have been historically employed. In the *limiter* concept, a solid structure is inserted in direct contact with the plasma, defining its Last Closed Flux Surface (LCFS). In the *divertor* concept, a magnetic configuration with a null in B_θ is produced by an additional poloidal field using a divertor coil current I_d flowing in the same direction as I_p. The location of this null is called the *X-point*, and the flux surface that passes through it is known as the *separatrix*, which defines the LCFS of this configuration. A solid structure – the divertor – cuts through the flux surfaces that surround I_d, leaving the confined region to be the closed surfaces surrounding I_p. Any particle that crosses the separatrix will then follow the open field lines to strike the divertor targets, depositing their energy. In general, the plasma outside the LCFS is known as Scrape-Off Layer (SOL), a narrow region whose properties are crucial for the operation of a fusion device. Divertors are currently favored over limiters, mainly due to reduced impurity contamination of the main plasma, improved energy confinement and more efficient pumping of the helium ash [26]. A divertor magnetic configuration is shown in figure 1.1(b).

1.2.2 Plasma heating

Different processes are employed to reach fusion-relevant temperatures in a tokamak.

The central solenoid provides a time-varying magnetic flux that induces a loop voltage around the plasma. The resulting parallel electric field produces an Ohmic current which also provides intrinsic **Ohmic heating**, caused by resistance to its flow by electron-ion collisions. In practice, this method reaches limited temperatures due to the decrease of plasma resistivity with temperature, as $\eta \sim T_e^{-3/2}$. Another self-heating mechanism is **alpha heating**, in which energetic alpha particles produced by fusion thermalize through collisions with the main plasma species, transferring their energy. The alpha power, $P_\alpha \approx P_{\text{fus}}/5$, becomes comparable to the auxiliary input power at $Q_{\mathrm{fus}} = 5$ (by definition). This is still far from current fusion performance but it is expected to be surpassed by ITER. Alpha heating will be the dominant heating mechanism in fusion reactors.

External auxiliary heating is necessary in devices without significant fusion reactions (all present-day tokamaks) or to reach thermonuclear conditions in a reactor starting from a cold plasma. Two main heating concepts are routinely applied in current devices. In **Neutral Beam Injection (NBI) heating**, beams of energetic neutral particles are introduced into the plasma, where they ionize and transfer their energy by collisional thermalization. The particles must be neutral to penetrate through the magnetic field. For **electromagnetic wave heating**, incident waves couple to the plasma at certain resonant frequencies, transferring their electromagnetic energy for kinetic energy of the particles. The Electron Cyclotron Resonance Heating (ECRH) system uses waves at frequencies of $\omega \sim \omega_{ce} \sim$ 100–200 GHz, in the microwave range, while the Ion Cyclotron Resonance Heating (ICRH) operates in radio-frequency, with $\omega \sim \omega_{ci} \sim$ 20–100 MHz. There is also Lower Hybrid (LH) heating at frequencies of a few GHz, resonating close to the frequency of a longitudinal oscillation of electrons and ions with $\omega \sim ((\omega_{ce}\omega_{ci})^{-1} + \omega_{pi}^{-2})^{-1/2}$, where $\omega_{pi} = (e^2 n_i/(\varepsilon_0 m_i))^{1/2}$ is the ion plasma oscillation frequency. Both NBI and wave heating contribute to non-inductive current drive (j_{cd}), while NBI also introduces torque in the system which can lead to strong toroidal rotation of the plasma.

1.2.3 Confinement regimes

During the course of fusion research, an unfavorable behavior of energy confinement that degrades with higher heating power was observed. The energy losses due to temperature-gradient-driven microinstabilities increase faster than the stored plasma energy as the heating power is increased. The temperature gradients cannot be increased significantly past a certain critical gradient, because the heat diffusivity grows non-linearly with temperature and its gradient, what is known as stiff transport. The core temperature is directly coupled to the edge temperature, but the latter is constrained by material limitations at the plasma facing components.

Fortunately, a spontaneous transition to an improved confinement regime takes place after exceeding an input power threshold, leading to an abrupt two-fold increase in τ_{E} [27]. This operational regime of high confinement is known as *H-mode*, with the previously standard regime becoming the *L-mode*, for low confinement. In H-modes a layer of strongly reduced transport develops at the edge [28], forming a thin region of steep density and temperature gradients, named *pedestal*, as it lifts the core profiles which have milder gradients [29]. Even though a degradation of confinement with power is still present, the fact that the temperatures and density at the top of this pedestal are significantly increased leads to higher boundary conditions for the stiff core profiles inside the pedestal top, meaning that the stored energy in H-modes is significantly higher than in L-mode.

Lacking a complete physical understanding of plasma transport, confinement can also be described using empirical scaling laws. A widely-used scaling for τ_{E} in terms of engineering parameters, developed using a multi-machine database [30], is

$$\tau_{\mathrm{E,IPB98(y,2)}} = 0.0562\, I_p^{0.93}\, B_\varphi^{0.15}\, P_{\mathrm{loss}}^{-0.69}\, \overline{n}_e^{0.41}\, A_i^{0.19}\, R^{1.97}\, \epsilon^{0.58}\, \kappa^{0.78}, \tag{1.8}$$

where the parameters are measured in {MA, T, MW, $10^{19}\,\mathrm{m}^{-3}$, – , m, – , –} respectively, and $\overline{n}_e$ is the line-averaged electron density, A_i is the average ion mass number and κ is the plasma elongation. The quality of confinement of a particular discharge can be characterized by the H-factor, defined as the ratio of the measured confinement time to the value of a given scaling, e.g. $H_{98(\mathrm{y},2)} = \tau_\mathrm{E}/\tau_{\mathrm{E,IPB98(y,2)}}$.

H-modes are an attractive operational regime due to the better fusion performance associated with higher confinement, but they also present drawbacks. Large ELMs typically present in this regime lead to strong cyclical heat loads at the PFCs. These are tolerable in current tokamaks but will not be allowed in reactors. The development of operational scenarios that improve on these issues while retaining good confinement is an important branch of present tokamak research.

1.3 Impurities and their role in the core-edge integration challenge of fusion devices

Any particle species in a fusion plasma other than the fuel ions and the electrons is considered an impurity. Impurities are introduced intrinsically during operation of the device: helium is produced in the fusion reactions, whereas different elements enter the system due to plasma-wall interactions. Extrinsic impurities can also be purposefully deployed into the plasma through gas puffing and pellet injection.

The operation of future fusion reactors requires the simultaneous fulfillment of good core confinement (for better fusion power performance) and tolerable heat and particle exhaust at the edge (to avoid damaging to the reactor structures). In principle these two requirements seem incompatible, and the integration of a hot core with a cold edge is a fundamental challenge in fusion research.

Impurities are an unavoidable component of fusion plasmas, and they play fundamental roles in this core-edge integration. Impurity accumulation in the core has deleterious effects on fusion performance, mainly due to radiative cooling by heavy impurities and fuel dilution by light impurities, and it must be avoided. On the other hand, controlled injection of impurities at the edge is necessary to achieve an acceptable power exhaust, since they radiate energy away uniformly, reducing the localized heat flux at the divertor. In a fusion reactor, these effects are potentially prohibitive and indispensable for operation, respectively. Modelling the transport of impurities and their effects on the plasma is the main objective of this thesis.

1.3.1 Radiative cooling and fuel dilution

The choice of plasma-facing materials is delicate, as it can greatly impact plasma performance. Historically, carbon fiber composite (CFC) walls have often been used for their heat shock resistance without direct sublimation and the low charge number Z of the material. However, in preparation for next-generation devices, several machines have transitioned to all-metal walls. Tungsten (W) has been selected as the material that will receive the peak heat fluxes at the divertors of ITER [31] and SPARC [19]. Its advantages are low tritium retention (which is a show-stopper for CFC walls in a reactor), low sputtering rate, and high melting point [31]. The price to pay is the presence of a high-Z material that contaminates the plasma more efficiently. This makes tungsten a particularly relevant impurity in fusion. AUG is an example of a device with full tungsten divertor and walls [32].

Two main deleterious effects on fusion plasma performance are caused by impurities. The first of these processes is radiative cooling, in which impurities radiate energy away from the plasma, cooling down the fuel below thermonuclear conditions. The power radiated by impurities in a plasma can be calculated as

$$P_{\mathrm{rad}}^{\mathrm{imp}} = \int_V n_e \sum_z n_z L_z \,\mathrm{d}V \tag{1.9}$$

where L_z $[\mathrm{W\,m^3}]$ is the cooling factor of the given species, which is a strong function of the electron temperature [33]. It encompasses different atomic processes that lead to the emission of electromagnetic radiation. Line radiation emitted by partially-ionized heavy impurities is typically the dominant radiation channel in tokamak plasmas [34]. Other radiative loss mechanisms such as Bremsstrahlung and synchrotron radiation are discussed in section 4.1.

Increased radiative cooling requires more auxiliary heating to maintain power balance at a given temperature. A strong core accumulation of impurities can lead to radiation losses which surpass the heating power in the plasma, causing a radiative collapse. This is exemplified in figure 1.2, where time traces of AUG discharge #30484 show that a large increase in core tungsten concentration causes the radiated power to exceed the total auxiliary heating at around 2.3 s, leading to a prompt loss of central electron temperature and degradation of confinement (the H-factor decrease indicates that the H-mode is lost). Shortly after $P_{\mathrm{rad}} > P_{\mathrm{aux}}$ a disruption was triggered and the discharge was terminated by the control systems.

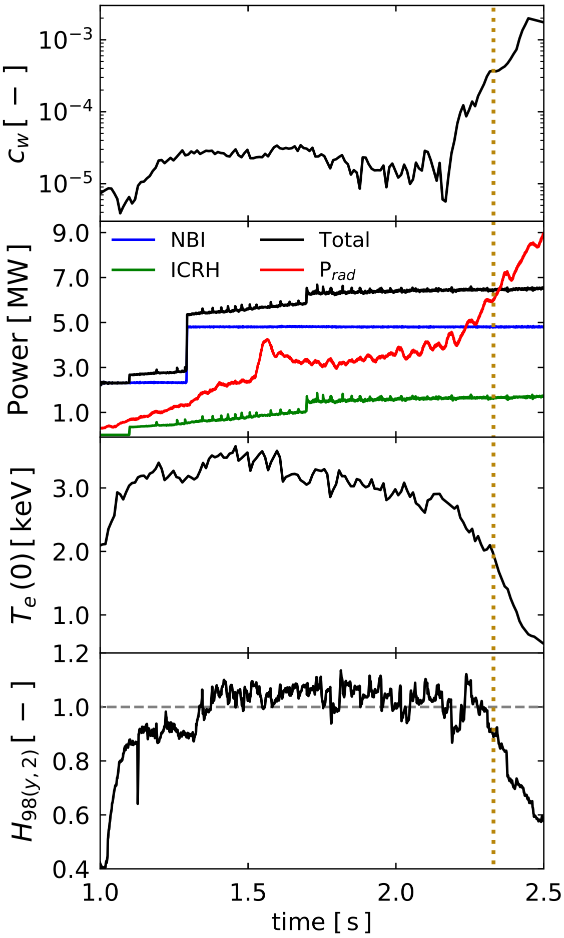

Figure 1.2: Radiative collapse by tungsten accumulation in AUG pulse #30484.

The second detrimental effect of impurities is fuel dilution. The quasi-neutrality property of plasmas indicates that, macroscopically, the (negative) electron charge density and the (positive) charge density of all the ions must balance each other out, such that $n_e = \sum Z_i n_i$. Since tokamaks are characterized by an upper limit on the allowed electron density at a given current [35], n_e is typically actively controlled with the fuelling actuators to stay below this density limit. However, impurities entering the plasma act as electron sources when they become ionized, meaning that the source of fuel neutrals injected in the plasma must be reduced, thereby decreasing the amount of fuel ions. In terms of the concentration of each species, $c_\sigma = n_\sigma / n_e$, this implies for the fuel ions that

$$c_{\mathrm{DT}} = 1 - 2\, c_{\mathrm{He}} - \sum_{z \geq 3} Z\, c_z < 1, \tag{1.10}$$

where the helium concentration is explicitly written because it is the one truly unavoidable impurity in a reactor even in ideal conditions, being the product of the D–T fusion process in the core. The produced fusion power is given by

$$P_{\mathrm{fus}} = \frac{1}{4}\, E_{\mathrm{fus}} \int_V \langle \sigma v \rangle\, n_{\mathrm{DT}}^2 \,\mathrm{d}V = \frac{1}{4}\, E_{\mathrm{fus}} \int_V \langle \sigma v \rangle\, c_{\mathrm{DT}}^2\, n_e^2 \,\mathrm{d}V \tag{1.11}$$

where $E_{\mathrm{fus}} = 17.6$ MeV is the energy produced by each fusion reaction and $\langle \sigma v \rangle$ is the reactivity of the D–T process. At a given pressure, an increase in the impurity content dilutes the D–T fuel, reducing the concentration of the hydrogenic isotopes. It follows from equation (1.11) that concentrations of 5% He ash and 1% Ne (as potential seeding species) yield a 36% reduction of the produced fusion power, as a simple example. This effect is due mostly to low-Z impurities, which become fully stripped at much lower temperatures and radiate via less intense Bremmstrahlung, allowing for higher tolerable concentrations. High-Z impurities would cause a radiative collapse long before they can significantly dilute the fuel.

The combination of light impurity content (e.g. helium ash) that dilutes the fuel and heavy impurities that generate radiative energy losses (e.g. sputtered tungsten transported into the confined plasma) can severely restrict the operational space of a fusion reactor [36–38]. Predicting their behavior and effects is therefore essential.

1.3.2 Power exhaust and impurity seeding

Impurities can nonetheless be useful, even necessary, during the operation of a high-power magnetic confinement device. Excess heat and particles crossing the separatrix are rapidly transported parallel to the open field lines through the scrape-off layer, being deposited to the divertor targets. A suitable power exhaust scheme must be implemented in next-generation fusion reactors such that localized overheating of the targets is avoided and their erosion is limited. For currently envisioned tungsten divertors, tolerable power exhaust includes maintaining the heat loads below 10 $\mathrm{MW\,m^{-2}}$ (the operational limit of the material) and the target temperature below 5 eV (to avoid excessive sputtering) [31].

A promising technique to achieve these requirements is impurity seeding, in which a controlled amount of impurities is injected such that the same radiative dissipation of plasma energy that is so problematic in the core allows for the desired colder peripheral conditions. If suitable species are used (low to mid-Z impurities that become fully stripped at lower temperatures), the cooling factor L_z is maximum at the plasma edge and low in the core. This energy is radiated volumetrically, so it is deposited uniformly in a wider area on the reactor walls, unlike the energy carried by charged particles which is deposited in a very localized region on the magnetic strike points at the divertor targets.

Impurity seeding is routinely employed in present-day devices, in preparation for high-power reactors for which it will be indispensable [39]. Figure 1.3 shows an example of an AUG experiment where high Argon (Ar) gas puffing was applied, and bolometric measurements show a corresponding increase in the power radiated inside the confined plasma, reducing the power crossing the separatrix.

Different gases are used for impurity seeding in fusion plasmas. Nitrogen (N) is routinely applied for divertor cooling in AUG and JET [40]. However, being chemically active, N can pose challenges for the tritium supply in future fusion environments by forming tritiated ammonia (NT_3) [41–43], affecting the duty cycle of the power plant. Noble gases are preferred in this sense. Neon (Ne) is an intermediate Z element that is planned as the primary seeding species in the ITER baseline scenario [44]. For reactors with even higher core heating by alpha power, like EU-DEMO [45], more efficient radiators with a higher Z such as Ar, Krypton (Kr) or Xenon (Xe) are considered to meet requirements of high core radiated power fractions ($f_{\mathrm{rad}} = P_{\mathrm{rad}}/P_{\mathrm{heat}} > 50\%$) without excessive fuel dilution [39]. Plasma scenarios with high impurity radiation are presently being investigated to address power exhaust in future reactors [46–50].

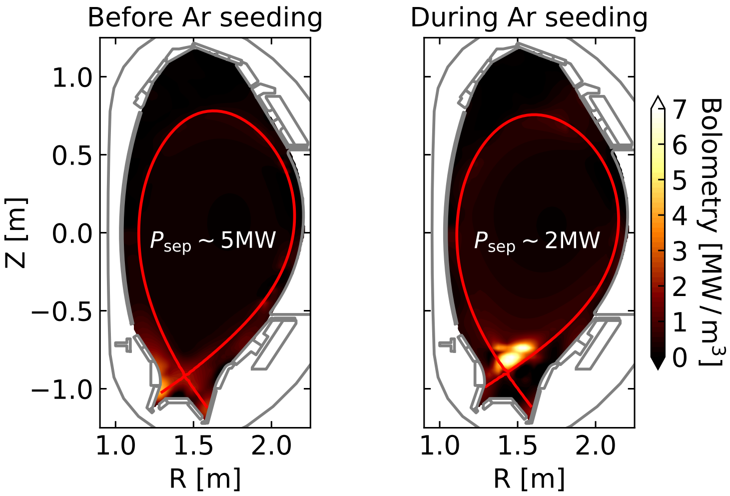

Figure 1.3: Radiated power measurements during a phase without impurity seeding and one with high Argon seeding in AUG pulse #37041.

1.3.3 Impact on confinement

The effect of impurities on energy confinement is an important aspect of plasma scenarios with impurity seeding for power exhaust control. The presence of impurities can reduce core turbulent heat transport by diluting the main ions, which has a stabilizing effect on the turbulence [51–55], thereby increasing confinement. However, the influence of impurity radiation on pedestal transport affects the stability of H-mode scenarios in general, and seeded H-modes in particular, leading to mixed observations of plasma confinement degradation or enhancement [56–60]. The transition from carbon to metallic walls in AUG and JET led to a decrease on the quality of confinement that could be partially recovered with seeding of low and mid-Z impurities (N, Ne) [57,61,62]. Overall, the effects of impurity radiation, main plasma confinement (core transport and pedestal structure) and impurity transport couple non-linearly.

1.3.4 Other effects and uses of impurities in fusion plasmas

Impurities play a role in several other processes in fusion plasmas. Some are listed below to illustrate the overarching influence of impurities in tokamaks, even if not all are directly of interest for this thesis.

- Disruptions are a very fast loss of thermal energy and plasma current [63]. They cause large heat loads during the thermal quench, electromagnetic forces on the vessel walls during the current quench, and the formation of runaway electron beams (electrons accelerated to relativistic speeds) [64]. Going to reactor conditions, these effects are intolerable and need to be mitigated in case they are triggered. Two main disruption mitigation systems are massive gas injection (MGI) and shattered pellet injection (SPI), where a large amount of impurities are introduced in very short time frame to terminate the discharge in a more controlled way. These systems must satisfy stringent requirements of rapid shutdown and uniform dissipation of plasma stored energy [65–67].

- An important diagnostic to measure ion temperatures, toroidal rotation speeds and impurity densities is Charge-Exchange Recombination Spectroscopy (CXRS). The physical principle of CXRS systems is the following: a neutral atom from the NBI beam reacts with a fully-stripped low-Z impurity ion, transferring an electron to the impurity. The impurity ion, now with charge $Z-1$, is left in an excited state, subsequently relaxing into a lower energy level and emitting a photon with a characteristic spectrum that is measured by the spectrometers [68]. The intensity, Doppler shift and broadening of this spectrum provides information about the impurity ion temperature, velocity distribution and density [69–71].

- The effective plasma charge, which is quantified as

  $$Z_{\mathrm{eff}} \equiv \frac{\sum_{\mathrm{all\,ions}} Z_{\mathrm{ion}}^2\, n_{\mathrm{ion}}}{\sum_{\mathrm{all\,ions}} Z_{\mathrm{ion}}\, n_{\mathrm{ion}}} = \frac{\sum_i Z_i^2\, n_i}{n_e} = 1 + \sum_{z\geq 2} Z(Z-1)\, c_z \geq 1\,, \tag{1.12}$$

  characterizes the effect of all impurities in general on many collisional processes. For instance, the plasma conductivity decreases with Z_{eff} because there are more highly-charged ions opposing the flow of electrons. A more resistive plasma increases flux consumption and ultimately can affect the duration of an inductive tokamak pulse. Likewise, impurities influence the interactions between the energetic neutral beam from NBI and the plasma, enhancing the ionization of beam neutrals (the fast ion birth rate is proportional to Z_{eff}) and increasing their thermalization [72, 73]. NBI current drive is possible because the ion current caused by fast neutral ionization is not exactly balanced by the electron current arising from slowing down processes, due to the presence of impurities, such that $j_{\mathrm{nbi}} \propto (1 - Z_{\mathrm{nbi}}/Z_{\mathrm{eff}})$ [74], with typically $Z_{\mathrm{nbi}} = 1$.

- Periodic wall conditioning has been shown to increase plasma performance and reproducibility of operational scenarios [75] by reducing contamination with high-Z impurities and controlling recycling of hydrogenic isotopes at the PFCs [76]. A routine technique at AUG is the *boronization*, in which a thin coating of boron (B) is deposited on the walls. The erosion of the B layer serves as a source of this species into the plasma, causing B to be a relevant low-Z impurity in our transport analysis of AUG.

1.4 Integrated modelling of tokamaks

Fusion plasmas are complex systems. Coupled physical processes span orders of magnitude in temporal and spatial scales, from magnetohydrodynamic equilibrium and stability, to particle gyromotion, to turbulence and the transport it causes, to the full length of a tokamak pulse and the size of the device. Simultaneously, external sources of heat, particles and magnetic flux can change in time as actuators that the tokamak operators use to control the plasma.

To model such a system, it is useful to identify characteristic time and length scales for these physical processes and separate them whenever possible, such that different models for specific physics elements can be applied (instead of a single model that covers all of the time and length scales) [77]. For example, since the time scales of turbulence are much faster than the transport time scales, we can consider turbulence saturation to develop almost instantaneously as compared to the evolution of the temperature and density profiles.

Integrated modelling refers to the simulation of the fundamental quantities of a fusion plasma, such as the radial profiles of temperature, density and current and their time evolution, along with the magnetic equilibrium. For this purpose, suitable models for transport, sources and magnetic geometry are necessary. This is typically done by coupling, or integrating, separate modules for the calculation of each of these physics and engineering elements. The code that we will use throughout this thesis for integrated modelling of tokamak plasmas is ASTRA [78,79]. ASTRA is a flexible modelling suite where different descriptions of transport, sources and magnetic equilibrium are put together to obtain a comprehensive prediction of all the required plasma profiles or for interpretative studies of experiments.

In tokamak geometry, the plasma configuration is determined by the Grad-Shafranov equation, which is a convenient 2D form of the magnetic equilibrium (equation (1.5)) in (R, Z) coordinates [25]. The toroidal symmetry of the tokamak can be exploited to express the 3D vectors of magnetic field and current density in terms of the scalar functions I (related to the poloidal current) and ψ (related to the poloidal flux), like in equation (1.6). Different equilibrium codes can be selected in ASTRA [80,81] to solve the (non-linear) Grad-Shafranov equation,

$$R^2\,\nabla\cdot\left(\frac{\nabla\psi}{R^2}\right) = R\frac{\partial}{\partial R}\left(\frac{1}{R}\frac{\partial\psi}{\partial R}\right) + \frac{\partial^2\psi}{\partial Z^2} \equiv \Delta^*\psi = -\mu_0\,R^2\frac{\mathrm{d}p}{\mathrm{d}\psi} - I\frac{\mathrm{d}I}{\mathrm{d}\psi}\,, \tag{1.13}$$

for $\psi(R, Z)$. The total plasma pressure, $p = n_eT_e + n_iT_i$, is determined by transport. The heat transport equations describe the time evolution of the electron and ion temperatures in the presence of sources and transport fluxes, such that

$$\begin{aligned} \frac{3}{2}\frac{\partial(n_eT_e)}{\partial t} - \nabla\cdot(n_e\chi_e\nabla T_e) &= q_{\mathrm{ohm}} + q_e^{\mathrm{ecr}} + q_e^{\mathrm{nbi}} + q_e^{\mathrm{icr}} + q_e^{\alpha} - q_{\mathrm{rad}} - q_{e\to i}^{\mathrm{coll}}\,, \\ \frac{3}{2}\frac{\partial(n_iT_i)}{\partial t} - \nabla\cdot(n_i\chi_i\nabla T_i) &= q_i^{\mathrm{nbi}} + q_i^{\mathrm{icr}} + q_i^{\alpha} + q_{e\to i}^{\mathrm{coll}}\,. \end{aligned} \tag{1.14}$$

A stationary condition is reached when the temperature profiles develop a gradient such that the fluxes due to Fourier-like heat diffusion balance the sources and sinks of energy into the system.

On the right-hand-side of equations (1.14) are the sources and sinks of heat, in terms of power densities, deposited by the heating mechanisms and removed by the radiative losses, with also the collisional heat exchange between electrons and ions (present whenever there is a difference between their respective temperatures) which couples both equations. The heat diffusivities $\chi_{e,i}$ characterize the capacity of plasmas to lose heat, which is (unfortunately) very high: typical values of heat diffusivities for plasmas ($\sim 1.0\ \mathrm{m^2\,s^{-1}}$) are of the order of 10^7 times larger than the heat diffusivity of room temperature water [82], for comparison.

The equations for the transport of particles are discussed in more detail later on, with particular interest on the evolution equation for impurity densities. Furthermore, the final transport equation in ASTRA is the current diffusion, which determines the time evolution of the poloidal flux by assuming a longitudinal Ohm's law of the form $j_\parallel = \sigma_\parallel E_\parallel + j_{\mathrm{bs}} + j_{\mathrm{cd}}$, where $\sigma_\parallel$ is the parallel conductivity and $E_\parallel$ is the parallel electric field due to the loop voltage around the tokamak.

Integrated models that simultaneously solve 1D transport equations and the 2D equilibrium are commonly referred to as 1.5D modelling frameworks. The solution of the equilibrium equation determines the magnetic geometry, which in turn affects transport, from which the pressure gradient and current density in the equilibrium are calculated. These equations are strongly and non-linearly coupled, which causes tokamak modelling to be a complex endeavor. However, the continuous development of predictive models over the last decades has allowed for the successful simulation of tokamak plasmas [83], validating these capabilities on experiments and paving the way for a more confident extrapolation to future reactors by means of theory-based models instead of relying purely on empirical scaling laws.

1.5 Outline and objectives of this thesis

The main goal of this thesis is to self-consistently simulate the transport and effects of impurities in tokamak plasmas within the context of integrated modelling, applying physics-based transport models only.

For this purpose, we shall first summarize the most relevant elements in the theory of impurity transport in chapter 2. Chapter 3 will then present the derivation of an analytical model for the calculation of collisional impurity transport coefficients including the crucial effects of toroidal plasma rotation. With the addition of this model, a modelling workflow which integrates impurity transport and radiation to the ASTRA modules for the main plasma transport, heat and particle sources, and magnetic equilibrium, will be developed and tested in chapter 4. The integrated modelling framework will be employed in chapter 5 to simulate ASDEX Upgrade L-mode plasmas from the magnetic axis to the separatrix including multiple impurity species, to validate the model against a robust suite of diagnostics measuring the main plasma profiles, the impurity densities and the radiated powers. In chapter 6, we will demonstrate the capability of the workflow to quantitatively reproduce the beneficial effects of central wave heating in controlling high-Z impurity accumulation in the core of beam-heated H-mode plasmas. Having validated the workflow, we will obtain predictions of the transport and effects of tungsten in ITER plasma conditions at full current and high power. Finally, a summary of the results, concluding remarks, and plans for future work will be provided in chapter 7.

Chapter 2

Theory of impurity transport in tokamaks

Unlike for the main plasma species, heavy impurity transport requires the description of parallel, collisional and turbulent transport simultaneously and on equal footing. In this chapter we will review theoretical elements that will be important for the modelling of impurities, particularly tungsten, in the following chapters.

2.1 Kinetic and fluid descriptions of plasmas

The motion of the $\mathcal{O}(10^{21} - 10^{23})$ charged particles in a fusion plasma can be described self-consistently. Newton's second law is considered for each particle, with the acceleration being caused by the Lorentz force. The electric and magnetic fields can be both externally applied and generated by the particles themselves, through charge and current densities (which in turn depend on the position and velocity of the particles) that serve as source terms in Maxwell's equations. In practice, however, describing a plasma in this way becomes computationally prohibitive.

A statistical description of the behavior of each plasma species can be constructed instead, with the help of the distribution function $f_\sigma(\mathbf{x}, \mathbf{v}, t)$. Here, σ represents the particle species ('e' for electrons, 'i' for main ions and 'z' for the different impurity species), while $(\mathbf{x}, \mathbf{v})$ are the position-velocity coordinates in phase space and t is time. The distribution function is defined such that its value at any point gives the number of particles per phase space volume element at that point. The average number density of particles in real space is then given by

$$n_\sigma(\mathbf{x}, t) = \int f_\sigma \, \mathrm{d}^3 v. \tag{2.1}$$

Other relevant mean quantities can be obtained by taking velocity-space averages of the distribution function. The mean or fluid velocity of the particles is

$$\boldsymbol{u_\sigma}(\mathbf{x}, t) = \frac{1}{n_\sigma} \int \mathbf{v} f_\sigma \, \mathrm{d}^3 v. \tag{2.2}$$

The temperature of a species is defined as

$$\frac{3}{2} T_\sigma(\mathbf{x}, t) = \frac{1}{n_\sigma} \int \frac{1}{2} m_\sigma (\mathbf{v} - \boldsymbol{u_\sigma})^2 f_\sigma \, \mathrm{d}^3 v, \tag{2.3}$$

which is simply stating that the total energy is the sum of the kinetic energy of the mean flow and the thermal energy due to random particle motion. A factor of the Boltzmann constant is implied, so T_σ has units of energy. The pressure tensor is

$$\mathbf{P}_{\boldsymbol{\sigma}}(\mathbf{x},t) = \int m_\sigma(\mathbf{v}-\boldsymbol{u}_{\boldsymbol{\sigma}}) \otimes (\mathbf{v}-\boldsymbol{u}_{\boldsymbol{\sigma}}) f_\sigma \,\mathrm{d}^3v = p_\sigma \,\mathbf{I} + \boldsymbol{\pi}_{\boldsymbol{\sigma}}, \tag{2.4}$$

and it is usually decomposed into the isotropic pressure, which satisfies $p_\sigma = n_\sigma T_\sigma$, and the anisotropic stress, described by the viscosity tensor $\boldsymbol{\pi}_{\boldsymbol{\sigma}}$.

The evolution of the distribution function (and therefore of all the previous mean quantities) under the influence of macroscopic forces, like electromagnetic fields, and microscopic interactions, such as collisions, is governed by the kinetic equation

$$\frac{\partial f_\sigma}{\partial t} + \mathbf{v}\cdot\frac{\partial f_\sigma}{\partial \mathbf{x}} + \frac{q_\sigma}{m_\sigma}(\mathbf{E}+\mathbf{v}\times\mathbf{B})\cdot\frac{\partial f_\sigma}{\partial \mathbf{v}} = \left(\frac{\partial f_\sigma}{\partial t}\right)_{\mathrm{coll}} + \left(\frac{\partial f_\sigma}{\partial t}\right)_{\mathrm{src}}. \tag{2.5}$$

Here, $\mathbf{E}$ and $\mathbf{B}$ are regarded as the macroscopic fields, whose variation due to the discreteness of the charged particles is averaged out. The change in the distribution function due to microscopic electromagnetic interactions (collisions) is grouped into the collision operator $\mathbb{C}_\sigma[f_\sigma] = (\partial f_\sigma/\partial t)_{\mathrm{coll}}$. Sources, such as heat and particles deposited by auxiliary heating systems, are described by the $(\partial f_\sigma/\partial t)_{\mathrm{src}}$ term.

The fluid description of a plasma consists of relating the different mean plasma quantities, equations (2.1)–(2.3), to the corresponding fluxes

$$\boldsymbol{\Gamma}_{\boldsymbol{\sigma}} = \int \mathbf{v} f_\sigma \,\mathrm{d}^3v, \quad \boldsymbol{\Pi}_{\boldsymbol{\sigma}} = \int m_\sigma \mathbf{v}\otimes\mathbf{v}\, f_\sigma \,\mathrm{d}^3v, \quad \boldsymbol{q}_{\boldsymbol{\sigma}} = \frac{1}{2}\int m_\sigma (v-u_\sigma)^2(\mathbf{v}-\boldsymbol{u}_{\boldsymbol{\sigma}}) f_\sigma \,\mathrm{d}^3v, \tag{2.6}$$

by taking velocity moments of the kinetic equation. Here, the terms are the particle flux, the stress tensor (comprising momentum fluxes) and the heat flux. A suitable closure relation must be imposed, because the equation resulting from the k^{th} moment of f_σ involves fluid quantities that are solved for in the equation of the $(k+1)^{\mathrm{th}}$ moment. The dependence on velocity space is averaged out and some kinetic effects can be lost. On the other hand, in the kinetic description of a plasma one solves the kinetic equation for the distribution function, which is then integrated to obtain macroscopic quantities of interest. More physics is retained, however solving the full (6+1)D equation can become computationally impractical, in particular in the presence of a complex magnetic geometry and stochastic fluctuations of the system.

2.1.1 Scale separation in magnetized plasmas

Gyromotion

The presence of a strong magnetic field introduces characteristic length and time scales: the gyroradius and gyrofrequency (equation (1.2)). A crucial condition for confinement is to have a small gyroradius compared to the size of the reactor, which sets a lower limit on the necessary strength of $\mathbf{B}$; in turn, large magnetic fields lead to fast particle gyration. At typical $B \sim 3\,\mathrm{T}$, $T_\sigma \sim 5\,\mathrm{keV}$ we have $(\rho_e,\, \omega_{ce}^{-1}) \sim (\mu\mathrm{m}, \mathrm{ns})$, $(\rho_i,\, \omega_{ci}^{-1}) \sim (\mathrm{mm}, \mu\mathrm{s})$. We are often not interested in the exact position of a particle along its gyro-orbit but rather on its general motion across the device. A useful coordinate transformation is $(\mathbf{x}, \mathbf{v}) \to (\mathbf{X}_{\boldsymbol{\sigma}}, v_\parallel, v_\perp, \vartheta)$, with the guiding center position

$$\mathbf{X}_{\boldsymbol{\sigma}} = \mathbf{x} - \boldsymbol{\rho}_{\boldsymbol{\sigma}} = \mathbf{x} - \frac{\mathbf{b} \times \mathbf{v}}{\omega_{c\sigma}}, \tag{2.7}$$

and decomposing the velocity of a particle into the directions parallel and perpendicular to the magnetic field (since the dynamics in these directions are very different), the latter being restricted by gyration, such that

$$\mathbf{v} = v_\parallel \mathbf{b} + v_\perp (\cos\vartheta\, \mathbf{e_2} - \sin\vartheta\, \mathbf{e_1}), \qquad \mathbf{e_2} \times \mathbf{e_1} = \mathbf{b} \equiv \mathbf{B}/B, \tag{2.8}$$

where the gyro-angle ϑ satisfies $\dot{\vartheta} = \omega_{c\sigma}$. We can then reduce the dimensionality of the kinetic equation by removing the explicit dependence on ϑ with the gyro-average

$$\langle y(\mathbf{x}) \rangle_\vartheta = \frac{1}{2\pi} \oint y(\mathbf{X}_{\boldsymbol{\sigma}} + \boldsymbol{\rho}_{\boldsymbol{\sigma}}(\vartheta))\, \mathrm{d}\vartheta \approx y(\mathbf{X}_{\boldsymbol{\sigma}}), \tag{2.9}$$

allowing us to have kinetic models with less stringent computational demands which, while still expensive, are more easily within reach of modern computational power.

A useful property of the gyro-average is that finite Larmor radius (FLR) effects can be retained in Fourier space as multiplication by a Bessel function,

$$\langle y \rangle_\vartheta = \sum_{\mathbf{k}} y_k\, e^{i\mathbf{k}\cdot\mathbf{X}_{\boldsymbol{\sigma}}} \frac{1}{2\pi} \oint e^{ik_\perp \rho_\sigma \sin\vartheta}\, \mathrm{d}\vartheta = \sum_{\mathbf{k}} J_0(k_\perp \rho_\sigma)\, y_k\, e^{i\mathbf{k}\cdot\mathbf{X}_{\boldsymbol{\sigma}}}, \tag{2.10}$$

where $k_\perp$ is the wavenumber perpendicular to the magnetic field.

Turbulent fluctuations

The thermodynamic gradients in a fusion plasma act as sources of free energy that can drive unstable a wide spectrum of micro-instabilities, which can amplify stochastic fluctuations in the electromagnetic fields, plasma density and temperature. This leads to plasma turbulence which, combined with the drift motion of particles caused by an inhomogeneous magnetic field, is responsible for the majority of transport of the main plasma species and a significant fraction of the transport of impurities.

Linear instabilities can grow and then saturate non-linearly. In core tokamak plasmas, the most relevant types of turbulence are the Ion Temperature Gradient (ITG) mode (driven by ion temperature gradients), Trapped Electron Mode (TEM) (driven by electron temperature and density gradients), and Electron Temperature Gradient (ETG) mode, which are electrostatic micro-instabilities. Electromagnetic micro-instabilities, such as kinetic-ballooning and micro-tearing modes (KBMs, MTMs), become relevant as the ratio between plasma and magnetic pressures, $\beta = p/(B^2/2\mu_0)$, increases and as we approach the periphery of the plasma.

We can decompose quantities of interest into background and fluctuating parts,

$$f_\sigma = F_\sigma + \delta f_\sigma, \qquad \phi = \Phi + \tilde{\phi}, \tag{2.11}$$

where the left expression implies that also the fluid densities and temperatures will have background and fluctuating components $n_\sigma + \tilde{n}_\sigma$, $T_\sigma + \tilde{T}_\sigma$. These are defined such that time averaging over time intervals larger than the fluctuation timescales ($\tilde{\tau} \gg 1/\omega_{\mathrm{turb}}$, where ω_{turb} is the fluctuation frequency) leads to $\langle \delta f_\sigma \rangle_{\tilde{\tau}} = 0$, $\langle \tilde{\phi} \rangle_{\tilde{\tau}} = 0$.

Orderings

From our discussion in this chapter so far, we can identify different time scales and length scales. We assume they can be ordered by the same small parameter as

$$\frac{\dot{F}_\sigma/F_\sigma}{\omega_{\text{turb}}} \sim \frac{\omega_{\text{turb}}}{\omega_{c\sigma}} \sim \frac{\delta f_\sigma}{F_\sigma} \sim \frac{\tilde{\phi}}{\Phi} \sim \frac{k_\parallel}{k_\perp} \sim \frac{\rho_{L\sigma}}{L_\perp} \equiv \rho_{*\sigma} \ll 1\,. \tag{2.12}$$

The first two terms are time scale orderings, and they indicate that fluctuations are much faster than the evolution of the background plasma and that gyrofrequency is much faster than the fluctuations. The next two are fluctuation amplitude orderings, which say that the fluctuations are small compared to the background fields and mean fluid variables. The last two are length scale orderings. Respectively, they indicate that the fluctuations perpendicular to the magnetic field happen on much lower length scales as in the parallel direction (thus turbulence in tokamaks is approximately 2D on the poloidal plane), and that gyro-radii are much smaller than the characteristic scales of the background gradients ($L_\perp^{-1} \sim |\nabla p/p|$). This last condition allows for a *local* description of the plasma (in contrast to a *global* description), in the sense that the plasma background does not change significantly within a gyro-radius. Throughout this thesis we will limit ourselves to local models.

In L-modes or in the core of H-modes $\rho_{L\sigma} \ll L_\perp$ is typically fulfilled, but it can fail in the steep gradient region of the H-mode pedestal. Likewise, close to the last closed flux surface and in the scrape-off layer the turbulent fluctuation amplitudes can be comparable to the background quantity itself, and one needs to consider the full distribution function and fields. This, in combination with the possible presence of electromagnetic modes and modes at electron length scales like the ETG mode, leads to a more complex edge turbulence compared to core turbulence.

The orderings of equation (2.12) allow us to expand both the background and the fluctuating components of the distribution function, such that

$$\begin{aligned} f_\sigma = F_\sigma + \delta f_\sigma = F_{0\sigma} + F_{1\sigma} + F_{2\sigma} + \mathcal{O}(\rho_{*\sigma}^3) \\ + \delta f_{1\sigma} + \delta f_{2\sigma} + \mathcal{O}(\rho_{*\sigma}^3). \end{aligned} \tag{2.13}$$

2.1.2 Drift-kinetic and gyrokinetic models

The motion of the gyro-center $\mathbf{X}_{\boldsymbol{\sigma}}$ is determined by parallel motion (with respect to $\mathbf{B}$), perpendicular drifts $\mathbf{v}_{\boldsymbol{d\sigma}}$ (discussed next), and the turbulent E×B drift (considered separately since it causes the majority of turbulent transport), such that

$$\begin{aligned} \frac{\mathrm{d}\mathbf{X}_{\boldsymbol{\sigma}}}{\mathrm{d}t} = v_\parallel \mathbf{b} + \frac{\mathbf{b} \times \left(\mu_\sigma \nabla B/m_\sigma + v_\parallel^2\, \mathbf{b}\cdot\nabla\,\mathbf{b}\right)}{\omega_{c\sigma}} + \frac{\mathbf{b}\times\nabla\Phi}{B} \\ + 2v_\parallel \frac{\boldsymbol{\Omega}_\perp}{\omega_{c\sigma}} - \frac{R\,\Omega_\varphi^2}{\omega_{c\sigma}}\mathbf{b}\times\nabla R + \frac{\mathbf{b}\times\nabla\langle\tilde{\phi}\rangle_\vartheta}{B} = \mathbf{v}_\parallel + \mathbf{v}_{\boldsymbol{d\sigma}} + \tilde{\mathbf{v}}_{\mathbf{E}}\,. \end{aligned} \tag{2.14}$$

The drift velocity $\mathbf{v}_{\boldsymbol{d\sigma}}$ is composed of ∇B and curvature drifts (where $\mu_\sigma = m_\sigma v_\perp^2/(2B)$ is the magnetic moment, an adiabatic invariant of motion), E×B drift due to background potentials, Coriolis drift due to plasma angular velocity $\boldsymbol{\Omega} \perp \mathbf{B}$, and centrifugal drift due to toroidal rotation with angular frequency Ω_φ. The drifts due to the magnetic geometry are ubiquitous, the (non-turbulent) E×B drift is present when an equilibrium radial electric field develops, and the rotational terms are kept since they can be relevant for heavy impurities (which have lower thermal speeds).

Inserting the expansion of f_σ into the kinetic equation (2.5), the lowest-order gyro-averaged equation has two surviving terms, parallel advection and collisions,

$$v_\parallel \mathbf{b} \cdot \frac{\partial F_{0\sigma}}{\partial \mathbf{X}_{\boldsymbol{\sigma}}} = \langle \mathbb{C}_\sigma[F_{0\sigma}] \rangle_\vartheta \ , \tag{2.15}$$

from where it can be shown that collisions drive the lowest order distribution function towards a local Maxwellian in a frame of reference co-moving with the plasma [84],

$$F_{0\sigma}(\mathbf{X}_{\boldsymbol{\sigma}}, \mathbf{v}, t) = n_\sigma(\mathbf{X}_{\boldsymbol{\sigma}}, t) \left[\frac{m_\sigma}{2\pi T_\sigma(\mathbf{X}_{\boldsymbol{\sigma}}, t)} \right]^{3/2} \exp\left\{ -\frac{m_\sigma \left[\mathbf{v} - \boldsymbol{u}_{\boldsymbol{\sigma}}(\mathbf{X}_{\boldsymbol{\sigma}}, t)\right]^2}{2T_\sigma(\mathbf{X}_{\boldsymbol{\sigma}}, t)} \right\}. \tag{2.16}$$

A system in thermodynamic equilibrium described by a purely Maxwellian distribution function does not generate the radial transport of particles and energy that is observed in fusion plasmas. Deviations from a Maxwellian distribution, $f_\sigma - F_{0\sigma}$, need to be calculated by considering next orders in the kinetic equation.

The mean and fluctuating quantities can be separated via the turbulence average $\langle \cdot \rangle_{\tilde{T}}$. Then, we can find the $\mathcal{O}(\rho_{*\sigma})$ correction to the background distribution function $F_{1\sigma}$, described by what is known as *neoclassical* theory, and the $\mathcal{O}(\rho_{*\sigma})$ fluctuating part of the distribution function $\delta f_{1\sigma}$, described by *gyrokinetic* theory.

The first-order Drift-Kinetic Equation (DKE) for $F_{1\sigma}$ is [85]

$$v_\parallel \mathbf{b} \cdot \frac{\partial F_{1\sigma}}{\partial \mathbf{X}_{\boldsymbol{\sigma}}} + \mathbf{v}_{\boldsymbol{d\sigma}} \cdot \frac{\partial F_{0\sigma}}{\partial \mathbf{X}_{\boldsymbol{\sigma}}} = \sum_{\sigma'} \Big(\mathbb{C}_{\sigma\sigma'}[F_{1\sigma}, F_{0\sigma'}] + \mathbb{C}_{\sigma\sigma'}[F_{0\sigma}, F_{1\sigma'}] \Big) \ , \tag{2.17}$$

and it can be solved to describe neoclassical transport. The right hand side is the linearized collision operator, describing collisions between species σ and σ', for which models of increasing complexity can be used [86–88].

For the turbulent component, it is convenient to split the perturbed distribution function into an adiabatic response and a gyrotropic distribution h_σ,

$$\delta f_{1\sigma} = -\frac{Z_\sigma e F_{0\sigma}}{T_\sigma} \tilde{\phi} + h_\sigma(\mathbf{X}_{\boldsymbol{\sigma}}, v_\parallel, v_\perp, t) \ , \tag{2.18}$$

such that in the collisionless limit, the first-order Gyrokinetic Equation (GKE) is

$$\frac{\partial h_\sigma}{\partial t} + \frac{\mathrm{d}\mathbf{X}_{\boldsymbol{\sigma}}}{\mathrm{d}t} \cdot \frac{\partial h_\sigma}{\partial \mathbf{X}_{\boldsymbol{\sigma}}} = \frac{Z_\sigma e F_{0\sigma}}{T_\sigma} \frac{\partial \langle \tilde{\phi} \rangle_\vartheta}{\partial t} - \tilde{\mathbf{v}}_{\mathbf{E}} \cdot \frac{\partial F_{0\sigma}}{\partial \mathbf{X}_{\boldsymbol{\sigma}}}, \tag{2.19}$$

where the right hand side terms act as sources. The solutions of equations (2.17) and (2.19), and the fluid models derived from them, are discussed in the following sections in terms of parallel and perpendicular particle transport they generate.

2.2 Parallel transport and poloidal asymmetries

The fast transport parallel to the magnetic field lines determines the poloidal distribution of the densities and temperatures of the plasma species on the flux surfaces. Other important effects of parallel transport in tokamaks, like the bootstrap current [22], are not considered in this section.

The densities of electrons and ions are typically poloidally symmetric, however for heavy and highly-charged impurities there are several mechanisms that can lead to poloidally asymmetric densities. In this section we will shortly summarize them, providing a theoretical picture without diving into rigorous details. More comprehensive reviews of both experimental evidence and theory of poloidal asymmetries in impurity densities can be found in [89, 90].

We consider the steady-state momentum balance equation of an impurity species by taking the first velocity moment of the drift-kinetic equation, such that

$$m_\sigma n_\sigma \left(\boldsymbol{u_\sigma} \cdot \nabla\right) \boldsymbol{u_\sigma} = -\nabla p_\sigma + Z_\sigma e\, n_\sigma(-\nabla\Phi + \boldsymbol{u_\sigma} \times \mathbf{B}) + \mathbf{F_\sigma} - \nabla \cdot \boldsymbol{\pi_\sigma}, \tag{2.20}$$

where the macroscopic friction force is the first moment of the collision operator

$$\mathbf{F_\sigma} = \int m_\sigma \mathbf{v}\, \mathbb{C}_\sigma[F_{1\sigma}]\, \mathrm{d}^3 v. \tag{2.21}$$

The parallel momentum balance equation is obtained by taking the projection of equation (2.20) with $\mathbf{b}$, such that

$$\frac{\nabla_\| n_\sigma}{n_\sigma} = -\frac{Z_\sigma e\, \nabla_\| \Phi}{T_\sigma} + \frac{m_\sigma \nabla_\| u_\sigma^2}{2T_\sigma} + \frac{F_{\sigma\|}}{n_\sigma T_\sigma} - \frac{\mathbf{b} \cdot \nabla \cdot \boldsymbol{\pi_\sigma}}{n_\sigma T_\sigma}, \tag{2.22}$$

where $\nabla_\| = (\mathbf{b} \cdot \nabla)$ and isothermal flux surfaces are assumed. Two main effects related to the first two terms on the right hand side will be discussed next. The third term, parallel friction, can have non-negligible effects on the poloidal distribution of heavy impurities in conditions where the collisionality is very high or the gradients are very strong [91–95]. However, these types of effects will not be included in the modelling of this thesis, since they are rather limited to the very edge of the confined plasma. The last term, parallel viscosity, is typically neglected.

2.2.1 Centrifugal asymmetries

The first effect, and most relevant for this thesis, that generates poloidally-asymmetric heavy impurity densities is the centrifugal force that arises from the toroidal rotation of the plasma. Tokamaks can present strong toroidal rotation speeds, primarily due to the torque introduced by the NBI heating systems. While the main plasma species are not strongly affected by these centrifugal forces, the larger mass of high-Z impurities (like W) causes them to localize on the outboard side of the device when the plasma rotates toroidally. This effect can be described by neglecting friction and viscosity in equation (2.22) and assuming rigid-body rotation with angular frequency Ω_φ, such that

$$\frac{\nabla_\| n_z}{n_z} = -\frac{Ze\nabla_\| \Phi}{T_z} + \frac{m_z \Omega_\varphi^2 \nabla_\| R^2}{2T_z}, \tag{2.23}$$

where $R(r,\theta)$ gives the major radius at all poloidal locations on a flux surface. This can be integrated to obtain the poloidal distribution of the impurity density,

$$n_z(r,\theta) = n_z(r,\theta_0)\exp\left\{-\frac{Ze\,\Phi^*(r,\theta,\theta_0)}{T_z} + \frac{m_z\Omega_\varphi^2}{2T_z}\left[R(r,\theta)^2 - R(r,\theta_0)^2\right]\right\}, \quad (2.24)$$

where θ_0 is a reference poloidal location, usually $\theta_0 = 0$ at the LFS. The perturbed background potential is $\Phi^*(r,\theta,\theta_0) = \Phi(r,\theta) - \Phi(r,\theta_0)$. Since the potential can be defined to be zero anywhere, we will take $\Phi(r,\theta_0 = 0) = 0$ such that $\Phi^*(\theta) = \Phi(\theta)$.

For convenience, we define the impurity normalized energy E_z as the sum of the terms inside the brackets in equation (2.24), such that $n_z(r,\theta) = n_z(r,\theta_0)\exp(-E_z)$.

The equilibrium electrostatic potential develops from the charge separation caused by the differing centrifugal forces on the electrons and ions, leading to an electric force that partially compensates the centrifugal force on the heavy impurity [96]. Φ^* can be calculated analytically by imposing quasi-neutrality, assuming an adiabatic electron response, bundling non-trace light impurities (with $Z/A \sim 1/2$) into a Z_{eff} term with a density asymmetry equivalent to that of the main ions, and considering the heavy impurities (with a stronger asymmetry) to be trace. In this way,

$$\frac{e\Phi^*}{T_e} = \frac{Z_{\text{eff}}\,T_i}{Z_{\text{eff}}\,T_e + T_i}\,\frac{R(r,\theta)^2 - R(r,\theta_0)^2}{R_0^2}\,M_i^2, \quad (2.25)$$

assuming collisional thermalization of impurities with the main ions, $T_z = T_i$, which we shall do throughout this thesis. Here, the main ion Mach number is defined as the ratio between the toroidal rotation speed and the thermal speed of the main ion,

$$M_i(r) = \frac{v_\varphi(r)}{v_{ti}(r)} = \frac{R_0\,\Omega_\varphi(r)}{\sqrt{2\,T_i(r)/m_i}}. \quad (2.26)$$

This normalized parameter will serve as a reference for the strength of the centrifugal effects on impurity transport, which typically scale as M_i^2. Typical values of M_i in core plasmas of conventional tokamaks are $0.2-0.3$, but the highest recorded value was obtained in KSTAR (which has low error fields), at $M_i \approx 0.8$ [97]. For ITER, the higher inertia of the plasma compared to the NBI torque means that the expected rotation is low [98, 99], at $M_i \leq 0.1$.

Replacing equation (2.25) into (2.24), a useful expression for the asymmetry of the impurity density can then be obtained as

$$\frac{n_z(r,\theta)}{n_z(r,\theta_0)} = \exp\left[\frac{R(r,\theta)^2 - R(r,\theta_0)^2}{R_0^2}\,M_z^*(r)^2\right], \quad (2.27)$$

where the *effective* impurity Mach number is defined as

$$M_z^{*2} = \left(\frac{A}{A_i} - \frac{Z}{Z_i}\,\frac{Z_{\text{eff}}}{Z_{\text{eff}} + T_i/T_e}\right) M_i^2, \quad (2.28)$$

which is smaller than the usual impurity Mach number $M_z^2 = (A/A_i)M_i^2$ due to the compensation by the electrostatic potential. Note that this is the Mach number that a heavy, trace impurity actually experiences, and it can still be super-sonic (meaning, the rotation speed of the impurity is larger than its thermal speed) as shown later on in figure 3.3(a). M_z^* is the central parameter used in the construction of the analytical model for neoclassical impurity transport described in chapter 3.

2.2.2 Temperature anisotropies

In plasmas with ICRH (and to a lesser extent, with NBI), ion species can present bi-Maxwellian distributions with different temperatures in the directions parallel and perpendicular to the magnetic field, $T_\parallel \leq T_\perp$. These temperature anisotropies (TA) perturb the background electrostatic potential [100–103], which affects the poloidal distribution of heavy impurity densities. In particular, TAs lead to an increased trapping of fast ions on the low field side, modifying the background electrostatic potential and pushing positively charged high-Z impurity ions to the high field side (HFS), partially compensating the LFS localization due to centrifugal effects.

The temperature anisotropy is characterized by the factor $\eta(\theta) = T_\perp(\theta)/T_\parallel - 1$. A profile of $T_\perp(\theta_0)/T_\parallel$ is shown later on for an AUG discharge with ICRH, in figure 6.6. The perturbed potential can be approximated as [100]

$$\frac{e\Phi^*_{\mathrm{TA}}}{T_e} \approx \frac{Z_m f_m\, \epsilon \cos\theta}{Z_{\mathrm{eff}} + T_e/T_i} \, \frac{b_c\, \eta}{1 + (1-b_c)\eta}, \tag{2.29}$$

where $f_m = n_m/n_e$ is the fraction of the minority ion used for heating, Z_m is its charge, $b_c = B_i^{\mathrm{res}}/B_0$, B_i^{res} is the magnetic field where the ICRH frequency matches the fundamental cyclotron resonance of the minority ion, and B_0 is the magnetic field on axis. Of course if both rotation and temperature anisotropies are present, the total perturbed electrostatic potential is the sum of equations (2.25) and (2.29). In cases where the rotation is not very strong and the ICRH is high, inboard localization of heavy impurities at the HFS can be observed [104].

2.3 Collisional impurity transport

Coulomb collisions between charged particles in a plasma give rise to classical and neoclassical cross-field particle fluxes. In the case of classical transport, particles are displaced from the magnetic field line they are gyrating around with a characteristic diffusive step size of a gyro-radius ($\Delta\mathrm{x} \sim \rho_L$) and a time step of a Coulomb collision time ($\Delta t \sim 1/\nu$). The classical diffusivity is on the order of $D_{\mathrm{cl}} \sim (\Delta\mathrm{x})^2/\Delta t \sim \nu\rho_L^2 \sim \mathcal{O}(0.01\,\mathrm{m}^2\,\mathrm{s}^{-1})$, much lower than the measured transport which is $\mathcal{O}(1\,\mathrm{m}^2\,\mathrm{s}^{-1})$. Neoclassical transport arises from the modification, by collisions, of the guiding center orbits in the inhomogeneous magnetic field of toroidal devices. If we average over a flux surface, we obtain a net radial flux of particles because the magnetic field is not uniform on a flux surface ($B \propto 1/R$). This Flux Surface Average (FSA) is defined as the volume average between infinitesimally adjacent flux surfaces,

$$\langle Q \rangle = \lim_{\Delta V \to 0} \frac{1}{\Delta V} \int_{\Delta V} Q \,\mathrm{d}V = \frac{\partial}{\partial V} \int Q \,\mathrm{d}V\,, \tag{2.30}$$

and it is useful to describe 2D quantities in a 1D picture.

The characteristic step size of neoclassical diffusion is related to the size of the guiding center orbits, which is much larger than the Larmor radius. For example, for trapped particles orbits (see next subsection) we have that $\Delta x \sim q\rho_L/\sqrt{\epsilon}$. Likewise, the associated scattering time step is lower than the classical counterpart ($\Delta t \sim \epsilon/\nu$, in the banana collisionality regime), since collisions only need to detrap particles, rather than scatter them by 90°. Therefore, neoclassical transport is dominant over classical transport, typically by well over an order of magnitude: $D_{\mathrm{ncl}} \sim (q^2/\epsilon^{3/2}) D_{\mathrm{cl}} \sim \mathcal{O}(0.1\,\mathrm{m}^2\,\mathrm{s}^{-1})$, in this example of banana transport.

The remaining *anomalous* transport up to the measured levels is produced by turbulent transport, which typically dominates for the main plasma species and light impurities. However, for heavy impurities the poloidal asymmetries we discussed in the previous section can greatly enhance the radial neoclassical transport, bringing it to comparable or even dominant magnitudes compared to turbulent transport.

2.3.1 Trapped and circulating particle motion

The simultaneous conservation of $\mu \propto v_\perp^2/B$ and $\mathcal{E} \propto v_\parallel^2 + v_\perp^2$ implies that parallel velocity must decrease as a particle drifts on its flux surface towards the high-field side. If its initial parallel velocity is not sufficiently high, it will be reflected back towards the low-field side. Particles that fulfill the condition $v_\parallel^2/v^2 < 1 - B/B_{\mathrm{max}}$ (where B_{max} is the maximum value of B on the flux surface) are effectively trapped on the outboard of the torus, while all other particles can follow the field lines freely and trace the entire flux surface. The guiding centers of the trapped particles follow *banana* orbits, so called due to the shape of their projection on the poloidal plane. These orbits are shown in figure 2.1, with the toroidal precession of the trapped particle motion and the banana shape it traces.

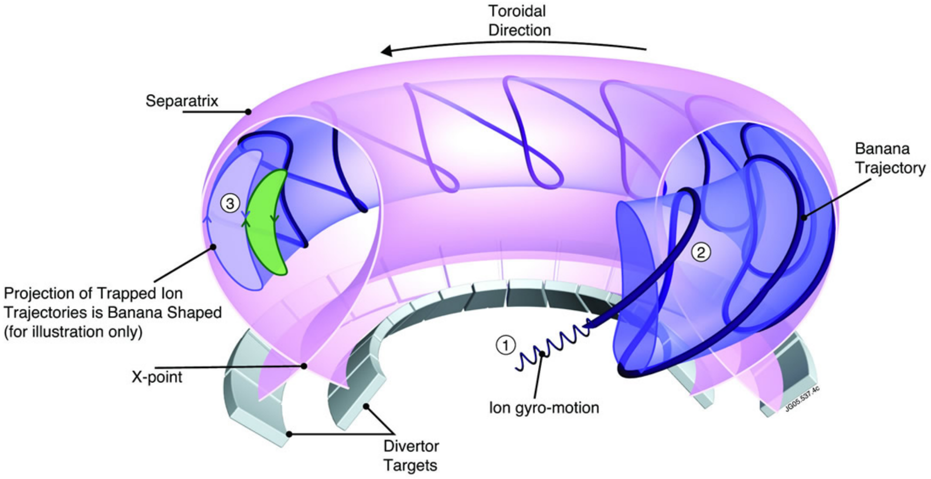

Figure 2.1: Trapped particle orbits in a tokamak [105].

The trapped particle fraction can be calculated as

$$f_t = 1 - \frac{3}{4}\langle B^2\rangle \int_0^{\lambda_m} \frac{\lambda\,\mathrm{d}\lambda}{\langle\sqrt{1-\lambda B}\rangle} \approx 1 - \frac{(1-\epsilon)^{3/2}}{\sqrt{1+\epsilon}\,(1+1.46\sqrt{\epsilon})} \approx \sqrt{2\epsilon}\,, \qquad (2.31)$$

where $\lambda_m = 1/B_{\mathrm{max}}$. The circulating particle fraction is $f_c = 1 - f_t$. The width of banana orbits, $\mathrm{w}_b \sim (q/\sqrt{\epsilon})\rho_L$, characterizes the step size of neoclassical scattering. The collision frequency that causes a trapped particle to scatter by a step w_b is $\nu_{\mathrm{eff}} \sim \nu/\epsilon$, and it is a faster scattering process of the velocity pitch angle in the case of trapped particles, because it is associated with a sign reversal of the parallel velocity only [106]. This is the neoclassical enhancement for trapped particles with respect to classical transport that is a direct consequence of the magnetic field curvature in toroidal fusion devices, leading to $D_{\mathrm{banana}} \sim f_t\,\mathrm{w}_b^2\,\nu_{\mathrm{eff}} \sim (q^2/\epsilon^{3/2}) D_{\mathrm{classical}}$.

2.3.2 Radial particle flux

The different components of the radial flux caused by collisional processes can be obtained by manipulating the momentum balance equation (2.20). A detailed derivation can be found e.g. in [84, 107], but the resulting components are

$$\langle \boldsymbol{\Gamma}_{\boldsymbol{\sigma}} \cdot \nabla\psi \rangle = \left\langle \frac{\mathbf{F}_{\boldsymbol{\sigma}}}{Z_\sigma e} \cdot \frac{\mathbf{B} \times \nabla\psi}{B^2} \right\rangle - \frac{I(\psi)}{Z_\sigma e} \left\langle \frac{\mathbf{F}_{\boldsymbol{\sigma}} \cdot \mathbf{B}}{B^2} \right\rangle - \frac{I(\psi)}{Z_\sigma e} \frac{\langle \mathbf{B} \cdot \nabla \cdot \boldsymbol{\pi}_{\boldsymbol{\sigma}} \rangle}{\langle B^2 \rangle}, \tag{2.32}$$

where the radial coordinate is the poloidal flux ψ.

The first term corresponds to the classical cross-field fluxes, which are present irrespective of the magnetic field geometry. They are driven by perpendicular friction, and are typically sub-dominant to the sum of the other two terms, which are the neoclassical fluxes. The second term is the Pfirsch-Schlüter (PS) flux, caused by parallel friction acting on the guiding center orbits. This friction causes a finite resistivity along the field lines that leads to a poloidally-varying electrostatic potential and ultimately to a radial flux. The last term is the Banana-Plateau (BP) flux, caused by the stress anisotropy due to poloidal flows.

The relative dominance between the neoclassical physical processes depends on the relative magnitude of the collision frequency and the orbit transit frequency. The latter is taken as the inverse of the time it takes a particle to go around a field line with length qR_0 travelling with thermal speed $v_{t\sigma} = \sqrt{2T_\sigma/m_\sigma}$. The parameter we will use to quantify this *collisionality* is denoted g and it is evaluated with respect to the main ion species, such that

$$g = \frac{qR_0}{v_{ti}\tau_{ii}} = \nu_i^* \epsilon^{3/2}, \tag{2.33}$$

where τ_{ii} is the Braginskii ion-ion collision time. The BP flux is typically dominant at low collisionalities, where the collisions are not frequent enough to isotropize the pressure tensor. In contrast, the PS fluxes are dominant at high collisionalities, where the reduction of viscosity by collisions reduces the BP transport.

For an impurity species in a plasma with main ions and electrons, each collisional flux component can be written as a linear combination of the impurity density gradient and the main ion density and temperature gradients [108],

$$\frac{R\Gamma_z^c}{\langle n_z \rangle} = D_z^c \frac{R}{L_{\langle n_z \rangle}} - K_z^c \left(\frac{R}{L_{\langle n_i \rangle}} + \frac{H_z^c}{K_z^c} \frac{R}{L_{T_i}} \right) = D_z^c \frac{R}{L_{\langle n_z \rangle}} + RV_z^c, \tag{2.34}$$

for $c \in \{\mathrm{CL}, \mathrm{PS}, \mathrm{BP}\}$, and diffusive and convective components are present. The FSA has been used to account for possible asymmetries in the densities, and the normalized gradient of a profile $X(r)$ is defined as $R/L_X = -(R/X)(\partial X/\partial r)$.

For collisional transport, the convective flux is larger than the diffusive flux by a factor of the impurity charge Z. This stems from the diamagnetic nature of the flows that cause the friction force between the impurity and the main ion, which scale as $\nabla p_\sigma / Z_\sigma$. Since neoclassical convection is typically radially inwards, this provides neoclassical impurity transport with a mechanism to generate strong heavy impurity accumulation in the core, as we will discuss in later chapters. In practice, this is reflected by the relation $K_z^c = (Z/Z_i)D_z^c$ and the negative sign in equation (2.34).

Fortunately, heat flows also enter into the friction forces on the impurity, and their corresponding contribution to the impurity neoclassical convection can be outwards, leading to what is known as *temperature screening.* The conditions for a protective outward impurity convection are that the coefficient H in equation (2.34) is negative (since $K > 0$ always), and that the normalized ion temperature gradient is strong enough with respect to the ion density gradient, such that

$$\frac{1}{\eta_i} = \frac{R/L_{\langle n_i \rangle}}{R/L_{T_i}} < -\frac{H_z}{K_z} \, . \tag{2.35}$$

The temperature screening coefficient H/K can also be positive, in which case the ion temperature gradient contributes to a detrimental inward impurity convection. The magnitude and direction of the ion temperature contribution to the neoclassical convection depend strongly on collisionality, plasma toroidal rotation and trapped particle fraction [109, 110]. This will be investigated in detail in chapter 3.

Conventional neoclassical theory [106, 107] assumes poloidally homogeneous densities, however extensive theoretical works have shown that poloidally asymmetric density distributions strongly modify neoclassical transport [91, 93, 111–117], by assigning different weights to the poloidal locations on a flux surface. Upon a flux surface average, the resulting radial particle fluxes are typically greatly enhanced. Hence the importance of considering parallel impurity transport (section 2.2) simultaneously with radial impurity transport.

Expressions for the PS, BP and CL components of the radial collisional flux in terms of the thermodynamic gradients can be obtained by relating the friction and viscous forces in equation (2.32) to particle and heat flows. These constitutive relations can be constructed analytically by an expansion of the distribution function $F_{1\sigma}$ in velocity space, used to solve the DKE obtaining friction and viscosity coefficients [107]. This ultimately allows us to obtain expressions for the diffusion coefficients D_z^c and convective coefficients K_z^c and H_z^c.

2.3.3 Pfirsch–Schlüter transport coefficients

The parallel friction force which causes Pfirsch–Schlüter transport can be written as

$$F_{z\|} = -m_z \langle n_z \rangle \nu_z \left(u_{z\|} - u_{i\|} + C_0^z \frac{2\, q_{i\|}}{5\, p_i} \right) , \tag{2.36}$$

where ν_z is the collision frequency of the impurity with the main ion, $u_{\sigma\|}$ are the parallel particle flows and $q_{i\|}$ is the parallel main ion heat flow. The coefficient C_0^z depends on the collisionality and plays a key role on the strength of the temperature screening in the PS regime [108, 109]. The resulting transport coefficients are

$$D_z^{\mathrm{PS}} = q^2 \rho_{Lz}^2 \nu_z \left(\frac{\mathcal{C_G}}{2\epsilon^2} \right) , \qquad K_z^{\mathrm{PS}} = \frac{Z}{Z_i} D_z^{\mathrm{PS}} \, , \tag{2.37}$$

$$H_z^{\mathrm{PS}} = \left\{ - \left[1 + \frac{Z}{Z_i} \Big(C_0^z - 1 \Big) \right] + \frac{Z}{Z_i} \frac{\mathcal{C_U}}{\mathcal{C_G}} \Big(C_0^z + k_i \Big) \right\} D_z^{\mathrm{PS}} \, , \tag{2.38}$$

where k_i is the neoclassical ion flow coefficient, and the factors

$$\mathcal{C}_{\mathcal{G}} = \left\langle \frac{n}{b^2} \right\rangle - \frac{1}{\langle b^2/n \rangle}, \qquad \mathcal{C}_{\mathcal{U}} = \left\langle \frac{n}{N} \right\rangle - \frac{\langle b^2/N \rangle}{\langle b^2/n \rangle}, \tag{2.39}$$

with $b^2 \equiv B^2/\langle B^2 \rangle$, $n \equiv n_z/\langle n_z \rangle$, $N \equiv n_i/\langle n_i \rangle$, characterize the poloidal asymmetries of the densities, providing the enhancement of neoclassical transport with respect to the case with poloidally homogeneous densities [116, 118].

2.3.4 Banana–Plateau transport coefficients

The parallel viscosity that gives rise to Banana–Plateau transport can be written as

$$\langle \mathbf{B} \cdot \nabla \cdot \boldsymbol{\pi_z} \rangle = 3 \left\langle (\mathbf{b} \cdot \nabla B)^2 \right\rangle \left[K_{11}^z \, u_{z\theta} + \left(K_{12}^z - \frac{5}{2} K_{11}^z \right) \frac{2\, q_{z\theta}}{5\, p_z} \right], \tag{2.40}$$

where $u_{z\theta}$ and $q_{z\theta}$ are the poloidal particle and heat flows, and K_{ij}^{σ} are the viscosity coefficients (which capture the dependence of BP transport on collisionality, trapped particle fraction and rotation [110]). The resulting transport coefficients are

$$D_z^{\mathrm{BP}} = \frac{3\, T_i}{2\, Z^2 e^2 \langle n_z \rangle\, I(r)^2} \left(\frac{1}{1/K_{11}^i + 1/K_{11}^z} \right), \tag{2.41}$$

$$K_z^{\mathrm{BP}} = \frac{Z}{Z_i} D_z^{\mathrm{BP}}, \quad H_z^{\mathrm{BP}} = \left[\frac{Z}{Z_i} \left(\frac{K_{12}^i}{K_{11}^i} - \frac{3}{2} \right) - \left(\frac{K_{12}^z}{K_{11}^z} - \frac{3}{2} \right) \right] D_z^{\mathrm{BP}}. \tag{2.42}$$

2.3.5 Classical transport coefficients

The classical transport coefficients are obtained from an expression for perpendicular friction in a similar way as the PS coefficients, and are ultimately given by

$$D_z^{\mathrm{CL}} = \frac{\rho_{Lz}^2\, \nu_z}{2} \left\langle \frac{n}{b^2} \right\rangle, \quad K_z^{\mathrm{CL}} = \frac{Z}{Z_i} D_z^{\mathrm{CL}}, \quad H_z^{\mathrm{CL}} = -\left[1 + \frac{Z}{Z_i} \left(C_0^z - 1 \right) \right] D_z^{\mathrm{CL}}, \tag{2.43}$$

where the FSA is taken in order to obtain a surface-averaged particle flux. The temperature screening coefficient H/K of classical transport can be derived analytically, and in the limit of heavy and highly charged impurities ($Z \gg Z_i$, $A \gg A_i$), where the friction coefficient C_0^z tends to 3/2, it becomes $H_{\mathrm{CL}}/K_{\mathrm{CL}} = -1/2$.

2.4 Turbulent impurity transport

Collisional transport is the minimum and unavoidable level of transport in magnetically confined plasmas, and it is generally well understood (at least in the local limit). In contrast, plasma turbulence and the transport of particles and heat it generates are more challenging, presenting non-linear dynamics and depending on a wide set of plasma parameters. The solution of the full non-linear problem is a computationally intensive endeavour, but a linearized description allows one to identify physically-relevant components of the fluxes. We will present a simple analytical model for the linear amplitude of a turbulent mode and the cross-field radial transport it causes, followed by a discussion on how its non-linear saturation is described with *quasi-linear* models.

2.4.1 Linearized description

In order to calculate turbulent transport from the gyrokinetic equation (2.19), we consider the limit without strong mean flows. We expand the fluctuating potential and distribution function in Fourier modes of the form $\exp(-i\omega t + i\mathbf{k}\cdot\mathbf{x})$, such that

$$\tilde{\phi}(\mathbf{x},t) = \sum_{\mathbf{k},\omega} \tilde{\phi}_k \, e^{-i\omega t + i\mathbf{k}\cdot\mathbf{X}_{\boldsymbol{\sigma}}} \, e^{i\mathbf{k}\cdot\boldsymbol{\rho}_{\boldsymbol{\sigma}}}, \quad h_\sigma(\mathbf{X}_{\boldsymbol{\sigma}},t) = \sum_{\mathbf{k},\omega} h_{\sigma k} \, e^{-i\omega t + i\mathbf{k}\cdot\mathbf{X}_{\boldsymbol{\sigma}}}, \tag{2.44}$$

and we will focus on the equations for a single mode k in the following.

The left-hand-side of the linearized GKE is simply $-i(\omega - \omega_{g\sigma k})h_{\sigma k}$, defining the drift frequency and the generalized gyro-center frequency as

$$\omega_{d\sigma k} \equiv \mathbf{k}\cdot\mathbf{v}_{\boldsymbol{d\sigma}}, \qquad \omega_{g\sigma k} \equiv k_\parallel v_\parallel + \omega_{d\sigma k}, \tag{2.45}$$

respectively. The non-linear term $\tilde{v}_{\mathrm{E}}\, h_\sigma$ is omitted from this linear derivation, but it is the one responsible for mode coupling and the subsequent development of zonal flows that lead to the saturation of the turbulence amplitude [119].

For the source terms on the right-hand-side of the GKE, it is convenient to define a normalized fluctuating potential, $\hat{\phi}_k \equiv e\tilde{\phi}_k/T_e$. We then have that

$$\frac{Z_\sigma e F_{0\sigma}}{T_\sigma}\frac{\partial\langle\tilde{\phi}\rangle_\vartheta}{\partial t} \longrightarrow -i\omega\,\frac{Z_\sigma T_e}{T_\sigma}F_{0\sigma}J_{0\sigma}\,\hat{\phi}_k, \qquad \tilde{\mathbf{v}}_{\mathbf{E}} \longrightarrow \frac{iJ_{0\sigma}T_e}{eB}\,\hat{\phi}_k\,(\mathbf{b}\times\mathbf{k}), \tag{2.46}$$

where $J_{0\sigma} = J_0(k_\perp \rho_\sigma)$. The radial gradient of the background distribution is

$$\frac{\partial F_{0\sigma}}{\partial \mathbf{X}_{\boldsymbol{\sigma}}} \approx \frac{\partial F_{0\sigma}}{\partial r}\nabla r = -\left[\frac{R}{L_{n_\sigma}} + \left(\frac{E_\sigma}{T_\sigma} - \frac{3}{2}\right)\frac{R}{L_{T_\sigma}} + \frac{m_\sigma v_{t\sigma} v_\parallel}{T_\sigma}\,u'_\sigma\right] F_{0\sigma}\frac{\nabla r}{R}, \tag{2.47}$$

where the gyro-center energy is $E_\sigma = m_\sigma v_\parallel^2/2 + \mu_\sigma B$ and $u'_\sigma \equiv (-R/v_{t\sigma})(\partial u_\sigma/\partial r)$. The thermodynamic gradients, being the source of free energy for the microinstabilities driving the turbulence, come into play as the terms in the square brackets, denoted $\mathcal{G}_\sigma$ in the following. The second term on the right of the GKE is then

$$\tilde{\mathbf{v}}_{\mathbf{E}} \cdot \frac{\partial F_{0\sigma}}{\partial \mathbf{X}_{\boldsymbol{\sigma}}} \longrightarrow \frac{ik_y T_e}{eBR}\,\mathcal{G}_\sigma\, F_{0\sigma}J_{0\sigma}\,\hat{\phi}_k = i\,\frac{Z_\sigma T_e}{T_\sigma}\,\omega_{f\sigma k}\,\mathcal{G}_\sigma\, F_{0\sigma}J_{0\sigma}\,\hat{\phi}_k \tag{2.48}$$

where $k_y = \mathbf{k}\cdot(\nabla r \times \mathbf{b})$ is the binormal wavenumber, orthogonal to both the magnetic field and the radial direction, and we have defined a generic fluid drift frequency $\omega_{f\sigma k} \equiv k_y T_\sigma/(Z_\sigma e B R)$. Finally, we arrive at the GKE for each Fourier mode:

$$h_{\sigma k} = \frac{Z_\sigma T_e}{T_\sigma}\,\frac{\omega - \omega_{f\sigma k}\,\mathcal{G}_\sigma}{\omega - \omega_{g\sigma k}}\,F_{0\sigma}J_{0\sigma}\,\hat{\phi}_k, \tag{2.49}$$

We can decompose the frequency of the mode into real and imaginary parts, $\omega_k = \omega_{rk} + i\gamma_k$, corresponding to the pure frequency and the growth rate, respectively. The dispersion relation $\omega(\mathbf{k})$ is determined by Poisson's equation

$$-\varepsilon_0\nabla^2\tilde{\phi} = \sum_\sigma Z_\sigma e\,\tilde{n}_\sigma = \sum_\sigma Z_\sigma e \int \delta f_{1\sigma}\,\mathrm{d}^3 v\,. \tag{2.50}$$

In the trace impurity limit, $Zn_z/n_e \ll 1$, the contribution of impurities to quasineutrality can be neglected and therefore they do not affect the background turbulence, but rather are only affected by it [120]. This means that even with non-linear terms in the GKE, the impurity flux is linear in the background gradients.

2.4.2 Radial particle flux

Cross-field turbulent transport arises from out-of-phase fluctuations in density (for particle fluxes) or pressure (for heat fluxes) and velocity, typically the turbulent E×B velocity caused by electrostatic potential fluctuations. A schematic representation of electrostatic E×B particle transport is shown in figure 2.2.

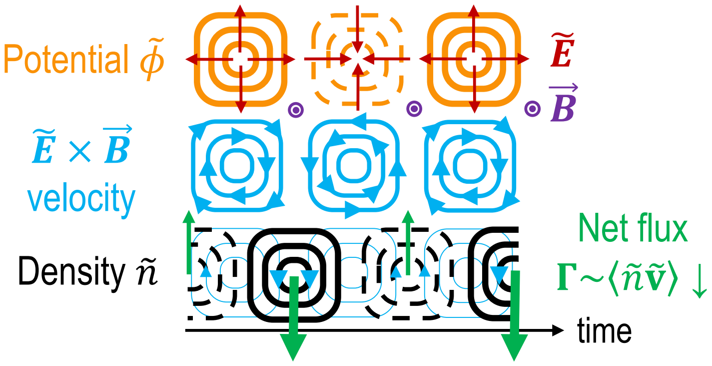

Figure 2.2: Diagram of the basic mechanism for E×B transport. Fluctuations in the electrostatic potential in the presence of a background magnetic field lead to a fluctuating E×B drift velocity. If the fluctuations in the density of a species are not in phase with the potential fluctuations, there is a net particle flux in the radial direction.

The time and flux surface averaged radial impurity particle flux caused by a single Fourier mode can be calculated as

$$\Gamma^{\mathrm{trb}}_{\sigma k} = \langle \tilde{n}_{\sigma k} \tilde{v}_{\mathrm{E}} \rangle = \left\langle \mathfrak{Re} \left(\int h_{\sigma k} \, \tilde{\mathbf{v}}^{*}_{\mathbf{E}} \cdot \nabla r \, \mathrm{d}^3 v \right) \right\rangle_{\psi, \bar{\tau}}, \tag{2.51}$$

where the adiabatic component of $\delta f_{1\sigma}$ does not contribute to the turbulent flux since it is in phase with the electrostatic potential fluctuations. Combining the solution of the GKE with the fluctuating E×B velocity (equations (2.49) and (2.46)), normalizing all frequencies to $\omega_{fik} = Z_\sigma \omega_{f\sigma k}$, and extracting the real part of the resulting expression, the flux can be written as

$$\Gamma^{\mathrm{trb}}_{\sigma k} = \frac{k_y c_s^2}{\omega_{ci}} \frac{T_e}{T_\sigma} \left\langle J_{0\sigma}^2 \, |\hat{\phi}_k|^2 \int \frac{\hat{\gamma}_k \left(\mathcal{G}_\sigma - Z_\sigma \hat{\omega}_{g\sigma k} \right)}{(\hat{\omega}_{rk} - \hat{\omega}_{g\sigma k})^2 + \hat{\gamma}_k^2} F_{0\sigma} \, \mathrm{d}^3 v \right\rangle, \tag{2.52}$$

where the sound speed is $c_s = \sqrt{T_e/m_i}$. Note that most terms in the drift velocity $\mathbf{v}_{d\sigma}$ (equation 2.14) are $\propto 1/Z_\sigma$, so the last term in the numerator is approximately independent of charge. In contrast, the drift frequency term subtracted from the real eigenfrequency in the denominator does have an implicit $1/Z_\sigma$ dependence, leading to shifts in the resonant frequencies between impurities and main ions (or electrons).

This means that heat diffusivities ($\chi_{i,e}$) and impurity particle diffusivities (D_z) have maxima at different frequencies, leading to non-monotonic dependencies of $D_z/\chi_{i,e}$ on the turbulence properties [121], which is an effect that will be important to the physics investigated in chapter 6.

Expanding out the gradients $\mathcal{G}_\sigma$ from equation (2.47) we can identify the components of the turbulent particle flux,

$$\Gamma^{\mathrm{trb}}_{\sigma k} \propto \int \frac{\hat{\gamma}_k \left[R/L_{n_\sigma} + \left(E_\sigma/T_\sigma - 3/2\right) R/L_{T_\sigma} + \left(m_\sigma v_{t\sigma} v_\parallel / T_\sigma\right) u'_\sigma - Z_\sigma \hat{\omega}_{g\sigma k}\right]}{\left(\hat{\omega}_{rk} - \hat{\omega}_{g\sigma k}\right)^2 + \hat{\gamma}_k^2} F_{0\sigma} \mathrm{d}^3 v. \tag{2.53}$$

We finally obtain a general expression for the turbulent impurity flux, with a diffusive component proportional to the impurity density gradient and also several convective terms, which is the main result of this derivation:

$$\frac{R\,\Gamma^{\mathrm{trb}}_z}{\langle n_z \rangle} = D^{\mathrm{trb}}_z \frac{R}{L_{\langle n_z \rangle}} + D_{T_z} \frac{R}{L_{T_z}} + D_{uz} u'_z + R\,V_{pz} = D^{\mathrm{trb}}_z \frac{R}{L_{\langle n_z \rangle}} + R V^{\mathrm{trb}}_z. \tag{2.54}$$

The turbulent convection is composed of thermo-diffusion, roto-diffusion and pure pinch contributions. These components can be obtained from analytical fluid models too [122–124]. In contrast to neoclassical convection, the turbulent impurity convection does not scale strongly with the impurity charge [125,126], and therefore it does not present a mechanism for core accumulation of heavy impurities. This means that in situations where turbulent transport is expected to be dominant over neoclassical transport even for high–Z impurities, such as at reactor-relevant temperatures, heavy impurities are not expected to be very peaked [127]. In particular,

- thermo-diffusion scales as $\propto 1/Z$, since it is diamagnetic in nature, so it becomes weak for heavy impurities. Its radial direction depends on the direction of propagation of turbulence (in the ion or electron drift directions). The thermo-diffusive flux is outward in ITG turbulence and inward for TEM.

- Roto-diffusion is proportional to the mass-to-charge ratio, so it does not necessarily decrease for heavy impurities, but it is only present when there is a radial rotation shear $u'_z = -R^2 \Omega'_\varphi / v_{tz}$. Its direction follows that of thermo-diffusion.

- The pure convection arises from the compression of the E×B flow due to the inhomogeneity of the magnetic field, and it is independent of the impurity mass or charge. It is typically an inward pinch.

2.4.3 Quasilinear description

A quasilinear model aims to reproduce the non-linear turbulent fluxes by combining a quasilinear weight and a model for the amplitude of the turbulent fluctuations, and its purpose is to provide an accurate yet more computationally accessible description of turbulent transport. The total quasilinear flux is then

$$\Gamma_\sigma = \sum_k \Gamma^{\mathrm{QL}}_{\sigma k} \, |\hat{\phi}_k|^2. \tag{2.55}$$

The quasilinear weight $\Gamma_{\sigma k}^{\mathrm{QL}}$ is derived from the linearized model, either fluid or kinetic, to obtain an expression for the linear correlation between density and turbulent E×B velocity fluctuations leading to radial transport (e.g. equation (2.52)). The amplitude and spectral shape of the turbulent fluctuations, $|\hat{\phi}|^2(\mathbf{k})$, are described by a *saturation rule* or mixing length model that captures the non-linear saturation of turbulence by mode coupling [128], typically by fitting results of non-linear gyrokinetic simulations.

The main quasilinear turbulent transport model that we will use in this thesis is the Trapped Gyro–Landau Fluid (TGLF) model [129–131]. It consists of a system of velocity moments of the gyrokinetic equation, with a unified description of trapped particles [129] and the inclusion of kinetic Landau damping through a dissipative term in the fluid closure [132]. The saturation rules of TGLF were obtained from databases of non-linear CGYRO [133, 134] simulations.

In particular, the version that will be our workhorse to model turbulent impurity transport is TGLF-SAT2 [131].

Chapter 3

Neoclassical impurity transport model including rotation

The results presented in this chapter have been published in Ref. [110], used here under the terms of the Creative Commons Attribution 4.0 licence.

The toroidal rotation of the plasma can cause strongly poloidally asymmetric heavy impurity densities, as we have seen in section 2.2.1. These centrifugal effects are exemplified in figure 3.1(a), where the distribution of the W density on the 2D poloidal plane, calculated using equation (2.27), is shown for the rotation of AUG discharge #36315 (a standard H-mode). The W impurities are pushed to the outboard side of the torus by the centrifugal force, such that the density on the LFS is up to three times larger than on the HFS for this particular case.

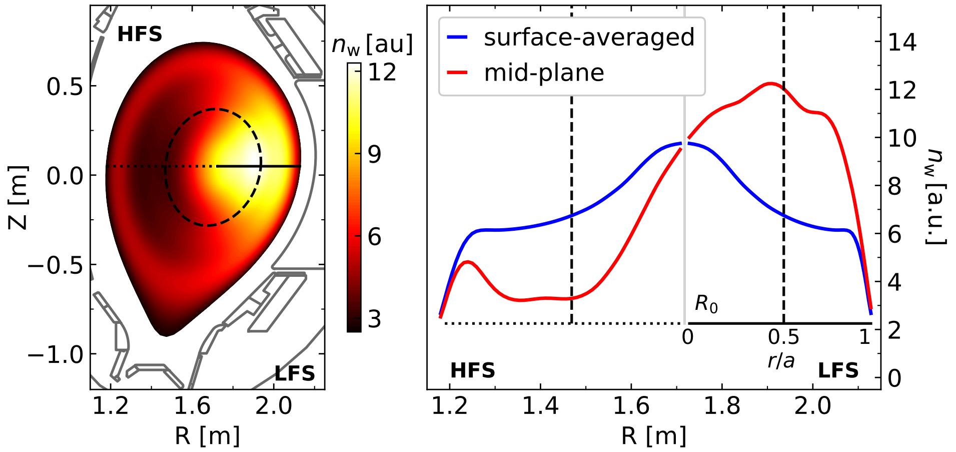

Figure 3.1: 2D distribution of W density (left) and comparison of equivalent mid-plane and flux-surface-averaged 1D W densities (right), under centrifugal effects for an AUG standard H-mode (#36315 at 4.5 s).

Having a 2D impurity density $n_z(r, \theta)$ means that there is freedom to select a representation of the density for 1D analyses. The flux surface averaged (FSA) $\langle n_z(r, \theta) \rangle (r)$ and low field side (LFS) $n_{z,0}(r) = n_z(r, \theta = 0)$ densities are the two most common 1D representations. FSA densities are typically used in 1.5D transport modelling codes like ASTRA [78, 79] and JINTRAC [135], while the LFS representation is used in kinetic solvers like NEO [85,88,136] (drift-kinetic) and GKW (gyrokinetic) [137]. These two 1D pictures are shown in panel (b) for the same 2D density distribution from figure 3.1(a), where the difference between the two is clear.

At every point on a flux surface, the neoclassical impurity flux points in the same direction on the major radius coordinate R, for example towards the center of the torus in figure 3.2. In the conventional neoclassical ordering of homogeneous densities [106], with zero rotation, the flux pointing into the plasma (on the LFS in this example) and out of the plasma (on the HFS) would balance each other out exactly, were it not for the inhomogeneity of the magnetic field due to the toroidicity of the system. That is, the fact that $B = B(\theta)$ on a given flux surface leads to a net neoclassical flux, inward into the plasma in this example. In the case of Pfirsch-Schlüter (PS) transport, this translates to a geometrical factor in equation (2.39) of $\langle 1/b^2 \rangle - 1 \neq 0$ even if the impurity density is homogeneous ($n = n_z / \langle n_z \rangle = 1$).

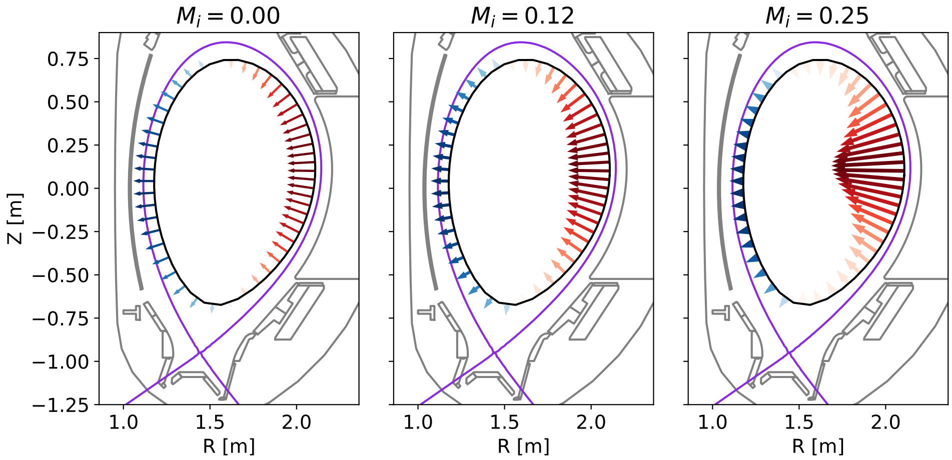

Figure 3.2: Schematic representation of the magnitude and direction of the neoclassical W flux around a flux surface, at increasing levels of toroidal rotation.

However, the toroidal rotation of the plasma can strongly enhance neoclassical impurity transport and change its direction because it modifies the weight of the contribution of each poloidal position on the flux surface to the average flux. In the center and right panels of figure 3.2, the plasma rotation is increased, leading to outboard localization of the W density and consequently to a more unbalanced poloidal distribution of the radial flux, whose flux surface average becomes more strongly inward with higher rotation.

This is a schematic example to illustrate centrifugal effects on neoclassical impurity transport whose precise theoretical description is more complex [93,113,116–118]. But it serves to understand why widely-used fluid codes like NCLASS [138] and NEOART [139,140], which assume homogeneous impurity density distributions, are not well suited to model the neoclassical transport of high-Z impurities.

In contrast, NEO [85,88,136] is a code that solves the drift-kinetic equation at arbitrarily high rotation. It includes multi-species collisions and uses a full-linearized Fokker-Planck collision operator. This makes NEO a very complete tool for neoclassical transport calculations in the community. At the same time, integrated tokamak modelling requires low computational times that are not compatible with a drift-kinetic solver like NEO, especially in simulations of strongly rotating plasmas.

An analytical model capable of describing the effects of poloidally asymmetric densities on neoclassical impurity transport would therefore be a useful tool for fast applications in interpretive analysis and predictive modelling. The FACIT model [109, 110, 118] has been developed to obtain accurate and fast calculations of neoclassical impurity transport. It was first developed to describe effects of poloidal asymmetries at very high collisionality [95, 118]. The Banana-Plateau (BP) flux, which is more dominant at low collisionality, was subsequently included in the non-rotating limit [109]. Here we present the further extension of the effects of rotation at all collisionalities.

3.1 Effects of rotation across collisionality regimes

A database of drift-kinetic NEO calculations was built to better understand the effects of rotation across the different collisionalities and radial locations. Parameter scans in collisionality, rotation and trapped particle fraction for a tungsten impurity were performed keeping all other input quantities constant. The full database and NEO resolution are described in appendix B. In appendix A of [110], additional tests on different assumptions (like the geometry and the impurity concentration) are also discussed.

3.1.1 Parameters selected to describe the effects

In order to describe these rotational effects, it is important to select dimensionless parameters that capture the physics involved across the combination of dimensional parameters of different tokamaks (like temperatures, densities, machine sizes).

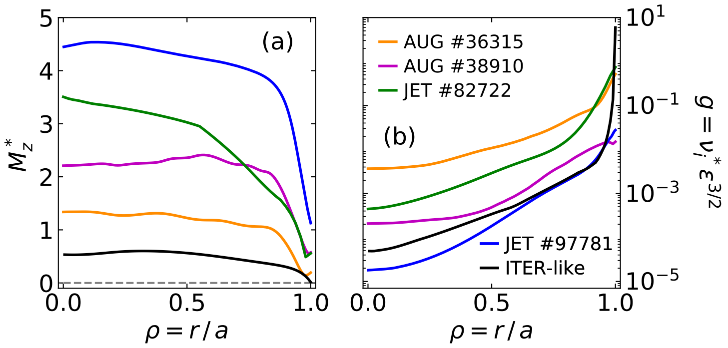

Figure 3.3: Radial profiles of (a) effective impurity Mach number and (b) collisionality parameter g, for the different discharges under consideration

The magnitude of the rotation will be described in the model by the effective impurity Mach number M_z^*, introduced in equation (2.28). This parameter captures not only the effect of the centrifugal force on the heavy impurities but also the partial compensation by the electrostatic potential that develops due to rotation. At the same time, the main ion Mach number will be used as an impurity-independent reference parameter to compare quantitatively the rotation between different machines. The collisionality will be described by the parameter g, introduced in equation (2.33), which is more independent of geometry than the more commonly used ν^*, since the latter has a factor of the inverse aspect ratio $\epsilon^{-3/2}$. All other collision frequencies scale proportionally to g.

Figure 3.3 shows radial profiles of M_z^* and g, in panels (a) and (b) respectively, for an AUG standard H-mode (discharge #36315), an AUG advanced tokamak (AT) scenario [141] (#38910), JET low (#82722) and high (#97781 [142]) power hybrid H-modes, and an ITER-like 15 MA standard scenario (with kinetic profiles from [143] and a rotation profile approximated by an average of predictions from [98,99]). These parameters vary widely between machines, within the same machine in different operational scenarios, and within the same discharge from core to edge. Finally, the observation of [144] that geometry variations are more robustly captured by using f_t, instead of ϵ, to describe effects at different radial positions motivates the use of f_t as the third parameter in the scans. Since AUG, JET and ITER have a similar aspect ratio of $R_0/a \sim 3$, the profile of f_t is similar in all machines, $f_t \sim \sqrt{2\epsilon} = \sqrt{(2a/R_0)\rho}$, recalling equation (2.31), so it is not included in figure 3.3.

The main feature of the model that will be introduced in section 3.2 is the analytical description of the influence on the transport coefficients of the interplay between rotation (M_z^*) and collisionality (g) at different radial locations (f_t).

3.1.2 Drift kinetic results with NEO

Collisionality scans at increasing values of rotation and trapped particle fraction for tungsten in a trace concentration were performed with NEO in order to study the influence of these parameters on the neoclassical convection coefficient K_z and the temperature screening coefficient H_z/K_z. From section 2.3.2 we have that the diffusion coefficient is related to the convective coefficient K_z by $D_z = K_z/Z$, so describing K_z and H_z/K_z is enough to completely describe the neoclassical impurity flux.

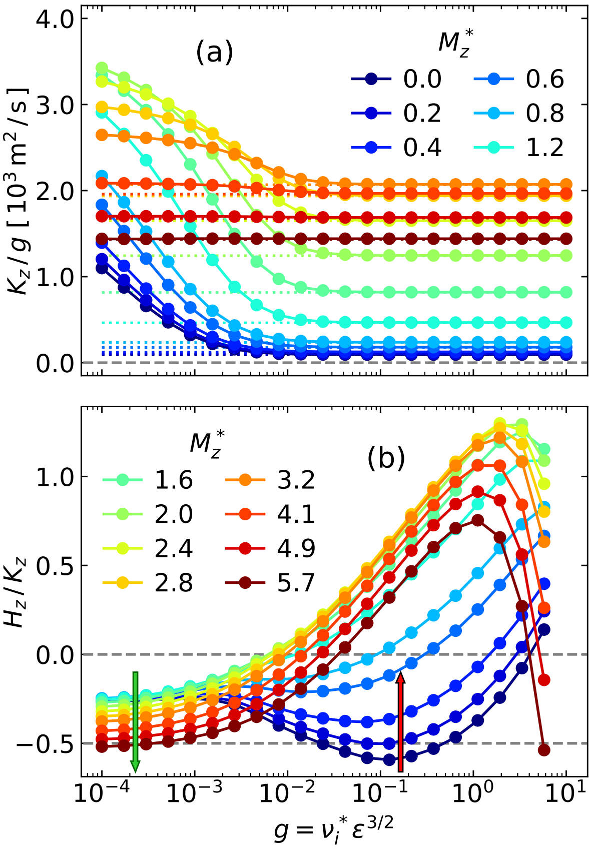

Figure 3.4: Collisionality dependence of convective (K_z) and screening (H_z/K_z) coefficients at increasing values of rotation.

Figure 3.4(a) shows an example of such a collisionality scan at a value of $f_t = 0.39$ corresponding to the core ($r/a \sim 0.25$ for a conventional aspect ratio $R_0/a \sim 3$), for W^{44+} with 14 values of rotation, increasing from blue to red (with M_i ranging in 0–0.7, and correspondingly the effective W Mach number M_z^* in 0–5.7). Note that a factor of the collisionality is removed in order to study the underlying structure, because both K_z and H_z are proportional to g. There is a clear difference in the behavior of K_z between the low and high collisionality limits: we identify K_z to consist entirely of its K_z^{PS} component in the latter regime, with the K_z^{BP} component going to zero, while the former regime has a more prominent BP contribution, with a transition (at this particular f_t) around $g \approx 10^{-2}$. The PS component of the ratio K_z/g is independent of g, so it corresponds to horizontal lines in figure 3.4(a) that are plotted in dotted lines. The BP component of K_z/g sits on top of these lines, and it is zero at high g (where collisions isotropize the pressure tensor, cancelling its viscous contribution), starts to increase at intermediate g and saturates to a constant value at very low g. This different behavior of the BP and PS components is an important feature that shall be returned to in section 3.2.1. In terms of the impact of rotation, we observe that an increase in M_z^* quickly enhances K_z^{PS} (and therefore the overall magnitude of the neoclassical transport) until a particular value of M_z^*, which depends on f_t, and is around $M_z^* = 3.2$ in the case of figure 3.4(a). At higher M_z^*, K_z^{PS} starts to decrease from its maximum value. K_z^{BP} also increases from its non-rotating value up to a maximum (located in this example around $M_z^* = 1.6$), after which increasing rotation promptly brings it to zero. We also note that K_z converges to its PS component at higher collisionalities as rotation increases.

In figure 3.4(b), collisionality scans of the temperature screening coefficient H_z/K_z are similarly shown with increasing rotation. Here, the clear distinction between PS and BP components is lost. We reiterate that a more negative H_z/K_z is beneficial as it leads to a stronger outward flux driven by the temperature gradient, while a less negative H_z/K_z reduces this protective screening and a positive H_z/K_z reverses the effect, leading to an inward flux due to the temperature gradient. In these collisionality scans, we see that at intermediate and high collisionalities ($g > 0.01$) an increasing rotation promptly reduces and subsequently reverses the screening of impurities, in agreement with known PS results [116]. However, if the collisionality is low enough, rotation causes H_z/K_z to increase in magnitude while remaining negative, leading to a mitigation of the inward convection or its reversal to an outward flux (depending on the ion gradients). This result was first observed recently in [145], in NEO simulations at different radial positions in a highly rotating KSTAR experiment. We reproduce the numerical observation of this effect, and extend it through a more systematic study under variations of collisionality and trapped particle fraction in addition to rotation via scans in each parameter when the others are kept constant, thereby uncoupling the radial variation of each of (M_z^*, g, f_t) to understand the underlying physical mechanisms at play.

In order to study the screening effects in more detail, we define

$$\Delta_{\text{HK}}(M_i) = \frac{H_z(M_i = 0)}{K_z(M_i = 0)} - \frac{H_z(M_i)}{K_z(M_i)}, \tag{3.1}$$

such that if $\Delta_{\text{HK}}(M_i) > 0$, then H/K has become more negative due to rotation, intensifying the effect of the thermal screening, and vice versa.

The variation of Δ_{HK} through combinations of rotation and collisionality is shown in figure 3.5, in this case at a higher $f_t = 0.67$ corresponding to the edge ($r/a \approx 0.85$).

Two regimes of favorable (blue) and unfavorable (red) rotation on the screening become apparent, with their boundary (in black) at $\Delta_{\text{HK}} = 0$. The combination of (M_i, g) from the experimental profiles of the different scenarios mentioned in this section are plotted on this parameter space, with each symbol representing the values at the radial position where $f_t = 0.67$ (right at the pedestal top for these discharges). Note that from core to edge, the symbols travel on their corresponding curves from bottom right to top left. The shape of the two regions remains similar under variations of f_t, with the favorable region growing slightly with increasing f_t. The magnitude of the effects (both favorable and unfavorable) decreases slightly with f_t. It is important to consider that while the influence of f_t on H_z/K_z is not dramatic (yet present), in the high rotation limit K_z grows strongly as $\sim 1/f_t^4$ due to the $1/2\epsilon^2$ enhancement of neoclassical transport due to rotation [116].

If the favorable rotation region is accessed by a plasma after reaching sufficiently high rotation at sufficiently low collisionalities, an operational regime with enhanced temperature screening of heavy impurities like W becomes available.

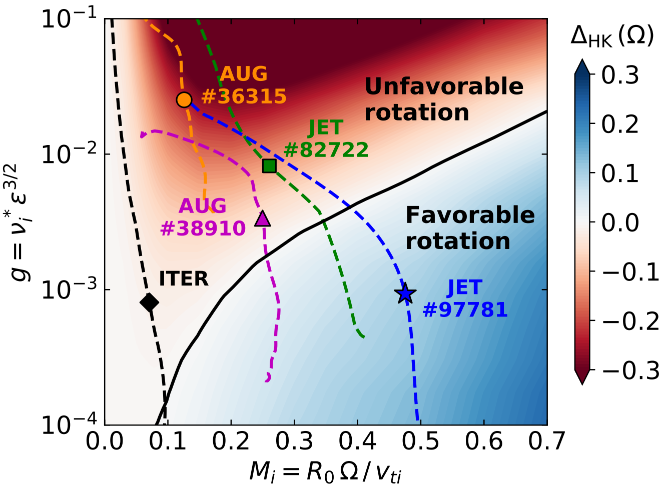

Figure 3.5: Enhancement or decrease of tungsten screening in the space of collisionality and rotation. Dashed lines are the combination of both parameters in the different discharges. Symbols are the values at the trapped particle fraction (radial location, since all aspect ratios are approximately equal) where the colormap has been produced, in this case $f_t = 0.67$, $\rho = r/a \approx 0.85$.

From figure 3.5, we see that AUG #36315 (a high-density standard H-mode with 8 MW of input power) lays entirely inside the unfavorable regime. In contrast, JET #97781, a high power (> 30 MW) hybrid H-mode with a hot, low density pedestal optimized for better W screening, enters this beneficial operational window across most of the minor radius, only exiting in the strongly-varying pedestal. JET #97781 [142] and other recent JET discharges [146] have been observed to exhibit reduced impurity accumulation, and the presently discussed effects are a possible factor to explain this. “Intermediate” discharges in each machine are also included in figure 3.5: AUG #38910 is a high-temperature AT H-mode, and JET #82722 is a low power hybrid H-mode performed soon after JET’s transition to the ITER-like wall. While already in the unfavorable region at the radial position where $f_t = 0.67$, both manage to enter the favorable regime, although only in the core, and they do it through different paths: AUG #38910 by reaching lower collisionalities at intermediate rotation, and JET #82722 by rotating faster at a higher collisionality. Finally, we make some remarks based on current predictions for ITER. Although there is still uncertainty around the ITER rotation profiles, it is expected that its magnitude will be low. The presently discussed effects of rotation on neoclassical transport of heavy impurities in ITER, while present, would be small. In terms of the direction of the convection, the low collisionality of ITER allows it to avoid the fast loss of screening with rotation in the PS regime. While it would be in the unfavorable regime, ITER would operate in a region where these effects are very mild ($|\Delta_{HK}| < 0.05$). The low $M_z^* \approx 0.5$ would not yield a significant increase in the magnitude of the flux. These properties are included in the integrated modelling of ITER presented in chapter 6.

The effect of collisionality on the BP transport is directly related to the transition to the PS regime, as more frequent collisions will isotropize the pressure tensor (thereby rendering the viscosity, which causes BP transport, negligible) and “destroy” the banana orbits. In the *collisionless* limit (meaning banana orbits are completed before a collision occurs, not $g = 0$), we propose a simple physical interpretation of the beneficial effect of rotation on the BP transport. In the non-rotating, collisionless limit, an increase in the trapped particle fraction increases the temperature screening. This can be seen in figure 3.6, where f_t scans of H_z/K_z are shown at $g = 10^{-4}$ for increasing levels of rotation. The blue curve at no rotation becomes more negative as f_t increases. As shown in [147], rotation widens the trapping cone, increasing the effective trapped particle fraction at the same radial position with respect to the non-rotating case through a centrifugal push of particles towards the LFS. Therefore, rotation increases the effective trapped particle fraction, which in turn increases the impurity screening. In figure 3.6, whose x-axis is the simple formula for $f_t(\epsilon)$ from equation (2.31) without rotation dependence, one sees how the increase in rotation can then be interpreted as a mapping to a higher f_t.

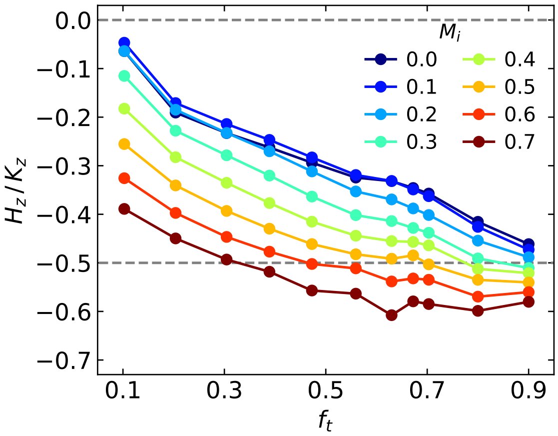

Figure 3.6: Dependence of the temperature screening coefficient of W on the trapped particle fraction at low collisionality and increasing levels of rotation.

3.2 Extension of FACIT model to include rotation

In this section, we extend the FACIT model to analytically encapsulate the effects discussed in the previous section, by means of theory-based assumptions, analysis of the structure of the transport coefficients in collisionality, and fitted factors (given explicitly in appendix B) which are introduced to minimize the difference with the drift-kinetic results of NEO across a wide range of the (M_z^*, g, f_t) parameters.

3.2.1 Splitting of NEO output into PS and BP components

Being a kinetic code, NEO solves for the neoclassical distribution function and then integrates it in velocity moments to obtain the neoclassical fluxes. This means that only the total fluxes and transport coefficients are directly available, and not the physically distinct BP and PS components (which arise from fluid concepts like viscosity and friction, respectively). However, it is possible to extract these components from NEO by analyzing the structure of the coefficients in the limits of the parameter space and applying theory-based assumptions. This will be an important feature of the proposed model that allows for additional physical insights.

A key observation is that the BP and PS components of K_z are clearly differentiated at low and high collisionalities, as in figure 3.4(a), where the K_z^{PS} component is shown in dotted lines at each rotation, and the K_z^{BP} component can be extracted as the difference with the total K_z from NEO (solid lines). For H_z, and consequently H_z/K_z, the path is not as straightforward. We rely on the fact that the theory of PS transport with rotation is more developed, in order to obtain a suitable physical model for H_z^{PS}. This allows us to isolate the H_z^{BP} component from the total NEO H_z to model it. We then verify that the total temperature screening coefficient $H_z/K_z = (H_z^{\mathrm{BP}} + H_z^{\mathrm{PS}})/(K_z^{\mathrm{BP}} + K_z^{\mathrm{PS}})$ is sufficiently accurate with respect to NEO.

3.2.2 K_z coefficient

From equation (2.37), we have that the PS component of K_z is given by

$$K_z^{\mathrm{PS}} = \frac{Z}{Z_i}\, q_*^2\, \rho_z^2\, \nu_z\, \frac{\mathcal{C}_{\mathcal{G}}}{2\epsilon^2}, \tag{3.2}$$

where the generalized safety factor is $q_* = \epsilon I/\partial_r\psi$. The geometric term $\mathcal{C}_{\mathcal{G}}$ depends on the asymmetries of the impurity density and the magnetic field, such that

$$\mathcal{C}_{\mathcal{G}}^{\mathrm{FSA}} = \left\langle \frac{n}{b^2} \right\rangle - \frac{1}{\langle b^2/n \rangle}, \quad \mathcal{C}_{\mathcal{G}}^{\mathrm{LFS}} = \frac{1}{b^2(\theta_0)} - \frac{1}{n(\theta_0)}\frac{1}{\langle b^2/n \rangle}, \tag{3.3}$$

where $\theta_0 = 0$. These expressions can be obtained by manipulating equations (A.9) and (A.22) of [95]. $\mathcal{C}_{\mathcal{G}}$ is a strong function of the rotation in both LFS and FSA pictures. In the rest of this section, the transport coefficients will be considered in their LFS representation. We can extract the complete dependence of $\mathcal{C}_{\mathcal{G}}(M_z^*, f_t)$ by isolating the K_z^{PS} component from NEO, profiting from the fact that at high collisionalities, e.g. at $g > 0.1$ in figure 3.4(a), the BP component goes to zero. Thus, the known value of $\mathcal{C}_{\mathcal{G}}(0, f_t)$ from FACIT in the non-rotating limit [109] can be used in combination with the results of the K_z^{PS} obtained from NEO, such that

$$\frac{\mathcal{C}_{\mathcal{G}}(M_z^*, f_t)}{\mathcal{C}_{\mathcal{G}}(0, f_t)} = \frac{K_z^{\mathrm{PS}}(M_z^*, f_t)}{K_z^{\mathrm{PS}}(0, f_t)} \approx f_{\mathcal{G}}(M_z^*, f_t), \tag{3.4}$$

where the NEO values for the middle expression are fitted in the $f_{\mathcal{G}}$ factor, whose general dependence on M_z^* is found to be

$$f_{\mathcal{G}}(M_z^*) = \frac{(1 + a_1 M_z^{*a_2})^{a_3}(1 + 0.2 M_z^{*a_4})}{1 + a_5 M_z^{*a_6}}, \tag{3.5}$$

with the $a_i(f_t)$ coefficients given explicitly in equations (B.3–B.4). This allows us to obtain $\mathcal{C}_{\mathcal{G}}(M_z^*, f_t)$, which is important for modelling purposes, as it is adimensional and only depends on the asymmetries, not on the specific plasma profiles.

Once the K_z^{PS} component is set by $\mathcal{C}_{\mathcal{G}}$, the BP component can be modelled from its general form from equation (2.42). The dependence of BP transport on (M_z^*, g, f_t) is given by the viscosity coefficients

$$K_{jk}^{\sigma} = \frac{c_{jk}^{\sigma,\mathrm{B}}\, g}{(1 + c_{jk}^{\sigma,\mathrm{P}}\, g)(1 + c_{jk}^{\sigma,\mathrm{PS}}\, g)}, \tag{3.6}$$

where j, k are 1 or 2. This arises from an interpolation of the viscosity coefficients in the individual banana (B), plateau (P) and Pfirsch–Schlüter collisionality regimes [107, 108]. The dependence of the c^{σ}_{jk} coefficients on the plasma profiles and geometry is calculated following appendix A of [108], with a more complete dependence on the impurity charge and trapped particle fraction from [109], and a complete dependence on rotation, which is obtained here. For trace impurities, only K^z_{11} is necessary to model $K^{\rm BP}_z$, because $K^{\sigma}_{jk} \propto n_\sigma$ and $n_i \gg n_z$, such that K^i_{11} can be neglected in equation (2.42). Knowing the NEO $K^{\rm BP}_z$ component, we solve for K^z_{11} and introduce factors of M^*_z and f_t into the c^{σ}_{jk} coefficients that help to reproduce its dependence on rotation, preserving the collisionality structure of equation (3.6), such that $c^{\sigma}_{jk}(M^*_z) = v^{\sigma}_{jk}(M^*_z)c^{\sigma}_{jk}(0)$, with the general form

$$v^{\sigma}_{jk}(M^*_z) = \frac{1 + m_1 M_z^{*m_2}}{1 + m_4 M_z^{*m_5}} \exp\left(-m_3 M_z^{*2}\right), \tag{3.7}$$

and the coefficients given in equations (B.19–B.28).

The total K_z coefficient, normalized to its value in the non-rotating limit, is plotted in figure 3.7(a) as a function of collisionality and rotation at a mid-radius $f_t = 0.56$. Note the sharp increase in the magnitude of K_z with low and intermediate rotation, reaching a maximum at $M^*_z \approx 2$ (at this f_t) and decreasing from that point onward, though remaining greater than the non-rotating coefficient.

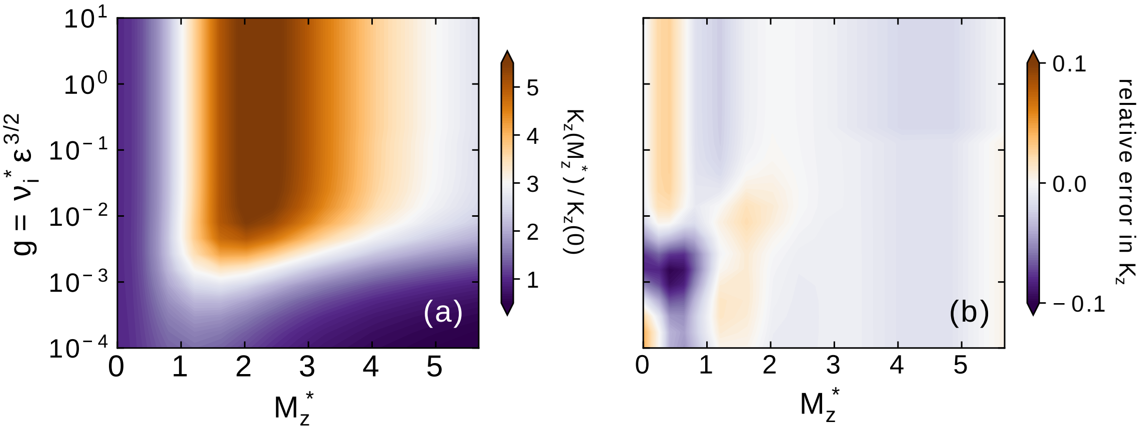

Figure 3.7: Dependence on rotation and collisionality of (a) the K_z coefficient, normalized to its non-rotating value, for W^{44+} at $f_t = 0.56$ ($r/a \sim 0.53$), and (b) the relative error in K_z of the model with respect to NEO.

In terms of the relative error of the model with respect to NEO, we have that the simpler K_z coefficient is within ±15%, although the error is considerably lower for most of the parameter space and is maximum at low collisionality with low but non-zero rotation, where both BP and PS components increase rapidly with rotation. This is shown in figure 3.7(b). We will see in the next subsection that the structure of the H_z coefficient is more complicated and therefore it has higher errors.

3.2.3 H_z coefficient

In general, the H_z coefficient has a more complex structure than K_z for both PS and BP components. Recalling equation (2.38), its PS component is given by

$$H^{\rm PS}_z = \left[-\frac{Z_i}{Z} + 1 - C^z_0 + \frac{\mathcal{C}_\mathcal{U}}{\mathcal{C}_\mathcal{G}}\left(C^z_0 + k_i\right)\right] K^{\rm PS}_z, \tag{3.8}$$

and the geometric term $\mathcal{C}_{\mathcal{U}}$ can be written in the LFS and FSA pictures as

$$\mathcal{C}_{\mathcal{U}}^{\mathrm{FSA}} = \left\langle \frac{n}{N} \right\rangle - \frac{\langle b^2/N \rangle}{\langle b^2/n \rangle}, \quad \mathcal{C}_{\mathcal{U}}^{\mathrm{LFS}} = \frac{1}{N(\theta_0)} - \frac{1}{n(\theta_0)} \frac{\langle b^2/N \rangle}{\langle b^2/n \rangle}. \tag{3.9}$$

In addition to the important role of $\mathcal{C}_{\mathcal{U}}$, we find that the ion flow coefficient k_i (which is a NEO output) has a dependence on rotation that is relevant to obtain the correct shape of H_z. While analytical formulae for k_i are available [144, 148], they do not describe the impact of rotation. We propose a new parametrization for the ion flow coefficient, now including rotation, given explicitly in appendix B.

Since H_z cannot be directly split into its PS and BP components, it becomes difficult to extract $\mathcal{C}_{\mathcal{U}}$ and fit its M_z^* dependence like it was done for $\mathcal{C}_{\mathcal{G}}$ in section 3.2.2 once K_z^{PS} was isolated. Instead, we find an analytical relation between $\mathcal{C}_{\mathcal{U}}$ and $\mathcal{C}_{\mathcal{G}}$. Assuming a small asymmetry of the main ion, i.e. $N \approx 1$ (based on the small mass of typical H, D, T), then from equations (3.3), (3.4) and (3.9) we have that

$$\mathcal{C}_{\mathcal{U}}^{\mathrm{LFS}} \approx \mathcal{C}_{\mathcal{G}}^{\mathrm{LFS}} + 1 - \frac{1}{b^2(\theta_0)} = \mathcal{C}_{\mathcal{G}}^{\mathrm{LFS}}(M_z^*) - \mathcal{C}_{\mathcal{G}}^{\mathrm{LFS}}(0) = \mathcal{C}_{\mathcal{G}}^{\mathrm{LFS}}(0)\,(f_{\mathcal{G}} - 1)\, f_{\mathcal{U}}, \tag{3.10}$$

where the $f_{\mathcal{U}}$ factor is introduced to minimize the differences with respect to NEO at high collisionality, accounting for errors due to this approximation. Its general form in M_z^* is given by

$$(f_{\mathcal{G}} - 1)\, f_{\mathcal{U}} = c_1 M_z^{*c_2} \frac{1 + c_3 M_z^{*c_4}}{1 + c_5 M_z^{*c_6}}, \tag{3.11}$$

with the coefficients $c_i(f_t)$ given explicitly in equations (B.6–B.7). At this point the H_z^{PS} can be fixed and used to extract the H_z^{BP} component from NEO. The structure of the H_z^{BP} component in terms of the viscosity coefficients K_{jk}^{σ} is given by

$$H_z^{\mathrm{BP}} = \left[\left(\frac{K_{12}^i}{K_{11}^i} - f_v \right) - \frac{Z_i}{Z} \left(\frac{K_{12}^z}{K_{11}^z} - f_v \right) \right] K_z^{\mathrm{BP}}. \tag{3.12}$$

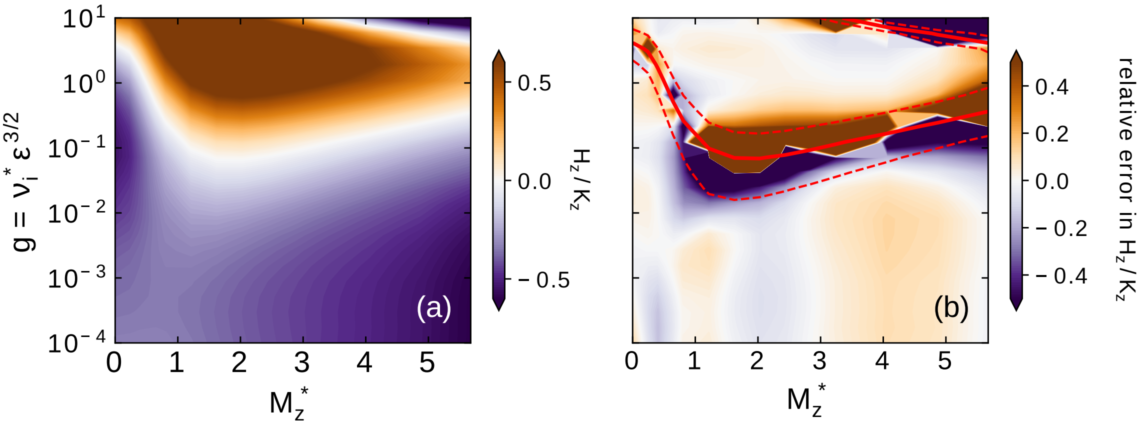

Figure 3.8: Dependence on rotation and collisionality of (a) the H_z/K_z coefficient, for W^{44+} at $f_t = 0.56$ ($r/a \sim 0.53$), and (b) the relative error in H_z/K_z of the model with respect to NEO. In (b), the solid red line shows the contour where H_z/K_z is zero (where the relative error becomes undefined), while the red dotted curves above and below show the $H_z/K_z = \pm 0.2$ contours.

The M_z^* dependence of the K_{11}^z coefficient is set by K_z^{BP}, while the dependence on K_{11}^i is assumed to be equivalent to K_{11}^z. This leaves the two $K_{12}^{i,z}$ coefficients as degrees of freedom to match $H_z^{\mathrm{NEO}} - H_z^{\mathrm{PS}}$, which is again accomplished via fitted factors on (M_z^*, f_t), from equation (3.7). The f_v coefficient reduces to $3/2$ at $M_z^* = 0$.

Having the BP and PS components of both K_z and H_z coefficients allows us to analyze the temperature screening coefficient H_z/K_z, for which the corresponding behavior in rotation and collisionality is shown in figure 3.8(a). A non-monotonic and coupled dependence is observed. The model is within ±30% of NEO when $|H_z/K_z| > 0.2$, but as $|H_z/K_z|$ becomes very small the error can be $> 50\%$. In absolute terms, if the H_z/K_z of NEO is 0.05 and the model predicts 0.08, the relative error is 60% but the model is quite close. When H_z/K_z approaches zero and changes sign the relative error can become arbitrarily large. Figure 3.8(b) shows the relative error in H_z/K_z. As we will show in section 3.3, these errors are low enough to reproduce profiles of transport coefficients with sufficient accuracy with respect to NEO. The strict regimes of applicability of these errors are the ranges of parameters of our NEO database, namely $10^{-4} \leq g \leq 10$, $M_i \leq 0.7$, $0.2 \leq f_t \leq 0.9$. The model can be used outside these ranges, where particularly in collisionality the transport coefficients tend to saturate to constant values, because the formulae are well behaved in the limits as $g \to 0$, $g \to \infty$, $M_z^* \to \infty$, $f_t \to 1$. However, statements on the errors in these limits cannot be made. In any case, the limit of high rotation at very low collisionalities is computationally challenging for NEO, which can give unreliable results with these parameters. At arbitrarily high collisionality the ordering of NEO in the parallel force balance, where the parallel friction is neglected, becomes inadequate, and a treatment like that of [92, 94, 95, 118] is necessary.

The effect on H_z/K_z is perhaps more illustrative when considering rotation scans at low, intermediate and high collisionalities ($g = 10^{-4}$, 10^{-2}, 10^{0}), i.e. slices of figure 3.8(a) in the collisionality plane. This is shown in figures 3.9(a), (b) and (c) respectively, for different values of f_t. Note that equivalent slices of 3.8(a) in the rotation plane are instead shown in figure 3.4(b). In the case of

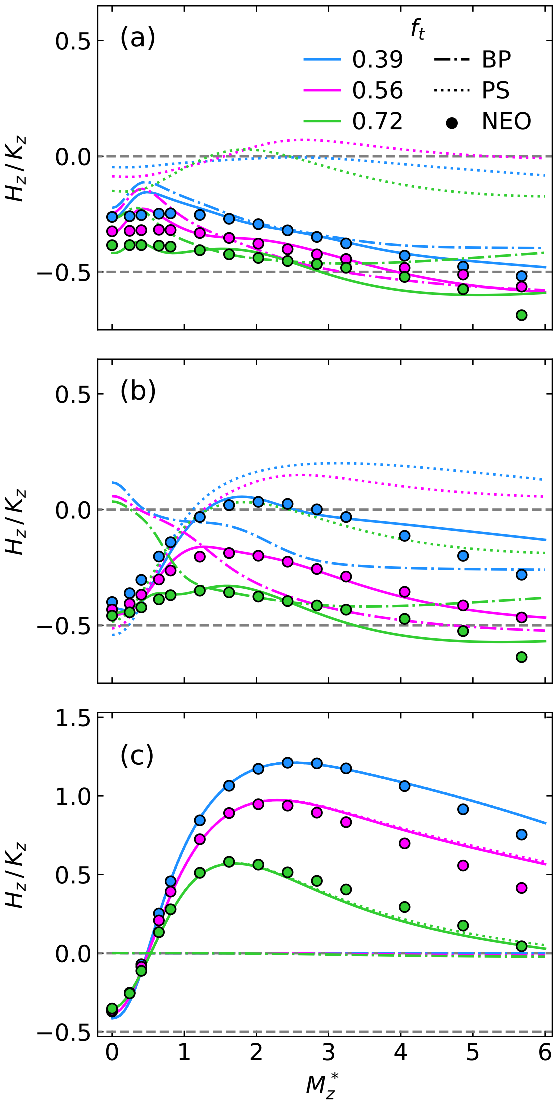

Figure 3.9: Dependence of the W temperature screening coefficient on rotation for different trapped fractions. (a-c) are at low, intermediate and high collisionality.

the temperature screening coefficient, the BP component of the model is defined as $H_z^{\mathrm{BP}}/(K_z^{\mathrm{BP}}+K_z^{\mathrm{PS}})$ and similarly for the PS component. These components are plotted in the dash-dotted and dotted curves respectively. In the high collisionality limit of figure 3.9(c), the BP component of the screening is negligible and the PS contribution quickly suppresses any positive effect of the temperature gradient, turning the thermal particle flux inward even at low $M_z^* \sim 1$. On the other hand, 3.9(a) demonstrates that the BP component is the one that manages to keep the temperature screening coefficient negative at low collisionalities as rotation increases, leading to the favorable rotation regime that has been discussed in section 3.1.2 of this chapter. The intermediate collisionality of figure 3.9(b) leads to a transitioning regime, where the PS component starts to lift the H_z/K_z towards detrimental positive values.

3.3 Applications to AUG and JET profiles

The new model introduced in section 3.2 is now implemented in the FACIT code, and in this section it is applied to the modelling of radial profiles of transport coefficients based on experimental plasma parameters in comparison with NEO results. An average W charge profile, calculated from coronal equilibrium $Z_{\mathrm{w}}(T_e)$, is used. For the experiments in question, Z_{w} varies from ∼50 in the core to ∼15 at the edge.

Since transport codes like ASTRA use a FSA representation of 1D profiles, and the model from section 3.2 was built on LFS analytical equations and fits of the LFS NEO output, the transport coefficients must be transformed from LFS to FSA representations. This transformation is detailed in Appendix A, following the derivation of [149]. In the rest of this section, all coefficients are flux-surface averaged.

Profiles of K_z and H_z/K_z with and without rotation are shown in figure 3.10 for the two most different considered discharges: the more collisional, slowly rotating AUG #36315 and the less collisional, highly rotating JET #97781. An advantage of the present model is the access to the independent BP and PS components, which are likewise included in the plots and help us to analyze the physics involved.

In (a) and (c), NEO shows a clear increase of K_z with rotation that is well reproduced by FACIT across the minor radius. The magnitude of the neoclassical transport in both discharges is enhanced by a factor of ∼ 5–12. The analytical model allows us to identify the PS component as the main cause of this enhancement, throughout most of the profile. For AUG #36315, the lower $M_z^* < 1.5$ is not enough to suppress K_z^{BP} and it is in fact in the region where the BP component is increased by rotation according to the scans from figure 3.4(a), leading to a subdominant but not negligible BP contribution necessary to accurately reproduce NEO's total K_z. For JET #97781, the high rotation ($M_z^* > 4$) reduces K_z^{BP} to a negligible contribution for most of the radius, making $K_z \approx K_z^{\mathrm{PS}}$ for $\rho \geq 0.2$. At $\rho < 0.2$, the strong dependence of the BP component on the inverse of f_t at high M_z^* increases its value to the point of overcoming the PS component, which is captured by FACIT.

An opposite behavior between these experiments is observed in the temperature screening coefficient. H_z/K_z is shown in (b) and (d) for each discharge, including the experimental profile of $-1/\eta_i$. Equation (2.35) indicates that the convection is outwards whenever H_z/K_z is below $-1/\eta_i$. For AUG #36315, which lays deep in the unfavorable rotation regime from the analysis of figure 3.5, the profile of the screening coefficient becomes less negative. This causes H_z/K_z to be above $-1/\eta_i$

across most of the radial profile when rotation is present, while it was below in the non-rotating limit. Thus, for AUG #36315, rotation reverses the neoclassical convection, causing it to become mostly inward while also significantly increasing its magnitude. FACIT reproduces this behavior on H_z/K_z well with respect to NEO in this discharge, although the most challenging regions for it to model are the ones where the BP and PS components interact more strongly, such as at $\rho \approx 0.9$ where there is a transition from dominant BP to PS components of the screening, and in the inner core, where both components strongly increase in opposite directions.

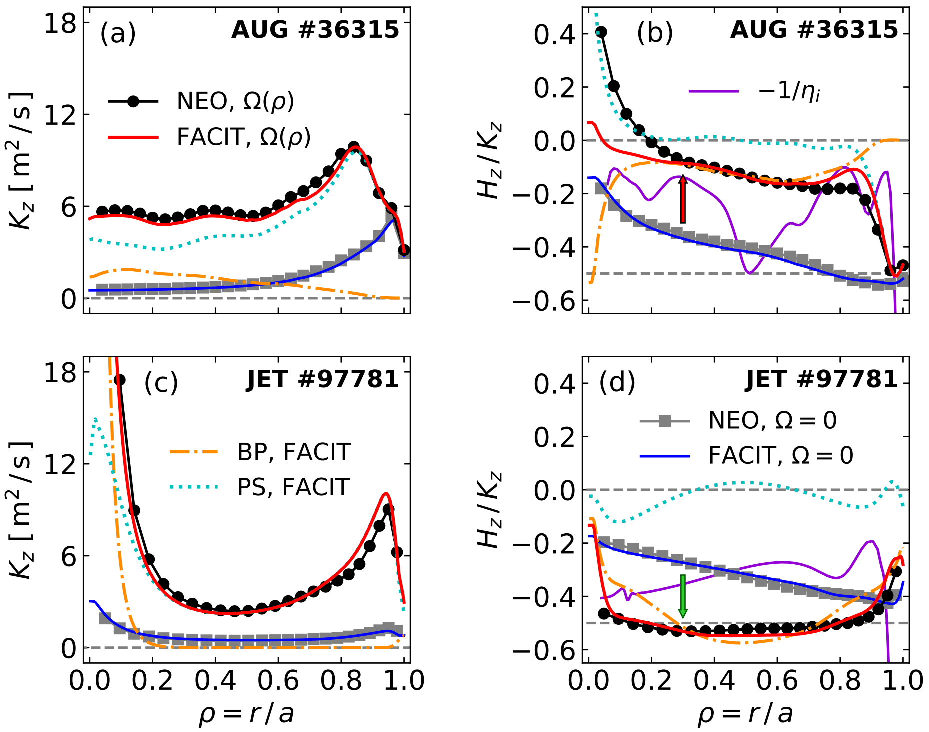

Figure 3.10: Application of the model against NEO results for AUG #36315 (top) and JET #97781 (bottom), for the convective coefficient K_z (left), and the temperature screening coefficient (right). Results with and without rotation are included, as well as the PS and BP components from FACIT. The red and green arrows in (b) and (d) indicate the respective decrease and increase of the temperature screening by rotation.

In contrast, in the case of JET #97781 the temperature screening coefficient becomes considerably more negative with rotation, allowing it to be below $-1/\eta_i$ across most of the radius ($\rho < 0.94$) and increasing the magnitude of the subsequent outward flux. This is consistent with its occurrence in the favorable rotation regime and the experimental observation of enhanced screening/reduced W accumulation reported in [142]. The BP-PS decomposition allows us to separately identify the dominant transport processes across the radius: in both cases, the PS contribution to H_z/K_z becomes less negative in the presence of rotation, thus decreasing the screening. On the other hand, the BP component keeps H_z/K_z sufficiently negative at high rotation, whenever it is large enough to overcome the deleterious PS behavior (like JET #97781 and unlike AUG #36315). In general, the BP component of the screening coefficient is the one that produces the favorable rotation regime, while the PS component leads to the unfavorable region. The BP neoclassical impurity transport, for which limited work in terms of modelling with rotation had been carried out until now, is necessary to model heavy impurities under current experimental conditions.

A final application is shown in figure 3.11, where the radial flux density $\Gamma_z/\langle n_z\rangle$ of W for AUG #38910 is compared for three models: the robust drift-kinetic calculations at arbitrary rotation of NEO, the fluid solution of NCLASS and the presently developed model in FACIT. This discharge is chosen for illustrative purposes due to comparable BP and PS contributions to the total flux. Using a model that omits the influence of rotation on neoclassical heavy impurity transport is not a suitable option: here, NCLASS largely underpredicts the flux. FACIT is able to analytically reproduce the NEO profile to good accuracy. In the case of AUG #38910, there is a strongly inward flux mostly due to the PS component in the more collisional pedestal, an outward flux from pedestal top to mid-radius due to a dominant positive BP contribution, and finally an inward flux at $\rho < 0.5$ caused by the two components being negative. Using only the PS contribution leads to a substantially different W flux, both in magnitude and direction.

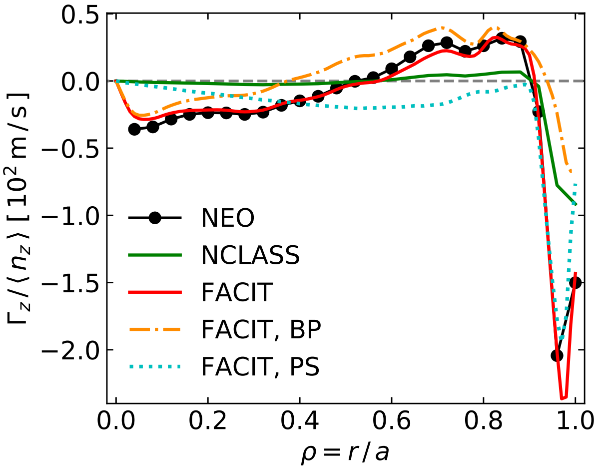

Figure 3.11: Flux density profile for AUG #38910 from NEO, NCLASS and FACIT.

Chapter 4

Modelling framework with impurities and their radiation

4.1 Impurity density evolution

The evolution of the density of an impurity is described by the continuity equation

$$\frac{\partial n_z}{\partial t} + \nabla \cdot \boldsymbol{\Gamma_z} = \mathrm{S}_z, \tag{4.1}$$

which follows from the 0^{th} moment of the kinetic equation (equation (2.5)). Here, S_z are the impurity sources. This conservation law states that the impurity density will evolve in time as long as there is an imbalance between the particle flux and the sources at a given location. In particular, the impurity density tends to develop a gradient such that the flux this gradient drives compensates the source term.

In previous chapters we have seen how in fusion plasmas we are typically interested in describing how particles and heat are transported radially from the core to the edge (and vice versa). A 1D flux surface averaged (FSA) description of the continuity equation is obtained, following [106], by first considering a flux surface labelled by a radial coordinate ρ and the volume enclosed by that surface, $V(\rho)$. Then, taking the volume integral of equation (4.1) inside this arbitrary surface (whose volume is assumed not to change strongly with time) we have that

$$\frac{\partial}{\partial t}\int_V n_z \,\mathrm{d}V + \int_V (\nabla \cdot \boldsymbol{\Gamma_z})\,\mathrm{d}V = \frac{\partial}{\partial t}\int_V n_z \,\mathrm{d}V + \oint_{\partial V} \boldsymbol{\Gamma_z} \cdot \nabla\rho \,\frac{\mathrm{d}A}{|\nabla\rho|} = \int_V \mathrm{S}_z \,\mathrm{d}V, \tag{4.2}$$

where the divergence theorem was used in the intermediate step and ∂V is the boundary surface of V. The unit vector radially normal to the flux surface is $\boldsymbol{\hat{e}_\rho} = \nabla\rho/|\nabla\rho|$. Two useful properties of the FSA (defined in equation (2.30)), namely

$$\langle Q\rangle = \frac{1}{\partial V/\partial\rho}\oint_{\partial V} Q \,\frac{\mathrm{d}A}{|\nabla\rho|} \qquad \text{and} \qquad \int_V Q\,\mathrm{d}V = \int_0^\rho \frac{\partial V}{\partial\rho}\,\langle Q\rangle\,\mathrm{d}\rho, \tag{4.3}$$

are used to bring equation (4.2) to

$$\frac{\partial}{\partial t}\int_0^\rho \frac{\partial V}{\partial\rho}\,\langle n_z\rangle\,\mathrm{d}\rho + \frac{\partial V}{\partial\rho}\,\langle \boldsymbol{\Gamma_z}\cdot\nabla\rho\rangle = \int_0^\rho \frac{\partial V}{\partial\rho}\,\langle \mathrm{S}_z\rangle\,\mathrm{d}\rho\,. \tag{4.4}$$

Differentiating with respect to ρ, we arrive at the 1D FSA transport equation:

$$\frac{\partial}{\partial t}\left(\frac{\partial V}{\partial \rho}\langle n_z\rangle\right)+\frac{\partial}{\partial \rho}\left[\frac{\partial V}{\partial \rho}\langle \boldsymbol{\Gamma_z}\cdot\nabla\rho\rangle\right]=\frac{\partial V}{\partial \rho}\langle \mathrm{S}_z\rangle . \tag{4.5}$$

This general form of the transport equation is used in the transport solvers we will employ in this thesis, namely ASTRA [78, 79] and STRAHL [150] (also in other transport codes like TGYRO [151] and JINTRAC [135] that are not used here). However, the radial coordinate ρ and the way the radial flux $\langle \boldsymbol{\Gamma_z}\cdot\nabla\rho\rangle$ is expressed might differ between these codes, meaning that metric coefficients need to be carefully transformed between them. These transformations are derived in detail, for reference, in Appendix C. The radial impurity flux is decomposed into diffusive and convective contributions, with their corresponding coefficients, such that

$$\langle \boldsymbol{\Gamma_z}\cdot\nabla r\rangle=\Gamma_z=-D_z\frac{\partial\langle n_z\rangle}{\partial r}+\langle n_z\rangle v_z, \tag{4.6}$$

where we chose $\rho = r$ (the mid-plane minor radius). In the absence of impurity sources, in steady state the impurity particle flux must go to zero. The density gradient will be such that the diffusive flux exactly balances the convection, with the resulting equilibrium normalized gradient being

$$\frac{R}{L_{\langle n_z\rangle}}=-\frac{R v_z}{D_z}. \tag{4.7}$$

This is an important relation that will be extensively used.

Atomic processes in plasmas

When an element of atomic number Z and mass number A enters a fusion plasma, it does not have a single density but rather a distribution of all its possible ionization stages $z \in \{0, 1, \cdots, Z\}$ in different fractional abundances, which vary from core to edge depending on the plasma temperature and density. Atoms of an element at the ionization state z undergo atomic processes with the electrons and other ions in the plasma, resulting in emission of electromagnetic radiation and also leading to transitions to higher or lower ionization stages.

The basic mechanism for emission of *line radiation* is the following. Coulomb collisions between electrons and impurity ions cause a transfer of electron thermal energy to the impurity internal energy. The impurity ion goes into an excited state and later decays back to its ground state, emitting a photon which ultimately escapes from the plasma (considering the low optical depth typical of fusion plasmas) [152]:

$$A^z+e^-\longrightarrow A^{z*}+e^-, \qquad\qquad A^{z*}\longrightarrow A^z+h\nu \tag{4.8}$$

where ν is the frequency of the emitted photon and h is Planck's constant. Line radiation constitutes the dominant channel of radiative losses in fusion plasmas that are contaminated with high-Z impurities. It can be characterized by a *cooling factor* L_z which in general depends on the plasma temperature and density, such that the radiated power density is given by

$$P^z_{\text{line}}=n_z n_e L_z(T_e,n_e)=c_z n_e^2 L_z(T_e,n_e). \tag{4.9}$$

Bremsstrahlung is the radiation emitted when electrons are accelerated by Coulomb scattering. Synchrotron radiation is caused by acceleration of charged particles due to their gyro-motion in the presence of a magnetic field (and it is only significant at relativistic gyration speeds). These loss mechanisms become increasingly important at reactor-relevant conditions of higher temperature, density and magnetic field, since their power densities scale as

$$P_{\text{brems}} \propto Z_{\text{eff}}\, n_e^2 \sqrt{T_e}\,, \qquad\qquad P_{\text{sync}} \propto B_\varphi^{5/2}\, T_e^{5/2} \sqrt{n_e}\,, \tag{4.10}$$

where Z_{eff} accounts for the presence of all the different ion species.

Overall, these three radiation mechanisms are electron energy sinks that need to be considered in the electron heat transport equation.

Other atomic processes represent sinks and sources of the ionization state A^z:

- Collisional ionization: $A^z + e^- \longrightarrow A^{(z+1)*} + 2e^-$.
- Collisional recombination: $A^z + e^- \longrightarrow A^{(z-1)*}$.
- Charge exchange: $A^z + B^{z'} \longrightarrow A^{(z-1)*} + B^{z'+1}$. Here, B can also be an initially neutral atom, for example from the NBI beam. Then this is the basic process in CXRS that was described in section 1.3.4.

If we consider the transport equation (4.5) of a single ionization stage of an impurity atom, for instance W^{34+}, then the source term

$$\begin{aligned} \langle \mathrm{S}_z \rangle = &- \left(n_e R_{(z\to z-1)} + n_e I_{(z\to z+1)} + n_i \alpha^{\text{cx}}_{z\to z-1} \right) \langle n_z \rangle \\ &+ \left(n_e R_{(z+1\to z)} + n_i \alpha^{\text{cx}}_{z+1\to z} \right) \langle n_{z+1} \rangle + n_e I_{(z-1\to z)} \langle n_{z-1} \rangle \end{aligned} \tag{4.11}$$

couples the density of charge state z to the densities of the neighboring stages $z-1$ and $z+1$. Here, R, I and α^{cx} are the recombination, ionization and charge exchange rates that depend on the plasma temperature and density. They can be calculated with theoretical collisional-radiative models and experimental measurements [33, 152–154]. The OPEN-ADAS database [155], which is used throughout this thesis, contains tabulated data of these coefficients for all ionization stages of most fusion-relevant elements as a function of T_e and n_e.

Equation (4.5) becomes a system of Z coupled equations for the densities of all ionization stages of an impurity element. For example, taking W and considering only ionization and recombination we have that

$$\begin{aligned} \dot{n}_1 + \nabla\cdot\Gamma_1 &= n_e \left[-I_{(1\to2)} n_1 + R_{(2\to1)} n_2 \right] + \mathrm{S}_{0\leftrightarrow1}, \\ \dot{n}_2 + \nabla\cdot\Gamma_2 &= n_e \left[-R_{(2\to1)} n_2 - I_{(2\to3)} n_2 + R_{(3\to2)} n_3 + I_{(1\to2)} n_1 \right], \\ &\vdots \\ \dot{n}_{73} + \nabla\cdot\Gamma_{73} &= n_e \left[-R_{(73\to72)} n_{73} - I_{(73\to74)} n_{73} + R_{(74\to73)} n_{74} + I_{(72\to73)} n_{72} \right] \\ \dot{n}_{74} + \nabla\cdot\Gamma_{74} &= n_e \left[-R_{(74\to73)} n_{74} + I_{(73\to74)} n_{73} \right]. \end{aligned} \tag{4.12}$$

$\mathrm{S}_{0\leftrightarrow1}$ is the source/sink of the first charge state, coming from ionization of neutral atoms of the impurity species and recombination of the first charge state. In the case of tungsten these neutrals can arise from the erosion of vessel walls and divertor through their interaction with the plasma, while in the case of seeded impurities they can be introduced by gas puffing.

The so-called *coronal equilibrium* is the steady-state distribution of ionization stages in the absence of transport, where ionization and recombination processes balance each other [156]. That is, we refer as coronal equilibrium to the solution of the system of equations (4.12) in the limit when the left-hand-side is zero.

We can also describe the evolution of the total density of an impurity element in a plasma, by summing the system of equations (4.12). This has the convenient property that virtually all terms on the right-hand-side cancel each other out. Then, defining the total density and weighted diffusion and convection coefficients as

$$\overline{n}_Z = \sum_{z=1}^{Z} n_z, \qquad \overline{v}_Z = \frac{\sum_{z=1}^{Z} v(z)\, n_z}{\sum_{z=1}^{Z} n_z}, \qquad \overline{D}_Z = \frac{\sum_{z=1}^{Z} D(z)\, \dfrac{\partial n_z}{\partial r}}{\sum_{z=1}^{Z} \dfrac{\partial n_z}{\partial r}}, \tag{4.13}$$

we can write an equation for the evolution of this newly-defined total density:

$$\frac{1}{V'}\frac{\partial(V'\overline{n}_Z)}{\partial t} + \frac{1}{V'}\frac{\partial}{\partial\rho}\left[V'\left\langle|\nabla\rho|^2\right\rangle\left(-\overline{D}_Z\frac{\partial\,\overline{n}_Z}{\partial\rho} + \overline{n}_Z\overline{v}_Z\right)\right] = \mathrm{S}_Z, \tag{4.14}$$

where $V' = \partial V/\partial\rho$, we adopt the metric convention of ASTRA, and the only source term is the total source of ionized impurities of the given species, $\mathrm{S}_Z = \mathrm{S}_{0\leftrightarrow 1}$.

4.2 Coupling of STRAHL to ASTRA 8

The ASTRA transport code can solve equations of the same form as equation (4.14), which in many situations can be useful to describe the evolution of the total density of an impurity species. Likewise, in ASTRA one typically assumes average charge and cooling factor profiles as a function of the local electron temperature, calculated as interpolations of coronal equilibrium data. The local value of the charge at a given radial location is used, for instance, in the calculation of transport coefficients by the turbulent and neoclassical transport models. The cooling factor is used to calculate the radiative losses in the power balance.

Examples of the default ASTRA formulas for $Z_{\mathrm{w}}(T_e)$ and $L_{\mathrm{w}}(T_e)$ are shown in blue in figure 4.1. These formulas come from fits of atomic data tables from 1977 [157]. More recent calculations of atomic data for W [33], plotted in black circles in figure 4.1, show that these expressions can be inaccurate in certain electron temperature ranges. For instance, at a reactor core relevant $T_e \approx 15$ keV, the default W cooling factor of ASTRA underestimates the data of [33] by a factor of 2, leading to the use of half of the radiated power by W in the power balance. We have introduced a new parametrization that better interpolates the data of [33], which is now being distributed in ASTRA.

The impurity transport code STRAHL [150, 158] can be used to perform more realistic and precise modelling of impurities, both in terms of the distribution of

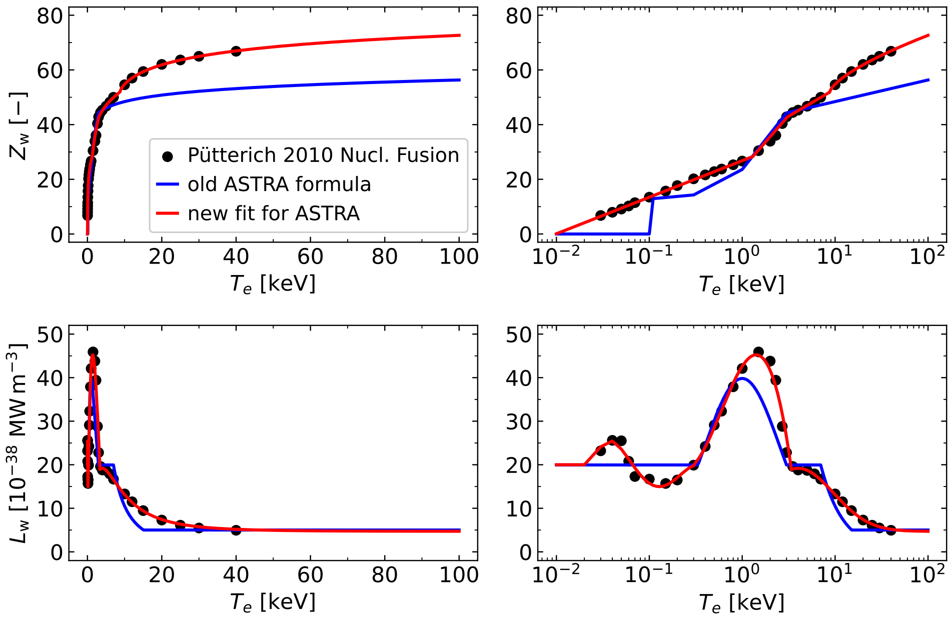

Figure 4.1: Coronal equilibrium formulae for the average W charge (top panels) and W cooling factor (bottom panels) in ASTRA, as a function of the electron temperature in linear (left panels) and logarithmic scales (right panels).

their charge state densities and of the radiation they produce. STRAHL solves the system of equations (4.5 + 4.11) for all ionization stages of a given impurity species, using atomic rates from ADAS. This allows us to calculate the ionization equilibrium distribution of the impurity considering both transport and sources. STRAHL also calculates the resulting radiated power profiles, such that we can consider the effect of impurities on the local power balance through radiative cooling of the electrons, in addition to the fuel dilution that arises by imposing quasi-neutrality.

STRAHL has been coupled to ASTRA 8, updating the previous coupling to ASTRA 7 and generalizing it to an arbitrary number of impurity species. The idea is to evolve the main plasma profiles of electron and ion temperatures and electron density in ASTRA, and the impurity densities in STRAHL, taking the radiated power densities from the STRAHL outputs as well.

STRAHL calculates the value of the impurity densities at the separatrix from the edge sources given as user input and the simplified scrape-off layer (SOL) model described in [159]. The SOL decay lengths of the temperature and density profiles are important, as they play a role in the incoming flux and energy at the targets. We use the heuristic drift model of [160] for the SOL parallel heat flux width $\lambda_{q_\parallel}$, and we calculate the SOL decay lengths of the plasma profiles, λ (where $X_{\mathrm{sol}}(r) = X_{\mathrm{lcfs}}\, e^{-r/\lambda}$), assuming a Spitzer-Härm conductivity relation $\lambda_{T_e} = 7\lambda_q/2$ along with the experimental observation of $\lambda_{n_e} \approx 3\lambda_{T_e}/2$ [161], and taking $\lambda_{T_i} \approx \lambda_{T_e}$, $\lambda_{n_z} \approx \lambda_{n_e}$ (for all impurity species). Typical values of the SOL Mach number [162] are applied.

We set a significantly lower time step for STRAHL than ASTRA (on the order of $10\,\mu$s vs $10\,$ms respectively), because STRAHL solves the impurity equations explicitly in time with ionization-recombination times much shorter than 10 ms. A lower time step is also required for numerical stability, particularly in cases with strong convection, given that the transport solver of STRAHL lacks the numerical scheme for stiff transport [163] of ASTRA.

4.2.1 Benchmarks of impurity density evolution

To verify the correct implementation of every step in the coupling of STRAHL into ASTRA, we begin with two important tests: ASTRA and STRAHL should obtain the same total impurity density profile if the same diffusion and convection coefficients (D_z, V_z) are used, and the average charge state and cooling factor calculated by STRAHL should converge to the coronal equilibrium data when the transport becomes very small (i.e. when the left-hand-side of equations (4.12) goes to zero).

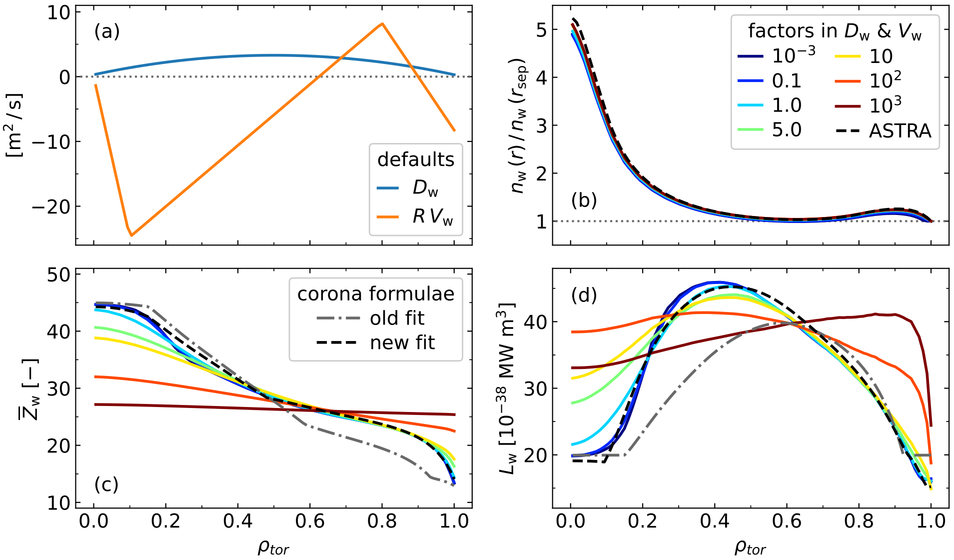

Figure 4.2: Comparison of W distributions in the corona limit against conditions with increasing transport. (a) Default input transport coefficients, to be scaled up and down. (b) Resulting evolved W density profiles by STRAHL (normalized to 1 at the separatrix) as both the diffusive and convective coefficients of W are multiplied by the factors in the legend. Evolution of total density by ASTRA in black dashed line. (c) Average W charge and (d) W cooling factor, calculated by STRAHL and with the old and new corona formulae from ASTRA for comparison.

To test these two elements we use simple analytical D_z and V_z coefficients, shown in figure 4.2(a), both in STRAHL and in the ASTRA equation for the impurity density. We use tungsten as a representative impurity because it has a large number of charge states (a low-Z impurity is not particularly interesting for this purpose since it becomes fully ionized already at the lower temperatures of the very edge of the plasma). We run multiple simulations to steady-state, multiplying both D_z and V_z by an increasing factor between 10^{-3} (coronal dominated limit) and 10^3 (transport dominated limit). The factor must be the same for both diffusion and convection if we want the steady-state density to converge to the same profile, recalling equation (4.7). In figure 4.2(b) we can see that the resulting impurity density profiles indeed converge to the same profile, both in ASTRA and in STRAHL for all factors in D_z and V_z. The radial coordinate used here is the square root of the normalized toroidal flux, $\rho_{\text{tor}} = (\Psi_{\text{tor}}/\Psi_{\text{tor}}^{\text{LCFS}})^{1/2}$, ranging from 0 at the magnetic axis to 1 at the last closed flux surface. The average W charge (calculated as $\overline{Z} = \sum_z Zn_z / \sum_z n_z$) and the W cooling factor are shown in panels (c) and (d) respectively. Indeed, in the low transport limit the resulting STRAHL quantities converge to the new, more accurate corona formulae in ASTRA, shown in black dashed lines (for comparison, the older formulae are shown in gray dash-dotted lines). As the magnitude of transport is increased, we see that the average charge and cooling factor profiles begin to deviate, and the simple coronal equilibrium assumption in ASTRA is no longer valid.

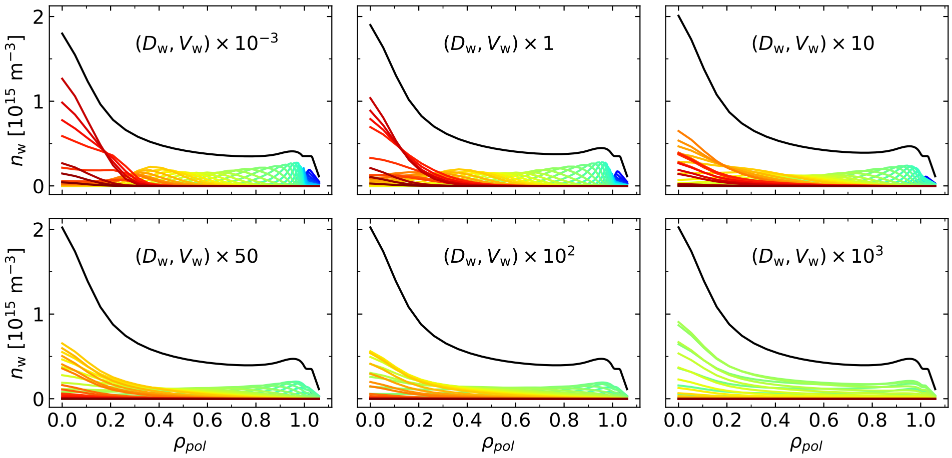

Figure 4.3: Depending on the level of transport, different distributions of charge states generate the same total density profile if the convection to diffusion ratio is constant. From the upper left to the lower right, the distribution goes from coronal equilibrium to deeply non-coronal. Even though the total density is practically unchanged, the average charge and cooling factor profiles change in the scan of tranport levels. The color scale goes from $Z = 1$ in dark blue to $Z = 50$ in dark red.

The difference in the distribution of the W charge states at different levels of transport is further investigated in figure 4.3, where the density profiles of all charge states are plotted in colors and the total density in black. Here the radial coordinate is the normalized poloidal flux, $\rho_{\mathrm{pol}} = [(\Psi_{\mathrm{pol}} - \Psi_{\mathrm{pol}}^{\mathrm{axis}})/(\Psi_{\mathrm{pol}}^{\mathrm{LCFS}} - \Psi_{\mathrm{pol}}^{\mathrm{axis}})]^{1/2}$. Even if the total impurity density is barely modified, the distribution of charge states changes significantly, which explains the differences in the average charge and total cooling factors in figure 4.2. In the coronal equilibrium limit and with moderate values of the transport coefficients (top panels), the distribution of each charge state is localized radially, with the lower charge states populating the colder edge and the higher charge states populating the hotter core. As the D_z and V_z are increased (lower panels), the lower and higher charge states are less populated and the intermediate charge states have a dominant fractional abundance throughout the radius. These values of the transport coefficients are quite extreme, and can be expected to be only approached at the edge of the plasma, where gradients are higher. We conclude that the coronal equilibrium approximation is adequate except at extreme values of the transport coefficients. This means that in the plasma core it remains a good approximation, but modelling of the plasma edge requires the inclusion of non-coronal effects by an impurity code like STRAHL.

4.2.2 Neoclassical transport coefficients calculated with an average impurity charge and with all charge states

A typical issue in the modelling of impurities with several charge states, like tungsten, is that in principle the transport coefficients differ between the charge states of a given species. Turbulent transport coefficients do not depend strongly on the impurity charge [126], but neoclassical coefficients do, since the frequency of Coulomb collisions depends on the charge of the colliding species.

A common approach for the calculation of D_z and v_z in transport codes like TGLF and FACIT is to take the input charge of the impurities at a given radial position as their average charge locally, assuming that, in the close vicinity to that location, ionization stages far from the average charge are not very populated. For turbulent transport codes, or neoclassical codes with higher computational demands like NEO, a simplifying approach like this is practically required, since considering all charge states (74 in the case of W) is unfeasible. In fact, TGLF is limited to 7 input species, at least two of which are the electrons and the main ions.

This results in a single profile of the transport coefficients: $D(\overline{Z})$ and $V(\overline{Z})$. On the other hand, a fast code like FACIT can calculate the transport coefficients for all individual charge states well within the low computational time requirements of integrated modelling, leading to a set of coefficients $\{D(z), V(z)\}_{z=1,\cdots,Z}$. This is illustrated in the top panels of figure 4.4 for neoclassical coefficients calculated with FACIT. If we perform a weighted average over the fractional abundance of each charge state, we see in the bottom panels that we approximately recover the profile calculated with the average charge, giving confidence to the use of the simpler-to-compute $D(\overline{Z})$ and $V(\overline{Z})$.

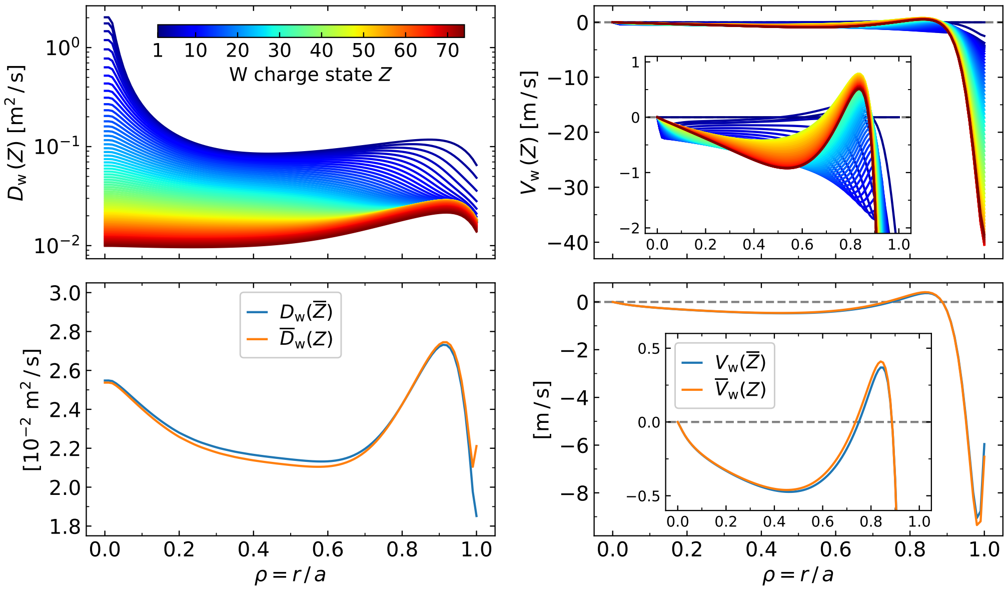

Figure 4.4: Profiles of neoclassical transport coefficients for all W charge states (top panels). Profiles of diffusion and convection calculated with an average charge profile and by averaging the charge-dependent coefficients (lower panels).

The impurity density can then be evolved using the same $D(\overline{Z})$ and $V(\overline{Z})$ profiles for all charge states, or using charge-dependent coefficients $\{D(z), V(z)\}_{z=1,\cdots,Z}$ for each individual charge state z. Verifying that both of these resulting impurity density profiles are close enough is an important test for the validity of the use of the simpler $D(\overline{Z})$ and $V(\overline{Z})$.

At present, STRAHL does not take separate transport coefficients for the individual charge states in input. It can calculate the charge dependent neoclassical diffusion and convection for all charge states internally, using the NEOART code [139, 140]. However, NEOART does not describe poloidally asymmetric impurity densities and its use also greatly increases the computational times of STRAHL.

Instead, we use the Aurora impurity transport code [164] for these tests. Aurora shares the main structure of STRAHL, but for our purposes the relevant difference is that it does take separate transport coefficients for each charge state of the impurity. We perform two simulations in Aurora, using the neoclassical transport coefficients from the top panels of figure 4.4, and the ones calculated with the average charge profile (blue curves in the bottom panels of figure 4.4). The resulting total impurity density profile, its normalized gradient and the resulting cooling factor are shown in figure 4.5 for a low value of the turbulent diffusivity.

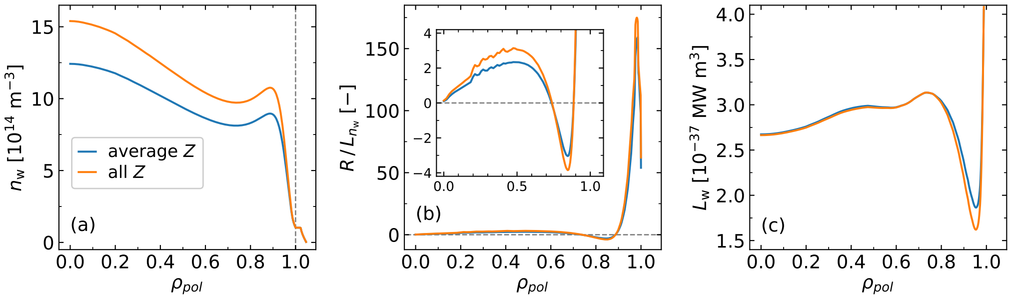

Figure 4.5: W distribution using transport coefficients calculated with an average charge profile or for each ionization stage. (a) Total density, (b) normalized gradient, (c) cooling factor. An additional turbulent diffusivity of 0.1 $\mathrm{m^2\,s^{-1}}$ is used.

While there are some differences in the final density profile, connected to a stronger gradient when the coefficients for all charge states are used, the two profiles are within 20% of each other. This can be considered an acceptable margin of error, considering the significantly higher complexity of including all $\{D(z), V(z)\}_{z=1,\cdots,Z}$ in the set of evolution equations for the densities of all charge states (in fact, this is not possible in STRAHL as we previously mentioned, and Aurora is not coupled to ASTRA so far). These differences are strongly reduced when the (approximately charge-independent) turbulent transport coefficients are increased, as shown in figure 4.6, where a higher (albeit still low) turbulent diffusivity is applied.

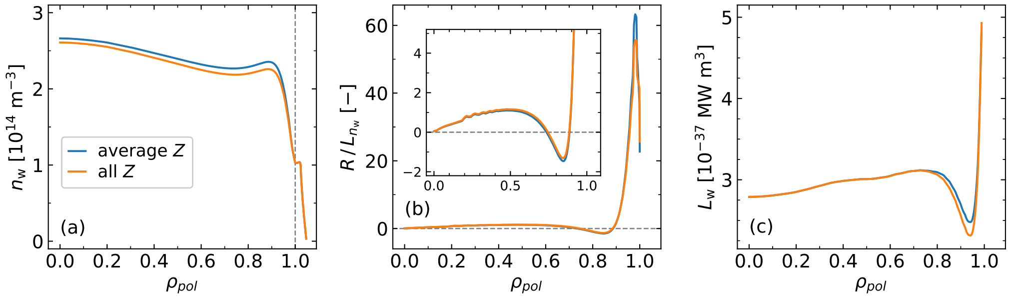

Figure 4.6: Same as figure 4.5, but with a turbulent diffusivity of 0.3 $\mathrm{m^2\,s^{-1}}$.

When transport is high, the distribution of charge states is strongly non-coronal, as we showed in figure 4.2. The strong edge neoclassical convection shown in figure 4.4 arises from the higher gradients and collisionality typical of the plasma periphery. The most significant deviation between the resulting cooling factors using an average charge and all charge states, in both figure 4.5(c) and 4.6(c), takes place at the edge ($\rho_{\mathrm{pol}} > 0.9$ in this case), where transport is strong and the distribution is farther from the coronal limit, in agreement with figure 4.2. The cooling factors can deviate by $\sim 20\%$, but this edge region has a larger share of the plasma volume, meaning that the radiated power is more sensitive to the edge cooling factor.

This highlights the complexity of modelling impurities at the plasma edge.

4.2.3 Decomposition of impurity flux into its diffusive and convective components

Transport models like TGLF-SAT2 usually give in output the heat and particle fluxes, and not the transport coefficients. For the impurities, in particular, this means that there is no direct access to the diffusive and convective coefficients D_z and V_z. The lack of access to the (turbulent) transport coefficients is unpractical not only because a lot of physics is encoded in the D_z and V_z, but also because correct values of the separate coefficients are essential for realistic ionization equilibrium calculations by STRAHL, as we will see next.

Assuming that the neoclassical coefficients are directly available (as is the case for codes like FACIT, NCLASS and NEOART but not NEO), a common approach consists on setting the entire turbulent flux Γ_z^{trb} into an effective convection $\hat{V}_z^{\mathrm{trb}}$,

$$\frac{R\,\Gamma_z}{n_z} = (D_z^{\mathrm{ncl}} + D_z^{\mathrm{trb}})\frac{R}{L_{n_z}} + R\,(V_z^{\mathrm{ncl}} + V_z^{\mathrm{trb}}) = D_z^{\mathrm{ncl}}\frac{R}{L_{n_z}} + R\,(V_z^{\mathrm{ncl}} + \hat{V}_z^{\mathrm{trb}}). \quad (4.15)$$

This approach is valid when the total impurity density is evolved with, for example, equation (4.14). However, if the densities of all ionization stages are evolved with a system of equations like the one in equation (4.12), this approach is no longer valid, because the gradient that is given as input to the transport model is typically the gradient of the total impurity density, which can be completely different from the gradients of each charge state density. This means that incorrect transport coefficients are used in the impurity transport code.

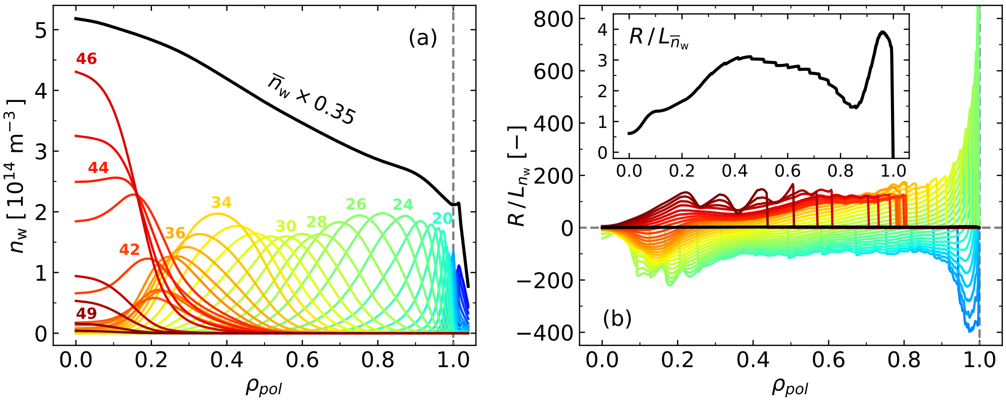

Figure 4.7: (a) Example of a charge state distribution of tungsten yielding a total density with a mild gradient. (b) Corresponding normalized gradients of each charge state density and the one of the total density, highlighting the need for a correct description of the diffusivity in STRAHL.

This is exemplified in figure 4.7, where on the left we see a total W density profile (in black) composed of many different charge state densities (in colors). Even if the normalized gradient of the resulting total density is mild, the gradients of each ionization stage can be very strong, as shown on the right panel.

To illustrate the difference between using realistic turbulent coefficients or setting the entire turbulent flux into an effective convection, we take simple constant coefficients as $D_z^{\mathrm{ncl}} = 0.05\ \mathrm{m^2\,s^{-1}}$, $D_z^{\mathrm{trb}} = 3\ \mathrm{m^2\,s^{-1}}$, $V_z^{\mathrm{ncl}} = -5\ \mathrm{m\,s^{-1}}$, $V_z^{\mathrm{trb}} = -0.5454\ \mathrm{m\,s^{-1}}$ such that $R/L_{n_z} = 3$, and $\hat{V}_z^{\mathrm{trb}} = +4.91\ \mathrm{m\,s^{-1}}$. The resulting equilibrium charge state distribution is shown in figure 4.8, where we can see that even though the resulting total density is the same (by construction), the distribution of the ionization stages and the resulting cooling factors are different.

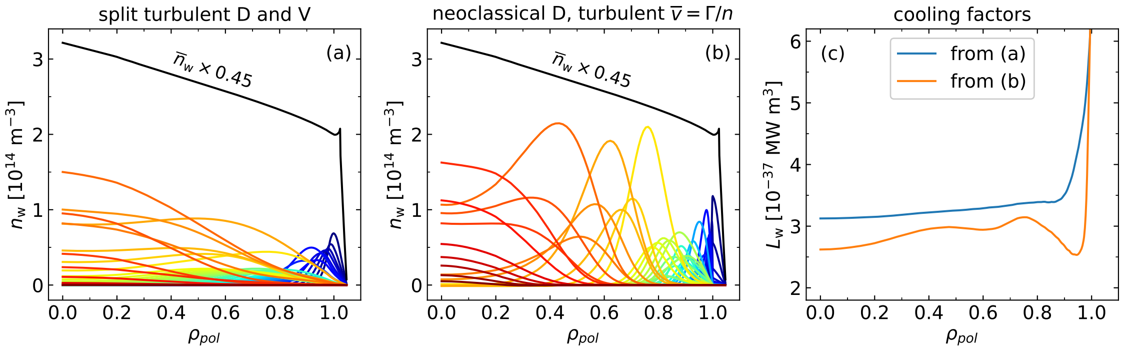

Figure 4.8: Equilibrium W distribution using a split turbulent diffusion and convection (a), or a neoclassical diffusion and a turbulent flux density as equivalent convection (b), with the resulting cooling factors (c).

In the following we consider TGLF as the code that calculates the turbulent flux that needs to be split into diffusive and convective components. Two possible schemes to obtain the D_z and V_z are

- performing two TGLF runs, one with the real impurity density gradient and one setting the gradient to zero, or
- performing a single TGLF run, but adding an extra species of the same impurity but with a trace density (so that it does not affect the simulation) and with its gradient set to zero.

In both methods the impurity particle flux of the "second" impurity (meaning the one with its gradient set to zero) is entirely convective, such that $\Gamma_2/n_2 = V$, from where we readily obtain the convective coefficient. This can be replaced in the first computed flux, $\Gamma_1/n_1 = D/L_n + V$, to yield the diffusion coefficient $D = (\Gamma_1/n_1 - \Gamma_2/n_2)L_n$. The densities n_1 and n_2 and the gradient R/L_n are known, and the fluxes Γ_1 and Γ_2 are obtained in the output of the transport model.

We have to note that the computational bottleneck in integrated modelling workflows is typically the turbulent transport calculations. The two aforementioned methods will certainly increase the computational times of the simulation, and it is therefore important to determine how these times scale as we increase the number of impurities, in order to decide which method is more convenient.

The cost of the TGLF matrix inversion grows approximately with the square of the number of species, N_{spc}^2. With two background species (electrons and one main ion), the computational times of the “two-call” and “duplicate-trace” methods grow as $2 \times (2 + N_{\mathrm{imp}})^2$, $(2 + 2\,N_{\mathrm{imp}})^2$ for N_{imp} impurities.

The growth of the TGLF execution time as a function of the number of impurities under consideration is shown in figure 4.9, for both methods (in orange and green) as well as the case where there is no splitting of the flux (in blue). We will typically consider at least two impurities for the applications presented in chapters 5 and 6, for which the two-call method is already faster than the duplicate-trace method. Furthermore, since the total number of species in TGLF is limited to 7, the duplicate-trace method cannot be applied to a simulation with more than two impurities. In contrast, the two-calls method can be applied to up to five impurities.

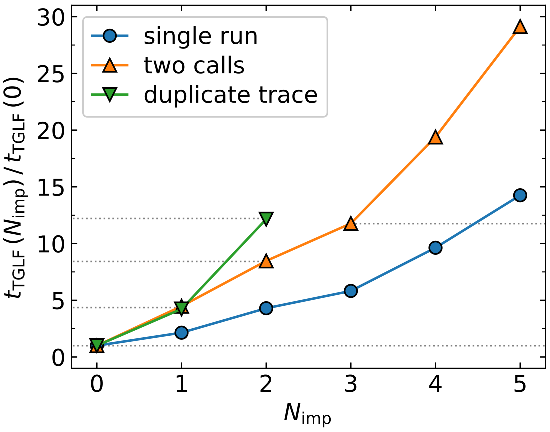

Figure 4.9: TGLF execution time as a function of the number of impurities, normalized to the case without impurities.

In this sense, the preferred splitting scheme will be the two-call method. However, we must note that the validity of this method applies when the relation between the impurity flux and the impurity density gradient is linear. This is strictly satisfied only in the trace impurity limit, where the impurities do not affect the background turbulence. We have tested this flux-gradient linearity by performing standalone TGLF scans on the charge concentration $Z\,c_z$ of an argon impurity, and the results are shown on the left panel of figure 4.10.

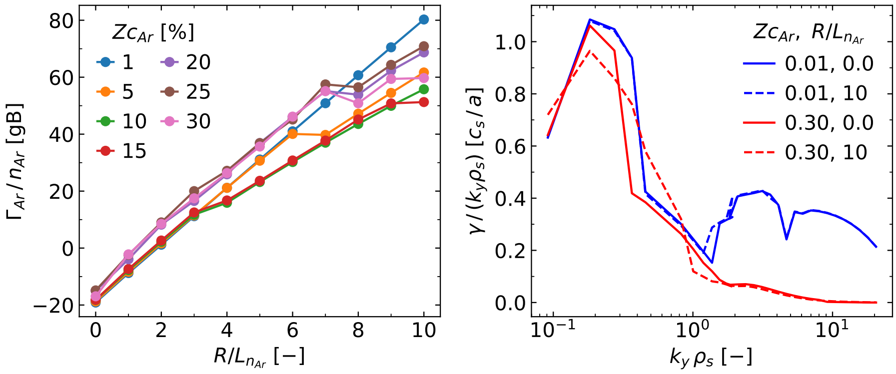

Figure 4.10: TGLF flux-gradient relation as the Argon charge concentration Zc_z increases (left). Growth rate spectrum for the lowest and highest Zc_z (right).

The growth rate spectra for the extreme cases of low and high gradients with low and high charge concentrations are shown on the right. Even for quite high concentrations (for reference, in our applications in the following chapters $Z\,c_z$ is never above 10–15 %) and high normalized gradients the relation remains close to linear.

Finally, we must verify that splitting the flux into diffusive and convective components we recover the same impurity density profile as when we use the total flux, since the same transport physics is being described in all methods. For this, we perform a simulation of the evolution of a boron (B) impurity in an ASDEX Upgrade discharge (#34017 at 3.8s) using the TGLF flux ("single run") as well as the two splitting methods. The resulting B densities and their gradients are shown in figure 4.11. On the right, the peaking factor $-RV/D$ is plotted in dashed lines. We recall from equation (4.7) that the normalized gradient converges to this ratio of transport coefficients in steady state. We find satisfactory agreement between the resulting impurity density profiles and their gradients, giving confidence to our implementation of the D–V splitting. The $-RV/D$ of the single run method presents strong oscillations because there is only the (small) neoclassical diffusion. The resulting B transport coefficients for this discharge are shown in figure 4.12. Both coefficients calculated with the two different schemes coincide quite well with each other on the left panel, and on the right we verify that the total flux goes to zero in steady state.

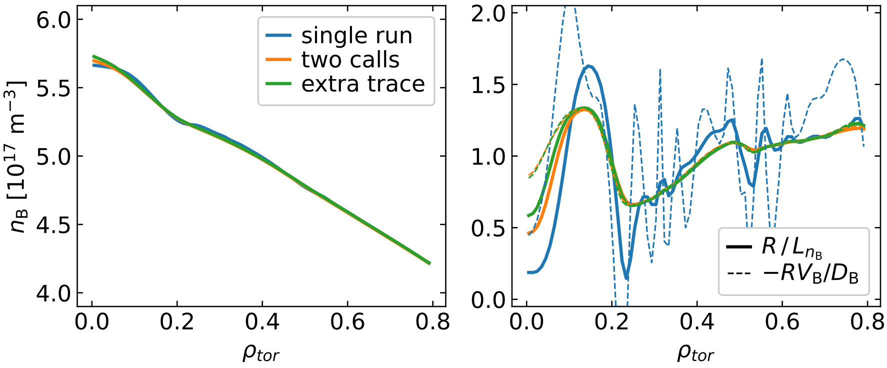

Figure 4.11: Comparison of the TGLF splitting methods, for boron in AUG #34017 at 3.8s, with the resulting density (left) and its normalized gradient (right).

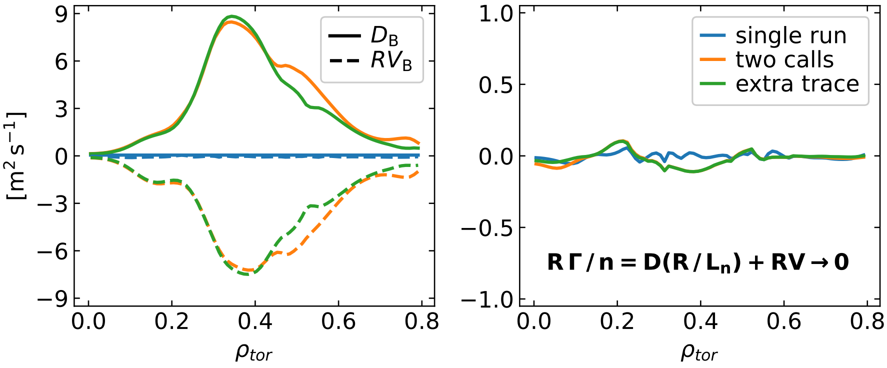

Figure 4.12: Diffusion and convection coefficients from the three splitting methods (left). Total flux density (right), which should go to zero as the simulation converges.

4.3 Validation of TGLF-SAT2 impurity transport

TGLF has been extensively validated for the prediction of main plasma profiles, but systematic experimental comparisons of its impurity transport capabilities are limited thus far. In this section we make use of a database of 42 AUG H-mode phases obtained in [165] from a set of dedicated experiments with varying NBI and ECRH auxiliary power mixtures and consistent measurements of boron profiles from the CXRS diagnostics [71]. We focus on mid-radius gradients, averaged over $\rho_{\mathrm{tor}} \in \{0.4, 0.6\}$. The range in temperature and density gradients caused by the differing heating mixtures allows the database to probe both ITG and TEM turbulence.

The database of experimental boron profiles was accompanied in [165] by a corresponding set of linear gyrokinetic and drift-kinetic simulations using GKW [137] and NEO [85, 88, 136], respectively. These simulations are included in the analysis of this section as a verification of the quasilinear models against a more complete gyrokinetic code like GKW. Non-linear GKW calculations of this database have shown no significant difference with respect to the linear calculations [166].

Standalone calculations with TGLF-SAT2 have been performed for all elements in the database at mid-radius, obtaining the diffusion and convection coefficients of boron using the duplicate trace method discussed in the previous section. Neoclassical coefficients are calculated with NCLASS [138], which is solidly applicable to light impurities with core parameters. The steady-state normalized boron gradient is calculated as $R/L_{n_{\mathrm{B}}} = -R\,V_{\mathrm{B}}/D_{\mathrm{B}}$ for both GKW+NEO and TGLF-SAT2+NCLASS. These gradients are compared to the CXRS measurements in figure 4.13, as a function of the normalized ion temperature gradient R/L_{T_i} (the strongest correlating main plasma parameter found in [165]).

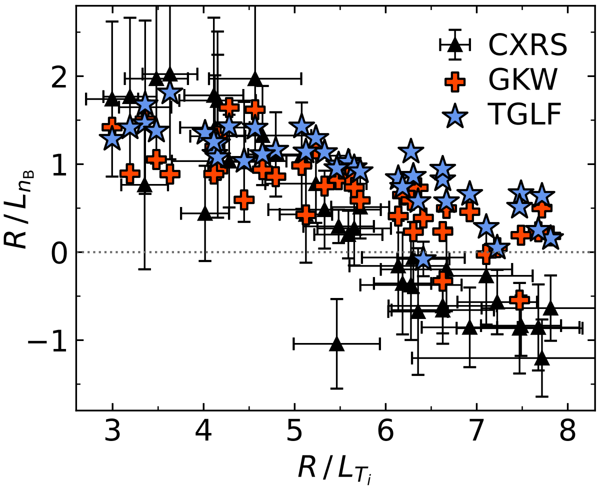

Figure 4.13: Measured and predicted mid-radius logarithmic gradients of the boron densities against the corresponding measured logarithmic gradients of the ion temperatures. Measurements have been performed by CXRS, while computations compare the results of the gyrokinetic code GKW with those of the turbulent transport model TGLF-SAT2.

There is close agreement between TGLF and GKW, and reasonable agreement to the measurements up to when the B densities are hollow. The lack of predicted hollow light impurity profiles is a well-known open question [167–171]. At $R/L_{T_i} \lesssim 6$ we find sufficient agreement in the predictions of TGLF-SAT2.

Two recent theoretical results point in the direction of this so-far unexplained hollowness, albeit through different physical mechanisms. In [171], the proposed explanation is the different role of the polarization drift in ITG and TEM (driving outward and inward turbulent impurity fluxes respectively). In [172], it is proposed that the torque injected by the NBI is absorbed by all ion species, which develop a turbulent momentum flux that can be considered to be distributed between main ions and impurities in the ratio of their respective mass densities. Neoclassical viscosity then responds to this turbulent momentum flux, leading to modified poloidal flows which in turn generate a neoclassical impurity flux which is proportional to the turbulent momentum flux and directed outward for co-current externally applied torque. This effect is not expected in reactor conditions due to the low NBI torque, but it could be included in a new set of simulations of the ASDEX Upgrade boron database and figure 4.13 could be reproduced to verify if the results more closely follow the experiments at high R/L_{T_i}, but this is left for future work.

4.4 Modelling workflow

Parts of this section have been published in Ref. [173], used here under the terms of the Creative Commons Attribution 4.0 licence.

The models for transport, heat and particle sources, and equilibrium are integrated in ASTRA. The approaches for the main plasma and impurities are discussed in the following subsections. The entire workflow is summarized in figure 4.16.

4.4.1 Main plasma

The modelling of the main plasma is mostly based on that of [174].

Turbulent transport coefficients for the evolution of T_e, T_i, n_e are calculated with TGLF-SAT2, whereas NCLASS is used for the neoclassical heat diffusivities. NBI and ECRH sources are calculated with RABBIT [175] and TORBEAM [176] respectively. The particle source is set by the density of neutrals entering the separatrix, with a feedback loop on the volume-averaged electron density $\langle n_e \rangle_{\text{vol}}$, in analogy to the active control of the line-averaged density $\overline{n}_e$ in the experiments. $\langle n_e \rangle_{\text{vol}}$ is used in order to preserve the total particle content and, therefore, the heating power per particle. We assume the neutrals are Franck–Condon atoms with an incoming energy of $E_0 = 2\,\text{eV}$ and neglect charge exchange (CX) particle sources. This method to determine the particle source in the simulations has been tested in detail in [174]. The main ion density is calculated from n_e and the impurity densities, by imposing quasi-neutrality. The current density profile is also evolved, including the bootstrap current formulae from [144]. The 2D magnetic equilibrium is calculated in ASTRA from the simulated pressure and current density profiles using SPIDER [79, 80], setting the separatrix shape obtained from CLISTE [177] reconstructions.

We will typically simulate L-mode plasmas up to the separatrix (*full-radius* modelling), profiting from the fact that TGLF-SAT2 has been shown to be able to predict transport in the L-mode edge [174,178,179]. When modelling ASDEX Upgrade plasmas, in chapter 5, as boundary condition we will use the 2-point model for $T_{e,\text{sep}}$ [180], with a heat flux width λ_q from the heuristic drift model [160], and we set $T_{i,\text{sep}} = 1.5\, T_{e,\text{sep}}$, $n_{e,\text{sep}} = 0.3 \langle n_e \rangle_{\text{vol}}$ like in [174].

In contrast, in this thesis H-mode plasmas will be simulated with a boundary condition at the pedestal top, set inside the confined plasma typically at $\rho_{\text{tor}} \approx 0.85 - 0.9$. In these cases, in chapter 6, the boundary conditions for temperatures and densities will be taken from experimental measurements (in the case of AUG) or scalings (in the case of ITER). While there are integrated modelling frameworks capable of also describing the complex pedestal region (where not only transport but also magnetohydrodynamic stability is a crucial element) [181–185], full-radius simulations in H-mode are outside the scope of this thesis. In particular, impurity transport needs to be included in this type of workflows in a future work.

4.4.2 Treatment of radial electric field

The radial electric field E_r becomes particularly relevant at the edge of ion heated discharges at powers approaching the L-H transition, through its role on the E×B shearing [178]. Our description is based on the work of [186], where, in the absence of a complete model to predict the radial electric field up to the separatrix in the present treatment, the observed edge E_r well is mimicked by solving the ion force balance until a radial position ρ_{min} in the normalized poloidal flux ρ_{pol}, then forcing E_r to zero at the separatrix (thus E_r has a local minimum at ρ_{min}), such that

$$E_r = \begin{cases} \dfrac{\nabla p_i}{Z_i e\, n_i} - \mathrm{v}_{i\theta} B_\varphi + \mathrm{v}_{i\varphi} B_\theta, & \rho_{\mathrm{pol}} \le \rho_{\mathrm{min}}\,, \\[2ex] \left(\dfrac{1-\rho_{\mathrm{pol}}}{1-\rho_{\mathrm{min}}}\right)^2 E_r(\rho_{\mathrm{min}}), & \rho_{\mathrm{min}} < \rho_{\mathrm{pol}} \le 1\,, \end{cases} \tag{4.16}$$

where we use $\rho_{\mathrm{min}} = 0.985$, informed by AUG L-mode measurements [187, 188].

This E_r is used to calculate the E×B shearing rate $\gamma_{\mathrm{E\times B}}$ (an input of TGLF), using the Waltz-Miller formula [189]

$$\gamma_{\mathrm{E\times B}} = -\frac{r}{q}\frac{\partial}{\partial r}\left(\frac{E_r}{R B_\theta}\right). \tag{4.17}$$

Higher values of $\gamma_{\mathrm{E\times B}}$ lead to lower turbulent transport, since sheared E×B flows decorrelate turbulence by tearing apart the turbulent eddies [190].

A sensitivity study on the choice of radial location for the minimum of the E_r well is shown in figure 4.14, for AUG discharge #39323 at 5.0–6.0 s where, even though it is in L-mode, the measured T_i data shows a strong edge gradient. Here, 'floating' means E_r is allowed to go as negative at the separatrix as the simple ion force balance predicts. Bonanomi *et al* recently showed that TGLF-SAT2 can form pedestal-like structures [186], in situations where the simulation enters a feedback loop: $\gamma_{\mathrm{E\times B}}$ reduces the edge turbulence, which in turn raises the edge pressure gradient, deepening the E_r well, thereby increasing $\gamma_{\mathrm{E\times B}}$. This happens in figure 4.14 for the cyan and orange curves, which largely exceed typical minimum E_r values of −5 to −10 kV/m for L-modes at AUG [188]. This leads to considerably stronger simulated edge pressure gradients than the experiment, and to H-mode-like edge profiles. However, decreased core gradients in these

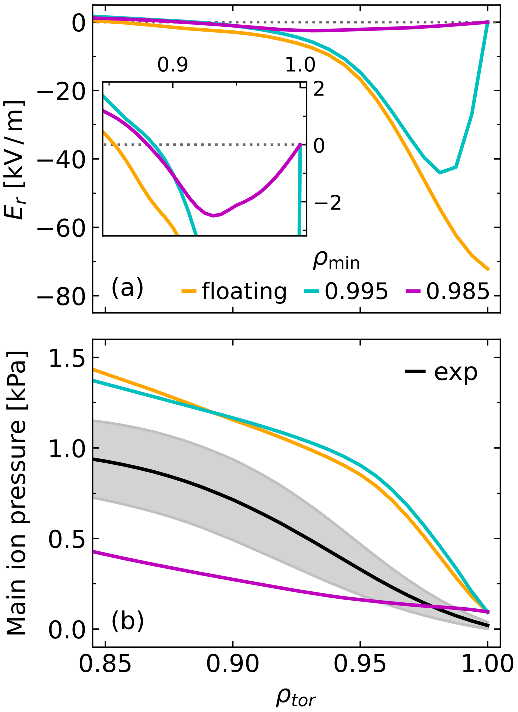

Figure 4.14: Sensitivity to the choice of location of the E_r minimum in equation (4.16), in simulations of AUG #39323 at 5.0–6.0 s. (a) Edge radial electric field. (b) Main ion pressure predicted by TGLF, with experimental estimation in gray.

two cases partially compensate the increased edge pressure, such that the global confinement is 'only' overestimated by 20%. The magenta line corresponds to the default $\rho_{\mathrm{min}} = 0.985$, for which the E_r well is instead somewhat underpredicted. The edge gradients are weaker and more L-mode-like (in this particular example the resulting core pressure is higher, and the confinement is within 5% of the experiment). This is the boundary condition chosen for all L-mode simulations in this thesis. For reference, a simulation without E×B shearing in TGLF underpredicts both edge and core, leading to a 13% lower simulated confinement.

Given that the edge impurity convection is mostly neoclassical (so it is quite sensitive to the main plasma gradients, see equation (2.34)) and the impurity turbulent diffusivity is also reduced by the E×B shearing, these elements are critical to correctly describe the peripheral impurity transport.

Missing physics, such as the impact of self-generated Reynolds stresses on the different rotation terms entering in the radial force balance [191–193] or effects due to ion orbit losses [194–196], could in the future provide a self-consistent description of the E_r well that is better reconciled with the positive scrape-off layer E_r values set by parallel dynamics on the open field lines and sheath boundary conditions at the target [197]. This would go beyond the artificial treatment presently used in equation (4.16), which mimics the experimental observations of the edge E_r in L-mode conditions, but it is quite outside the scope of this thesis.

4.4.3 Centrifugal effects on high-Z turbulent coefficients

It has been shown in [198] that there are non-negligible centrifugal effects on the turbulent transport of heavy impurities like tungsten, due to the increased impurity density on the low field side (LFS), where the turbulence balloons. This is exemplified on the left panel of figure 4.15.

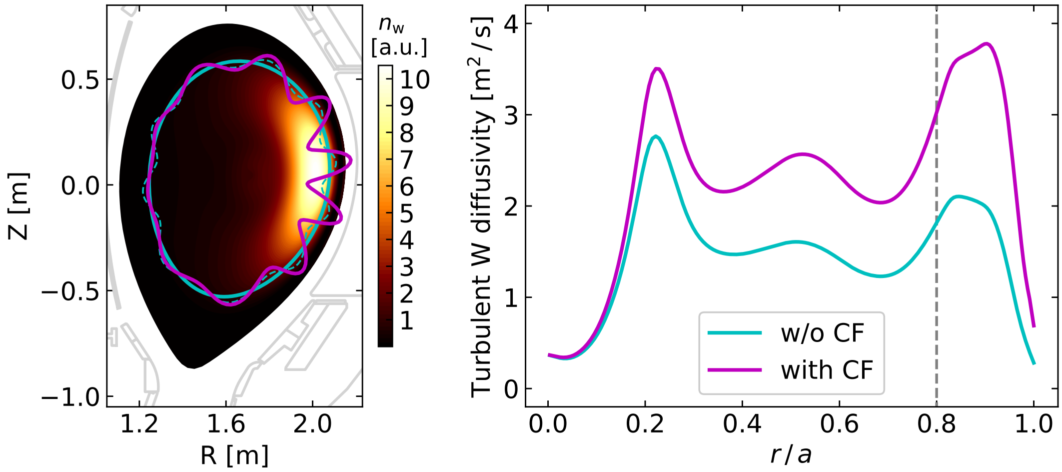

Figure 4.15: (left) Schematic example of the simultaneous LFS localization of W due to rotation (background) and the poloidal ballooning of the potential fluctuations (in magenta, exaggerated for illustration). A poloidally-symmetric potential is sketched in the cyan dashed lines. (right) Enhancement of the turbulent diffusivity calculated with a Mach number of 0.3 (magenta) with respect to no rotation (cyan).

These effects can be included in post-processing via the analytical formulae derived in [198], as done already in the QuaLiKiz model [199].

We have now implemented this missing physics in the TGLF interface to ASTRA, under the simplifying assumptions that the poloidal functional form of the amplitude of the electrostatic potential fluctuations is given by $|\tilde{\phi}|^2 \propto \exp\{[-\theta^2/(2\,\theta_{\rm rms})^2]\}$, and that its mean width follows the GLF23 parametrization [132] given by $\theta_{\rm rms}^{-1} \approx (3/\pi)\,[1+0.2\,(q/2-1)]\,\sqrt{1+0.1\,(s-1)^2}$, where q is the safety factor and $s = (r/q)\,dq/dr$ is the magnetic shear. The resulting coefficients are LFS coefficients, so they need to be transformed to FSA. The resulting FSA turbulent coefficients are enhanced by a factor of $\langle\langle \exp(-E_z)\rangle\rangle\,/\,\langle\exp(-E_z)\rangle \sim 1$–3, ranging within typical values of the rotation. E_z is the normalized impurity energy, defined in equation (2.24) and the paragraphs below it. Here, the FSA is represented by single brackets as usual, and the mode envelope average $\langle\langle\,\cdot\,\rangle\rangle$ is defined as

$$\langle\langle f(\theta)\rangle\rangle = \oint f(\theta)|\tilde{\phi}|^2\,J d\theta \Big/ \oint |\tilde{\phi}|^2\,J d\theta\,, \qquad (4.18)$$

where J is the Jacobian of the coordinate system. A concrete example of these effects is shown in the right panel of figure 4.15. The diffusion coefficient of W in AUG #37041 at 5.25 s coming directly from TGLF (that is, without the centrifugal effects) is plotted in cyan, whereas the coefficient including the centrifugal effects following the formulae of [198] and the assumption for $\theta_{\rm rms}$ is shown in magenta. A non-negligible enhancement of the turbulent transport coefficients of W with rotation is evident, which we can now consider in our TGLF simulations in ASTRA.

4.4.4 Full workflow schematics

We conclude this chapter by summarizing the modelling workflow in the schematic diagram shown in figure 4.16. All elements discussed in this chapter are included.

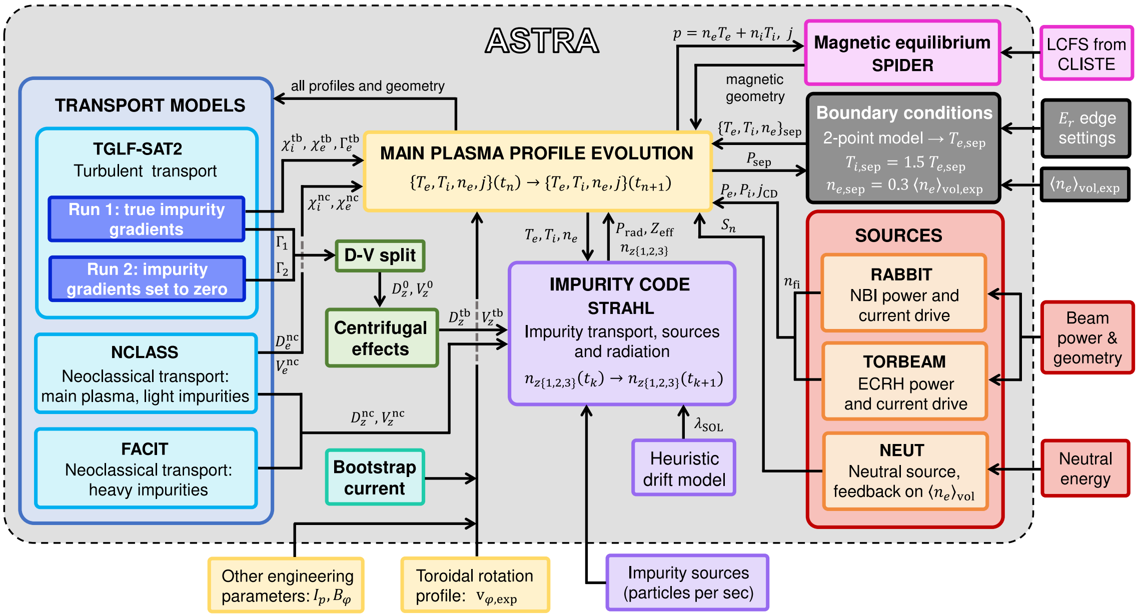

Figure 4.16: Schematic representation of the modelling workflow including impurities. The blocks outside of the dashed lines represent external user inputs, whereas everything inside them is self-consistently integrated in ASTRA.

During a typical time step $t_n \to t_{n+1} = t_n + \Delta t_a$ of ASTRA, the following key elements of the workflow take place:

- The main plasma profiles of electron and ion temperatures are evolved using equations of the form of equation (1.14), with heat sources calculated at t_n by calling modules for auxiliary heating (represented by the red box in figure 4.16) and calculating the Ohmic and (if there is DT fuel) the alpha heating. Heat diffusivities are calculated with the turbulent and neoclassical transport models, which are separate subroutines (enclosed in the blue box).
- The electron density is evolved using an equation of a similar form as equation (4.14), where the sources are ionization and recombination of the gas puff fuelling at the edge, particle sources due to NBI, and pellets. The entire turbulent particle flux is typically set into the electron particle convection, as it was described in equation (4.15). The Ware pinch [200], caused by the parallel electric field acting on the trapped particles, is also included.
- The poloidal flux is evolved in time using a transport equation that is similarly first order in temporal and second order in spatial derivatives, which is derived by combining Faraday's, Ampère's and Ohm's law [106]. The boundary condition for the poloidal flux is determined by the prescribed plasma current I_p. The current density in the plasma follows from the time derivative of the poloidal flux (times a neoclassical conductivity, for example from the formulae of [144, 148]) and the bootstrap and externally-driven currents.
- The 2D Grad-Shafranov equilibrium, equation (1.13), gives closure to the system of four equations previously mentioned, which constitute the main ASTRA transport solver (summarized by the yellow box in figure 4.16). The last closed flux surface can have a prescribed shape, provided as a set of coordinate pairs (R_j, Z_j), or calculated from the currents in the coils of the machine (the so-called free-boundary equilibrium, which is however not used in this thesis). The equilibrium solver and its boundary are represented by the pink boxes.
- Turbulent impurity transport coefficients undergo the splitting into diffusion and convection and the inclusion of centrifugal effects in subsequent subroutines (green boxes), before being passed to the impurity evolution equations.
- When impurities are evolved using STRAHL (purple box), the main plasma profiles and impurity transport coefficients from ASTRA at t_n are given as inputs. The impurity densities evolve over several STRAHL time steps, since $\Delta t_s \ll \Delta t_a$ (as it was discussed in section 4.2). The resulting impurity densities, effective charge and radiated power density (which goes into the energy sinks of the electron heat equation) are returned to ASTRA for the t_{n+1} step.

In the rest of this thesis we will apply this workflow to study ASDEX Upgrade and ITER plasmas in the presence of low-, mid- and (particularly) high-Z impurities.

Chapter 5

Full-radius modelling of ASDEX Upgrade L-mode experiments

The results presented in this chapter have been published in Ref. [173], used here under the terms of the Creative Commons Attribution 4.0 licence.

Full-radius integrated modelling capabilities for accurate predictions of confinement have recently been demonstrated in tokamaks, both in H-mode [181–184] and L-mode [174, 178]. In L-mode, the TGLF-SAT2 quasilinear transport model [131] has been shown to correctly predict transport up to the separatrix [179].

The use of theory-based transport models allows a more confident extrapolation to future devices, and 1.5D integrated modelling provides not only global quantities but entire profiles of the plasma parameters. So far, however, full-radius modelling frameworks do not self-consistently describe impurity transport.

Recent developments in integrated modelling have been dedicated to the description of impurity transport [201–208], including the evolution of the background plasma with radiative losses by impurities [209–211]. However, some limitations are present either because the boundary condition is set well inside the confined plasma, or because empirical impurity transport coefficients are used at the edge.

To our knowledge, physics-based quasilinear models have not been applied in a full-radius description of impurity transport so far.

In this chapter we apply the integrated modelling framework introduced in chapter 4 to full-radius simulations of ASDEX Upgrade L-mode plasmas, to validate its impurity transport predictive capabilities and study the feedback effects of impurities on the main plasma via radiation and dilution.

5.1 Experiments to be modelled

5.1.1 AUG L-modes without impurity seeding

We consider a set of six AUG L-mode phases in deuterium, which differ mostly in their NBI-ECRH heating mix and plasma current. The main parameters of each discharge are summarized in table 5.1. These experiments have no seeded impurities. We assume only W and B are present, entering the plasma due to its interaction with the boronized tungsten walls.

Shot #	Time	P_{NBI}	P_{ECRH}	I_p	q_{95}
35475	2.8−3.5	1.59	0.00	0.83	5.16
35475	4.3−5.0	0.80	0.72	0.83	5.15
35475	5.8−6.5	0.00	1.35	0.83	5.15
39255	2.5−3.0	0.77	0.87	1.24	3.34
39255	3.5−4.0	1.50	0.00	1.24	3.33
39323	5.0−6.0	1.49	0.00	0.52	8.17

Table 5.1: AUG L-modes to be simulated in section 5.2. The time column is the interval (in s) over which profiles are averaged, the injected NBI and ECRH powers are given in MW and the plasma current I_p in MA. q_{95} is the safety factor at 95% of the toroidal flux. AUG has an aspect ratio of 3.3 and $R_0 = 1.65$ m. The magnetic field and line-averaged density are similar for all cases: $B_\varphi \approx 2.5$ T and $\overline{n}_e \in \{2.0 - 2.6\} \times 10^{19}\mathrm{m}^{-3}$. The red and orange cells denote heating mix scans (at constant I_p), the blue and cyan cells denote I_p scans (at constant heating mix).

In addition to diagnostics measuring the main plasma, namely the integrated data analysis suite (IDA) [212] for n_e and T_e, and CXRS for T_i and v_φ [69], CXRS measurements of n_{B} [71] were available for all discharges except for the phase without NBI, as well as soft X-ray (SXR) data [213] that allow us to extract n_{w}. Likewise, bolometric estimations of the total radiated power [214] and IDA-based estimations of Z_{eff} (IDZ) [215] were available.

The experimental W density is calculated from FSAs of 2D SXR tomographic reconstructions [216,217], assuming that only W generates the emissivity ϵ_{sxr} [MW m^{-3}] (Bremsstrahlung is negligible in these cases), so that

$$\langle n_{\mathrm{w}}^{\mathrm{exp}} \rangle (r) \approx \frac{\langle \epsilon_{\mathrm{sxr}}(r,\theta) \rangle}{n_e^{\mathrm{exp}}(r)\, L_{\mathrm{w}}^{\mathrm{sxr}}(T_e^{\mathrm{exp}}(r))}, \tag{5.1}$$

where $L_{\mathrm{w}}^{\mathrm{sxr}}$ [MW m^3] is the W SXR cooling factor. Note that the absolute calibration of the SXR signal is highly uncertain. We typically need a scaling factor that is estimated such that the volume integral of the radiated power density caused by $\langle n_{\mathrm{w}}^{\mathrm{exp}} \rangle$ approximately matches the total radiation measured by bolometry. Nonetheless, SXR data are extremely valuable in terms of the profile shape and gradients they provide and the comparisons to the simulated W transport they allow, particularly from axis to mid-radius. The SXR cameras have a lower detection limit at $T_e \approx 1$ keV [213], below which the data is unavailable, so we lack edge W profiles in general.

5.1.2 High power, high confinement radiative L-mode

The experiment presented in [48], AUG #37041 at 5.0–5.5 s, is a high-power ($P_{\mathrm{NBI}} =$ 5 MW, $P_{\mathrm{ECRH}} = 2$ MW) radiative L-mode kept just below the L-H power threshold P_{LH} (calculated with the Martin scaling [218]) by active feedback control on the power crossing the separatrix, $P_{\mathrm{sep}} = P_{\mathrm{aux}} - P_{\mathrm{rad}}$, using argon (Ar) seeding as actuator. It also features a region of strong radiation localized above the X-point.

An interesting property of this discharge is that, after an initial H-mode phase, it transitions back to L-mode but retains high confinement ($H_{98} \approx 0.95$) without

ELMs. These high performing radiative L-modes have been obtained in different machines [219–222] and are currently investigated for potential reactor scenarios [49].

Relevant time traces summarizing the idea behind this experiment are shown in figure 5.1. The time windows during the H-mode and radiative L-mode phases of the discharge, which will be simulated in sections 5.3.5 and 5.3.2, are shown in dash-dotted and dashed vertical lines respectively.

AUG #37041 is an appealing application due to the high impurity content and radiated power, the presence of multiple species (intrinsic B and W, seeded Ar) and the high confinement with no ELM activity. Furthermore, it is a well-diagnosed discharge, with CXRS measurements of Ar^{16+} in addition to the diagnostics previously listed for the unseeded L-modes. On the other hand, it is also a challenging application since, despite being a stationary phase, the balance between heating and radiated powers is marginal, so a slow increase of the radiation can cause a radiative collapse (which in fact happens later on in the experiment).

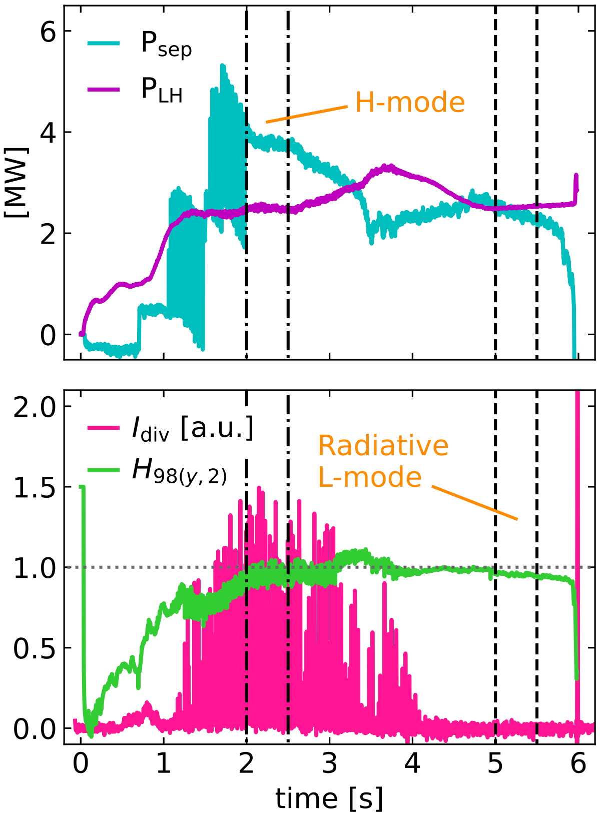

Figure 5.1: Time traces of AUG # 37041. Power crossing the separatrix and the L-H power threshold (top). Divertor shunt currents, as an indication of ELM activity, the confinement H-factor (bottom).

5.2 Simulations of ASDEX Upgrade L-modes without impurity seeding

5.2.1 Impurity sources in the simulation

An important question is how to set the impurity sources in STRAHL. For a given profile shape, determined by transport, these sources ultimately determine the content of each species by setting the value of its density at the separatrix. In STRAHL, this is determined by neutral puff rates for each impurity. In the experiments neither B nor W are puffed, but rather enter the plasma due to wall erosion and sputtering. However, a consistent modelling of real sources is outside the scope of this thesis. To compare impurity transport predictions and measurements one is interested in the impurity density gradients, because $R/L_{n_z} = -R\, v_z/D_z$ in steady-state, whereas the total content of impurities is relevant in terms of radiative losses and dilution.

If we estimate Z_{eff} using only CXRS B densities, we find a consistent under-estimation of the IDZ measurements. B is the most prominent light impurity in AUG plasmas due to routine wall boronizations [223], however several other species can be present in smaller concentrations to yield a non-negligible contribution to Z_{eff}. In particular, nitrogen (commonly seeded for diagnostics and heat exhaust) and helium (from glow discharges performed for the boronizations) can remain in the vessel from previous experiments, with smaller traces of oxygen, carbon and fluorine. Simulating all these species is unaffordable. We opt for considering that only B is present, but in a higher content that includes the other light impurities, assuming that the transport of these species is not too different due to the similar charge and charge-to-mass ratio. Furthermore, we observe that the measured line-averaged effective charge $\overline{Z}_{\mathrm{eff}}$ is quite constant across these six phases, at $\overline{Z}_{\mathrm{eff}} \approx 1.7$. The approach to select the B source consists on a feedback loop on the B neutral puff rate such that the simulated $\overline{Z}_{\mathrm{eff}}$ reaches a target value of 1.7 for all simulations. The W source is set by feedback on the simulated total radiated power, such that the total radiation estimated by bolometry is matched.

5.2.2 Simulated profiles

Figures 5.2 and 5.3 show relevant profiles of two phases with different engineering parameters, AUG #39255 at 2.5–3.0 s (high current, mixed heating) and AUG #39323 at 5.0–6.0 s (low current, NBI heated), with particular interest on the contrast between their impurity and radiation profile shapes. The profiles of these phases are described in detail. Equivalent figures for the other four phases are shown in figures (5.4–5.7), but they are more briefly described. General properties of the full set of simulations are discussed in section 5.2.3.

The temperature profiles of the high I_p, mixed heating discharge, shown in figure 5.2(a), are well reproduced, although they are somewhat overpredicted in the core. In (b), the predicted n_e has a weaker edge gradient and slightly higher core density. The experimental volume-averaged density is matched by a feedback on the neutral source, so if the transport does not predict a strong enough edge gradient the source increases, raising the entire n_e profile. The Z_{eff}, in figure 5.2(c), matches the experimental value by design. The radial location where the safety factor q equals 1 at the sawtooth crash is $\rho_{\mathrm{tor}} \approx 0.4$. The simulated n_{B}, shown in figure 5.2(d), has a similar gradient to the measurement at mid-radius and a larger gradient in the core. At the edge, the simulated B^{5+} density is more consistent with the B^{5+} measurement than the total B profile, since this charge state is less populated at the colder periphery. Following section 5.2.1, the B content that generates the target $\overline{Z}_{\mathrm{eff}}$ is 2.6 times larger than the CXRS measurements.

The measured core W profile shown in figure 5.2(e) is hollow, consistent with the presence of central ECRH (we will discuss the effects of wave heating on heavy impurity transport in depth in chapter 6). The simulated n_{W} is flat and even slightly hollow in the core, due to the reduced neoclassical pinch caused by the flat central n_i and a mild toroidal rotation of $\mathrm{v}_{\varphi} \approx 78$ km/s, $M_i \approx 0.15$. The simulated profile of the radiated power density, shown in figure 5.2(f), is therefore also quite hollow. Direct measurements of this quantity were not available, however from bolometry we have that the total radiated power from inside the separatrix (the volume integral of the radiation density) is 1.2±0.3 MW. The uncertainty of the bolometry is taken as the difference between the minimum and maximum of the signal within the time window under consideration. The contribution of B to the simulated total radiation is not negligible and it is localized at the very edge of the plasma, where the lower temperatures allow for line emissions of partially ionized B.

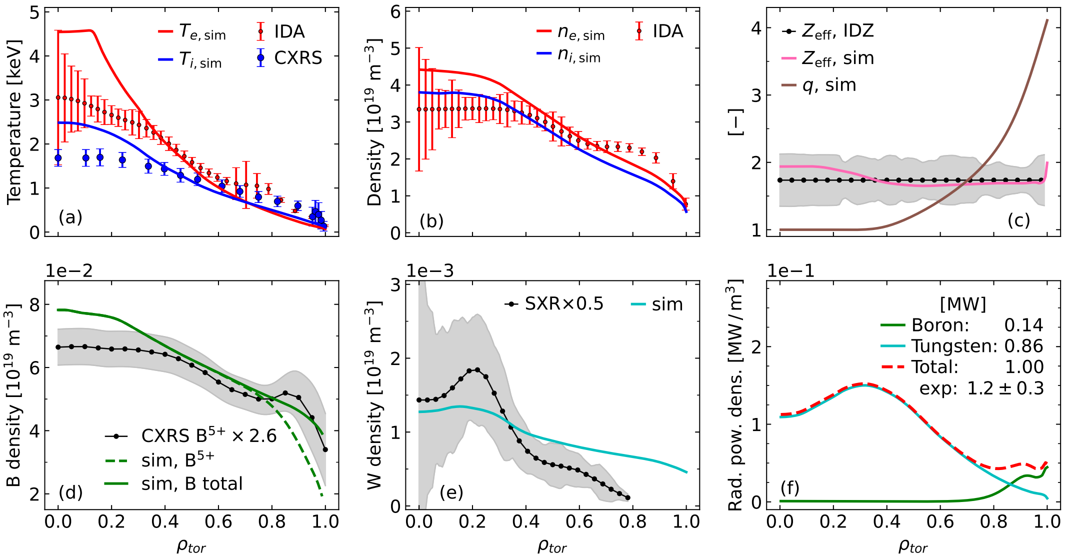

Figure 5.2: ASTRA simulation of AUG #39255 at 2.5–3.0 s (high current, mixed heating). (a) Electron (red) and main ion (blue) temperatures, with measurements in circles and simulations in solid lines. (b) Electron and main ion densities, color-coded as in (a). (c) Effective charge and safety factor simulated profiles in the solid pink and brown lines. (d) Total simulated boron (solid) and B^{5+} (dashed) densities in green. (e) Tungsten density simulation in the solid cyan line. Measurements in (c–e) are shown in black dots with uncertainty bands in gray. The scaling factors of the experimental data in (d) and (e) are discussed in the text. (f) Radiated power density calculated by STRAHL (red) with contributions of W (cyan) and B (green); the core total radiated power, its components and measured value are in the label.

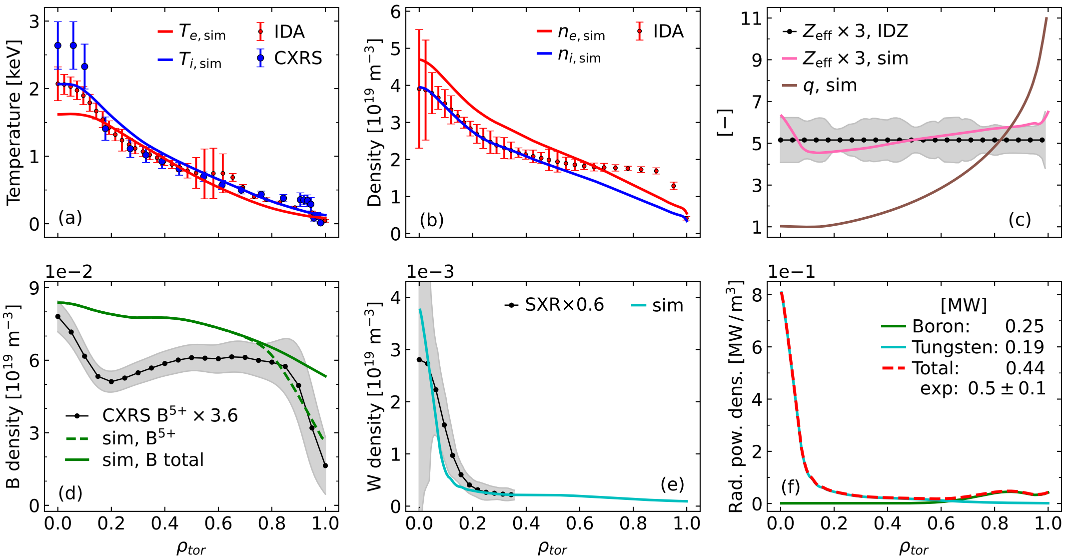

Figure 5.3: ASTRA simulation of AUG #39323 at 5.0–6.0 s (low current, beam heating only). (a–f) Same description as in figure 5.2.

The main profiles of the low I_p, beam heated discharge are presented in figure 5.3. Both temperatures are close to the experimental data, as shown in panel (a). The strong edge gradient in the experimental T_i is the reason why this discharge was used in section 4.4.2. The high core n_e peaking is well reproduced, but its large edge gradient is not, as shown in figure 5.3(b). The Z_{eff} profile, in (c), is peaked deep in the core, where the W content is not negligible. The edge q profile is large (since I_p is lower at constant B_φ), and $q = 1$ at the sawtooth crash lays at $\rho_{\mathrm{tor}} \approx 0.2$.

The measured n_{B} of figure 5.3(d) has a strong edge gradient, but it is then flat until mid-radius, after which it becomes slightly hollow and then quite peaked in the center. The simulated total B density does not capture these strong changes in the profile shape, being mildly peaked throughout the radius, however the B^{5+} agrees more with the steep edge gradient as before. In figure 5.3(e), the SXR data results in a very peaked experimental n_{w}, whose profile shape is well reproduced by the simulation. The combination of a very peaked central n_i and a high rotation ($M_i \approx 0.36$) gives rise to the strong neoclassical pinch that causes this peaking. The radiated power density in figure 5.3(f) is therefore also very peaked, and the 0.5 ± 0.1 MW measured by bolometry are well matched. Note that the B contribution to the total radiation is even dominant in this case, given that W has accumulated in the core whereas B radiates in the edge, which has a larger share of the plasma volume.

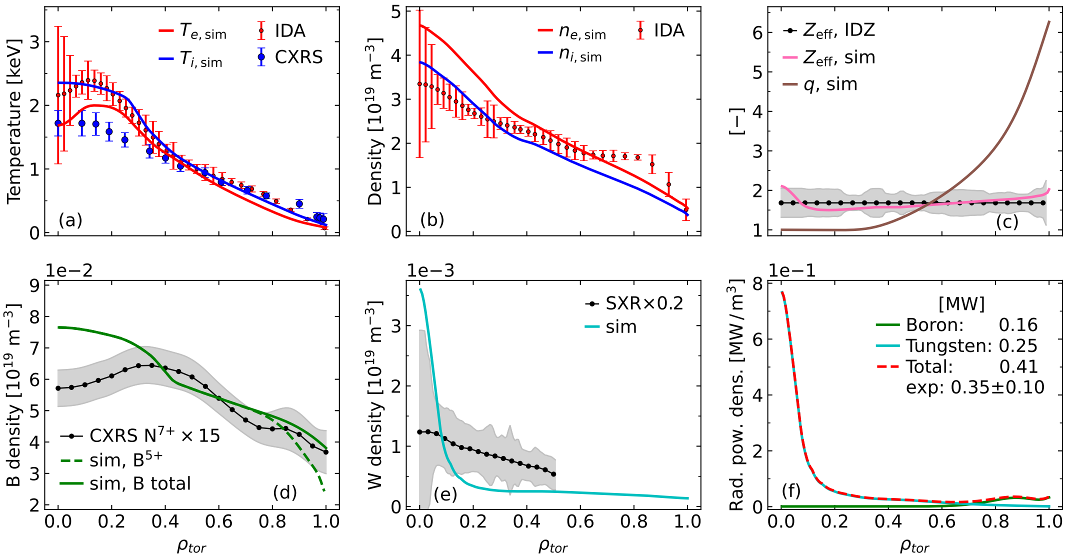

Figure 5.4: ASTRA simulation of AUG #35475 at 2.8–3.5 s (intermediate current, beam heating only). (a–f) Same description as in figure 5.2.

Figure 5.4 shows the profiles of a phase with intermediate current and NBI heating only. The temperatures are well reproduced, with a hollow central T_e in both simulation and measurement that is caused by the very peaked radiative losses by W. The B profile is well matched except near axis, where the measurement is hollow but the simulation is peaked. We note, however, that for this discharge the CXRS system measured N^{7+}, not B^{5+}; we assume that the transport of B and N is not too different, since they have similar charges and charge-to-mass ratios, and compare the CXRS N^{7+} profile to the simulated B^{5+}. The W density is very peaked (consistent with a purely NBI-heated plasma), due to a peaked plasma density (whose gradient is overestimated, though the measured profile is indeed quite peaked).

Figure 5.5 shows the profiles of a phase of the same discharge with intermediate current, but with reduced NBI and with additional ECRH. The B density gradient is similarly well matched except near the magnetic axis. The simulated W density is relatively flat, with a slightly hollow experimental W density profile in the center.

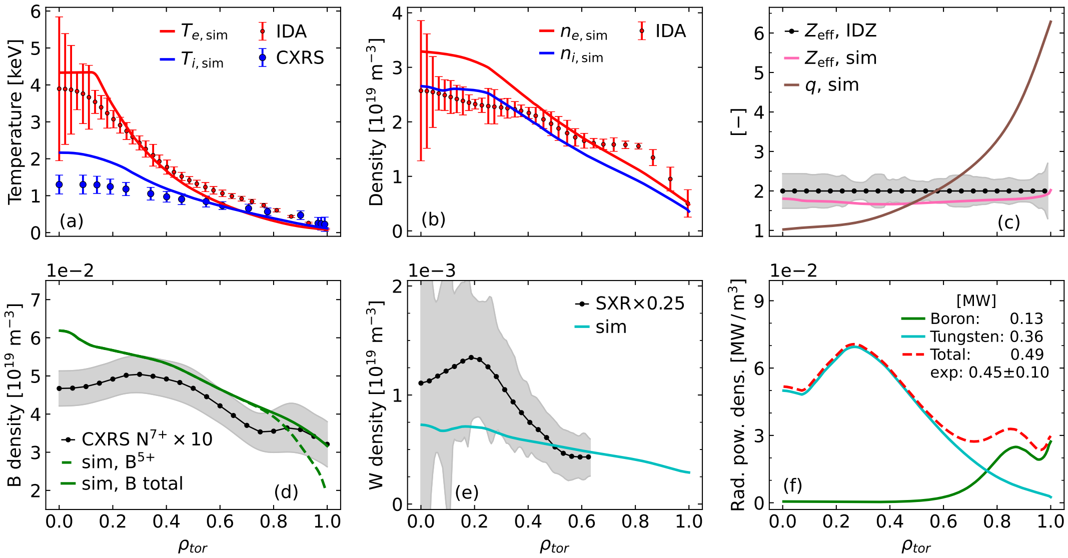

Figure 5.5: ASTRA simulation of AUG #35475 at 4.3–5.0 s (intermediate current, mixed heating). (a–f) Same description as in figure 5.2.

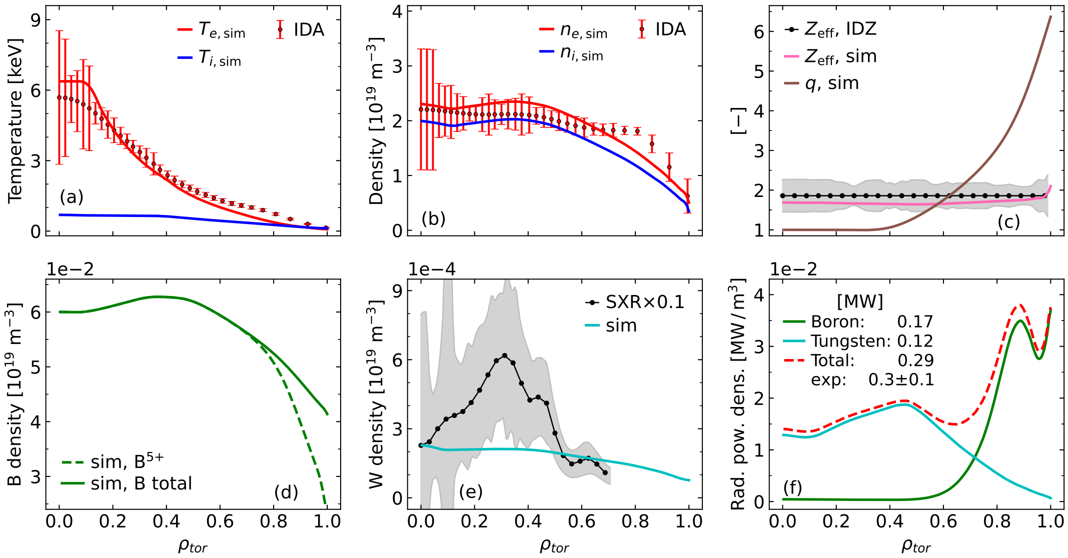

Figure 5.6: ASTRA simulation of AUG #35475 at 5.8–6.5 s (intermediate current, wave heating only). (a–f) Same description as in figure 5.2.

Figure 5.6 shows the profiles of the final phase with intermediate I_p, in this case with ECRH only. The fact that there are no beams means that there are no available CXRS measurements, so we lack experimental data for T_i and the B density. The simulated T_e is much higher than T_i, which is consistent with having a low-density, purely electron-heated plasma. The simulated B density is the only one in the set of simulations that is hollow in the center. The simulated W density profile is flat, and the SXR-reconstructed central W density is strongly hollow. This lack of hollowness might stem from the lack of the effects of (1,1) MHD modes [224, 225] on W in the simulations. There is a significant contribution of B to the radiation at the edge, which is mostly line radiation, since it is located in the region where the B^{5+} charge state is not the only populated ionization stage in the total B density.

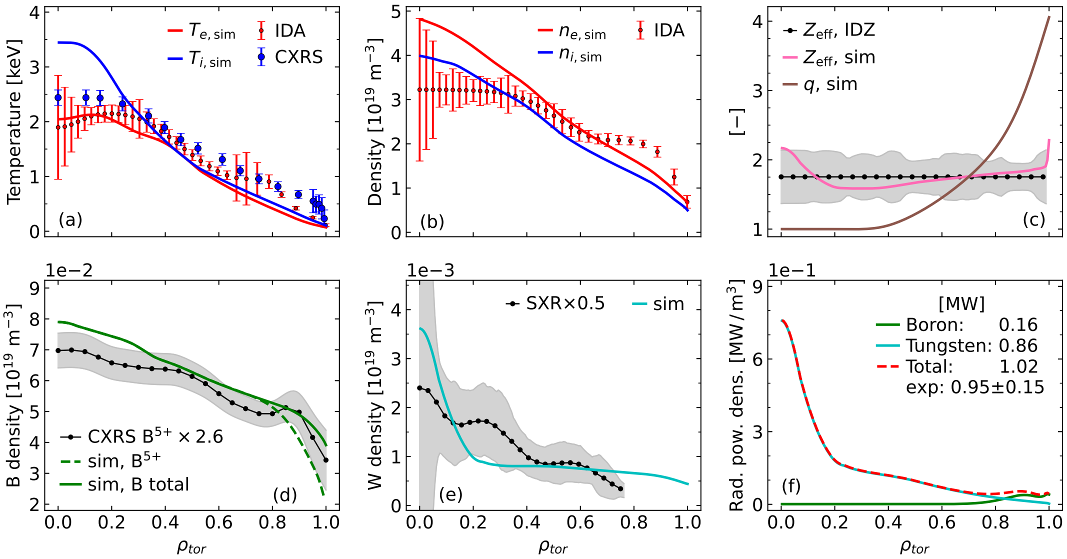

Figure 5.7: ASTRA simulation of AUG #39255 at 3.5–4.0 s (high current, beam heating only). (a–f) Same description as in figure 5.2.

Finally, figure 5.7 shows representative profiles of the high I_p, purely NBI-heated phase. The measured ion temperature has a strong edge gradient that is not well reproduced by the simulation with the E_r settings from section 4.4.2. The B density is quite well reproduced. The W density is peaked in the center, causing a radiated power density that leads to a slight hollowing of the central electron temperature.

5.2.3 General properties of the L-mode database

Some general properties of the set of simulations are presented in figure 5.8.

An important test for the modelling workflow is to verify that the trend of increased confinement with higher current is reproduced. This is investigated in figure 5.8(a), where a clear I_p dependence of the stored thermal energy W_{th} is observed and the experimental values are well matched by the simulations. It has been shown in [178] that including the E×B shearing $\gamma_{\mathrm{E\times B}}$, equation (4.17), in ASTRA/TGLF-SAT2 simulations is an essential element to capture this dependence.

Note that the ITER physics basis (IPB) scaling of L-mode confinement is $\propto I_p^{0.96}$ [30]. While the limited set of simulations hinders a proper statistical analysis, we can nonetheless fit the current dependence of the six simulations for comparison to scaling laws and previous modelling results. We recover a dependence of $I_p^{0.87}$ that is consistent with the $I_p^{0.84}$ of [174] and lower than the almost linear IPB scaling. We note that while the auxiliary power is approximately matched in these discharges, the total power is not, considering the different Ohmic heating. Accounting for this reduces the current scaling due to the small increase of stored energy produced by the Ohmic power at higher I_p [174].

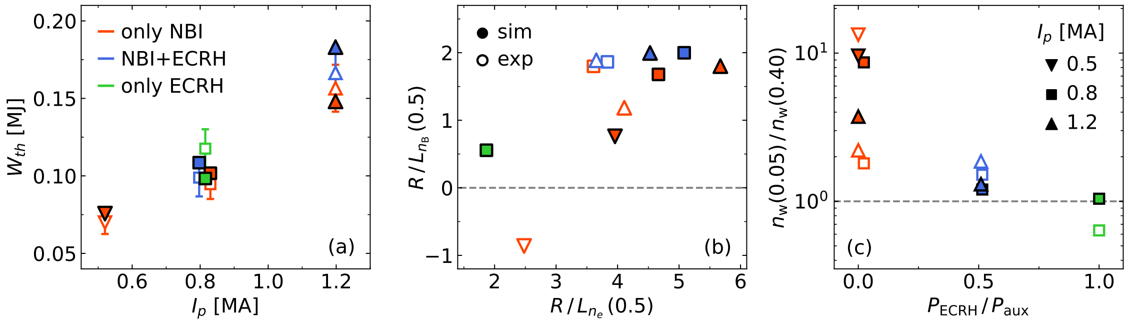

Figure 5.8: Simulated (solid) and measured (open): (a) plasma thermal energy as a function of the plasma current. (b) Boron logarithmic density gradient as a function of the electron density gradient, at mid radius ($\rho_{\mathrm{tor}} \approx 0.5$). Open green square is missing due to the lack of measured B profile with ECRH only. (c) Tungsten peaking (on- to off-axis n_{w} ratio) as a function of the ECRH fraction. Different colors represent different heating mixes, and different markers correspond to different I_p.

Figure 5.8(b) presents a correlation between the mid-radius electron and boron logarithmic density gradients. The trends of the measurements and the simulations coincide. There is, however, a general overestimation of the n_e peaking. We miss the measured B gradient with ECRH only (there are no beam ions for CX reactions with impurities). This is unfortunate, since it is the flattest n_{B} in the modelling. Standalone TGLF calculations were performed to analyze the difference in mid-radius B turbulent transport in two extreme cases at the same current (0.8 MA): a purely beam-heated phase with more peaked B and e^- (orange square) and an ECRH-only phase with flatter B and e^- (green square), corresponding to AUG #35475 at 2.8–3.5 s and 5.8–6.5 s respectively. The multiple convective components, from equation (2.54), are split by setting the corresponding B gradients to zero. The beam-heated case has a dominant pure pinch that is partially compensated by smaller outward thermo- and roto-diffusive fluxes. In contrast, the ECRH-heated case presents an outward pure convection that is slightly overcome by inward thermo-diffusion (with negligible roto-diffusion), leaving a smaller inward convection. Finally, we note that the CXRS profile at low current is hollow, but the modelling predicts no hollow profiles. The lack of predicted light impurity hollowness is a well documented missing piece of theoretical understanding, as we discussed in section 4.3.

Figure 5.8(c) studies the effect of ECRH on the core W peaking. Applying central wave heating to control heavy impurity accumulation is an established experimental technique [226–228] with a solid theoretical understanding [229, 230]. In the set of simulated discharges we have a scan in ECRH power fraction at approximately constant total heating, which allows for comparisons between the SXR-measured and predicted ratio of W densities on and off axis. We find a strong reduction of the W peaking with increasing ECRH fraction, in agreement with the experiment.

5.3 High confinement radiative L-mode

5.3.1 Impurity sources in the simulation

The approach to determine the impurity sources in STRAHL for the simulation of this radiative L-mode differs from the one previously discussed for the unseeded

L-modes. Here the seeded argon has dominant contributions to both the radiated power and the effective charge. The neutral Ar puff rate in STRAHL is increased proportionally to $(P_{\mathrm{sep}} - P_{\mathrm{LH}})$, calculating P_{LH} with the Martin scaling [218], in close analogy to the experiment. The W source also follows this proportionality, although with a feedback loop 10 times weaker, with the idea of mimicking a higher W sputtering by a higher number of Ar particles. In contrast, the B source is set as a constant trying to match the line average of the CXRS-measured B profile.

5.3.2 Simulated kinetic profiles and radiated power

Figure 5.9 presents relevant profiles of this experiment. T_e, T_i and n_e are very well reproduced (particularly the latter two, with a somewhat overestimated core T_e), as shown in figures 5.9(a) and (b). In figure 5.9(c), the high Z_{eff} of the discharge, approaching 3 due to the high Ar seeding, is matched within uncertainties. The radial location where $q = 1$ at the sawtooth crash is $\rho_{\mathrm{tor}} \approx 0.3$.

The core n_{B} is more peaked than the flat CXRS profile, as shown in figure 5.9(d). The peripheral transport reproduces the gradient at $\rho_{\mathrm{tor}} > 0.7$, but we lack CXRS data at $\rho_{\mathrm{tor}} > 0.86$ for complete edge comparisons.

In this experiment, extracting a W density from SXR measurements is not as simple as in section 5.2, because the high Ar content means that it dominates the SXR emissions. For the W profile, two simulations are run with different neoclassical transport from FACIT: the first considers collisions with the main deuterium ions only, and the second has an additional flux component where FACIT is applied with argon as the main ion. The latter approach has not been systematically validated with respect to NEO (unlike the former, in chapter 3 and in [109, 110]), but for the specific profiles in this simulation, standalone NEO calculations show quantitative agreement with the increase in the magnitude of the neoclassical diffusion and qualitative agreement with the decrease of the temperature screening associated with a higher effective collisionality when collisions with Ar are considered. Both resulting W profiles are shown in figure 5.9(e). The profiles are quite similar for most of the radius, being slightly peaked in $0.3 < \rho_{\mathrm{tor}} < 1$. Inside $\rho_{\mathrm{tor}} \approx 0.3$ both profiles peak considerably, but the one without Ar collisions then flattens. The increased core peaking in the case with Ar collisions is due to the more inward neoclassical convection associated with the reduced temperature screening. All other profiles in figure 5.9 are not noticeably modified between the two simulations, so moving forward we consider only the simulation with collisions of W and D only (where FACIT is known to coincide with NEO).

To compare the simulated and measured Ar density, shown in figure 5.9(f), we recall that the CXRS diagnostic observes a single line, in this case Ar^{16+}. This line is typically the most abundant at AUG temperatures, but lower ionization states are more populated at the edge, at lower T_e, and the two higher ionization states dominate in the hotter core. This is why the measured Ar^{16+} is hollow in the center. The measured line has gradients and content inconsistent with the simulated total Ar density, but the correct comparison is against the simulated Ar^{16+} density, which is an output of STRAHL. For Ar^{16+}, the simulation matches the shape and content of the measured profile quite well, with a slight shift from the core to the edge that can be explained by the higher simulated core T_e and differences in the Ar transport.

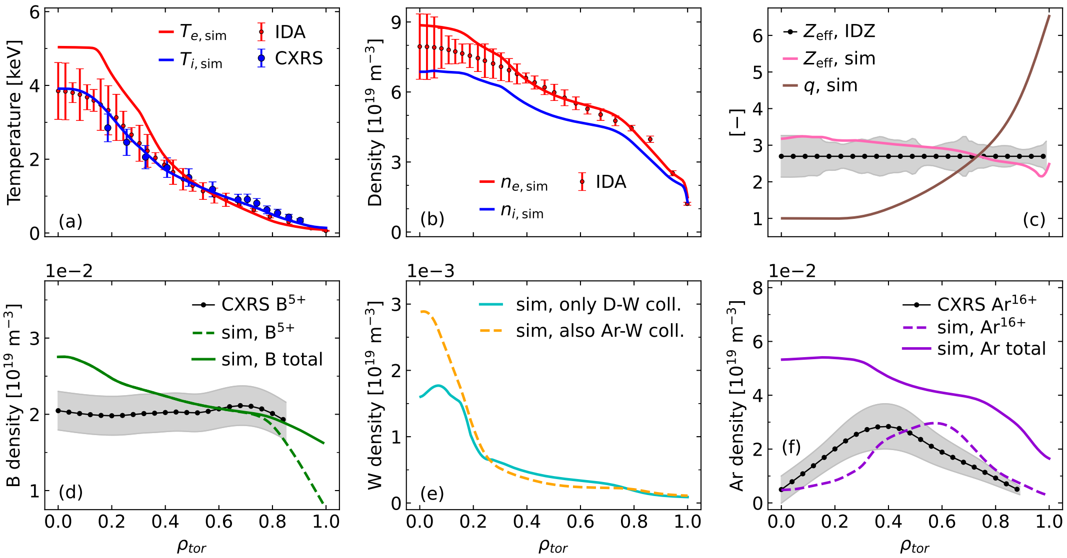

Figure 5.9: ASTRA simulation of the radiative L-mode AUG #37041 at 5.0–5.5 s, with $I_p = 0.8$ MA, $B_\varphi = 2.5$ T. (a–d) Same as figure 5.2.(e) Simulated W density profile, considering only D-W collisions (solid cyan) and also Ar-W collisions (dashed orange) in FACIT. (f) Total Ar density (solid purple), Ar^{16+} density (dashed purple), and CXRS-measured Ar^{16+} (black dotted).

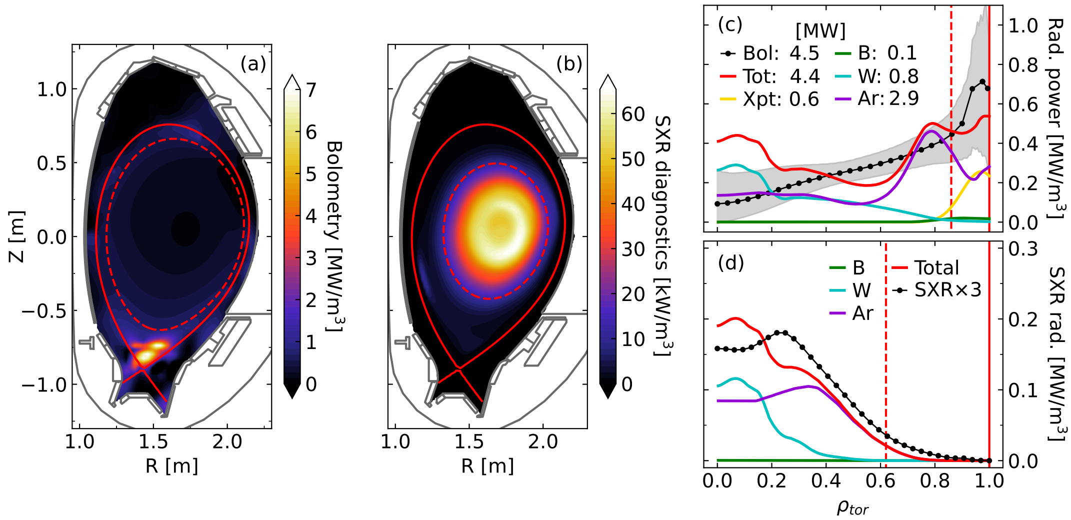

Figure 5.10: Radiated power density measurements and simulations for AUG #37041 at 5.0–5.5 s. (a) 2D tomography of the bolometry. The solid red contour is the separatrix and the dashed red contour marks $\rho_{\mathrm{tor}} \approx 0.85$. (b) SXR measurements. Here the dashed red line is the surface at $T_e \approx 1$ keV. (c) Radiated power profiles: FSA of bolometry from (a) in black, simulated radiation in red with its components by W (cyan), Ar (purple), B (green) and the X-point radiation (yellow, see section 5.3.3). The volume integral of each contribution is given in the label. Vertical lines correspond to the contours in (a). (d) SXR power profiles: FSA of measurements from (b) in black, with reconstruction from the modelling using temperatures and densities from figure 5.9 and SXR cooling factors.

In figure 5.10 we expand on the simulation of radiated power densities for this discharge. 2D tomographic reconstructions of the total radiated power density from bolometry were available for AUG #37041, and are shown in figure 5.10(a). An X-point radiator (XPR) [40, 231], caused by the increased Ar seeding and located outside $\rho_{\mathrm{tor}} > 0.85$, can be identified. By comparison, not much radiation is seen in the core (although the uncertainty of the bolometry increases towards the center due to lower line-of-sight coverage). The 2D SXR tomography is shown in figure 5.10(b), where we see that the experimental SXR emissions increase towards the center but decrease again deep in the core, and there is a slight in-out poloidal asymmetry.

Figures 5.10(c) and (d) present results of the 1D ASTRA simulations in comparison to flux surface averages of (a) and (b), respectively. In figure 5.10(c), the Ar radiation is the dominant component and it peaks at $\rho_{\mathrm{tor}} \approx 0.8$, where Ar is partially ionized but has a higher content than farther out radially, due to the edge gradient. W radiates only in the core. We note that a separate X-point contribution to the radiation is added. This is described in section 5.3.3. In total, the simulation obtains a high radiated power of 4.4 MW, in close agreement with the 4.5 ± 0.5 MW estimated by bolometry. P_{sep} matches the Martin scaling value for P_{LH} of 2.5 MW. The shape of the SXR radiation profile, in figure 5.10(d), is well reproduced from edge to $\rho_{\mathrm{tor}} \approx 0.25$, where n_{w} peaks and with it the modelled SXR emissions.

5.3.3 Model for X-point radiation

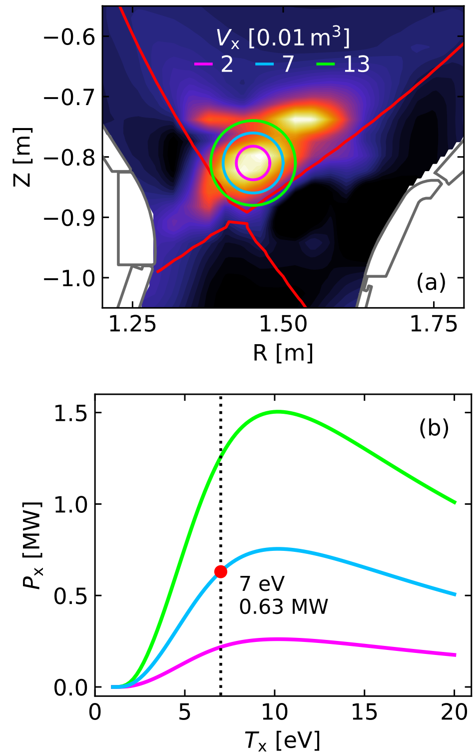

Figure 5.11: (a) X-point radiation bolometry, with cross sections of possible volumes in equation (5.2). (b) X-point radiated power as function of the X-point temperature, using the same color codes as in (a).

2D processes that produce a cold, dense region at the X-point (power balance between parallel heat conduction from the upstream and losses due to atomic processes [232]) cannot be modelled by ASTRA, which adopts a FSA approach to the transport equations. The formation of an XPR causes high radiation in a small edge region. Omitting this peripheral radiation leads to powers radiated inside the separatrix that are considerably lower than the measurements, while compensating with higher core radiation would trigger, by experience, a radiative collapse in the simulation.

We implemented a simple model to account for this peripheral radiation, estimating its magnitude as

$$P_{\mathrm{x}} = L_z(T_{\mathrm{x}})\, n_{\mathrm{x}}(T_{\mathrm{x}})^2\, c_{z\mathrm{x}}\, V_{\mathrm{x}}, \qquad (5.2)$$

where L_z is the total impurity cooling factor, n_{x} and T_{x} are the electron density and temperature of this dense, cold region above the X-point, $c_{z\mathrm{x}}$ is the impurity concentration in this region and V_{x} is its volume. Pressure balance along the field lines yields $n_{\mathrm{x}} \approx n_{\mathrm{u}} T_{\mathrm{u}} / T_{\mathrm{x}}$, where the subscript ‘u’ denotes upstream values, here taken as the separatrix values in ASTRA. The key assumption of this model is the value of T_{x}. We select 7 eV as a typical value in the range of 1-10 eV obtained in AUG SOLPS-ITER simulations [233] and divertor Thomson scattering measurements [234]. Two further assumptions are that the X-point impurity concentration is equal to its upstream value, i.e. the impurity density is compressed by the same amount as the electron density, and the value for the volume of the region (taken as a ring of circular cross section with radius R_0). The chosen parameters are illustrated in figure 5.11. We obtain 0.6 MW of additional radiation, added to the ASTRA simulation in a Gaussian profile with location and width in $\rho_{\rm tor}$ of 0.97 and 0.10 respectively.

5.3.4 Impact of impurities on confinement

Impurity dilution has long been known to stabilize ITG turbulence [51–53]. This is the explanation for the H-mode-like confinement of this radiative L-mode provided in [48]. We investigate this further in this section by performing an additional simulation without impurities, such that $n_i = n_e$ and $Z_{\rm eff} = 1$, but keeping the radiation profile fixed so the power balance is unchanged. TGLF is run with two kinetic species instead of five. In this case there is no dilution, the cause of ITG stabilization by impurities. Figure 5.12 shows the resulting simulations with and without impurities. The thermal pressure profile $p = n_eT_e + (n_i + n_{\rm B} + n_{\rm Ar} + n_{\rm w})\,T_i$, whose volume integral corresponds to the stored thermal energy and ultimately characterizes confinement, is plotted in figure 5.12(a). The one with impurities is higher than the one without even though the main ion density of the latter is not diluted and the electron densities are equal, which means that the difference is caused by increased temperatures. Both edge pressures ($\rho_{\rm tor} > 0.8$) are practically identical, indicating that this is a core effect. The predicted ion and electron heat diffusivities, χ_i and χ_e, are shown in figure 5.12(b). Both are reduced from the pure to the impure plasma, particularly in $0.3 < \rho_{\rm tor} < 0.8$. The result is a 33% increase in the predicted confinement, with $H_{98} = 1.06$ and 0.80 with and without impurities.

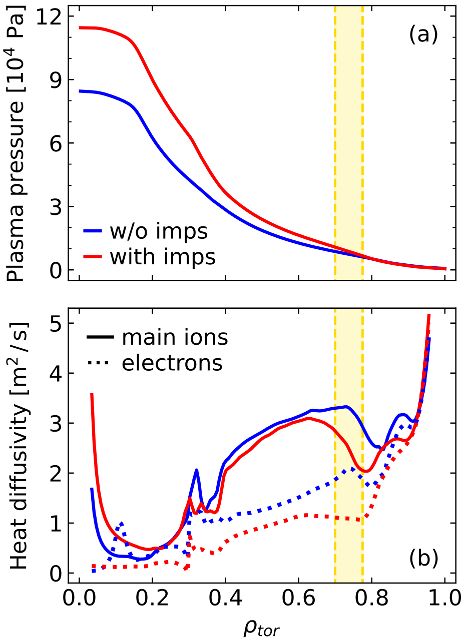

Figure 5.12: (a) Simulated pressure for AUG #37041 at 5.0–5.5 s without (blue) and with impurities (red). (b) Main ion (solid) and electron (dotted) heat diffusivities. The yellow region is where the turbulent spectra is analyzed in figure 5.13.

To look deeper into the reduction of turbulent transport by impurities, we performed two standalone TGLF simulations using input data taken from radial averages in the yellow region in figure 5.12, where the pressure gradients differ most (R/L_p of 25 and 17 with and without impurities). In particular, we build the inputs using the ASTRA simulation with impurities (red in figure 5.12) and then remove the impurities for the second standalone run, to have a more direct comparison of the role of impurities on the turbulence at the exact same background gradients.

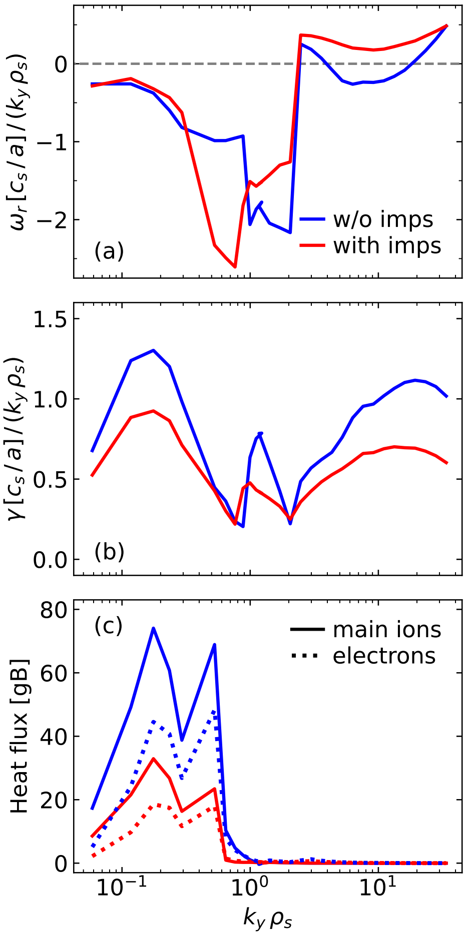

Figure 5.13: TGLF spectra for AUG #37041 at 5.0–5.5 s at $0.70 < \rho_{\rm tor} < 0.78$. (a) Real eigenfrequency of the dominant mode. Negative and positive values represent the ion and electron drift directions. (b) Growth rate of dominant mode. Both variables in (a) and (b) are normalized to the sound speed over the minor radius and divided by the wavenumber. (c) Electron and ion heat fluxes in gyro-Bohm units.

The corresponding turbulent spectra are shown in figure 5.13. The real eigenfrequency ω_r, in panel (a), indicates turbulence propagation in the ion drift direction (negative ω_r in the TGLF convention) at the larger length scales for both cases. At small scales, the simulation with impurities presents propagation in the electron drift direction but the one without impurities has parts of the spectrum on both signs of ω_r. In figure 5.13(b), the growth rate γ shows three peaks, at large, intermediate and small scales. All three are reduced going from the pure to the impure plasma. Note that both ion and electron heat fluxes (Q_i, Q_e) peak at larger length scales, around a normalized wavenumber of 0.3 characteristic of ITG turbulence, as shown in figure 5.13(c). Heat flux contributions from small scales are negligible. The inclusion of impurities reduces Q_i and Q_e by approximately a factor of 3.

The increased performance due to ITG stabilization by impurities begs the question of whether this effect would balance the deleterious fuel dilution in a fusion reactor. Fusion power grows with the square of the fuel density, $P_{\rm fus} \propto n_{\rm DT}^2$. In our simulation, the core fuel is reduced to 75% of the electron density by the presence of the seeded impurities. Given the 33% increase in confinement, this requires a scaling of $P_{\rm fus}$ with at least the square of the confinement (which was found numerically for the confinement enhancement factor, $P_{\rm fus} \sim H_{98}^{2.15}$, in [235]). However, the high confinement of this radiative L-mode is due to increased core temperatures and, as pointed out in [48], the D-T cross section decreases with T_i at high enough temperatures. Still, this is an interesting scenario that is both ELM-free and has a high core radiated fraction ($P_{\rm rad}/P_{\rm aux} \sim 0.67$), which are essential requirements for a safe power exhaust in a future reactor.

5.3.5 H-mode phase of this discharge

As we showed in figure 5.1, AUG #37041 had an initial H-mode phase before transitioning back to L-mode when the high Ar seeding was injected. Quasilinear transport models are typically not applied in full-radius H-mode simulations because they usually do not form strong pedestals. However, we saw in section 4.4.2 that suitable

E_r boundary conditions can result in pedestal-like structures with TGLF-SAT2.

As an exploratory endeavor, we performed a full-radius simulation of the H-mode phase of AUG #37041 (at 2.0-2.5 s), allowing E_r to evolve freely up to the separatrix, i.e. 'floating' boundary condition in equation (4.16). Note that using this choice in E_r in the radiative L-mode phase would result in higher edge gradients than what was obtained in figure 5.9, overestimating the confinement. In the experiment only the Ar puffing rate is different, leading to a reduced radiation and thus higher $P_{\mathrm{sep}} > P_{\mathrm{LH}}$. All other engineering parameters (P_{aux}, I_p, B_φ, $\overline{n}_e$, etc.) are constant. For this simulation, we use the same B source as in the L-mode phase, whereas both the Ar and W sources were reduced by a factor of 10, considering that in the experiment the Ar puff rate increased by around this much going from the H-mode to the radiative L-mode.

Figure 5.14 presents the resulting simulated profiles. The main plasma profiles are of particular interest in this case, because we are applying TGLF-SAT2 up to the separatrix in an H-mode. We find surprisingly good agreement between the simulation and the experiment. Strong edge temperature and density gradients are obtained in figures 5.14(a) and (b), consistent with the experimental data. All three profiles of T_e, T_i and n_e are within the error bars of the measurements across the full radius. In figure 5.14(c), Z_{eff} also matches the IDZ estimate, which is about two thirds of the one in the radiative L-mode phase.

These H-mode-like profiles of the main plasma allow us to test the impact of the presence of a pedestal on the impurity density profile predictions.

There is a strong simulated edge n_{B} gradient, as shown in figure 5.14(d), that unfortunately cannot be compared to measurements due to the lack of edge CXRS data in this phase (this lack is also evident in the T_i measurements). The simulated profile is peaked, in contrast to the experimental profile which is flat at mid-radius and hollow in the core, and the B content is well reproduced. The W profile shown in figure 5.14(e), in contrast to the radiative L-mode phase, has a very steep edge gradient arising from the higher neoclassical pinch due to the n_e pedestal and the lower edge turbulent diffusivity. It is then hollow in the region $0.6 < \rho_{\mathrm{tor}} < 0.8$ (where n_e is flat while T_i is peaked, so there is temperature screening), and it finally peaks in the core, although less than in the radiative L-mode phase. The magnitude of the effect of adding collisions with Ar are smaller than in figure 5.9(e) because the Ar content is lower in this phase, with a qualitatively similar increase in the core peaking. Both measured and simulated Ar contents, shown in figure 5.14(f), are about 1/6 of the ones in the radiative L-mode phase, even though the seeding rate was reduced by a factor of 10, because Ar also presents a stronger edge gradient that increases the core density from its separatrix value.

In figure 5.15 a similar analysis of the radiation as in figure 5.10 is presented. Figures 5.15(a) and (b) show the tomographic inversions of the measured total radiation density and its SXR share of the spectrum. We note the lack of the XPR in this phase of the discharge. The contribution of W to the radiation is twice as in the L-mode phase even though the source is reduced by a factor of 10, as shown in figure 5.15(c), because the W density is more distributed in the edge. Ar radiation is reduced by a factor of 5. The total 2.3±0.5 MW estimated from bolometry is well matched by the simulated 2.2 MW. In figure 5.15(d) we see that Ar still contributes significantly to the SXR emissions.

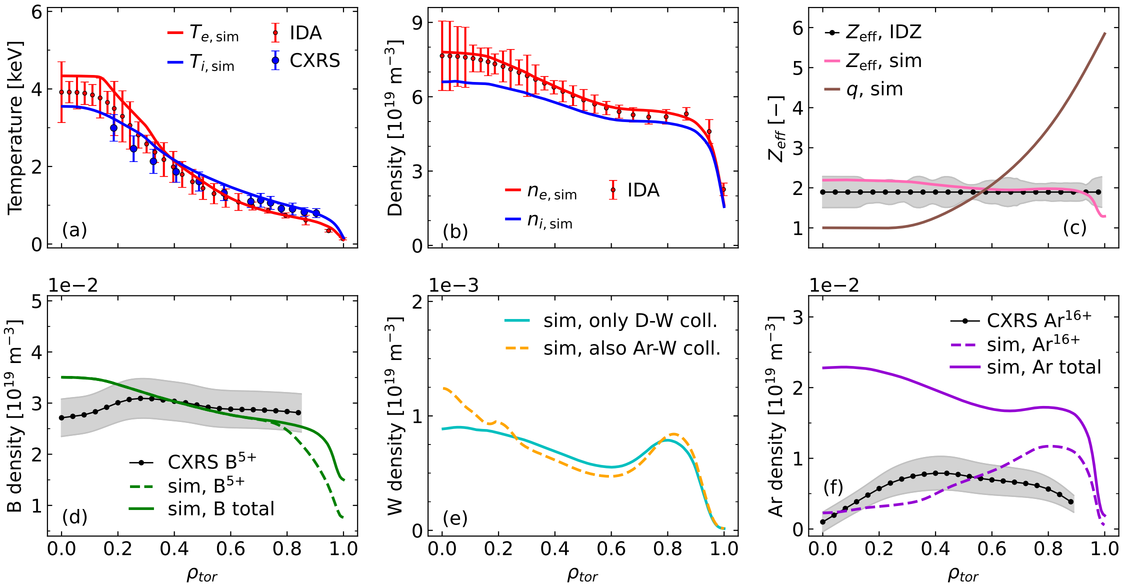

Figure 5.14: ASTRA simulation of the H-mode phase of AUG #37041, at 2.0–2.5 s. (a–f) Same description as figure 5.9.

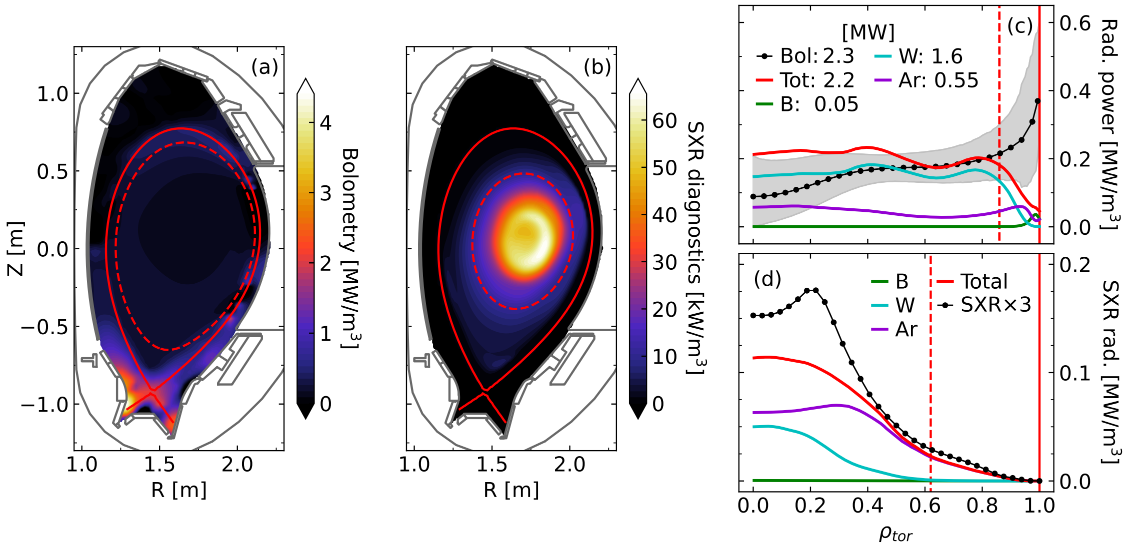

Figure 5.15: Radiated power measurements and simulations for AUG #37041 at 2.0–2.5 s. (a–d) Same description as figure 5.10.

Chapter 6

Effects of central wave heating on tungsten transport in ASDEX Upgrade and ITER H-modes

The results presented in this chapter have been published in Ref. [236], used here under the terms of the Creative Commons Attribution 4.0 licence.

A key aspect of tokamak scenario design revolves around avoiding central heavy impurity accumulation. This problem becomes particularly sensitive in NBI-heated H-mode plasmas, due to the enhancement of toroidal rotation by the beam torque and the more peaked plasma density due to the central particle source [203, 237], both of which increase the neoclassical high-Z impurity transport.

The use of central wave heating, like ECRH and ICRH, for the control of high-Z impurity accumulation has been well established experimentally across multiple fusion devices such as Alcator C-Mod [238], AUG [226], DIII-D [239], TCV [240], JET [227], KSTAR [241] and EAST [242]. Several physical mechanisms contribute to the effectiveness of this technique at increasing wave heating power:

- an enhanced central turbulent impurity diffusivity [229, 243] leads to flatter heavy impurity profiles, following equation (4.7);
- flatter electron density [230] and toroidal rotation profiles [244] reduce the neoclassical pinch, following equation (2.34);
- modified neoclassical transport by ICRH-induced temperature anisotropies that affect the poloidal asymmetries of the impurity density [100, 102]. ICRH can also increase the neoclassical screening, in case of heating schemes with significant ion heating fractions or by fast particle effects that reduce turbulent ion heat transport [245, 246], enhancing the ion temperature gradients;
- the combination of central ECRH and $(m, n) = (1, 1)$ MHD modes that cause outward high-Z impurity transport [224, 225].

In ASDEX Upgrade, in particular, the operational experience with tungsten walls is that NBI-heated H-mode plasmas without central ECRH usually survive only at low current ($\lesssim$ 600 kA), because at low current the pedestal is weaker and these lower pedestal gradients do not pinch W into the confined plasma so much, leading to a sufficiently low W concentration at the pedestal top. At high current with stronger pedestals, the neoclassical pinch is large and thus the W concentration at the pedestal top is already high. Without ECRH (with NBI alone), the core neoclassical pinch can lead to a strong central peaking of the W density, causing a radiative collapse of the discharge. For this reason, AUG is seldom operated in H-mode with high current and with NBI heating only.

Figure 6.1 shows an example of an AUG pulse with 7.5 MW of beam heating and three levels of ECRH during different phases of the discharge. The top panels show the measured soft X-ray emissions, which are dominated by tungsten. The bottom panels show the corresponding W densities reconstructed from the SXR measurements, using equation (5.1). The W density is flat (and even hollow) in the central region when there is some ECRH power, and it becomes strongly peaked when the wave heating is turned off (after which a radiative collapse was promptly triggered by the high W content in the core).

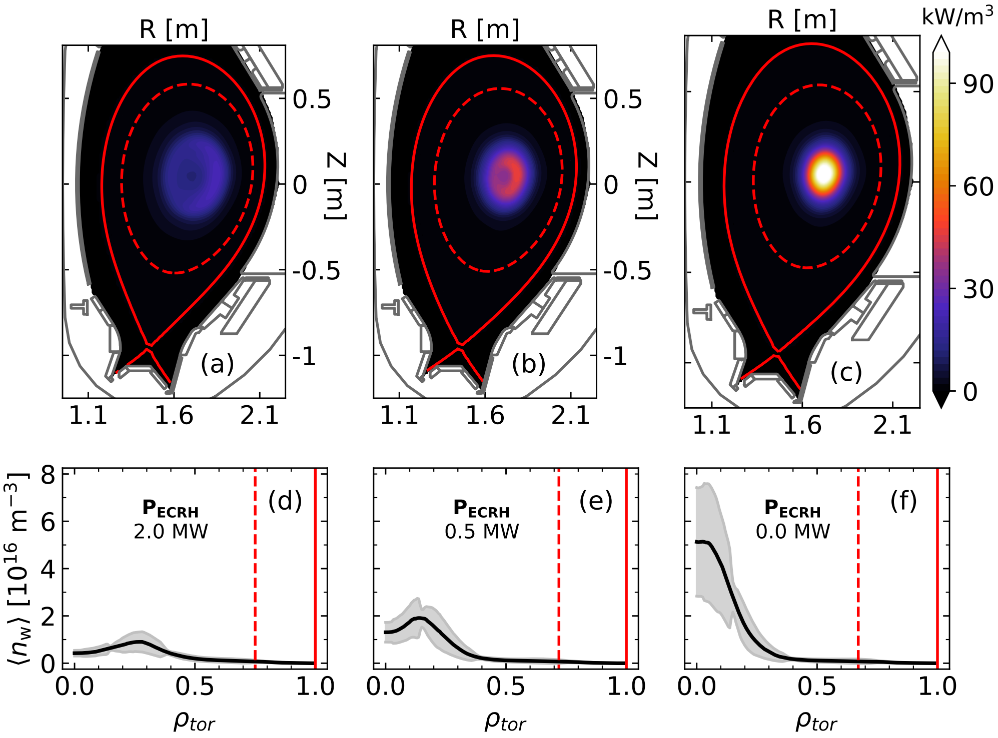

Figure 6.1: Progressive W accumulation in AUG #32408, as ECRH power is reduced. (a–c) Tomography inversion of soft X-ray emissions at $P_{\mathrm{ECRH}} \in \{2.0, 0.5, 0.0\}$ MW. Solid and dashed red contours are the separatrix and the surface at $T_e = 1$ keV respectively. (d–f) W density based on FSAs of the SXR radiation in (a–c).

The ability to reproduce the effects of central wave heating on heavy impurity transport is an important validation for a modelling framework that predicts impurity transport and radiation self-consistently. In this chapter, we demonstrate that the workflow introduced in chapter 4 recovers essential physics of core W transport in the presence of central wave heating, reproducing experimental observations of four ASDEX Upgrade H-modes with constant NBI and power steps in ECRH and ICRH. After this validation, we will apply the models to study the role of ECRH on core W transport in the ITER 15 MA baseline scenario.

6.1 ASDEX Upgrade H-mode experiments with wave heating power steps

Four AUG discharges, presented in detail in [228], will be investigated with integrated modelling in section 6.2. Their common feature are descending power steps in central wave heating, keeping all other engineering parameters fixed: 7.5 MW of NBI, line-averaged density $\overline{n}_e \approx 7 \times 10^{19}$ m^{-3}, magnetic field $B_\varphi = 2.5\,\mathrm{T}$, and plasma current $I_p = 1\,\mathrm{MA}$ ($q_{95} \approx 4$). These H-mode discharges are:

- #32408: *localized* ECRH, with three gyrotrons at a frequency of $f_{\mathrm{ECRH}} =$ 140 GHz focused at the same central location $\rho_{\mathrm{tor}} \approx 0.1$, in six power steps $P_{\mathrm{ECRH}} \in \{2.0, 1.6, 0.8, 0.5, 0.2, 0.0\}$ MW approximately 1.1 seconds long each;
- #32413: *broad* ECRH, with three steerable launchers aiming the gyrotrons at $\rho_{\mathrm{tor}} \in \{0.1, 0.2, 0.3\}$, in the same power steps;
- #32404: ICRH with a hydrogen minority heating scheme at a frequency of $f_{\mathrm{ICRH}} = 36.5$ MHz, in six power steps $P_{\mathrm{ICRH}} \in \{3.6, 2.6, 2.0, 1.3, 0.7, 0.1\}$ MW, using the B-coated 2-straps antenna and the W-coated 3-straps antenna (the latter of which produces a lower W source at similar power [247]);
- #32414: ICRH with finer steps at low power, $\{2.5, 1.0, 0.8, 0.6, 0.4, 0.2\}$ MW.

The purpose of the broad ECRH is to mimic the ICRH power deposition, which was calculated in [228] using the coupled wave and Fokker-Planck solver TORIC-SSFPQL [248–250]. Figure 6.2 shows the idea behind this experimental setting. The power density profiles are shown on the left, while the total powers deposited inside a given radial position are shown on the right. At the same input power, the broad ECRH and the ICRH have very close power depositions by design.

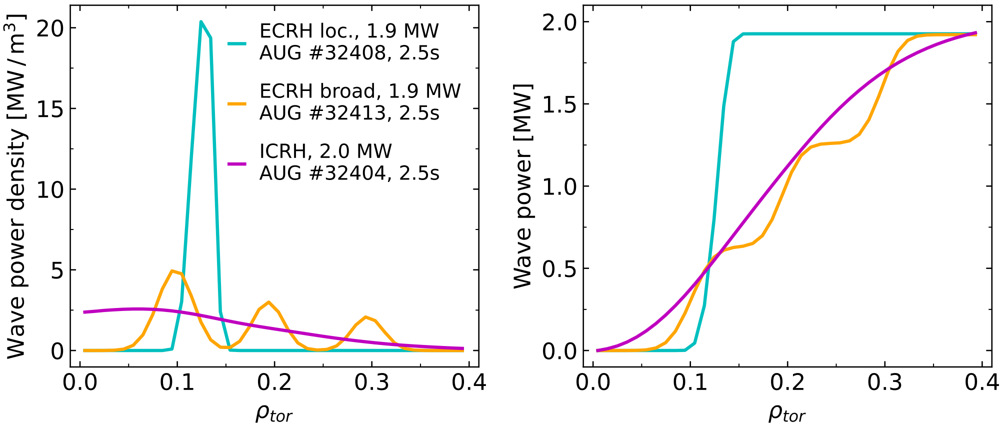

Figure 6.2: (left) Wave heating power density profiles in the different heating schemes used in the experiments to be modelled: localized ECRH (cyan), broad ECRH (pink) and ICRH (yellow). (right) Total deposited heating power inside the corresponding radial location (cumulative volume integral of the curves on the left).

For the simulations of these discharges, the W density boundary condition is set such that an initially flat profile produces the radiated power measured by bolometry at the start of the flattop, and this boundary value is kept constant throughout the wave heating steps. In this way, any effects observed as the wave heating power decreases throughout the discharge will be due to the changing shape of the core profile due to transport, and not due to changing W sources at the edge. The W radiation is calculated with the cooling factor from [33].

A boron (B) species is included with a concentration to match the measured effective charge $Z_{\text{eff}} \approx 1.5$. All other time-dependent ASTRA experimental inputs were prepared with the newly-developed TRVIEW interface [251]. The electron and ion temperatures, the current density, and the electron and tungsten densities are predicted, while the measured rotation is prescribed.

6.2 Dynamical integrated modelling of AUG plasmas with ECRH and ICRH

6.2.1 Localized ECRH

Figure 6.3 shows relevant experimental and simulated time traces for AUG #32408. Panel (a) presents the auxiliary heating mix and shows how the predicted and measured radiations are constant as long as some ECRH is applied, and rise out of control after the last step in the ramp. Panel (b) shows the trajectories of on- and off-axis W concentrations, measured by grazing incidence spectrometers (GIW) [153] and simulated, in close agreement with each other. The radiation is matched using only W, so a factor is applied to GIW. The central W concentration increases continuously throughout most of the flattop, but the radiation stays constant because the off-axis concentration slightly decreases. Panel (c) shows the simulated core (averaged over $\rho_{\text{tor}} \leq 0.3$) W transport coefficients and their neoclassical components. The diffusion is purely turbulent, while the convection is entirely neoclassical. The diffusivity is higher at high ECRH and decreases at lower ECRH, down to the neoclassical level. The convection increases as the ECRH is ramped down. The behaviors of D_{w} and V_{w} both contribute to a more peaked W density in time.

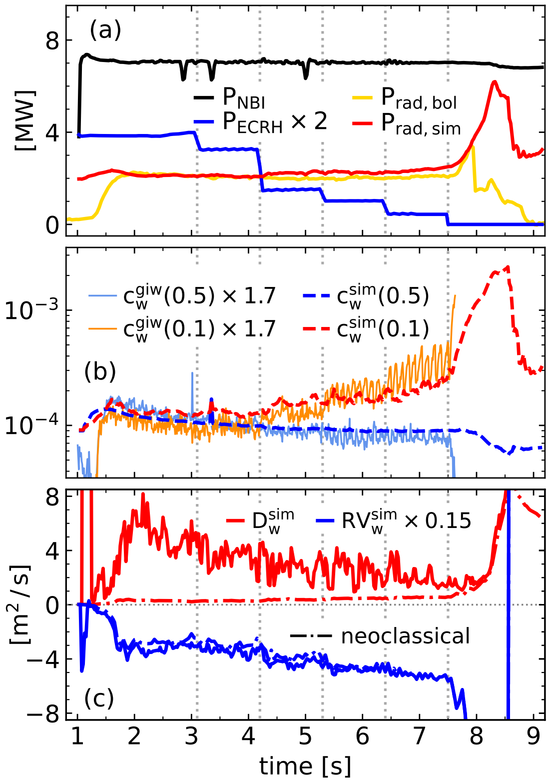

Figure 6.3: Timetraces for AUG 32408. (a) NBI (black) and ECRH (blue) powers; radiated power bolometry (yellow) and simulation (red). (b) W concentrations: GIW measurements (solid), on-axis (orange) and off-axis (light blue); simulation (dashed), on-axis (red) and off-axis (dark blue). (c) Simulated central W diffusivity (red) and convection (blue), with neoclassical components (dash-dotted).

During the radiative collapse ($t > 7.5\,\mathrm{s}$) the toroidal rotation greatly increases, contributing to an abrupt acceleration of the W accumulation and the collapse itself. This can be understood through the theoretically-predicted effects of rotation on neoclassical transport and particularly on the temperature screening, which are well described by FACIT. The cause of the sudden increase of the rotation during the collapse phase can also be explained. With the increase of the central radiation, T_e decreases fast and becomes lower than T_i, with the collisional energy exchange now becoming a sink for the ions. This drags T_i down following T_e, eventually producing flat and then hollow temperature profiles. Concomitantly with the reduction of the net energy source and the relaxation of the temperature gradients, the turbulent transport is strongly reduced. The simultaneous reduction of the turbulent ion heat conductivity and of the turbulent toroidal viscosity, in the presence of a still constant externally applied NBI torque, explains the observed sudden and strong acceleration of the toroidal rotation.

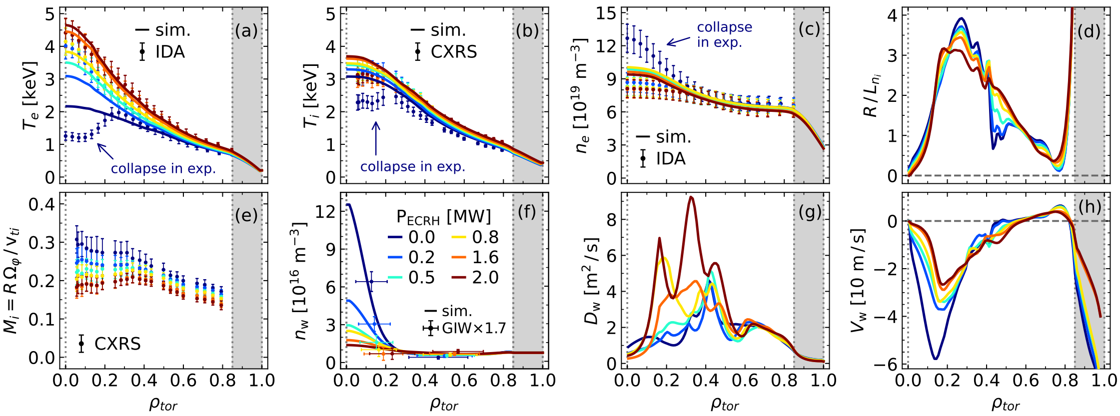

Figure 6.4: Profiles at different ECRH powers: (a) electron and (b) ion temperatures, (c) electron density, (d) main ion density peaking, (e) main ion Mach number, (f) W density, (g) W diffusivity, (h) W convection, averaged over the last 0.3 s of each ECRH step, except at 0 MW (averaged over the first 0.3 s).

Relevant profiles at different ECRH levels are presented in figure 6.4, along with available measurements. In panel (a), T_e decreases as both the ECRH is reduced and the W peaks. The effect on T_i is milder but still present in panel (b). The electron density, in panel (c), is less peaked at higher ECRH, contributing to a reduced W neoclassical pinch. Note that in (a–c), the experimental profiles are deep in the collapse during the last step, while the simulation is still in a less extreme phase. Overall, these simulated profiles closely reproduce the measurements. Panel (d) shows the reduction in the simulated main ion density peaking with more ECRH, and panel (e) presents the decrease in the measured rotation profiles. The increased peaking of W as the ECRH power is reduced becomes more apparent in panel (f). In panels (g) and (h) the profiles of the W diffusive and convective coefficients are plotted respectively, with clearly higher magnitudes of central D_w and V_w at higher and lower ECRH, respectively. The combination of effects shown in panels (d–e) causes the increase in the neoclassical convection as the ECRH is decreased.

An additional simulation with twice the total radiated power shows that there is little sensitivity of the results to the total radiation. This confirms that the collapse is triggered by the local central power balance going negative in response to the local core W transport. In section 6.4 we will show that in ITER the opposite takes place: the critical element is the total volumetric radiative loss of the power.

6.2.2 Broad ECRH

Figure 6.5 shows equivalent time traces for the broad ECRH discharge (AUG #32413) as figure 6.3 for the localized ECRH. In the case of broad ECRH deposition the most notable difference is that, using the same power steps, the discharge presents a radiative collapse much earlier (halfway through the step at 0.5 MW), as we can see in panel (a). The measured radiated power greatly and quickly increases at around 5.5 s, with the simulated radiation also rising out of control (albeit more smoothly).

In panel (b), we can see that the GIW measurements of on-axis W concentration rise steadily after 4 s, while the off-axis W concentration slightly decreases, indicating a central peaking of the W density profile. These trends in the trajectories are well matched by the simulations. The central diffusive and convective transport coefficients are similarly shown in panel (c). The magnitude of the W diffusion, which is mostly turbulent before the collapse of the plasma, is lower with broad ECRH than with localized ECRH (by around a factor of 2). This contributes to a more peaked W density. The diffusivity is similarly reduced in time as the wave heating power is decreased, down to the neoclassical level during the collapse. The convection, which is mostly neoclassical, is inward and it strongly increases in magnitude towards the later phase of the simulation.

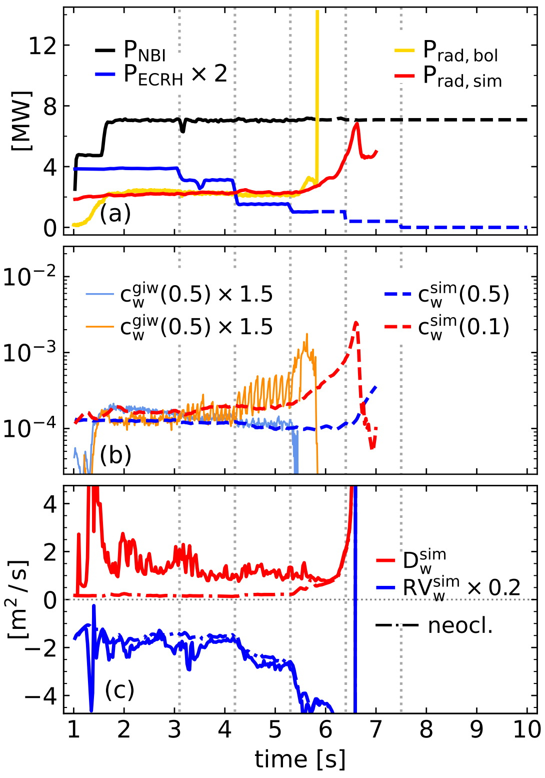

Figure 6.5: Timetraces for AUG 32413. (a–c) Same as figure 6.3.

Less electron heating is deposited within the inner core region (e.g. $\rho_{tor} \leq 0.2$), which has been shown in figure 6.2. As we will discuss in more detail in section 6.3, the electron to ion heat flux ratio is a crucial parameter in determining the effectiveness of wave heating in controlling high-Z impurity peaking.

6.2.3 ICRH with larger and finer steps

Modelling of ICRH temperature anisotropies

As we previously discussed in section 2.2.2, the ICRH-induced temperature anisotropies (TA) tend to push the highly-charged impurities towards the high-field side, partially compensating the low-field-side localization due to centrifugal effects. The end effect is a reduction of the (typically inward) neoclassical transport, which is one of the reasons why ICRH is effective in the control of core W accumulation. Including this effect is important to describe the discharges with ICRH power steps.

To model the ICRH TA, our main assumption will be that the parametrizations of FACIT from section 3.2, which are mostly in terms of the effective impurity Mach number M_z^*, will describe these effects if we use a modified M_z^*,

$$M_z^{*2} \approx {M_{z\Omega}^*}^2 - {M_{z\eta}^*}^2, \tag{6.1}$$

with a centrifugal component, labeled by Ω for the toroidal rotation angular frequency and given by the usual equation (2.28), and a temperature anisotropy component. The work of chapter 3 was built on rotating plasmas without temperature anisotropies, that is on ${M_{z\Omega}^*}^2$ only, but the physical effect at play is the poloidal asymmetry of the density, whose modifications by ICRH TA are assumed to be described by an ${M_{z\eta}^*}^2$. If the minority fraction is small, $f_m = \langle n_m \rangle / n_e \ll 1$, such that its impact on the quasi-neutrality is negligible compared to the majority ion, $Z_m \langle n_m \rangle \ll Z_i \langle n_i \rangle$, then following [100] we can approximate

$${M_{z\eta}^*}^2 \approx \frac{Z}{Z_i} \frac{Z_m T_e}{T_i + Z_{\mathrm{eff}} T_e} \frac{f_m \, \eta^{3/4}}{1 + (b_{\mathrm{ic}} - 1)(1 + \eta^{3/4})}, \tag{6.2}$$

where $b_{\mathrm{ic}} = B_{\mathrm{res}}/B_0$ is the ratio between the magnitudes of the magnetic field at the resonance of the ICRH, $2\pi f_{\mathrm{ICRH}} = Z_m e B_{\mathrm{res}}/m_m$, and on axis.

It was pointed out in [252] that the more complete but more complex model of [103] can still be approximately recovered with the model of [100] by using $\eta \to \eta^{3/4}$, which we have implemented here, already shown in the powers of η in equation (6.2).

This temperature anisotropy factor $\eta = T_\perp(\theta_0)/T_\parallel - 1$ is an output of TORIC-SSFPQL. Figure 6.6 shows an example of a radial profile of $\eta + 1$ for one of the ICRH discharges under consideration, as well as the modified effective impurity Mach number and its centrifugal and TA components.

As a final note, we will take equation (6.1) to be valid only if the resulting $M_z^* \geq 0$. If $M_{z\Omega}^* < M_{z\eta}^*$, we will simply take $M_z^* = 0$. Physically, this means that with FACIT we cannot describe a reversal of the rotation-induced LFS localization of the impurities to a HFS localization due to the ICRH; at most we can have completely poloidally symmetric densities in a balance of centrifugal and temperature anisotropy effects.

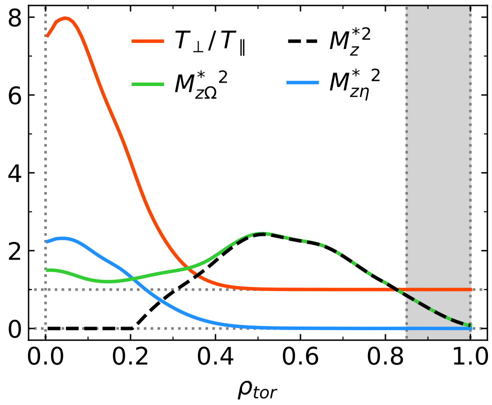

Figure 6.6: Ratio of perpendicular to parallel minority temperature (orange), effective W Mach number (black), and its centrifugal and temperature anisotropy components (green, blue), for AUG #32404 at 3s.

Simulation results

Time traces resulting from the simulations, along with experimental measurements, are shown in figures 6.7 and 6.8 for the ICRH discharges with high (#32404) and low (#32414) power steps. Unlike the equivalent figures 6.3 and 6.5 with ECRH, here the ICRH power is not multiplied by a factor of 2 in panel (a). Approximately twice the wave heating power is applied in these ICRH discharges, since again, as we will discuss further in section 6.3, the critical parameter is the electron heating, but ICRH also heats the ions. The finer steps at low power in #32414 (right figure) can be difficult to differentiate with this scale, but we keep it in this way to better compare the ICRH power at a given time with respect to the figure on the left.

In the case of #32404 with higher ICRH, the radiated power measured by bolometry is constant throughout the discharge and it quickly rises when the last power step is finished and the ICRH is turned off. In #32414, the measured radiation begins to rise shortly before the end of the last power step. In the case of #32404 (left figure), the simulated radiated power is approximately constant up to the second-to-last power step ($t \lesssim 6.2\,\mathrm{s}$), it begins to steadily rise during the last power step and finally quickly increases when the ICRH is turned off. For #32414 (right figure), the simulated radiation rises more steadily after $t \approx 4\,\mathrm{s}$. We notice that, even if it happens at different times, the ICRH powers at which the radiated powers in the simulations start to rise are almost equal (0.7 and 0.6 MW).

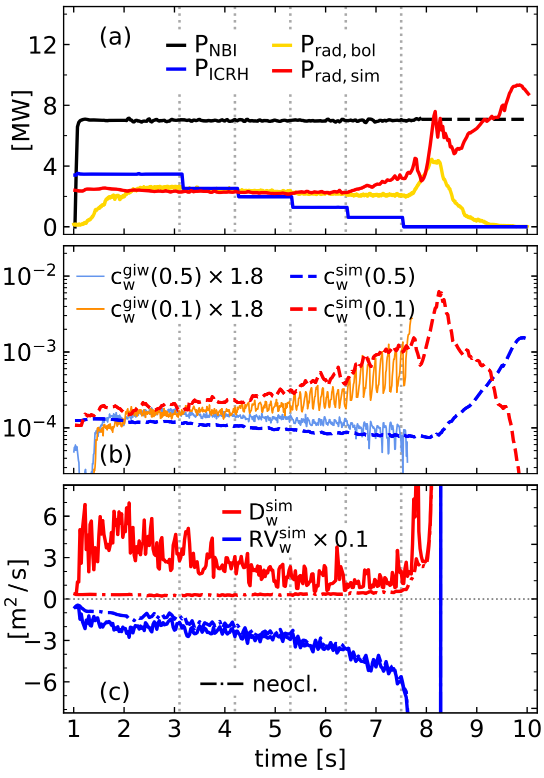

Figure 6.7: Timetraces for AUG 32404. (a–c) Same as figure 6.3, but with ICRH power in (a).

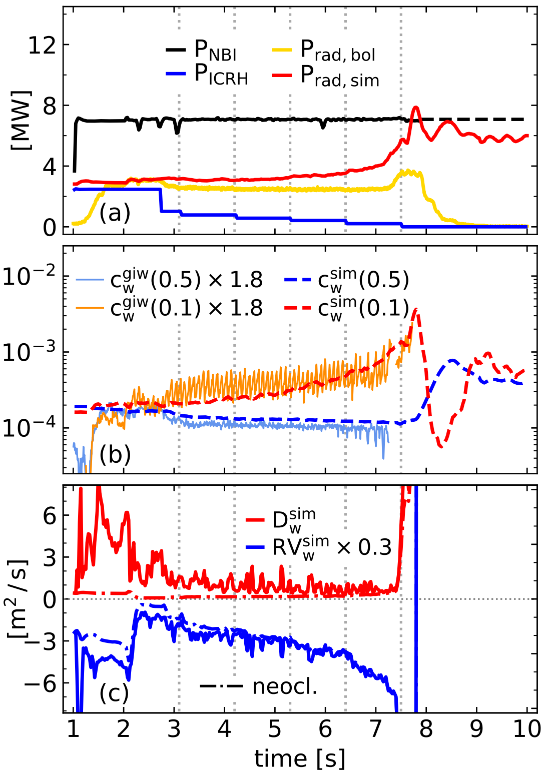

Figure 6.8: Timetraces for AUG 32414. (a–c) Same as figure 6.3, but with ICRH power in (a).

The simulated on-axis and off-axis W concentrations, in panels (b), follow the experimental time trajectories quite well in both cases, with an off-axis concentration slightly decreasing in time and an on-axis concentration that progressively increases.

The comparison between both ICRH discharges in terms of transport coefficients, shown in panels (c), is interesting because it is clear that, after the initial step with high power where the W diffusivity is high in both cases, the ICRH power is more slowly ramped down for #32404 (left figure) and consequently the W diffusivity decreases more slowly, remaining with considerable magnitude for longer. In contrast, the turbulent W diffusion for #32414 decreases to very low values after the first power step, because the ICRH is strongly reduced. In both cases the neoclassical convection becomes more strongly inwards as time advances, due to more peaked electron density and rotation profiles. For #32414, there is a strong and sudden reduction of the convection during the first power step (at $t \approx 2\,\mathrm{s}$), which is due to a (3,2) mode that flattens the core rotation (this will be further discussed in section 6.3.1), after which the inward convection monotonically increases in magnitude.

Again, the reduction in (turbulent) diffusion and the increase in the inward (neoclassical) convection lead to the increased peaking in the W density evidenced in panels (b), recalling equation (4.7).

6.3 General properties of W transport in AUG plasmas with wave heating

The simulations of the four wave-heated discharges presented in the previous sections share qualitative properties of increased core W peaking, decreased turbulent diffusivity and increased neoclassical pinch as the wave heating is ramped down. However, quantitative differences arise from physical effects that we will discuss in the following subsections.

6.3.1 Tungsten peaking

The ratio of central to mid-radius ($\rho_{\mathrm{tor}} \sim 0.1, 0.5$) W densities as a function of the wave heating power is compared to GIW data in figure 6.9(a) and (c) for all discharges. In the simulations, like in the experiments, the localized ECRH is more efficient in reducing the W peaking in terms of total heating power than the broad ECRH (which collapses before reaching the lower power steps, only avoiding W accumulation for $P_{\mathrm{ECRH}} \geq 0.8\,\mathrm{MW}$) and the high ICRH (which requires about twice the power for equivalent flattening of W).

The ECRH cases are somewhat shifted to larger W peaking at the higher powers due to a stronger simulated R/L_{n_e} than the experiment, leading to a stronger neoclassical pinch. With ICRH, R/L_{n_e} is closer to the experiment. Hollow W profiles are not obtained because sawteeth are modelled as an average increase of diffusivity inside $q = 1$ ($\rho_{\mathrm{tor}} < 0.3$), and effects like those of [224, 225] are not described. However, on the scale of a full radiative collapse, the quantitative agreement between simulation and experiment is satisfactory.

In [228], the local electron heat flux fraction, Q_e/Q_{tot}, was shown to order the experimental data for the different heating schemes: the relevant physical quantity is how much heat is locally deposited to the electrons, as seen in panel (d). The experimental Q_e/Q_{tot} are calculated from power balance in interpretative simulations. In panel (c), the simulated Q_e/Q_{tot} are shifted to higher values, particularly for the ECRH cases and at low Q_e/Q_{tot}. In this inner core region there is sensitivity to the collisional heat exchange $q_{ei} \propto (T_e - T_i)\, n_e^2/T_e^{3/2}$, so slight deviations in the temperature profiles (especially if $T_e \approx T_i$ and exacerbated by slightly higher n_e) can cause this heat to flow from the ions to the electrons, opposite to what results from the experimental profiles. Regarding the W flattening efficiency, since ICRH heats the ions too (ion heating fractions ranging in 20–70%) and has a broader deposition, it is less effective in terms of power in MW. When ordered with Q_e/Q_{tot}, the additional effect of ICRH-induced temperature anisotropies contributes to the efficiency of ICRH. This effect, which we model like in [100] up to where it fully compensates the low-field-side centrifugal asymmetries of W (but not up to having high-field-side localization), could be somewhat overestimated in the simulations.

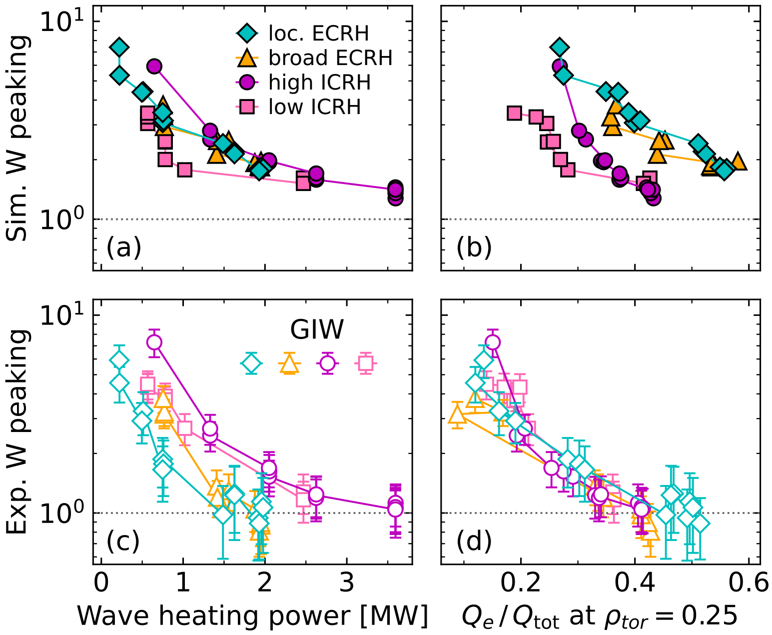

Figure 6.9: Tungsten peaking as a function of the total wave heating power (left panels) and central electron heat flux fraction (right panels). Simulated values and GIW measurements are shown in the top panels and bottom panels respectively

Discharge #32414, with finer ICRH steps at low power, has a reduced and flatter rotation profile in $\rho_{\text{tor}} \leq 0.5$ than the other three discharges, due to a (3,2) mode starting at the first power step that remains active during the entire I_p flattop. Its impact is significant on the core rotation (halving it), but it is small on the temperatures and stored energy. While presence of the mode is not included in our modelling, the measured rotation profiles are used as inputs and the reduced rotation impacts the W neoclassical predictions of this discharge as compared to the other three. The effect of this (3,2) mode can be clearly seen in the W convection of #32414 in figure 6.8(c) at $t \approx 2\,\text{s}$, where the reduction in central rotation leads to a sudden reduction of the pinch.

6.3.2 Relative efficiency of turbulent tungsten flattening and turbulent heat losses

The ratio of impurity particle and ion heat diffusivities D_{w}/χ_i characterizes how efficiently the enhancement of core turbulence by wave heating flattens the W profile compared to how fast it removes the plasma energy.

Analytical and non-linear gyrokinetic analyses [229] indicate that this ratio is a non-monotonic function of the local electron to ion heat flux ratio, Q_e/Q_i, due to the shift in the resonant real eigenfrequency at which D_w and χ_i peak as the properties of the turbulence change in response to the applied heating scheme.

In figure 6.10, TGLF predictions for the dependence of D_w/χ_i on Q_e/Q_i are plotted for different time frames in the four simulations. Q_e/Q_i orders D_w/χ_i for all wave heating schemes in approximately a single curve. The increase in D_w/χ_i at the lower Q_e/Q_i, a maximum at $Q_e/Q_i \sim 2$, and subsequent decrease as $Q_e/Q_i \gg 1$, is completely consistent with the analytical and non-linear results of [229], showing that TGLF captures important physics of high-Z turbulent impurity transport.

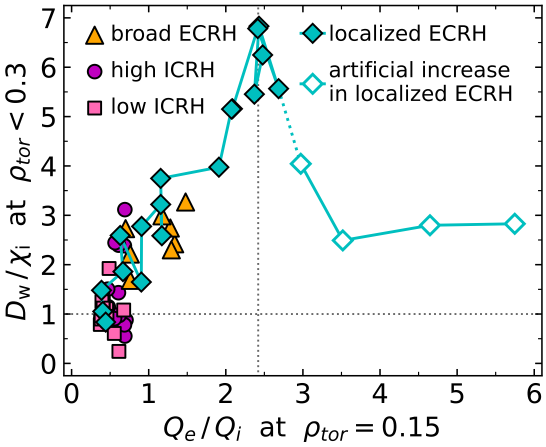

Figure 6.10: Ratio of turbulent W diffusivity to ion heat diffusivity, as a function of the electron to ion heat flux ratio.

The localized ECRH is the only heating scheme that reaches the maximum in D_w/χ_i in this set of discharges, because it deposits heating to electrons only and it does so in the very center of the plasma. The broad ECRH deposits the heat spread farther out, so the Q_e/Q_i at $\rho_\mathrm{tor} = 0.15$ is lower. Both ICRH cases not only have a broad heat deposition, but they also give a fraction of the heat to the ions, increasing not only Q_e but also Q_i, thereby having a more limited effect on Q_e/Q_i even if more power in MW is applied.

To obtain points at $Q_e/Q_i \gg 1$, not reached in the experiments, we performed an additional simulation with artificially increased $P_\mathrm{ECRH} \in \{2.5, 3, 4, 5\}$ MW, shown in open diamonds in figure 6.10.

6.4 Tungsten transport in the ITER 15 MA baseline scenario

The recently announced new ITER baseline [253] aims to accelerate the scientific exploitation of ITER, minimizing risks in the project and optimizing the machine assembly. A key element for risk mitigation, particularly in terms of nuclear licensing, is the replacement of beryllium (Be) with tungsten as a first wall material. Since tungsten was already envisioned as the divertor material, ITER plasmas will now be surrounded by a full-W metallic environment. Considering the low tolerance to core contamination with high-Z impurities in reactor conditions [37], it is necessary to understand and predict the transport and effects of tungsten in ITER plasmas.

6.4.1 Modelling settings

To simulate the ITER 15 MA baseline scenario ($B_\varphi = 5.3\,\mathrm{T}$, $R = 6.2\,\mathrm{m}$) we start by setting a conservative pedestal top pressure (p_pt) of 108 kPa at $\rho_\mathrm{tor} = 0.9$. This is approximately 20% lower than the value at the peeling-ballooning (PB) stability boundary calculated using the EPED1 model [254, 255], and it was selected as a proxy for ELM-suppressed or ELM-mitigated operation. The boundary conditions for the main plasma profiles are $T_e^{\mathrm{pt}} = T_i^{\mathrm{pt}} = 4.4\,\mathrm{keV}$ and $n_e^{\mathrm{pt}} = 8 \times 10^{19}\ \mathrm{m}^{-3}$. We use a 50/50 D–T fuel mix (as a single ion of mass 2.5 in TGLF), with a bundled light impurity equivalent to 5% He and 1% B charge concentrations, yielding a $Z_{\mathrm{eff}} \approx 1.4$.

Constant 30 MW of NBI are applied, with prescribed deposition profiles to electrons and ions from [98], and the rotation profile predicted in [98, 99] is also prescribed. Central ECRH is applied with a Gaussian profile with location and width in ρ_{tor} of 0.1 and 0.05. The ECRH power is scanned in separate simulations up to the maximum installed power, $P_{\mathrm{ECRH}} \in \{0, 10, 20, 50, 70\}\,\mathrm{MW}$. The NBI power density profiles are kept fixed. This assumption can be justified by the practically constant density and the limited variations in T_e ($\pm 12\%$) which are obtained across the scans in P_{ECRH}. Moreover, core W transport in ITER is not sensitive to slightly modified NBI power density profiles, considering the low torque and core particle source.

The simulations are evolved for over 10 confinement times τ_{E}, to guarantee convergence. The main free parameter is the W concentration at the pedestal top, $c_{\mathrm{w}}^{\mathrm{pt}}$. We scan this quantity in 5 runs for each ECRH power as $c_{\mathrm{w}}^{\mathrm{pt}} \in \{0, 1, 2, 5, 10\} \times 10^{-5}$, for a total of 25 simulations. In these H-mode simulations, we scan the pedestal top W concentration, instead of the separatrix concentration, in order to make our studies independent of the large uncertainties in pedestal transport. Amongst the unknowns present with our local reduced models are the quantitative predictions of turbulent transport in the pedestal, the influence of 3D resonant magnetic perturbation (RMP) fields on heavy impurities [256] and global effects on neoclassical transport [257,258]. Profiles are evolved inside $\rho_{\mathrm{tor}} \leq 0.9$, but a pedestal W density is built to calculate the W radiation up to the separatrix, using neoclassical convection and diffusion from FACIT and $0.3\ \mathrm{m}^2\,\mathrm{s}^{-1}$ of turbulent diffusion (lacking reliable turbulent transport predictions in the pedestal with theory-based models). This value is consistent with IMEP [183–185] predictions of χ_i in ITER's pedestal [259] and is used to be less optimistic than a fully neoclassically-screened pedestal W density. This assumption leads to $n_{\mathrm{w}}^{\mathrm{sep}}/n_{\mathrm{w}}^{\mathrm{pt}} \sim 7$.

6.4.2 Predictions of W transport in ITER

In reactor conditions it is expected that core neoclassical convection is low, even for heavy impurities, mostly due to the significantly lower collisionality [127]. The lower rotation and NBI particle source also contribute to this. The impurity convection of high-Z impurities is therefore mostly turbulent in reactor conditions. We recall that a validation of TGLF predictions for the impurity convection was presented in section 4.3 for boron, whose low charge Z and low mass A imply that its convection is mostly turbulent also in AUG conditions.

Figure 6.11 shows W density profiles normalized at the pedestal top for all concentrations. The profile shapes are practically unaffected by the level of ECRH, and core accumulation is never observed.

The mid-radius peaking is $R/L_{n_{\mathrm{w}}} \sim 2$ for all cases, which is an indication of a mostly turbulent convection: with negligible roto-diffusion, most terms in the turbulent impurity convection are diamagnetic in nature, scaling as $1/Z$ and thus being small for W. The remaining term is the compression of the E×B flow due to the inhomogeneous magnetic field, for which the ∇B and curvature drifts contribute each as $\sim -1/R$, leading to a turbulent pinch of $R\,V_z \sim -2D_z$ [126]. The neoclassical temperature screening in the pedestal region can be clearly seen.

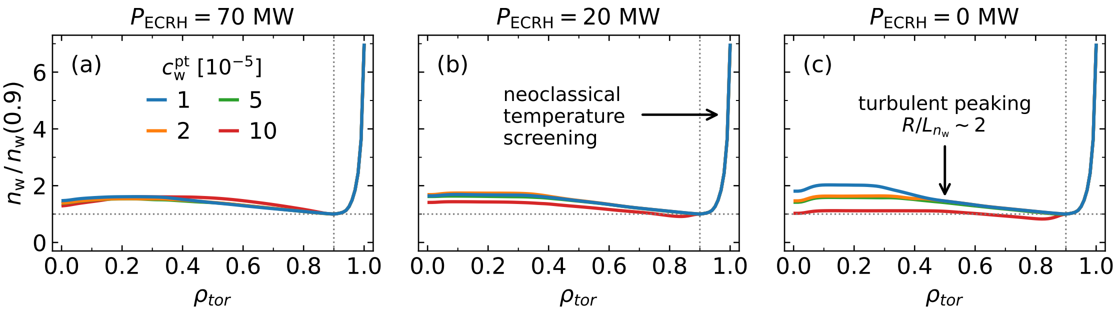

Figure 6.11: Normalized W density profiles, at different ECRH powers (across panels) and pedestal top concentrations (in colors).

The behavior of diffusive and convective W coefficients as wave heating power increases is shown in figure 6.12. ITER W diffusivities in the core and at mid-radius are presented in figure 6.12(a) for $c_{\mathrm{w}}^{\mathrm{pt}} = 5 \times 10^{-5}$. The neoclassical component is negligible at both radial locations. The turbulent core D_{w} is consistent with the physics of figure 6.10, considering the broad range of Q_e/Q_i here. Figure 6.12(b) shows that the neoclassical W pinch in the core and mid-radius of ITER is also very small, such that the convection is completely turbulent. An additional run at $P_{\mathrm{ECRH}} = 35$ MW is included.

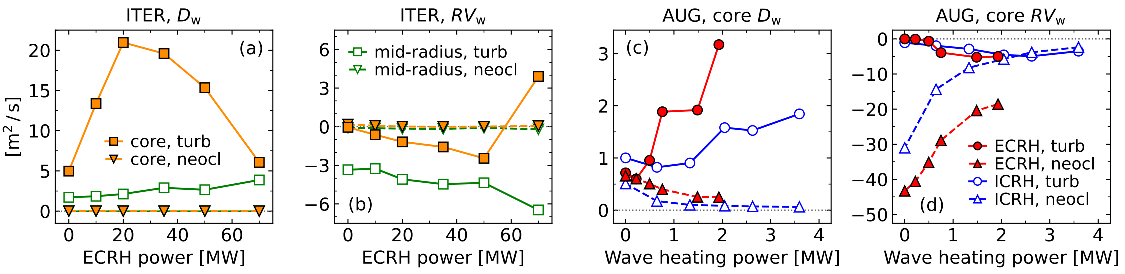

Figure 6.12: W transport coefficients as a function of wave heating power. (a) Diffusivity and (b) convection in ITER, core ($\rho_{\mathrm{tor}} \leq 0.3$) in full orange symbols and mid-radius ($0.45 \leq \rho_{\mathrm{tor}} \leq 0.55$) in open green symbols, with turbulent and neoclassical components in squares and downward triangles respectively. (c) Diffusivity and (d) convection in AUG core ($\rho_{\mathrm{tor}} \leq 0.3$), with ECRH in full red symbols and ICRH in open blue symbols, turbulent and neoclassical components in circles and upward triangles respectively.

Centrifugal effects on neoclassical impurity transport scale with the Mach number squared, $M^2 \propto (R\,\Omega_\varphi)^2/T_i$. In ITER, these effects are small compared to current devices [110] due to the high core T_i and low predicted rotation. Results of simulations without rotation, using the rotation from [98, 99], or twice that rotation, are practically identical, since neoclassical transport is almost negligible in any case.

The transport regime for W in ITER will be markedly different from current machines due to the lower collisionality, rotation and NBI particle source. The turbulent convection does not scale strongly with the impurity charge or mass [126], unlike its neoclassical counterpart. Therefore, it does not have a mechanism for strong accumulation of high-Z impurities.

Panels (c–d) show that in AUG the situation is quite different. Again the core W diffusivity is mostly turbulent and it increases with wave heating power, more efficiently for central ECRH and less so for ICRH. However, the convection is mostly neoclassical and is strongly reduced by the wave heating, more efficiently with ICRH due to the temperature anisotropies.

6.4.3 Radiative losses, H-mode sustainment and fusion performance

Since a radiative collapse by a local negative power balance in the inner core due to W accumulation is not expected to occur in the ITER 15 MA scenario, the limiting effect as the W concentration increases is produced by the global radiative power losses, P_{rad}, which would not allow the power crossing the separatrix, P_{sep}, to sustain H-mode operation.

This is investigated in figure 6.13, where all quantities are time-averaged over the last $2\,\tau_{\mathrm{E}}$ of each simulation. In panel (a) P_{rad} is found to be mostly unaffected by ECRH power, in connection to the insensitivity of W densities to ECRH. In panel (b), P_{sep} is plotted along with the L–H power threshold at increasing levels of optimism: the Martin scaling [218], its correction as $2/A_{\mathrm{DT}} = 2/2.5$ due to isotope effects [260], and a further 25% reduction for full-W walls [261]. The uncertainty bands on P_{sep} correspond to W radiated powers inside the pedestal assuming fully turbulent (flat) or fully neoclassical (very hollow) pedestal profiles. Symbols correspond to the chosen assumption of purely neoclassical convection with small turbulent diffusion.

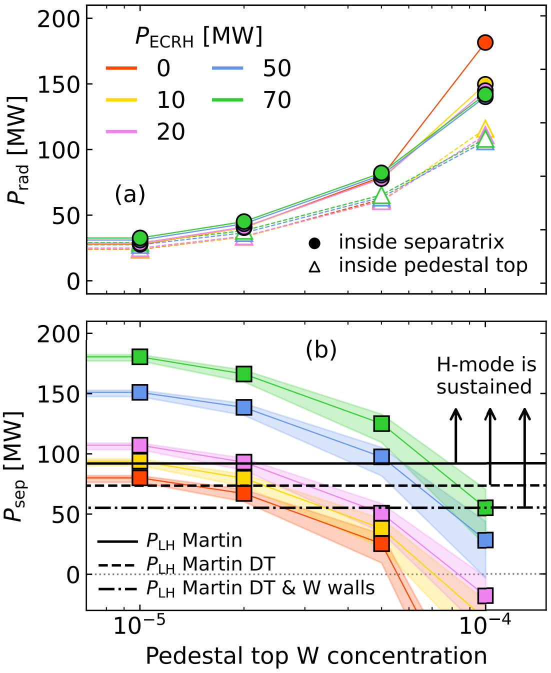

Figure 6.13: (a) Radiated power and (b) power crossing the separatrix, as a function of the pedestal top W concentration for different levels of ECRH. In (b) the black horizontal lines are L–H power thresholds under different assumptions.

Higher ECRH allows the plasma to tolerate a higher W concentration while remaining in H-mode, but this is true for any heating method in the global power balance. ECRH directly replaces the electron heat sink of impurity radiation, however, compensating the electron power losses with a more dominant ion heating fraction could have a favorable effect on the fusion power, since T_e/T_i is reduced (with a beneficial reduction of turbulent transport) and T_i is increased.

We do not simulate the transition back to L-mode when P_{sep} becomes arbitrarily low at high P_{rad}, since we keep fixed the initial pedestal profiles for $\rho_{\mathrm{tor}} > 0.9$. However, this exercise allows us to identify the maximum W concentrations that still allow H-mode operation. In the baseline case at 20 MW of ECRH, the marginal maximum $c_{\mathrm{w}}^{\mathrm{pt}}$ is $\sim 3.5 \times 10^{-5}$. Here, we consider a *marginal* sustainment of the H-mode when the ratio $P_{\mathrm{sep}}/P_{\mathrm{LH}}$ approaches 1, although for a robust operation of a reactor a safety margin of $P_{\mathrm{sep}}/P_{\mathrm{LH}} \gtrsim 1.2 - 1.3$ is likely necessary. Applying lower auxiliary heating for better performance in $Q_{\mathrm{fus}} = P_{\mathrm{fus}}/P_{\mathrm{aux}}$ reduces this tolerable $c_{\mathrm{w}}^{\mathrm{pt}}$ to $\leq 2 \times 10^{-5}$, whereas increasing the auxiliary heating in case of an increased W content can allow $c_{\mathrm{w}}^{\mathrm{pt}} \leq 8 \times 10^{-5}$. The limiting W concentrations at the separatrix are higher, since $n_{\mathrm{w}}^{\mathrm{sep}} \sim 7\, n_{\mathrm{w}}^{\mathrm{pt}}$ with our assumptions.

The total radiation increases proportionally to the plasma volume, and $V_{\mathrm{ITER}} \sim 65\, V_{\mathrm{AUG}}$. In contrast, the heating power is not scaled up as fast: the $\sim 150\,\mathrm{MW}$ (100 MW alpha and 50 MW auxiliary powers) in ITER are only 15 times the typical heating power in AUG of around 10 MW. This is why AUG can tolerate W concentrations $> 10^{-4}$, much higher than ITER.

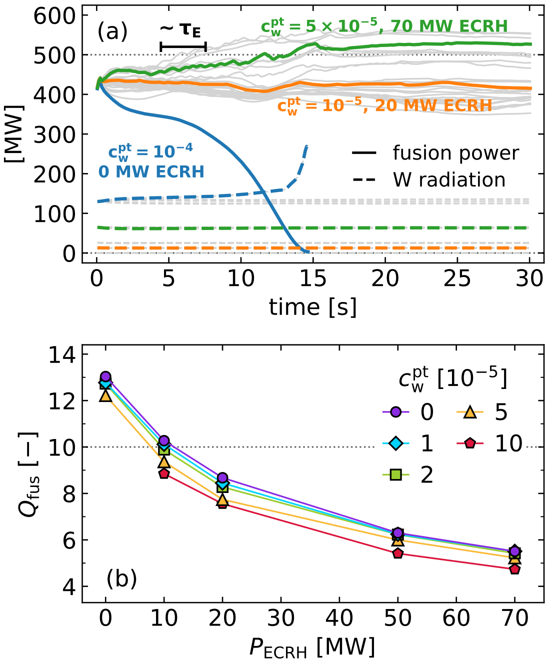

Figure 6.14: (a) Time traces of fusion power (solid) and tungsten radiated power (dashed). Three cases at different ECRH power and W concentrations are highlighted in colors; the other 22 simulations are shown in gray. (b) Fusion multiplication factor Q_{fus} as ECRH power increases, at different concentrations of W.

The fusion performance of these scenarios is shown in figure 6.14. In panel (a), time traces of the fusion power and W radiation are shown. We highlight 3 of the 25 simulations. Only one case out of 25 featured a radiative collapse, not caused by W accumulation, but rather by an increase in the cooling factor $L_{\mathrm{w}}(T_e)$ as T_e decreased due to the initially negative global power balance (highest $c_{\mathrm{w}}^{\mathrm{pt}}$ and $P_{\mathrm{ECRH}} = 0\,\mathrm{MW}$). Notice that a long simulation time is required to have quantities that are converged enough, considering the non-linearities of the system, particularly the coupling of alpha heating to the temperatures. Panel (b) shows the dependence of Q_{fus} on ECRH power and W concentration. Besides the obvious decrease of Q_{fus} when the auxiliary heating increases (as a consequence of stiff heat transport), we obtain a penalty of $\Delta Q_{\mathrm{fus}} \sim 1$ when the W concentration increases by a factor of 5.

At this conservative pedestal pressure and with the transport models employed, the target $Q_{\mathrm{fus}} = 10$ is obtained with 40 MW of auxiliary heating (30 MW of NBI + 10 MW of ECRH) at $c_{\mathrm{w}}^{\mathrm{pt}} \leq 2 \times 10^{-5}$ (with $P_{\mathrm{sep}}/P_{\mathrm{LH}} \geq 1.1$). This is promising since the adopted pedestal top pressure stays below the peeling-ballooning boundary by a margin of 20%, potentially fulfilling constraints of ELM-suppressed or ELM-mitigated operation. In these conditions our modelling assumptions lead to confinements below the IPB98(y,2) [30] and above the ITPA20-IL [262] scalings, in both cases by $\sim 15\%$. With $P_{\mathrm{aux}} = 50\,\mathrm{MW}$, Q_{fus} ranges between $\approx$ 9 for only Bremsstrahlung losses ($P_{\mathrm{brms}} \approx 16\,\mathrm{MW}$) and ≈ 8 at very high W concentrations.

Further reducing the auxiliary heating can allow access to $Q_{\mathrm{fus}} > 10$, provided that the combination of W concentration and ECRH power is such that the H-mode is sustained, as well as having a low-enough L–H threshold ($P_{\mathrm{LH}} \lesssim 70$ MW), in connection to figure 6.13.

6.4.4 Effect of a higher pedestal top pressure

To test the impact of the assumption on the pedestal top pressure (p_{pt}), an additional set of 10 simulations is carried out at the PB boundary prediction of EPED1, setting $p_{\mathrm{pt}} = 130$ kPa. For a low and a high pedestal top W concentration (10^{-5} and 5×10^{-5}), simulations at the same five ECRH powers are performed.

The resulting P_{sep} and Q_{fus} are shown as functions of P_{ECRH} in figure 6.15, with the new results at the higher pedestal top pressure plotted in red and the previous results from figures 6.13 and 6.14 in blue. The higher p_{pt} leads to a confinement factor of $H_{98} \approx 1.05$, while the predictions of the same TGLF transport model with a lower p_{pt} were $H_{98} \approx 0.85$. In panel (a), we see that the higher core confinement leads to a stronger alpha heating that provides a larger margin for H-mode sustainment, represented by the region above the black horizontal lines. These L-H power thresholds are calculated using the same scaling and assumptions as before.

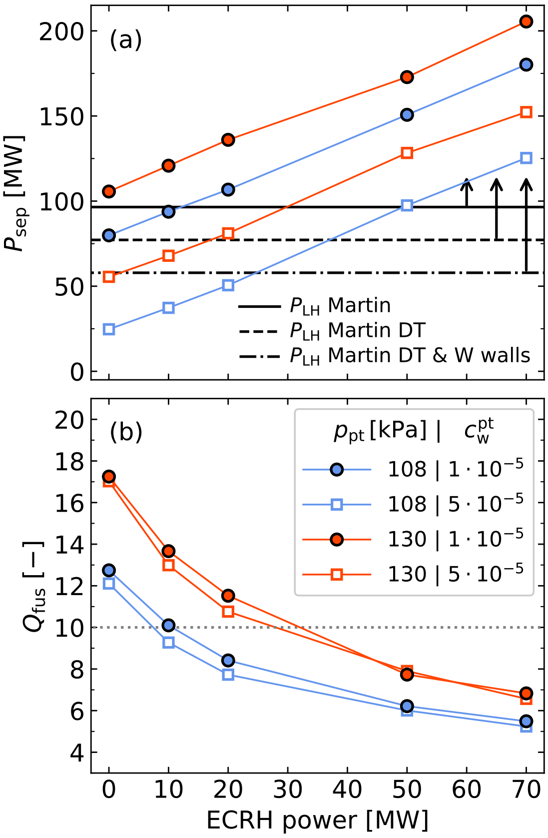

Figure 6.15: Comparison of ITER simulations with pedestal top pressure conservatively 20% below (blue) and at the PB limit from EPED1, as well as with intermediate (full symbols) and high (open) W concentrations. (a) Power crossing the separatrix, with different assumptions for the L-H power threshold in the horizontal lines, and (b) fusion power multiplication factor, as a function of the ECRH power.

The W concentration with 20 MW of ECRH and $p_{\mathrm{pt}} = 130$ kPa at which P_{sep} marginally exceeds the Martin P_{LH} with isotope effects (dashed line) is increased to $c_{\mathrm{w}}^{\mathrm{pt}} \sim 5 \times 10^{-5}$ (from $c_{\mathrm{w}}^{\mathrm{pt}} \sim 2 \times 10^{-5}$ at $p_{\mathrm{pt}} = 108$ kPa). If the W concentration remains closer to 10^{-5}, there is no problem with the sustainment of the H-mode even if the ECRH power is further reduced (shown in full circles). A reduction of P_{ECRH} increases Q_{fus}, as shown in panel (b). The confinement predicted by TGLF-SAT2 with the higher pedestal top pressure as boundary condition satisfies the ITER targets of $Q_{\mathrm{fus}} = 10$ and $P_{\mathrm{fus}} = 500$ MW, already at W concentrations at the pedestal top as high as 5×10^{-5}. The Q_{fus} target can even be exceeded by reducing the heating power, provided that the W concentration is not too high. This is consistent with recent non-linear gyrokinetic profile predictions [263] (which assumed a constant W concentration of 1.5×10^{-5}).

As in figure 6.11, all W density profiles throughout the 10 simulations were quite flat, due to a practically negligible neoclassical W transport. As already mentioned, turbulent transport does not have mechanisms leading to heavy impurity accumulation, and turbulent transport dominates for both diffusion and convection of W in the core of the ITER 15 MA scenario at $p_{\mathrm{pt}} = 108$ kPa and also at $p_{\mathrm{pt}} = 130$ kPa.

Chapter 7

Summary, conclusions and outlook

In this thesis, the transport and effects of impurities in tokamak plasmas were studied using an integrated modelling framework that was developed to be entirely based on theoretical transport models. The workflow was validated against experimental data in a variety of ASDEX Upgrade plasmas, and it was then applied to predict the behavior of impurities in ITER.

After a general introduction to fusion plasmas, the tokamak magnetic confinement concept and the effects of impurities in fusion devices in chapter 1, chapter 2 presented an overview of the most important theoretical elements of the transport of impurities in tokamak plasmas. The main results obtained during this thesis were presented in the subsequent chapters, and they are summarized as follows.

7.1 New version of FACIT that includes rotational effects at all collisionalitites

The behavior of the neoclassical transport of impurities across collisionality regimes and radial positions at increasing levels of rotation was investigated and modelled analytically in chapter 3. A comprehensive database of drift-kinetic calculations with the NEO code, composed of scans in rotation, collisionality and trapped particle fraction ranging between extreme values reachable by present-day and future devices, was constructed both to analyze these effects and to obtain a new version of the fast and accurate collisional impurity transport model (FACIT) which also describes the impact of rotation at all collisionalities.

We showed that the rotation-collisionality parameter space is divided into regions of favorable and unfavorable effects on the neoclassical temperature screening. The sign and intensity of the effects depend on the trapped particle fraction.

Experiments with significantly different values of rotation and collisionality were analyzed within this context. The favorable rotation regime becomes particularly attractive for high-power, low-density operation of present-day devices. Slowly rotating plasmas, or tokamaks operating at high density or low power, instead enter the unfavorable regime where rotation suppresses and even reverses the temperature screening, leading to a more inward flux. The expected rotation levels in ITER are small, so ITER is not predicted to significantly either profit from or be negatively affected by rotational effects on neoclassical impurity transport.

A drift-kinetic code like NEO is not well suited for applications with low computational time demands. With this in mind, we introduced an analytical model that includes the effects of rotation on neoclassical impurity transport at arbitrary collisionality and trapped particle fraction, which is now included in the FACIT code. This model was constructed through a novel approach to extract the physically-distinct banana-plateau and Pfirsch-Schlüter components from the NEO output flux, and by introducing a set of fitted factors to ensure close agreement with NEO.

Being analytical, the extended FACIT model is well suited for fast applications. It was shown to be accurate with respect to the more complete NEO code across a broad parameter space, and to be able to reproduce radial profiles of the transport coefficients computed with NEO using experimental plasma profiles.

The added feature of describing the banana-plateau and Pfirsch–Schlüter components individually provides a more complete physical understanding of the effects of rotation. As a notable example, it allowed us to identify the enhancement of the temperature screening as a banana-plateau effect. Overall, including the influence of rotation for both Pfirsch–Schlüter and banana-plateau transport was shown to be crucial for the neoclassical modelling of heavy impurities in rotating plasmas.

7.2 Integrated modelling framework with impurities and radiation

A modelling workflow that integrates the transport and radiation of impurities into the evolution of the main plasma profiles and magnetic equilibrium was developed and tested in chapter 4. The central element for developing the workflow was the coupling of the impurity transport code STRAHL to the ASTRA modelling suite.

After verifying that the ionization/recombination-dominated and transport-dominated limits of the charge state distribution of impurities are correctly recovered, the necessity of splitting the impurity flux into diffusive and convective coefficients for the correct modelling of impurities in STRAHL was demonstrated. This splitting increases the computational cost of the transport calculations, so different methods were tested, benchmarked, and an optimum was selected.

The impurity transport coefficients are calculated with the FACIT model, as described in chapter 3, for the neoclassical components and with the TGLF-SAT2 quasi-linear model for the turbulent components. A validation of the TGLF predictions for impurity transport against an ASDEX Upgrade database of boron density measurements was also provided in chapter 4.

The modelling workflow was then described in detail, including the models and assumptions employed for the main plasma species. The implementation of two particular effects was described: the treatment of the radial electric field (which is crucial for the correct description of transport at the periphery), and the inclusion of centrifugal effects on the turbulent transport coefficients of heavy impurities. Finally, the workflow was summarized in a single comprehensive schematic diagram.

7.3 Full-radius simulations of AUG L-mode plasmas

Employing the workflow introduced in chapter 4, results of full-radius (meaning, from the magnetic axis to the separatrix) integrated modelling of ASDEX Upgrade L-mode experiments were presented in chapter 5.

Particular emphasis was placed on the transport of multiple impurity species and their effects on the main plasma through radiative cooling and dilution of the main ions. The quasi-linear turbulent transport model TGLF-SAT2 was applied up to the separatrix to obtain impurity transport coefficients for the first time.

A set of six L-modes, including intrinsic boron and tungsten impurities in the plasma, was simulated to test the predictions of the workflow against experimental profiles under differing plasma currents and heating power mixtures. Important effects, such as the increase of confinement with plasma current and the reduction of core tungsten peaking with central ECRH, were reproduced in the modelling.

Furthermore, a radiative L-mode scenario with high confinement and no edge localized mode activity was modelled in close agreement to multiple diagnostics measuring the main plasma profiles, impurity densities and radiation. The effect of ion temperature gradient (ITG) turbulence stabilization due to impurity dilution of the main ions was confirmed to play a significant role on the enhanced confinement of this experiment. A simple X-point radiator model was applied to account for highly localized radiation at the edge. Finally, the radial electric field treatment of [186] proved sufficient to reproduce experimental profiles in the H-mode phase of this particular discharge, giving hope to future applications of edge transport modelling with quasi-linear models in H-mode.

7.4 Control of W accumulation with central wave heating in NBI-heated AUG H-mode plasmas

In chapter 6, we demonstrated that the integrated modelling framework is also capable to reproduce the reduction of core tungsten peaking in ASDEX Upgrade H-mode plasmas when central wave heating is applied, which is a routine experimental technique for the operation of neutral-beam-heated tokamaks. Dynamical simulations of four ASDEX Upgrade discharges, two with electron cyclotron resonance heating and two with ion cyclotron resonance heating descending power steps, were performed from the start of the current flattop phase all the way to the radiative collapse of each discharge. Quantitative agreement was obtained between the simulations and multiple diagnostics measuring the evolution of the main plasma temperatures and density profiles, tungsten density peaking, and radiated power. The self-consistent evolution of multiple transport channels was an essential element in order to recover these effects, because the tungsten transport is strongly coupled to the main plasma profiles and the main plasma profiles are affected by the impurity radiation losses.

The physics behind the control of high-Z impurity accumulation with central wave heating was analyzed, thanks to the availability of turbulent and neoclassical impurity transport diffusive and convective coefficients from the TGLF-SAT2 and FACIT models. It was demonstrated that they predict an increased (mostly turbulent) diffusivity and decreased (mostly neoclassical) pinch of tungsten with higher wave heating power, contributing to a strong reduction of central tungsten peaking in ASDEX Upgrade.

Finally, it was shown that TGLF-SAT2 is able to reproduce the non-monotonic dependence of the ratio of the turbulent tungsten diffusivity to the main ion heat diffusivity on the local electron-to-ion heat flux ratio that was found with non-linear gyrokinetic calculations in the past. This ratio of diffusivities characterizes how efficiently the enhancement in core turbulence by wave heating flattens the impurity density (which is desired) compared to how fast it removes energy from the plasma core (which is not). The fact that TGLF-SAT2 captures its behavior is a convincing verification of this quasi-linear model.

7.5 Predictions of tungsten transport in ITER

Having validated the modelling framework against experimental data from ASDEX Upgrade L-mode (chapter 5) and H-mode (chapter 6) plasmas, in section 6.4 we turned our attention to simulations of the ITER 15 MA baseline scenario with particular interest on tungsten transport.

The theory-based transport models we applied reproduced the expectation that the core of ITER at full power and current is in a different transport regime for tungsten as compared to present-day tokamaks. Since the collisionality is much lower (and the expected toroidal rotation is also not very large), the core neoclassical pinch of high-Z impurities is small and the convection, like the diffusion, is completely turbulent. The resulting tungsten density profiles are all quite flat, since turbulent heavy impurity transport lacks mechanisms of strong central accumulation, in contrast to neoclassical impurity transport. A consequence of this is that the tungsten profile shapes in ITER, and therefore the total radiated power, are predicted to be practically unaffected by electron cyclotron resonance heating, in stark contrast to the situation in present-day tokamaks like ASDEX Upgrade.

The tolerable tungsten concentration is limited not because of a local negative power balance in the center, but by the total radiated power losses that would not allow the power crossing the separatrix to sustain operation in the high confinement regime (H-mode). Applying higher auxiliary heating powers allows the plasma to tolerate higher tungsten contents, by keeping the excess heat in the global power balance above the L-H threshold. However, a higher auxiliary heating reduces the fusion power multiplication factor. On the other hand, lower auxiliary heating can be applied in order to obtain a higher fusion gain, depending on the power required to sustain the H-mode at given tungsten radiative losses. These conclusions can be directly expected to apply to DEMO-type machines.

Simulations at a higher pedestal top pressure complemented those at the more conservative value that was chosen as a proxy for edge localized mode suppressed or mitigated operation. The increased confinement associated with the higher pressure boundary condition led to a limiting pedestal top tungsten concentration for H-mode sustainment that is more than twice higher (5×10^{-5} vs 2×10^{-5}), due to the stronger core alpha heating. Furthermore, with a pedestal pressure at the peeling-ballooning boundary, the models and assumptions employed in section 6.4 predicted a comfortable achievement of the ITER $Q_{\mathrm{fus}} = 10$ objective.

The application of theory-based models allowed us to perform a first-of-its-kind analysis of the interplay between tungsten transport, required electron cyclotron heating power and fusion performance in ITER with integrated modelling. The prior validation against experimental data provided confidence in the physics understanding of tungsten transport for extrapolation to ITER. The self-consistent evolution of main plasma and impurities helped us further understand the operational space of ITER, in particular in view of its newly-proposed full-tungsten walls.

7.6 Future work

The work reported in this thesis has extended and validated the predictive capabilities of integrated modelling of tokamak plasmas through the coupled evolution of the densities of multiple impurity species and their feedback on the main plasma via radiative cooling and main ion dilution.

Further work can strengthen the confidence on the predictions of the modelling workflow by expanding the validation against experimental data to other machines beyond ASDEX Upgrade. Of particular interest for the extrapolations to ITER (and beyond, to DEMO-class reactors) are tokamaks larger than the medium-sized ASDEX Upgrade, such as JT-60SA [264] and JET. A sufficient diagnostic coverage, not only in terms of main plasma profile measurements but also of impurity densities and radiated powers, is necessary to cross-validate the multiple simulated transport channels (as it was done in this thesis).

Some elements of the framework that could be further developed are:

- the inclusion of momentum transport modelling, which would provide a self-consistent prediction of the toroidal rotation. The experimental rotation profiles have been prescribed, considering the difficulty of predicting momentum transport, particularly in the presence of low beam torque (the extrinsic source of momentum) or strong wave heating, and the high sensitivity of heavy impurity transport to rotation. The present approach enables an impurity transport validation which is de-coupled from the high uncertainties in predicting the plasma rotation. Recent reduced models for momentum transport [265, 266] could be applied in the future.

- The choice of the edge impurity sources, which are currently ad-hoc inputs used to approach expected radiated powers and effective charges. An accurate description of sources requires sophisticated plasma-wall interaction [267–270] and scrape-off layer transport [271] modelling capabilities beyond the scope of this thesis. Efforts in integrated wall erosion and scrape-off layer transport modelling have recently begun in the community [272, 273], but the computational cost of this type of simulations remains high.

- A more sophisticated treatment of magnetohydrodynamic transients, with particular emphasis on the effects on impurities, such as the hollowing of the central tungsten density due to sawtooth relaxations in the core and the flushing of impurities due to edge localized modes.

- A model to accurately predict the neutral density profile at the edge. This is necessary in order to include missing physics like the effect of charge exchange reactions on the peripheral impurity distribution and radiation [274]. The ionization electron source from partially stripped impurities could also be included by updating the STRAHL coupling to ASTRA.

- Improvements to the model to account for the peripheral X-point radiation in ASTRA. While this additional radiation was introduced retroactively for the discharge under consideration (that is, knowing that the X-point radiator was present by evaluating the experimental data), the access condition to the X-point radiator regime of [232] could be implemented in subsequent integrated modelling applications to consistently trigger the use of the model.

There is a need to further validate the treatment of multi-impurity collisions in FACIT against NEO, possibly extending parts of the model to better reproduce the drift-kinetic results. A precise description of multi-impurity effects with toroidal rotation still requires the use of NEO, which carries significant consequences on the computational time of the integrated modelling framework (at least doubling it).

A purely neoclassical tungsten pedestal in ITER is likely too optimistic, and small values of the turbulent diffusivity already modify its pedestal profile. Further studies on pedestal turbulent impurity transport are necessary to more realistically assess which reduction of tungsten density can be sustained by the neoclassical outward convection from the separatrix to the pedestal top.

Finally, a clear objective for future work is to extend the applicability of the framework to full-radius simulations of impurity seeded H-mode plasmas. This could be done by including a description of impurities in the IMEP workflow [183, 184]. Three key elements to be addressed, moving from full-radius L-mode to H-mode simulations, are the estimation of turbulent impurity transport coefficients in the pedestal, the impact of impurities on the scrape-off layer model that provides boundary conditions at the separatrix in IMEP, and effects of high impurity content and radiation on the pedestal magnetohydrodynamic stability. This would enable a validation against, for example, JET data from discharges with both neon seeding and D-T fuel, performed during DTE3 (JET's most recent and final experimental campaign), and integrated modelling predictions of ITER plasmas including not only tungsten but also the planned neon seeding for power exhaust.

Bibliography

[1] Bosch H. S. *et al.* “Improved formulas for fusion cross–sections and thermal reactivities”, *Nuclear Fusion* **32**(4) 611–631 (1992).

[2] Giancarli L. *et al.* “Breeding Blanket Modules testing in ITER: An international program on the way to DEMO”, *Fusion Engineering and Design* **81**(1-7) 393–405 (2006).

[3] Glugla M. *et al.* “The ITER tritium systems”, *Fusion Engineering and Design* **82**(5-14) 472–487 (2007).

[4] Pearson R. J. *et al.* “Tritium supply and use: a key issue for the development of nuclear fusion energy”, *Fusion Engineering and Design* **136** 1140–1148 (2018).

[5] JET Team. “Fusion energy production from a deuterium-tritium plasma in the JET tokamak”, *Nuclear Fusion* **32**(2) 187–203 (1992).

[6] Strachan J. D. *et al.* “Deuterium and tritium experiments on TFTR”, *Plasma Physics and Controlled Fusion* **36**(12B) B3–B15 (1994).

[7] Gibson A. *et al.* “Deuterium–tritium plasmas in the Joint European Torus (JET): Behavior and implications”, *Physics of Plasmas* **5**(5) 1839–1847 (1998).

[8] Maggi C. *et al.* “Overview of T and D–T results in JET with ITER-like wall”, *Nuclear Fusion* **64**(11) 112012 (2024).

[9] Stroth U. “Plasmaphysik – Phänomene, Grundlagen und Anwendungen”, 3rd ed. *Springer Berlin Heidelberg*, ISBN: 978-3-662-55236-0 (2018).

[10] Loarte A. *et al.* “Correlation of type–I ELM energy losses with pedestal plasma characteristics and global discharge parameters in JET ELMy H–modes”, *P-1.96* 30th EPS Conference on Plasma Physics (2003).

[11] Snipes J. A. *et al.* “Plasma stored energy and momentum losses during large MHD activity in JET”, *Nuclear Fusion* **30**(2) 205–218 (1990).

[12] Freidberg J. P. “Plasma Physics and Fusion Energy”, 1st ed. *Cambridge University Press*, ISBN: 978-0-511-27375-9 (2007).

[13] Wurzel S. E. *et al.* “Progress toward fusion energy breakeven and gain as measured against the Lawson criterion”, *Physics of Plasmas* **29**(6) 062103 (2022).

[14] Keilhacker M. *et al.* “High fusion performance from deuterium-tritium plasmas in JET”, *Nuclear Fusion* **39**(2) 209–234 (1999).

[15] Abu-Shawareb H. “Achievement of target gain larger than unity in an inertial fusion experiment”, *Physical Review Letters* **132**(6) 065102 (2024).

[16] Hurricane O. *et al.* “Energy principles of scientific breakeven in an inertial fusion experiment”, *Physical Review Letters* **132**(6) 065103 (2024).

[17] UKAEA (2024) “JET’s final tritium experiments yield new fusion energy record”.

[18] ITER Organization. “ITER Research Plan within the Staged Approach”. Tech. rep. Reference: ITR-18-003 (2018).

[19] Rodriguez-Fernandez P. *et al.* “Overview of the SPARC physics basis towards the exploration of burning–plasma regimes in high–field, compact tokamaks”, *Nuclear Fusion* **62**(4) 042003 (2022).

[20] Wesson J. “Tokamaks”, 4th ed. *Oxford University Press*, ISBN: 978-0-199-59223-4 (2011).

[21] Bock A. *et al.* “Non-inductive improved H-mode operation at ASDEX Upgrade”, *Nuclear Fusion* **57**(12) 126041 (2017).

[22] Peeters A. G. “The bootstrap current and its consequences”, *Plasma Physics and Controlled Fusion* **42**(12B) B231 (2000).

[23] Evans T. E. *et al.* “Suppression of large Edge-Localized Modes in high-confinement DIII-D plasmas with a stochastic magnetic boundary”, *Physical Review Letters* **92**(23) 235003 (2004).

[24] D’haeseleer W. D. *et al.* “Flux Coordinates and Magnetic Field Structure - A Guide to a Fundamental Tool of Plasma Theory”, 1st ed. *Springer Berlin Heidelberg*, ISBN: 978-3-642-75595-8 (1991).

[25] Zohm H. “Magnetohydrodynamic Stability of Tokamaks”, 1st ed. *Wiley-VCH*, ISBN: 978-3-527-67736-8 (2014).

[26] Stangeby P. C. “The plasma boundary of magnetic fusion devices”, 1st ed. *IOP Publishing*, ISBN: 978-0-367-80148-9 (2000).

[27] Wagner F. *et al.* “Regime of improved confinement and high beta in neutral-beam-heated divertor discharges of the ASDEX tokamak”, *Physical Review Letters* **49**(19) 1408–1412 (1982).

[28] Wagner F. *et al.* “Development of an edge transport barrier at the H–mode transition of ASDEX”, *Physical Review Letters* **53**(15) 1453–1456 (1984).

[29] Connor J. W. *et al.* “A review of theories of the L–H transition”, *Plasma Physics and Controlled Fusion* **42**(1) R1–R74 (1999).

[30] ITER Physics Expert Group on Confinement and Transport *et al.* “Chapter 2: Plasma confinement and transport”, *Nuclear Fusion* **39**(12) 2175–2249 (1999).

[31] Neu R. *et al.* “Preparing the scientific basis for an all metal ITER”, *Plasma Physics and Controlled Fusion* **53**(12) 124040 (2011).

[32] Neu R. *et al.* “Overview on plasma operation with a full tungsten wall in ASDEX Upgrade”, *Journal of Nuclear Materials* **438** S34–S41 (2013).

[33] Pütterich T. *et al.* “Calculation and experimental test of the cooling factor of tungsten”, *Nuclear Fusion* **50**(2) 025012 (2010).

[34] Morozov D. K. *et al.* “Impurity radiation from a tokamak plasma”, *Plasma Physics Reports* **33**(11) 906–922 (2007).

[35] Greenwald M. *et al.* “A new look at density limits in tokamaks”, *Nuclear Fusion* **28**(12) 2199–2207 (1988).

[36] Hogeweij G. M. D. *et al.* “Impact of W on scenario simulations for ITER”, *Nuclear Fusion* **55**(6) 063031 (2015).

[37] Pütterich T. *et al.* “Determination of the tolerable impurity concentrations in a fusion reactor using a consistent set of cooling factors”, *Nuclear Fusion* **59**(5) 056013 (2019).

[38] Mavrin A. A. “Effect of impurity radiation and helium particle confinement on tokamak–reactor plasma performance”, *Plasma Physics and Controlled Fusion* **62**(10) 105023 (2020).

[39] Kallenbach A. *et al.* “Impurity seeding for tokamak power exhaust: from present devices via ITER to DEMO”, *Plasma Physics and Controlled Fusion* **55**(12) 124041 (2013).

[40] Bernert M. *et al.* “Power exhaust by SOL and pedestal radiation at ASDEX Upgrade and JET”, *Nuclear Materials and Energy* **12** 111–118 (2017).

[41] Neuwirth D. *et al.* “Formation of ammonia during nitrogen-seeded discharges at ASDEX Upgrade”, *Plasma Physics and Controlled Fusion* **54**(8) 085008 (2012).

[42] Oberkofler M. *et al.* “First nitrogen-seeding experiments in JET with the ITER-like wall”, *Journal of Nuclear Materials* **438** S258–S261 (2013).

[43] Drenik A. *et al.* “Evolution of nitrogen concentration and ammonia production in N_2-seeded H-mode discharges at ASDEX Upgrade”, *Nuclear Fusion* **59**(4) 046010 (2019).

[44] Polevoi A. *et al.* “Analysis of fuelling requirements in ITER H-modes with SOLPS-EPED1 derived scalings”, *Nuclear Fusion* **57**(2) 022014 (2016).

[45] Zohm H. *et al.* “On the physics guidelines for a tokamak DEMO”, *Nuclear Fusion* **53**(7) 073019 (2013).

[46] Loarte A. *et al.* "High confinement/high radiated power H-mode experiments in Alcator C-Mod and consequences for International Thermonuclear Experimental Reactor (ITER) Q=10 operation", *Physics of Plasmas* **18**(5) (2011).

[47] Bernert M. *et al.* "X–point radiation, its control and an ELM suppressed radiating regime at the ASDEX Upgrade tokamak", *Nuclear Fusion* **61**(2) 024001 (2020).

[48] Fable E. *et al.* "High-confinement radiative L-modes in ASDEX Upgrade", *Nuclear Fusion* **62**(2) 024001 (2021).

[49] Frank S. *et al.* "Radiative pulsed L-mode operation in ARC-class reactors", *Nuclear Fusion* **62**(12) 126036 (2022).

[50] Lunt T. *et al.* "Compact radiative divertor experiments at ASDEX Upgrade and their consequences for a reactor", *Physical Review Letters* **130**(14) 145102 (2023).

[51] Dominguez R. *et al.* "Impurity effects on drift wave stability and impurity transport", *Nuclear Fusion* **33**(1) 51–62 (1993).

[52] Hill K. W. *et al.* "Tests of local transport theory and reduced wall impurity influx with highly radiative plasmas in the Tokamak Fusion Test Reactor", *Physics of Plasmas* **6**(3) 877–884 (1999).

[53] Tokar M. Z. *et al.* "Model for the transition to the radiatively improved mode in a tokamak", *Physical Review Letters* **84**(5) 895–898 (2000).

[54] McKee G. *et al.* "Impurity-induced suppression of core turbulence and transport in the DIII-D tokamak", *Physical Review Letters* **84**(9) 1922–1925 (2000).

[55] Pusztai I. *et al.* "Turbulent transport of impurities and their effect on energy confinement", *Plasma Physics and Controlled Fusion* **55**(7) 074012 (2013).

[56] Hughes J. W. *et al.* "Power requirements for superior H–mode confinement on Alcator C–mod: experiments in support of ITER", *Nuclear Fusion* **51**(8) 083007 (2011).

[57] Giroud C. *et al.* "Impact of nitrogen seeding on confinement and power load control of a high–triangularity JET ELMy H–mode plasma with a metal wall", *Nuclear Fusion* **53**(11) 113025 (2013).

[58] Urano H. *et al.* "Roles of argon seeding in energy confinement and pedestal structure in JT–60U", *Nuclear Fusion* **55**(3) 033010 (2015).

[59] Wolfrum E. *et al.* "Impact of wall materials and seeding gases on the pedestal and on core plasma performance", *Nuclear Materials and Energy* **12** 18–27 (2017).

[60] Wang H. Q. *et al.* "Effects of low–Z and high–Z impurities on divertor detachment and plasma confinement", *Nuclear Materials and Energy* **12** 942–947 (2017).

[61] Schweinzer J. *et al.* “Confinement of ‘improved H–modes’ in the all-tungsten ASDEX Upgrade with nitrogen seeding”, *Nuclear Fusion* **51**(11) 113003 (2011).

[62] Beurskens M. N. A. *et al.* “The effect of a metal wall on confinement in JET and ASDEX Upgrade”, *Plasma Physics and Controlled Fusion* **55**(12) 124043 (2013).

[63] Schuller F. C. “Disruptions in tokamaks”, *Plasma Physics and Controlled Fusion* **37**(11A) A135–A162 (1995).

[64] Boozer A. H. “Theory of tokamak disruptions”, *Physics of Plasmas* **19**(5) 058101 (2012).

[65] Whyte D. G. *et al.* “Mitigation of tokamak disruptions using high-pressure gas injection”, *Physical Review Letters* **89**(5) 055001 (2002).

[66] Hollmann E. M. *et al.* “Status of research toward the ITER disruption mitigation system”, *Physics of Plasmas* **22**(2) 021802 (2014).

[67] Lehnen M. *et al.* “Disruptions in ITER and strategies for their control and mitigation”, *Journal of Nuclear Materials* **463** 39–48 (2015).

[68] Fonck R. J. *et al.* “Determination of plasma-ion velocity distribution via charge-exchange recombination spectroscopy”, *Physical Review A* **29**(6) 3288–3309 (1984).

[69] Viezzer E. *et al.* “High–resolution charge exchange measurements at ASDEX Upgrade”, *Review of Scientific Instruments* **83**(10) 103501 (2012).

[70] McDermott R. M. *et al.* “Extensions to the charge exchange recombination spectroscopy diagnostic suite at ASDEX Upgrade”, *Review of Scientific Instruments* **88**(7) 073508 (2017).

[71] McDermott R. M. *et al.* “Evaluation of impurity densities from charge exchange recombination spectroscopy measurements at ASDEX Upgrade”, *Plasma Physics and Controlled Fusion* **60**(9) 095007 (2018).

[72] Janev R. *et al.* “Penetration of energetic neutral beams into fusion plasmas”, *Nuclear Fusion* **29**(12) 2125–2140 (1989).

[73] Koch R. *et al.* “Fast particle heating”, *Fusion Science and Technology* **57**(2T) 185–195 (2010).

[74] Lin-Liu Y. R. *et al.* “Trapped electron correction to beam driven current in general tokamak equilibria”, *Physics of Plasmas* **4**(11) 4179–4181 (1997).

[75] Douai D. *et al.* “Wall conditioning of JET with the ITER-Like Wall”, *Journal of Nuclear Materials* **438** S1172–S1176 (2013).

[76] Lunsford R. *et al.* “Active conditioning of ASDEX Upgrade tungsten plasma-facing components and discharge enhancement through boron and boron nitride particulate injection”, *Nuclear Fusion* **59**(12) 126034 (2019).

[77] Poli F. M. “Integrated tokamak modeling: When physics informs engineering and research planning”, *Physics of Plasmas* **25**(5) 055602 (2018).

[78] Pereverzev G. V. *et al.* “ASTRA: Automated System for TRansport Analysis”. Tech. rep. Max-Planck-Institut für Plasmaphysik, Garching bei München, Germany. Reference: IPP 5/98 (2002).

[79] Fable E. *et al.* “Novel free-boundary equilibrium and transport solver with theory-based models and its validation against ASDEX Upgrade current ramp scenarios”, *Plasma Physics and Controlled Fusion* **55**(12) 124028 (1998).

[80] Ivanov A. A. *et al* “New adaptive grid plasma evolution code SPIDER”, *P-5.063* 32nd EPS Conference on Plasma Physics, Tarragona, Spain (2005).

[81] Fable E. *et al.* “FEQIS: A new equilibrium solver for the Fenix flight simulator”, *P-1a.102* 48th EPS Conference on Plasma Physics (2022).

[82] James D. “The thermal diffusivity of ice and water between -40 and +60 C”, *Journal of Materials Science* **3**(5) 540–543 (1968).

[83] Staebler G. *et al.* “Advances in prediction of tokamak experiments with theory-based models”, *Nuclear Fusion* **62**(4) 042005 (2022).

[84] Helander P. *et al.* “Collisional Transport in Magnetized Plasmas”, 1st ed. *Cambridge University Press*, ISBN: 978-0-521-80798-2 (2002).

[85] Belli E. A. *et al.* “Kinetic calculation of neoclassical transport including self-consistent electron and impurity dynamics”, *Plasma Physics and Controlled Fusion* **50**(9) 095010 (2008).

[86] Connor J. “The neoclassical transport theory of a plasma with multiple ion species”, *Plasma Physics* **15**(8) 765–782 (1973).

[87] Hirshman S. *et al.* “Approximate Fokker-Planck collision operator for transport theory applications”, *Physics of Fluids* **19**(10) 1532 (1976).

[88] Belli E. A. *et al.* “Full linearized Fokker-Planck collisions in neoclassical transport simulations”, *Plasma Physics and Controlled Fusion* **54**(1) 015015 (2011).

[89] Reinke M. L. “Experimental tests of parallel impurity transport theory in tokamak plasmas”. Ph.D. thesis, *Massachussetts Institute of Technology* (2011).

[90] Odstrčil T. “On the origin, properties, and implications of asymmetries in the tungsten impurity density in tokamak plasmas”. Ph.D. thesis, *Technische Universität München* (2017).

[91] Helander P. “Neoclassical transport in a rotating impure plasma”, *Physics of Plasmas* **5**(4) 1209–1211 (1998).

[92] Helander P. “Bifurcated neoclassical particle transport”, *Physics of Plasmas* **5**(11) 3999–4004 (1998).

[93] Fülöp T. *et al.* "Nonlinear neoclassical transport in a rotating impure plasma with large gradients", *Physics of Plasmas* **6**(8) 3066–3075 (1999).

[94] Fülöp T. *et al.* "Nonlinear neoclassical transport in toroidal edge plasmas", *Physics of Plasmas* **8**(7) 3305–3313 (2001).

[95] Maget P. *et al.* "Natural poloidal asymmetry and neoclassical transport of impurities in tokamak plasmas", *Plasma Physics and Controlled Fusion* **62**(2) 025001 (2019).

[96] Wesson J. "Poloidal distribution of impurities in a rotating tokamak plasma", *Nuclear Fusion* **37**(5) 577–581 (1997).

[97] Lee S. G. *et al.* "Toroidal rotation and momentum transport studies in KSTAR", *P4.143* 42nd EPS Conference on Plasma Physics (2015).

[98] Singh M. J. *et al.* "Heating neutral beams for ITER: negative ion sources to tune fusion plasmas", *New Journal of Physics* **19**(5) 055004 (2017).

[99] Chrystal C. *et al.* "Predicting the rotation profile in ITER", *Nuclear Fusion* **60**(3) 036003 (2020).

[100] Reinke M. L. *et al.* "Poloidal variation of high–Z impurity density due to hydrogen minority ion cyclotron resonance heating on Alcator C–Mod", *Plasma Physics and Controlled Fusion* **54**(4) 045004 (2012).

[101] Kazakov Y. O. *et al.* "Poloidal asymmetries due to ion cyclotron resonance heating", *Plasma Physics and Controlled Fusion* **54**(10) 105010 (2012).

[102] Bilato R. *et al.* "Modelling the influence of temperature anisotropies on poloidal asymmetries of density in the core of rotating plasmas", *Nuclear Fusion* **54**(7) 072003 (2014).

[103] Bilato R. *et al.* "The impact of the ion-cyclotron-resonance location on the poloidal asymmetries of impurity density in an ICRF-heated rotating plasma", *Nuclear Fusion* **57**(5) 056020 (2017).

[104] Odstrčil T. *et al.* "The physics of W transport illuminated by recent progress in W density diagnostics at ASDEX Upgrade", *Plasma Physics and Controlled Fusion* **60**(1) 014003 (2017).

[105] EFDA - currently EUROfusion (2013) "From doughnuts to bananas".

[106] Hinton F. *et al.* "Theory of plasma transport in toroidal confinement systems", *Reviews of Modern Physics* **48**(2) 239–308 (1976).

[107] Hirshman S. *et al.* "Neoclassical transport of impurities in tokamak plasmas", *Nuclear Fusion* **21**(9) 1079–1201 (1981).

[108] Wenzel K. *et al.* "Neoclassical analysis of impurity transport following transition to improved particle confinement", *Nuclear Fusion* **30**(6) 1117–1127 (1990).

[109] Fajardo D. *et al.* “Analytical model for collisional impurity transport in tokamaks at arbitrary collisionality”, *Plasma Physics and Controlled Fusion* **64**(5) 055017 (2022).

[110] Fajardo D. *et al.* “Analytical model for the combined effects of rotation and collisionality on neoclassical impurity transport”, *Plasma Physics and Controlled Fusion* **65**(3) 035021 (2023).

[111] Hinton F. L. *et al.* “Neoclassical ion transport in rotating axisymmetric plasmas”, *Physics of Fluids* **28**(10) 3082 (1985).

[112] Stacey W. M. *et al.* “Rotation and impurity transport in a tokamak plasma with directed neutral–beam injection”, *Nuclear Fusion* **25**(4) 463–477 (1985).

[113] Wong S. K. “Transport of impure plasma with arbitrary toroidal rotation”, *Physics of Fluids* **30**(3) 818 (1987).

[114] Feneberg W. “Neoclassical impurity transport in the presence of toroidal and poloidal rotation”, *Nuclear Fusion* **29**(7) 1117–1124 (1989).

[115] Romanelli M. *et al.* “Effects of density asymmetries on heavy impurity transport in a rotating tokamak plasma”, *Plasma Physics and Controlled Fusion* **40**(10) 1767–1773 (1998).

[116] Angioni C. *et al.* “Neoclassical transport of heavy impurities with poloidally asymmetric density distribution in tokamaks”, *Plasma Physics and Controlled Fusion* **56**(12) 124001 (2014).

[117] Belli E. A. *et al.* “Pfirsch–Schlüter neoclassical heavy impurity transport in a rotating plasma”, *Plasma Physics and Controlled Fusion* **56**(12) 124002 (2014).

[118] Maget P. *et al.* “An analytic model for the collisional transport and poloidal asymmetry distribution of impurities in tokamak plasmas”, *Plasma Physics and Controlled Fusion* **62**(10) 105001 (2020).

[119] Diamond P. H. *et al.* “Zonal flows in plasma—a review”, *Plasma Physics and Controlled Fusion* **47**(5) R35–R161 (2005).

[120] Fülöp T. *et al.* “Turbulent and neoclassical impurity transport in tokamak plasmas”, *Physics of Plasmas* **16**(3) (2009).

[121] Angioni C. *et al.* “The impact of poloidal asymmetries on tungsten transport in the core of JET H-mode plasmas”, *Physics of Plasmas* **22**(5) 055902 (2015).

[122] Angioni C. *et al.* “Direction of impurity pinch and auxiliary heating in tokamak plasmas”, *Physical Review Letters* **96**(9) 095003 (2006).

[123] Camenen Y. *et al.* “Impact of the background toroidal rotation on particle and heat turbulent transport in tokamak plasmas”, *Physics of Plasmas* **16**(1) 012503 (2009).

[124] Fülöp T. *et al.* "Impurity transport in ITER-like plasmas", *Physics of Plasmas* **13**(11) (2006).

[125] Fülöp T. *et al.* "Impurity transport driven by ion temperature gradient turbulence in tokamak plasmas", *Physics of Plasmas* **17**(6) (2010).

[126] Angioni C. "Impurity transport in tokamak plasmas, theory, modelling and comparison with experiments", *Plasma Physics and Controlled Fusion* **63**(7) 073001 (2021).

[127] Angioni C. *et al.* "Gyrokinetic study of turbulent convection of heavy impurities in tokamak plasmas at comparable ion and electron heat fluxes", *Nuclear Fusion* **57**(2) 022009 (2017).

[128] Waltz R. E. *et al.* "Gyrokinetic simulation tests of quasilinear and tracer transport", *Physics of Plasmas* **16**(7) (2009).

[129] Staebler G. *et al.* "Gyro-Landau fluid equations for trapped and passing particles", *Physics of Plasmas* **12**(10) 102508 (2005).

[130] Staebler G. M. *et al.* "A theory-based transport model with comprehensive physics", *Physics of Plasmas* **14**(5) 055909 (2007).

[131] Staebler G. M. *et al.* "Verification of a quasi-linear model for gyrokinetic turbulent transport", *Nuclear Fusion* **61**(11) 116007 (2021).

[132] Waltz R. *et al.* "A gyro-Landau-fluid transport model", *Physics of Plasmas* **4**(7) 2482–2496 (1997).

[133] Candy J. *et al.* "An Eulerian gyrokinetic-Maxwell solver", *Journal of Computational Physics* **186**(2) 545–581 (2003).

[134] Candy J. *et al.* "A high-accuracy Eulerian gyrokinetic solver for collisional plasmas", *Journal of Computational Physics* **324** 73–93 (2016).

[135] Romanelli M. *et al.* "JINTRAC: A system of codes for integrated simulation of tokamak scenarios", *Plasma and Fusion Research* **9**(0) 3403023–3403023 (2014).

[136] Belli E. A. *et al.* "An Eulerian method for the solution of the multi-species drift-kinetic equation", *Plasma Physics and Controlled Fusion* **51**(7) 075018 (2009).

[137] Peeters A. G. *et al.* "The nonlinear gyro-kinetic flux tube code GKW", *Computer Physics Communications* **180**(12) 2650–2672 (2009).

[138] Houlberg W. A. *et al.* "Bootstrap current and neoclassical transport in tokamaks of arbitrary collisionality and aspect ratio", *Physics of Plasmas* **4**(9) 3230–3242 (1997).

[139] Peeters A. G. "Reduced charge state equations that describe Pfirsch–Schlüter impurity transport in tokamak plasma", *Physics of Plasmas* **7**(1) 268–275 (2000).

[140] Dux R. *et al.* “Neoclassical impurity transport in the core of an ignited tokamak plasma”, *Nuclear Fusion* **40**(10) 1721–1729 (2000).

[141] Reisner M. *et al.* “Increased core ion temperatures in high-beta advanced scenarios in ASDEX Upgrade”, *Nuclear Fusion* **60**(8) 082005 (2020).

[142] Field A. *et al.* “Peripheral temperature gradient screening of high-Z impurities in optimised ‘hybrid’ scenario H-mode plasmas in JET-ILW”, *Nuclear Fusion* **63**(1) 016028 (2023).

[143] Fable E. *et al.* “The role of the source versus the collisionality in predicting a reactor density profile as observed on ASDEX Upgrade discharges”, *Nuclear Fusion* **59**(7) 076042 (2019).

[144] Sauter O. *et al.* “Neoclassical conductivity and bootstrap current formulas for general axisymmetric equilibria and arbitrary collisionality regime”, *Physics of Plasmas* **6**(7) 2834–2839 (1999).

[145] Lee H. *et al.* “Neoclassical transport analysis of high rotational trace limit tungsten impurities in KSTAR tokamak”, *Physics of Plasmas* **29**(2) 022504 (2022).

[146] Garcia J. *et al.* “New H-mode regimes with small ELMs and high thermal confinement in the Joint European Torus”, *Physics of Plasmas* **29**(3) 032505 (2022).

[147] Casson F. J. *et al.* “Gyrokinetic simulations including the centrifugal force in a rotating tokamak plasma”, *Physics of Plasmas* **17**(10) 102305 (2010).

[148] Redl A. *et al.* “A new set of analytical formulae for the computation of the bootstrap current and the neoclassical conductivity in tokamaks”, *Physics of Plasmas* **28**(2) 022502 (2021).

[149] Angioni C. *et al.* “Tungsten transport in JET H-mode plasmas in hybrid scenario, experimental observations and modelling”, *Nuclear Fusion* **54**(8) 083028 (2014).

[150] Dux R. “STRAHL User Manual”. Tech. rep. Max-Planck-Institut für Plasmaphysik, Garching bei München, Germany. Reference: IPP 10/30 (2006).

[151] Candy J. *et al.* “Tokamak profile prediction using direct gyrokinetic and neoclassical simulation”, *Physics of Plasmas* **16**(6) (2009).

[152] Summers H. P. *et al.* “Ionization state, excited populations and emission of impurities in dynamic finite density plasmas: I. The generalized collisional-radiative model for light elements”, *Plasma Physics and Controlled Fusion* **48**(2) 263–293 (2006).

[153] Pütterich T. *et al.* “Modelling of measured tungsten spectra from ASDEX Upgrade and predictions for ITER”, *Plasma Physics and Controlled Fusion* **50**(8) 085016 (2008).

[154] Henderson S. S. *et al.* “Optimisation and assessment of theoretical impurity line power coefficients relevant to ITER and DEMO”, *Plasma Physics and Controlled Fusion* **59**(5) 055010 (2017).

[155] OPEN–ADAS: Atomic Data and Analysis Structure. URL: `https://open.adas.ac.uk/`

[156] Mosher D. “Coronal equilibrium of high–atomic-number plasmas”, *Physical Review A* **10**(6) 2330–2335 (1974).

[157] Post D. *et al.* “Steady-state radiative cooling rates for low-density, high-temperature plasmas”, *Atomic Data and Nuclear Data Tables* **20**(5) 397–439 (1977).

[158] Behringer K. “Description of the impurity transport code STRAHL”. Tech. rep. JET Joint Undertaking, Culham, United Kingdom. Reference: JET-R(87)08 (1987).

[159] Dux R. *et al.* “Main chamber sources and edge transport of tungsten in H-mode plasmas at ASDEX Upgrade”, *Nuclear Fusion* **51**(5) 053002 (2011).

[160] Goldston R. J. *et al.* “A new scaling for divertor detachment”, *Plasma Physics and Controlled Fusion* **59**(5) 055015 (2017).

[161] Sun H. J. *et al.* “Study of near scrape-off layer (SOL) temperature and density gradient lengths with Thomson scattering”, *Plasma Physics and Controlled Fusion* **57**(12) 125011 (2015).

[162] Aho-Mantila L. *et al.* “Outer divertor of ASDEX Upgrade in low-density L-mode discharges in forward and reversed magnetic field: I. Comparison between measured plasma conditions and SOLPS5.0 code calculations”, *Nuclear Fusion* **52**(10) 103006 (2012).

[163] Pereverzev G. *et al.* “Stable numeric scheme for diffusion equation with a stiff transport”, *Computer Physics Communications* **179**(8) 579–585 (2008).

[164] Sciortino F. *et al.* “Modeling of particle transport, neutrals and radiation in magnetically-confined plasmas with Aurora”, *Plasma Physics and Controlled Fusion* **63**(11) 112001 (2021).

[165] McDermott R. M. *et al.* “Validation of low-Z impurity transport theory using boron perturbation experiments at ASDEX Upgrade”, *Nuclear Fusion* **62**(2) 026006 (2022).

[166] Manas P. *et al.* “Nonlinear gyrokinetic simulations of boron density peaking: experimental comparisons and reduced transport model validation”, *P-1.13* 27th EU-US TTF, Nancy, France (2023).

[167] Casson F. *et al.* “Validation of gyrokinetic modelling of light impurity transport including rotation in ASDEX Upgrade”, *Nuclear Fusion* **53**(6) 063026 (2013).

[168] Manas P. *et al.* “Gyrokinetic modeling of impurity peaking in JET H-mode plasmas”, *Physics of Plasmas* **24**(6) 062511 (2017).

[169] Bonanomi N. *et al.* “Light impurity transport in JET ILW L-mode plasmas”, *Nuclear Fusion* **58**(3) 036009 (2018).

[170] Kappatou A. *et al.* “Understanding helium transport: experimental and theoretical investigations of low-Z impurity transport at ASDEX Upgrade”, *Nuclear Fusion* **59**(5) 056014 (2019).

[171] Palade D. “Peaking and hollowness of low-Z impurity profiles: an interplay between ITG and TEM induced turbulent transport”, *Nuclear Fusion* **63**(4) 046007 (2023).

[172] Fable E. *et al.* “Impurity outward particle flux from externally applied torque”, *Plasma Physics and Controlled Fusion* **65**(11) 115007 (2023).

[173] Fajardo D. *et al.* “Full-radius integrated modelling of ASDEX Upgrade L-modes including impurity transport and radiation”, *Nuclear Fusion* **64**(4) 046021 (2024).

[174] Angioni C. *et al.* “Confinement properties of L–mode plasmas in ASDEX Upgrade and full–radius predictions of the TGLF transport model”, *Nuclear Fusion* **62**(6) 066015 (2022).

[175] Weiland M. *et al.* “RABBIT: Real-time simulation of the NBI fast-ion distribution”, *Nuclear Fusion* **58**(8) 082032 (2018).

[176] Poli E. *et al.* “TORBEAM, a beam tracing code for electron-cyclotron waves in tokamak plasmas”, *Computer Physics Communications* **136**(1-2) 90–104 (2001).

[177] McCarthy P. J. *et al.* “The CLISTE interpretive equilibrium code”. Tech. rep. Max-Planck-Institut für Plasmaphysik, Garching, Germany IPP 5/85 (1999).

[178] Angioni C. *et al.* “The dependence of tokamak L-mode confinement on magnetic field and plasma size, from a magnetic field scan experiment at ASDEX Upgrade to full-radius integrated modelling and fusion reactor predictions”, *Nuclear Fusion* **63**(5) 056005 (2023).

[179] Staebler G. *et al.* “Successful prediction of tokamak transport in the L-mode regime”, *Nuclear Fusion* **64**(8) 085002 (2024).

[180] Stangeby P. C. “The plasma boundary of magnetic fusion devices”, 1st ed. *IOP Publishing*, ISBN: 978-0-367-80148-9 (2000).

[181] Meneghini O. *et al.* “Integrated fusion simulation with self-consistent core-pedestal coupling”, *Physics of Plasmas* **23**(4) 042507 (2016).

[182] Saarelma S. *et al.* “Integrated modelling of H-mode pedestal and confinement in JET-ILW”, *Plasma Physics and Controlled Fusion* **60**(1) 014042 (2017).

[183] Luda T. *et al.* “Integrated modeling of ASDEX Upgrade plasmas combining core, pedestal and scrape–off layer physics”, *Nuclear Fusion* **60**(3) 036023 (2020).

[184] Luda T. *et al.* “Validation of a full-plasma integrated modeling approach on ASDEX Upgrade”, *Nuclear Fusion* **61**(12) 126048 (2021).

[185] Luda T. *et al.* “Validation of IMEP on Alcator C-Mod and JET-ILW ELMy H-mode plasmas”, *Plasma Physics and Controlled Fusion* **65**(3) 034001 (2023).

[186] Bonanomi N. *et al* “From L-mode to the L-H transition, experiments on ASDEX Upgrade, gyrokinetic simulations and full-radius transport modeling”, *P-05.101* 48nd EPS Conference on Plasma Physics (2022).

[187] Plank U. *et al.* “Overview of L- to H-mode transition experiments at ASDEX Upgrade”, *Plasma Physics and Controlled Fusion* **65**(1) 014001 (2022).

[188] Plank U. *et al.* “Experimental study of the edge radial electric field in different drift configurations and its role in the access to H-mode at ASDEX Upgrade”, *Physics of Plasmas* **30**(4) 042513 (2023).

[189] Waltz R. E. *et al.* “Ion temperature gradient turbulence simulations and plasma flux surface shape”, *Physics of Plasmas* **6**(11) 4265–4271 (1999).

[190] Terry P. W. “Suppression of turbulence and transport by sheared flow”, *Reviews of Modern Physics* **72**(1) 109–165 (2000).

[191] Staebler G. M. *et al.* “H-mode transitions and limit cycle oscillations from mean field transport equations”, *Plasma Physics and Controlled Fusion* **57**(1) 014025 (2014).

[192] Staebler G. *et al.* “Limit cycle oscillations and L/H transitions from two dimensional mean field momentum transport equations”, *Nuclear Fusion* **55**(7) 073008 (2015).

[193] Zholobenko W. *et al.* “Electric field and turbulence in global Braginskii simulations across the ASDEX Upgrade edge and scrape-off layer”, *Plasma Physics and Controlled Fusion* **63**(3) 034001 (2021).

[194] Shaing K. *et al.* “Bifurcation theory of poloidal rotation in tokamaks: A model for l-h transition”, *Physical Review Letters* **63**(21) 2369–2372 (1989).

[195] Brzozowski R. W. *et al.* “A geometric model of ion orbit loss under the influence of a radial electric field”, *Physics of Plasmas* **26**(4) 042511 (2019).

[196] Zhu H. *et al.* “Effects of collisional ion orbit loss on tokamak radial electric field and toroidal rotation in an L-mode plasma”, *Nuclear Fusion* **63**(6) 066009 (2023).

[197] Brida D. *et al.* “Physics of the electric field in the scrape-off layer in ASDEX Upgrade L-mode discharges and comparison to experiments”, *Nuclear Materials and Energy* **33** 101262 (2022).

[198] Angioni C. *et al.* "Analytic formulae for centrifugal effects on turbulent transport of trace impurities in tokamak plasmas", *Physics of Plasmas* **19**(12) 122311 (2012).

[199] Citrin J. *et al.* "Tractable flux-driven temperature, density, and rotation profile evolution with the quasilinear gyrokinetic transport model QuaLiKiz", *Plasma Physics and Controlled Fusion* **59**(12) 124005 (2017).

[200] Ware A. A. "Pinch effect for trapped particles in a tokamak", *Physical Review Letters* **25**(1) 15–17 (1970).

[201] Casson F. *et al.* "Predictive multi-channel flux-driven modelling to optimise ICRH tungsten control and fusion performance in JET", *Nuclear Fusion* **60**(6) 066029 (2020).

[202] Meneghini O. *et al.* "Neural-network accelerated coupled core-pedestal simulations with self-consistent transport of impurities and compatible with ITER IMAS", *Nuclear Fusion* **61**(2) 026006 (2020).

[203] Breton S. *et al.* "High Z neoclassical transport: Application and limitation of analytical formulae for modelling JET experimental parameters", *Physics of Plasmas* **25**(1) 012303 (2018).

[204] Linder O. *et al.* "Flux-driven integrated modelling of main ion pressure and trace tungsten transport in ASDEX Upgrade", *Nuclear Fusion* **59**(1) 016003 (2018).

[205] Shi S. *et al.* "Understanding core tungsten (W) transport and control in an improved high-performance fully non-inductive discharge on EAST", *Nuclear Fusion* **62**(6) 066031 (2022).

[206] Shi S. *et al.* "Understanding core heavy impurity transport in a hybrid discharge on EAST", *Nuclear Fusion* **62**(6) 066032 (2022).

[207] Casiraghi I. *et al.* "First principle-based multi-channel integrated modelling in support of the design of the Divertor Tokamak Test facility", *Nuclear Fusion* **61**(11) 116068 (2021).

[208] Köchl F. *et al.* "W transport and accumulation control in the termination phase of JET H-mode discharges and implications for ITER", *Plasma Physics and Controlled Fusion* **60**(7) 074008 (2018).

[209] Marin M. *et al.* "Integrated modelling of neon impact on JET H-mode core plasmas", *Nuclear Fusion* **63**(1) 016019 (2022).

[210] Ostuni V. *et al.* "Core radiative collapse characterisation and integrated modelling in WEST plasmas", *Nuclear Fusion* **62**(10) 106034 (2022).

[211] Gabriellini S. *et al.* "Neon seeding effects on two high-performance baseline plasmas on the Joint European Torus", *Nuclear Fusion* **63**(8) 086025 (2023).

[212] Fischer R. *et al.* “Integrated Data Analysis of profile diagnostics at ASDEX Upgrade”, *Fusion Science and Technology* **58**(2) 675–684 (2010).

[213] Igochine V. *et al.* “Hotlink based Soft X-ray Diagnostic on ASDEX Upgrade”. Tech. rep. Max-Planck-Institut für Plasmaphysik, Garching, Germany IPP 1/338 (2010).

[214] David P. *et al.* “Optimization of the computation of total and local radiated power at ASDEX Upgrade”, *Nuclear Fusion* **61**(6) 066025 (2021).

[215] Rathgeber S. K. *et al.* “Estimation of profiles of the effective ion charge at ASDEX Upgrade with Integrated Data Analysis”, *Plasma Physics and Controlled Fusion* **52**(9) 095008 (2010).

[216] Odstrcil M. *et al.* “Modern numerical methods for plasma tomography optimisation”, *Nuclear Instruments and Methods in Physics Research A* **686** 156–161 (2012).

[217] Odstrčil T. *et al.* “Optimized tomography methods for plasma emissivity reconstruction at the ASDEX Upgrade tokamak”, *Review of Scientific Instruments* **87**(12) 123505 (2016).

[218] Martin Y. R. *et al.* “Power requirement for accessing the H-mode in ITER”, *Journal of Physics: Conference Series* **123** 012033 (2008).

[219] Messiaen A. M. *et al.* “High confinement and high density with stationary plasma energy and strong edge radiation in the TEXTOR-94 tokamak”, *Physical Review Letters* **77**(12) 2487–2490 (1996).

[220] Hill K. *et al.* “Highly radiative plasmas for local transport studies and power and particle handling in reactor regimes”, *Nuclear Fusion* **39**(11Y) 1949–1954 (1999).

[221] Ongena J. *et al.* “Overview of experiments with radiation cooling at high confinement and high density in limited and diverted discharges”, *Plasma Physics and Controlled Fusion* **41**(3A) A379–A399 (1999).

[222] Komm M. *et al.* “Power exhaust by core radiation at COMPASS tokamak”, *Nuclear Fusion* **61**(3) 036016 (2021).

[223] Kallenbach A. *et al.* “Non-boronized compared with boronized operation of ASDEX Upgrade with full-tungsten plasma facing components”, *Nuclear Fusion* **49**(4) 045007 (2009).

[224] Sertoli M. *et al.* “Interplay between central ECRH and saturated $(m, n) = (1, 1)$ MHD activity in mitigating tungsten accumulation at ASDEX Upgrade”, *Nuclear Fusion* **55**(11) 113029 (2015).

[225] Sertoli M. *et al.* “Modification of impurity transport in the presence of saturated $(m, n) = (1, 1)$ MHD activity at ASDEX Upgrade”, *Plasma Physics and Controlled Fusion* **57**(7) 075004 (2015).

[226] Neu R. *et al.* “Impurity behaviour in the ASDEX Upgrade divertor tokamak with large area tungsten walls”, *Plasma Physics and Controlled Fusion* **44**(6) 811–826 (2002).

[227] Puiatti M. E. *et al.* “Analysis of metallic impurity density profiles in low collisionality Joint European Torus H-mode and L-mode plasmas”, *Physics of Plasmas* **13**(4) 042501 (2006).

[228] Angioni C. *et al.* “A comparison of the impact of central ECRH and central ICRH on the tungsten behaviour in ASDEX Upgrade H-mode plasmas”, *Nuclear Fusion* **57**(5) 056015 (2017).

[229] Angioni C. “Gyrokinetic study of the impact of the electron to ion heating ratio on the turbulent diffusion of highly charged impurities”, *Physics of Plasmas* **22**(10) 102501 (2015).

[230] Manas P. *et al* “Tungsten transport in tokamaks: towards real-time kinetic-theory-based plasma performance optimisation”, *TH/P2-21* IAEA Fusion Energy Conference (2020).

[231] Bernert M. *et al.* “The X-point radiating regime at ASDEX Upgrade and TCV”, *Nuclear Materials and Energy* **34** 101376 (2023).

[232] Stroth U. *et al.* “Model for access and stability of the X-point radiator and the threshold for MARFES in tokamak plasmas”, *Nuclear Fusion* **62**(7) 076008 (2022).

[233] Pan O. *et al.* “SOLPS-ITER simulations of an X-point radiator in the ASDEX Upgrade tokamak”, *Nuclear Fusion* **63**(1) 016001 (2022).

[234] Cavedon M. *et al.* “Experimental investigation of L- and H-mode detachment via the divertor Thomson scattering at ASDEX Upgrade”, *Nuclear Fusion* **62**(6) 066027 (2022).

[235] Palermo F. *et al.* “Scaling laws from theory-based modeling for different regimes in the DEMO fusion reactor”, *Nuclear Fusion* **59**(9) 096010 (2019).

[236] Fajardo D. *et al.* “Integrated modelling of tungsten accumulation control with wave heating: validation in ASDEX Upgrade and predictions for ITER”, *Nuclear Fusion* **64**(10) 104001 (2024).

[237] Mantica P. *et al.* “Transport analysis of tungsten and beryllium in JET hybrid plasmas with the ITER-like wall”, *P-4.141* 50th EPS Conference on Plasma Physics (2013).

[238] Rice J. *et al.* “Double transport barrier plasmas in Alcator C-Mod”, *Nuclear Fusion* **42**(5) 510–519 (2002).

[239] Gohil P. *et al.* “Recent experimental studies of edge and internal transport barriers in the DIII-D tokamak”, *Plasma Physics and Controlled Fusion* **45**(5) 601–620 (2003).

[240] Scavino E. *et al.* “Effects of ECRH power and safety factor on laser blow-off injected impurity confinement in TCV”, *Plasma Physics and Controlled Fusion* **46**(5) 857–868 (2004).

[241] Hong J. *et al.* “Control of core argon impurity profile by ECH in KSTAR L-mode plasmas”, *Nuclear Fusion* **55**(6) 063016 (2015).

[242] Zhang L. *et al.* “Suppression of tungsten accumulation during ELMy H-mode by lower hybrid wave heating in the EAST tokamak”, *Nuclear Materials and Energy* **12** 774–778 (2017).

[243] Dux R. *et al.* “Influence of the heating profile on impurity transport in ASDEX Upgrade”, *Plasma Physics and Controlled Fusion* **45**(9) 1815–1825 (2003).

[244] McDermott R. M. *et al.* “Effect of electron cyclotron resonance heating (ECRH) on toroidal rotation in ASDEX Upgrade H-mode discharges”, *Plasma Physics and Controlled Fusion* **53**(3) 035007 (2011).

[245] Citrin J. *et al.* “Overview of tokamak turbulence stabilization by fast ions”, *Plasma Physics and Controlled Fusion* **65**(3) 033001 (2023).

[246] Bonanomi N. *et al.* “Turbulent transport stabilization by ICRH minority fast ions in low rotating JET ILW L-mode plasmas”, *Nuclear Fusion* **58**(5) 056025 (2018).

[247] Bobkov V. *et al.* “First results with 3-strap ICRF antennas in ASDEX Upgrade”, *Nuclear Fusion* **56**(8) 084001 (2016).

[248] Brambilla M. “Numerical simulation of ion cyclotron waves in tokamak plasmas”, *Plasma Physics and Controlled Fusion* **41**(1) 1–34 (1999).

[249] Brambilla M. *et al.* “Advances in numerical simulations of ion cyclotron heating of non-Maxwellian plasmas”, *Nuclear Fusion* **49**(8) 085004 (2009).

[250] Bilato R. *et al.* “Simulations of combined neutral beam injection and ion cyclotron heating with the TORIC-SSFPQL package”, *Nuclear Fusion* **51**(10) 103034 (2011).

[251] Tardini G. *et al.* “A package to bridge experimental tokamak data to modelling workflows for heating and transport”, *Nuclear Fusion* **64**(5) 056014 (2024).

[252] Peeters A. *et al.* “GKW how and why”. Tech. rep. University of Warwick, Warwick, UK GKW manual (2015).

[253] Loarte A. “The new ITER baseline, research plan and open R&D issues”, *I-258* EPS Conference on Plasma Physics (2024).

[254] Polevoi A. *et al.* “Assessment of operational space for long-pulse scenarios in ITER”, *Nuclear Fusion* **55**(6) 063019 (2015).

[255] Kim S. *et al.* “Investigation of key parameters for the development of reliable ITER baseline operation scenarios using CORSICA”, *Nuclear Fusion* **58**(5) 056013 (2018).

[256] Korving S. Q. *et al.* “Simulation of neoclassical heavy impurity transport in ASDEX Upgrade with applied 3D magnetic fields using the nonlinear MHD code JOREK”, *Physics of Plasmas* **31**(5) 052504 (2024).

[257] Pusztai I. *et al.* “Global effects on neoclassical transport in the pedestal with impurities”, *Plasma Physics and Controlled Fusion* **58**(8) 085001 (2016).

[258] Dominski J. *et al.* “Neoclassical transport of tungsten ion bundles in total-f neoclassical gyrokinetic simulations of a whole-volume JET-like plasma”, *Physics of Plasmas* **31**(3) 032303 (2024).

[259] Luda T. *et al* “Full-radius integrated modelling of H-mode confinement dependence on plasma size and predictions for ITER and DEMO”, *in preparation* (2024).

[260] Maggi C. *et al.* “Isotope effects on L-H threshold and confinement in tokamak plasmas”, *Plasma Physics and Controlled Fusion* **60**(1) 014045 (2017).

[261] Ryter F. *et al.* “Survey of the H-mode power threshold and transition physics studies in ASDEX Upgrade”, *Nuclear Fusion* **53**(11) 113003 (2013).

[262] Verdoolaege G. *et al.* “The updated ITPA global H-mode confinement database: description and analysis”, *Nuclear Fusion* **61**(7) 076006 (2021).

[263] Howard N. *et al.* “Prediction of performance and turbulence in ITER burning plasmas via nonlinear gyrokinetic profile prediction”, *Arxiv* (2024).

[264] Shirai H. *et al.* “Recent progress of the JT-60SA project”, *Nuclear Fusion* **57**(10) 102002 (2017).

[265] Zimmermann C. F. B. *et al.* “Analysis and modelling of momentum transport based on NBI modulation experiments at ASDEX Upgrade”, *Plasma Physics and Controlled Fusion* **64**(5) 055020 (2022).

[266] Zimmermann C. F. B. *et al.* “Experimental validation of momentum transport theory in the core of H-mode plasmas in the ASDEX Upgrade tokamak”, *Physics of Plasmas* **31**(4) (2024).

[267] Schmid K. *et al.* “An integrated model of impurity migration and wall composition dynamics for tokamaks”, *Journal of Nuclear Materials* **415**(1) S284–S288 (2011).

[268] Schmid K. *et al.* “Quantitative modeling of fuel retention in the JET-C and JET-ILW wall configurations by WallDYN and predictions for ITER”, *Journal of Nuclear Materials* **463** 66–72 (2015).

[269] Kumpulainen H. *et al.* “ELM and inter-ELM tungsten erosion sources in high-power, JET ITER-like wall H-mode plasmas”, *Nuclear Materials and Energy* **33** 101264 (2022).

[270] Lee S. *et al.* “A tungsten-wall sputtering model for the plasma start-up simulation in tokamaks”, *Plasma Physics and Controlled Fusion* **66**(9) 095013 (2024).

[271] Kumpulainen H. *et al.* “Comparison of DIVIMP and EDGE2D-EIRENE tungsten transport predictions in JET edge plasmas”, *Nuclear Materials and Energy* **25** 100784 (2020).

[272] Kumpulainen H. A. *et al.* “Validated edge and core predictions of tungsten erosion and transport in JET ELMy H-mode plasmas”, *Plasma Physics and Controlled Fusion* **66**(5) 055007 (2024).

[273] Navarro M. *et al.* “Erosion and impurity transport for the edge localized mode suppression window in KSTAR”, *Physics of Plasmas* **31**(8) (2024).

[274] Dux R. *et al.* “Influence of CX-reactions on the radiation in the pedestal region at ASDEX Upgrade”, *Nuclear Fusion* **60**(12) 126039 (2020).

List of acronyms

ASDEX Axially Symmetric Divertor Experiment.

ASTRA Automated System for Transport Analysis.

AT Advanced Tokamak (scenario).

AUG ASDEX Upgrade.

BP Banana-Plateau.

CFC Carbon Fiber Composites.

CX Charge Exchange.

CXRS Charge Exchange Recombination Spectroscopy.

DEMO Demonstration Fusion Power Plant.

DKE Drift-Kinetic Equation.

ECRH Electron Cyclotron Resonance Heating.

ELM Edge-Localized Modes.

ETG Electron Temperature Gradient.

FACIT Fast and Accurate Collisional Impurity Transport.

FSA Flux Surface Average.

GIW Grazing-incidence spectrometers (for tungsten, W).

GKE Gyrokinetic Equation.

HFS High Field Side.

ICRH Ion Cyclotron Resonance Heating.

IDA Integrated Data Analysis.

IMEP Integrated Modelling from Engineering Parameters.

IPB ITER Physics Basis.

IPP Max Planck Institute for Plasma Physics.

ITER *the way* in Latin, prev. International Thermonuclear Experimental Reactor.

ITG Ion Temperature Gradient.

JET Joint European Torus.

JT-60SA Japan Torus–60 Super Advanced.

KBM Kinetic Ballooning Modes.

KSTAR Korea Superconducting Tokamak Advanced Research.

LCFS Last Closed Flux Surface.

LFS Low Field Side.

MCF Magnetic Confinement Fusion.

MHD Magnetohydrodynamics.

MTM Micro-Tearing Modes.

NBI Neutral Beam Injection.

PFC Plasma Facing Components.

PS Pfirsch-Schlüter.

RMP Resonant Magnetic Perturbation.

SOL Scrape-Off Layer.

SXR Soft X-Rays.

TA Temperature Anisotropies.

TEM Trapped Electron Mode.

TFTR Tokamak Fusion Test Reactor.

TGLF Trapped Gyro–Landau Fluid.

XPR X-point Radiator.

Appendix

A Transformation of transport coefficients between low field side and flux surface average pictures

We have seen from chapter 3 and figure 3.1 that the introduction of a 2D poloidally asymmetric impurity density allows freedom in the representation of the 1D density. In particular, the low-field-side (LFS) and flux-surface-averaged (FSA) 1D pictures of the impurity density are of interest. Transport codes always use the FSA density, whereas the drift- and gyro-kinetic codes more regularly use the LFS (outer midplane) density. Imposing that the flux-surface-averaged impurity particle flux, split into diffusive and convective components, is equal in both pictures gives rise to a transformation between the 1D densities, their gradients, and the corresponding diffusion and convection coefficients. This transformation is summarized here for reference, following the derivation of the Appendix of [149], with a useful form of the transformation of the convection which follows from the equations in [149].

For clarity, we will keep explicit labels of 'fsa' and 'lfs', such that $\langle n_z(r,\theta)\rangle = n_{\mathrm{fsa}}$ and $n_z(r,\theta_0) = n_{\mathrm{lfs}}$. The FSA particle flux is decomposed in the usual diffusive and convective components in each 1D picture, such that

$$\begin{aligned} \Gamma &= -D_{\mathrm{fsa}}\frac{\mathrm{d}n_{\mathrm{fsa}}}{\mathrm{d}r} + n_{\mathrm{fsa}}V_{\mathrm{fsa}}\,, \\ \Gamma &= -D_{\mathrm{lfs}}\frac{\mathrm{d}n_{\mathrm{lfs}}}{\mathrm{d}r} + n_{\mathrm{lfs}}V_{\mathrm{lfs}}\,, \end{aligned} \tag{A.1}$$

and these representations of the flux are imposed to be equivalent. From the parallel transport properties presented in section 2.2, the densities (and their gradients, from the product rule) transform as

$$n_{\mathrm{fsa}} = n_{\mathrm{lfs}}\left\langle e^{-E_z}\right\rangle, \qquad \frac{\mathrm{d}n_{\mathrm{fsa}}}{\mathrm{d}r} = \frac{\mathrm{d}n_{\mathrm{lfs}}}{\mathrm{d}r}\left\langle e^{-E_z}\right\rangle + n_{\mathrm{lfs}}\frac{\mathrm{d}\left\langle e^{-E_z}\right\rangle}{\mathrm{d}r}\,, \tag{A.2}$$

which follows from taking a FSA of equation (2.24), where the normalized impurity energy E_z is defined as everything inside the brackets of equation (2.24). The transformation of the diffusion coefficients is obtained by direct comparison of the terms multiplying the density gradients in the expressions of equation (A.1), leading to

$$\frac{D_{\mathrm{fsa}}}{D_{\mathrm{lfs}}} = \frac{1}{\langle e^{-E_z}\rangle} = \frac{n_{\mathrm{lfs}}}{n_{\mathrm{fsa}}} \quad \longrightarrow \quad D_{\mathrm{fsa}} = \frac{D_{\mathrm{lfs}}}{\langle e^{-E_z}\rangle}\,. \tag{A.3}$$

The transformation of the convection is not a simple multiplicative factor like for the diffusion. From equation (A.1), we can factor out the diffusion and density terms on both sides, such that

$$\left(-\frac{\mathrm{d}n_{\mathrm{fsa}}}{\mathrm{d}r}\frac{1}{n_{\mathrm{fsa}}}+\frac{V_{\mathrm{fsa}}}{D_{\mathrm{fsa}}}\right)D_{\mathrm{fsa}}n_{\mathrm{fsa}}=D_{\mathrm{lfs}}n_{\mathrm{lfs}}\left(-\frac{\mathrm{d}n_{\mathrm{lfs}}}{\mathrm{d}r}\frac{1}{n_{\mathrm{lfs}}}+\frac{V_{\mathrm{lfs}}}{D_{\mathrm{lfs}}}\right), \tag{A.4}$$

where the terms outside of the parenthesis on both sides cancel out, following equation (A.3). Further manipulation leads to

$$\frac{V_{\mathrm{fsa}}}{D_{\mathrm{fsa}}}-\frac{\mathrm{d}\ln n_{\mathrm{fsa}}}{\mathrm{d}r}=\frac{V_{\mathrm{lfs}}}{D_{\mathrm{lfs}}}-\frac{\mathrm{d}\ln n_{\mathrm{lfs}}}{\mathrm{d}r}\quad\longrightarrow\quad\frac{V_{\mathrm{fsa}}}{D_{\mathrm{fsa}}}=\frac{V_{\mathrm{lfs}}}{D_{\mathrm{lfs}}}+\frac{\mathrm{d}\ln(n_{\mathrm{fsa}}/n_{\mathrm{lfs}})}{\mathrm{d}r}, \tag{A.5}$$

such that, again using equation (A.3), we finally obtain the transformation of the convection:

$$V_{\mathrm{fsa}}=\frac{V_{\mathrm{lfs}}}{\left\langle e^{-E_z}\right\rangle}+\frac{D_{\mathrm{fsa}}}{\left\langle e^{-E_z}\right\rangle}\frac{\mathrm{d}\left\langle e^{-E_z}\right\rangle}{\mathrm{d}r}=\frac{V_{\mathrm{lfs}}}{\left\langle e^{-E_z}\right\rangle}+D_{\mathrm{fsa}}\frac{\mathrm{d}\ln\left\langle e^{-E_z}\right\rangle}{\mathrm{d}r}\,. \tag{A.6}$$

To illustrate the effect of the transformation, we use profiles from an ASDEX Upgrade discharge with typical rotation values of $M_i \approx 0.2$. The transport coefficients are calculated with FACIT and they are plotted in their LFS and FSA forms in figure A.1, where a clear enhancement in the FSA picture is observed.

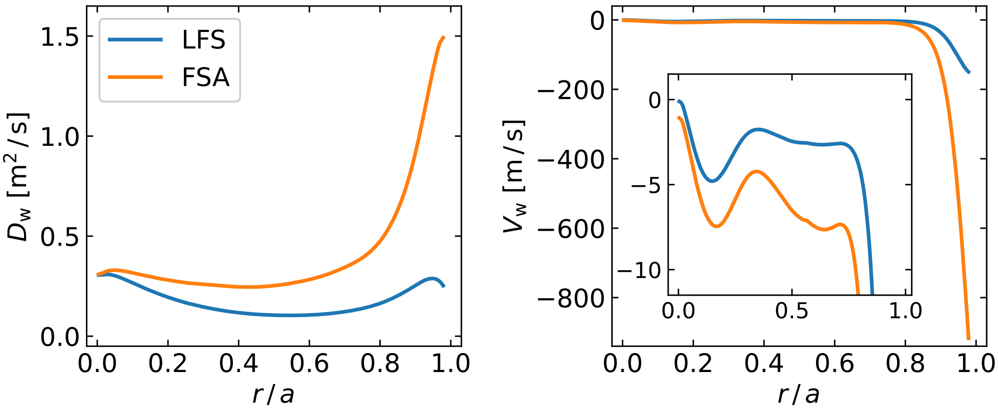

Figure A.1: Example of the difference between W transport coefficients in the low-field-side and flux-surface-average representation of the flux. Diffusion is on the left and convection on the right.

This is explained from the fact that with centrifugal effects there is LFS localization of the 2D impurity density, leading to a higher LFS density and stronger LFS gradient (like in the example of figure 3.1) that need to be compensated with higher FSA coefficients, given that the flux-surface-averaged fluxes are equal by definition using both 1D representations of the impurity density.

B Fitted factors of FACIT

The database of NEO simulations constructed to study the effects of rotation and collisionality and to build the analytical model in chapter 3 consists of 3388 NEO calculations: 154 collisionality scans of 22 points in $g \in \{10^{-4}, 10^{1}\}$, at 14 rotation levels $M_i \in \{0.0, 0.7\}$ times 11 trapped particle fraction values $f_t \in \{0.2, 0.9\}$. The resolution of NEO was $(N_\theta = 25, N_\xi = 29, N_x = 10)$ for the number of poloidal points, the number of Legendre polynomials in the pitch angle, and the number of energy polynomials respectively. We used Miller geometry with elongation $\kappa = 1.35$ and triangularity $\delta = 0.11$. The rest of the NEO inputs that are not modified in the scans are taken from an AUG standard H-mode at mid-radius.

The formulae for the set of fitted factors in (M_z^*, f_t) introduced in the model in order to minimize differences with NEO are given explicitly here. These factors are all implemented internally in FACIT.

We begin with the coefficients of the PS component. In equation (3.4), we have

$$\mathcal{C}_\mathcal{G}(0) = 0.96(1 - 0.54 f_t^{4.5})\, 2\epsilon^2, \tag{B.1}$$

$$f_\mathcal{G} = \frac{(1 + a_1 M_z^{*a_2})^{a_3}(1 + 0.2 M_z^{*a_4})}{1 + a_5 M_z^{*a_6}}. \tag{B.2}$$

The a_i coefficients are all functions of f_t, taking the general form

$$a_i = b_{i1} f_t^{b_{i2}} + b_{i3}(1 - b_{i4} f_t), \tag{B.3}$$

where

$$b_{ij} = \begin{pmatrix} -1.4 & 7 & 2.23 & 0.31 \\ 0 & 0 & 2.8 & 0.36 \\ 0 & 0 & 3.5/a_2 & 1 \\ 4 & 1 & 0 & 0 \\ 0.38 & 4 & 0 & 0 \\ -1.1 & 2 & 3.95 & -0.42 \end{pmatrix}. \tag{B.4}$$

In equation (3.10), it becomes more convenient to fit an expression for

$$(f_\mathcal{G} - 1)\, f_\mathcal{U} = c_1 M_z^{*c_2} \, \frac{1 + c_3 M_z^{*c_4}}{1 + c_5 M_z^{*c_6}}, \tag{B.5}$$

in order to avoid second-order errors in the product of the individual fits of $f_\mathcal{G}$ and $f_\mathcal{U}$. Similarly as for the a_i, the c_i coefficients take the form

$$c_i = d_{i1}(d_{i2} - d_{i3} f_t)^{d_{i4}} + d_{i5} f_t^{d_{i6}}, \tag{B.6}$$

with

$$d_{ij} = \begin{pmatrix} 2.72 & 1 & 0.91 & 1 & 0 & 0 \\ 2.98 & 1 & 0.47 & 1 & 0 & 0 \\ 0.95 & 1 & 1 & 4 & 0 & 0 \\ 0 & 1 & 1 & 0 & 4 & 1 \\ 0.13 & 0 & -1 & 2.84 & 3.18 & 11.4 \\ -9.4 & -0.5 & -1 & 2 & 4.64 & 0 \end{pmatrix}. \tag{B.7}$$

The neoclassical ion flow coefficient k_i is used in H_z^{PS}, and it is calculated by NEO as one of its explicit outputs. We introduce a parametrization in rotation, in this case on the main ion Mach number (because k_i is directly related to the main ions and not the impurity). It is an extension of the expression provided in equations (19) and (20) of [148] (where $\alpha = -k_i$). In the following formulae, we take $Z_{\mathrm{eff}} = 1$ to simplify the expressions, but the Z_{eff} dependence remains unchanged from that of [148]. Similarly to that work, we first define an auxiliary quantity

$$k_{i,0} = -\frac{e_{01}}{0.53} \frac{1 - f_t}{1 + e_{02} f_t + e_{03} f_t^2}, \tag{B.8}$$

where the rotation-dependent coefficients take the form

$$e_{0k} = h_{k1}(1 + h_{k2} M_i^{h_{k3}}), \tag{B.9}$$

and

$$h_{kj} = \begin{pmatrix} 0.53 & 0.65 & 1.5 \\ -1.16 & -0.97 & 1.56 \\ 0.98 & -1.23 & 1.7 \end{pmatrix}. \tag{B.10}$$

The total k_i with rotation is then given by

$$k_i = \left(\frac{k_{i,0} + l_1 \, (f_t \, \nu_i^*)^{0.5} + l_2 \, \nu_i^{*0.25}}{1 + l_3 \, \nu_i^{*0.5}} - l_4 \, l_5 \, \nu_i^{*2} f_t^6 + l_6 \, \nu_i^{*0.25} \right) \frac{1}{1 + l_4 \, \nu_i^{*2} f_t^6} \tag{B.11}$$

where the collisionality dependence is expressed in terms of ν_i^* following the original parametrization. From this expression we see that $k_{i,0}$ is simply the limit of k_i as $g \to 0$. The l_k coefficients depend both on f_t and M_i, with the general shape

$$l_k = s_{k1} + s_{k2} M_i^{s_{k3}}. \tag{B.12}$$

The simpler exponents are

$$s_{k3} \in \{0, 2.5(1 - 0.6 f_t), 0, 2.5, 1, 1.5\}, \tag{B.13}$$

for $k \in \{1, \cdots, 6\}$. The s_{k1} coefficients are given by

$$s_{k1} = \frac{u_{k1} + u_{k2}(1 - f_t)^{u_{k3}} f_t^{u_{k4}}}{1 + u_{k5} f_t^{u_{k6}}} \tag{B.14}$$

in their most general form, according to the coefficients

$$u_{kj} = \begin{pmatrix} 0.38 & 5.7 & 6.7 & 0 & 0 & 0 \\ -1.52 & 38.4 & 3 & 2.1 & 0 & 0 \\ 0.25 & 1.2 & 3.65 & 0 & 0 & 0 \\ 0 & 0.1 & 1.46 & 4.33 & 0 & 0 \\ 0.8 & 0 & 0 & 0 & 0 & 0 \\ -0.05 & 1.95 & 0 & 2.5 & 2.55 & 17 \end{pmatrix}, \tag{B.15}$$

while the s_{k2} factors are in general

$$s_{k2} = \frac{p_{k1} + p_{k2} f_t^{p_{k3}}}{1 + p_{k4} f_t^{p_{k5}}}, \tag{B.16}$$

with

$$p_{kj} = \begin{pmatrix} 0 & 0 & 0 & 0 & 0 \\ -1 & 2.6 & 1 & 0 & 0 \\ 0 & 0 & 0 & 0 & 0 \\ 0.05 & -0.04 & 1 & 0 & 0 \\ 0.585 & 1.25 & 1 & 0 & 0 \\ -0.22 & -14.6 & 6.3 & 5.62 & 5.72 \end{pmatrix}. \tag{B.17}$$

This concludes the PS component, so we now turn to the factors introduced into the BP expressions. The viscosity coefficients K^{σ}_{jk} determine the BP transport coefficients K^{BP}_z and H^{BP}_z, as presented in equation (2.42). From the general form of the viscosity coefficients, given in equation (3.6), we have that their structure in collisionality is characterized by $c^{\sigma,r}_{jk}$ factors. For each $(j,k) \in \{(1,1);(1,2)\}$ and $\sigma \in \{i,z\}$, there are three of these factors, denoted by $r \in \{\mathrm{B},\mathrm{P},\mathrm{PS}\}$ according to the collisionality regime where they become more dominant in equation (3.6): banana (B) for low, plateau (P) for intermediate, and Pfirsch-Schlüter (PS) for high collisionalities. The complete expression for the viscosity coefficients includes all three, in the interpolation formula of equation (3.6). These B, P and PS collisionality *regimes* are to be distinguished from the BP and PS *fluxes* and transport coefficients. The structure of the K^{BP}_z and H^{BP}_z transport coefficients in the high collisionality PS regime is described by $c^{\sigma,\mathrm{PS}}_{jk}$, but this is unrelated to the K^{PS}_z and H^{PS}_z coefficients.

In general, the $c^{\sigma,r}_{jk}$ are functions of rotation and trapped particle fraction,

$$c^{\sigma,r}_{jk}(M^*_z) = v^{\sigma,r}_{jk}(M^*_z, f_t)\, c^{\sigma,r}_{jk}(0), \tag{B.18}$$

where the $c^{\sigma}_{jk}(0)$ coefficients in the non-rotating limit are calculated following [108, 109], and the $v^{\sigma,r}_{jk}$ characterize the dependence on M^*_z and f_t.

The factors in K^{BP}_z are the three $v^{z,r}_{11}$, which are the same as the coefficients $v^{i,r}_{11}$ in each collisionality regime. The (1,1) banana-regime factor is given by

$$v^{z,\mathrm{B}}_{11} = v^{i,\mathrm{B}}_{11} = (1 + w_1 M^{*w_2}_z) \exp\bigl(-w_3 M^{*2}_z\bigr), \tag{B.19}$$

while the (1,1) plateau-regime factor is given by

$$v^{z,\mathrm{P}}_{11} = v^{i,\mathrm{P}}_{11} = \frac{1 + w_4 M^{*0.5}_z}{1 + w_5 M^{*10/3}_z}. \tag{B.20}$$

The w_i coefficients take the most general form

$$w_i = q_{i1} + q_{i2}(1 - f_t)^{q_{i3}} f_t^{q_{i4}} + q_{i5} f_t^{q_{i6}}, \tag{B.21}$$

with the coefficients

$$q_{ij} = \begin{pmatrix} 1 & 14.9 & 16.45 & 0 & 15.3 & 7.4 \\ 0.77 & 0 & 0 & 0 & 3.16 & 1 \\ 0.01 & 3.6 & 0 & 2.5 & 10.8 & 12 \\ 0.1 & 6.4 & 15.8 & 0 & 0 & 0 \\ 0.94 & 0 & 0 & 0 & 3.3 & 1 \end{pmatrix}. \tag{B.22}$$

The (1,1) PS-regime factor is given by

$$v_{11}^{z,\mathrm{PS}} = v_{11}^{i,\mathrm{PS}} = \frac{1}{1+2f_t M_z^*}. \tag{B.23}$$

For H_z^{BP}, we have to consider the (1,2) coefficients for the impurity and the main ion, which are not already set by K_z^{BP}. The (1,2) banana-regime coefficient of the impurity is given by

$$v_{12}^{z,\mathrm{B}} = \frac{1+y_1 M_z^{*y_2}}{1+y_3 M_z^{*y_4}}, \tag{B.24}$$

while the (1,2) plateau-regime coefficient of the impurity is given by

$$v_{12}^{z,\mathrm{P}} = \frac{1+y_5 y_6 M_z^{*y_7}}{1+y_6 M_z^{*y_7}}. \tag{B.25}$$

Apart from y_3, the y_i are in general

$$y_i = r_{i1} + r_{i2}(1-f_t)^{r_{i3}} f_t^{r_{i4}} + r_{i5} f_t^{r_{i6}}, \tag{B.26}$$

with the coefficients

$$r_{ij} = \begin{pmatrix} 6.1 & 336.3 & 11.7 & 0 & 28.2 & 2.1 \\ 0.5 & 9.55 & 1.4 & 1.14 & 0 & 0 \\ - & - & - & - & - & - \\ 3.6 & 0 & 0 & 0 & -1.3 & 1 \\ 0 & 1 & 8 & 0 & 0 & 0 \\ 0 & 0 & 0 & 0 & 113.5 & 8.5 \\ 0 & 11 & 1 & 0 & 0 & 0 \end{pmatrix}. \tag{B.27}$$

The y_3 factor is $(0.0009+4.5f_t^{3.5})/(1+0.87f_t^{3.5})$. The (1,2) PS-regime coefficient of the impurity is

$$v_{12}^{z,\mathrm{PS}} = \frac{1+0.35M_z^{*4}}{1+10M_z^{*4}}. \tag{B.28}$$

For the (1,2) coefficients of the main ion, the one in the banana regime is $v_{12}^{i,\mathrm{B}} = \exp\bigl(-10M_z^{*2}\bigr)$, while the plateau and PS coefficients are just 1. The factor in equation (3.12) is $f_v = 3\exp\bigl(-10M_z^{*2}\bigr)/2$. Finally, the H_z^{BP} component has an additional charge dependence not perfectly described by M_z^*, mostly at low-Z, so a multiplying factor,

$$f_{\mathrm{hbp}} = x_1(Z)\,\frac{1+x_2(Z)\,x_3(f_t)M_z^*}{1+x_2(Z)\,x_4(f_t)M_z^{*2}}, \tag{B.29}$$

is introduced, with

$$x_1 = 0.135 + 2.65\times10^{-3}Z^{1.46} + 3.48\times10^{-10}Z^{5.35}, \tag{B.30}$$

$$x_2 = 3/(1+10^{-7}Z^6), \tag{B.31}$$

$$x_3 = 1/(1+1.2\times10^5 f_t^{12}), \tag{B.32}$$

$$x_4 = 1.208 - 4.46f_t + 4.4f_t^2. \tag{B.33}$$

C Transforming transport coefficients: ASTRA, STRAHL & GACODE

In this thesis we refer as "transport codes" or "transport solvers" to the codes that solve the transport equations to evolve the kinetic profiles for given diffusive and convective transport coefficients. Particular emphasis is given to the evolution of impurity densities, although we also evolve the main plasma temperatures and density self-consistently in a majority of cases. The workhorse transport code used in this thesis is ASTRA. For the impurity densities, STRAHL is also widely used in this work. Aurora, a python-based code strongly inspired by STRAHL, is used to a lesser extent for standalone tests. A transport code that is not used in this thesis (but will nonetheless be important to consider in the following) is TGYRO, from the GACODE family of codes developed by General Atomics.

Likewise, by "transport models" we refer to the codes that calculate the diffusive and convective transport coefficients from neoclassical or turbulent physics descriptions. In this thesis we use FACIT, NEO and NCLASS as neoclassical transport models, and TGLF-SAT2 as a turbulent transport model.

The multiple transport *codes* use different radial grids and different forms of the transport equations, meaning that the transport coefficients obtained from the different transport *models* (which also have their one radial coordinates) require careful transformations before being passed to these transport codes. The transformations are typically in the form of metric coefficients to account for the different ways the 2D flux surface geometry is described by a 1D radial flux surface label.

In this appendix we will derive the transformations of transport coefficients between ASTRA, STRAHL, and the codes following the GACODE conventions.

ASTRA uses a radial flux surface label based on the toroidal magnetic flux, called `RHO` in the code, ρ in its manual, and r_{tor} here for clarity. It is defined as

$$\Psi_{\text{tor}} = \pi r_{\text{tor}}^2 B_0 \quad \longrightarrow \quad r_{\text{tor}} = \sqrt{\frac{\Psi_{\text{tor}}}{\pi B_0}}, \tag{C.1}$$

where Ψ_{tor} is the toroidal flux in units of [Wb], B_0 is a reference magnetic field in [T] (taken as the magnetic field on axis in ASTRA, `BTOR`), and the resulting r_{tor} has units of [m].

STRAHL uses a radial flux surface label based on the plasma volume enclosed by the corresponding flux surface, called r_{vol} here for clarity. It is defined as

$$V = (\pi r_{\text{vol}}^2)\,(2\pi R_0) \quad \longrightarrow \quad r_{\text{vol}} = \sqrt{\frac{V}{2\pi^2 R_0}}, \tag{C.2}$$

where V is the volume in units of [m^3] (ASTRA variable `VOLUM`), R_0 is the major radius on axis in [m] (`RTOR` in ASTRA), and the resulting r_{vol} has units of [m].

The GACODE radial coordinate is the average mid-plane minor radius, called r_{min} here for clarity, and defined at each flux surface contour R and Z as

$$r_{\text{min}} = \frac{\max\{R\} - \min\{R\}}{2}, \tag{C.3}$$

again in units of [m]. TGLF and NEO use this coordinate, as well as FACIT (being built from NEO). The corresponding ASTRA variable is `AMETR`.

To obtain the transformations between transport coefficients in ASTRA, STRAHL and GACODE, we will focus on the corresponding transport equations for an impurity density with flux-surface-averaged density $\langle n \rangle$ and source $\langle S \rangle$, based on the derivation sketched in section 4.1. Likewise, we will label the transport coefficients with 'a' for ASTRA, 's' for STRAHL and 'g' for GACODE.

The transport equation in ASTRA is

$$\frac{\partial}{\partial t}\left(\frac{\partial V}{\partial r_{\mathrm{tor}}}\langle n \rangle\right) = \frac{\partial}{\partial r_{\mathrm{tor}}}\left[\frac{\partial V}{\partial r_{\mathrm{tor}}}\left\langle |\nabla r_{\mathrm{tor}}|^2 \right\rangle \left(D_a \frac{\partial \langle n \rangle}{\partial r_{\mathrm{tor}}} - \langle n \rangle v_a\right)\right] + \langle S \rangle \frac{\partial V}{\partial r_{\mathrm{tor}}} . \tag{C.4}$$

The transport equation in STRAHL is

$$\frac{\partial V}{\partial r_{\mathrm{vol}}}\frac{\partial \langle n \rangle}{\partial t} = \frac{\partial}{\partial r_{\mathrm{vol}}}\left[\frac{\partial V}{\partial r_{\mathrm{vol}}}\left(D_s \left\langle |\nabla r_{\mathrm{vol}}|^2 \right\rangle \frac{\partial \langle n \rangle}{\partial r_{\mathrm{vol}}} - \langle n \rangle v_s \left\langle |\nabla r_{\mathrm{vol}}| \right\rangle\right)\right] + \langle S \rangle \frac{\partial V}{\partial r_{\mathrm{vol}}} , \tag{C.5}$$

however the actual transport coefficients in input and output of STRAHL absorb the metric factors, such that $D_s^* = D_s \left\langle |\nabla r_{\mathrm{vol}}|^2 \right\rangle$ and $v_s^* = D_s \left\langle |\nabla r_{\mathrm{vol}}| \right\rangle$.

The transport equation in TGYRO is

$$\frac{\partial V}{\partial r_{\mathrm{min}}}\frac{\partial \langle n \rangle}{\partial t} = \frac{\partial}{\partial r_{\mathrm{min}}}\left[\frac{\partial V}{\partial r_{\mathrm{min}}}\left(D_g \frac{\partial \langle n \rangle}{\partial r_{\mathrm{min}}} - \langle n \rangle v_g\right)\right] + \langle S \rangle \frac{\partial V}{\partial r_{\mathrm{min}}} . \tag{C.6}$$

From these equations we can directly see that one has an equivalent description of the evolution of $\langle n \rangle$ if the terms inside the square brackets in equations (C.4–C.6), i.e. the particle fluxes, are equal. When this condition is imposed, the coefficients transform as detailed in the following subsections.

C.1 Passing TGLF/FACIT transport coefficients to ASTRA

In an ASTRA simulation, one typically calls different transport models to obtain the diffusive and convective coefficients that would then go to the ASTRA equation, here equation (C.4). If these coefficients are calculated by transport models following the GACODE convention, like TGLF and FACIT throughout most of this thesis, then before going into ASTRA they must be transformed as

$$D_a = D_g \left(\frac{\mathrm{d}r_{\mathrm{tor}}}{\mathrm{d}r_{\mathrm{min}}}\right)^2 \frac{1}{\left\langle |\nabla r_{\mathrm{tor}}|^2 \right\rangle} , \tag{C.7}$$

$$v_a = v_g \left(\frac{\mathrm{d}r_{\mathrm{tor}}}{\mathrm{d}r_{\mathrm{min}}}\right) \frac{1}{\left\langle |\nabla r_{\mathrm{tor}}|^2 \right\rangle} , \tag{C.8}$$

which follows from equations (C.4) and (C.6). In ASTRA variables,

$$\left\langle |\nabla r_{\mathrm{tor}}|^2 \right\rangle = \frac{\mathtt{G11}}{\mathtt{VRS}} , \qquad \frac{\mathrm{d}r_{\mathrm{tor}}}{\mathrm{d}r_{\mathrm{min}}} = \frac{\mathrm{d}(\mathtt{RHO})}{\mathrm{d}(\mathtt{AMETR})} . \tag{C.9}$$

For reference, this transformation is implemented in `$AWD/xpr/tglf_interf.f90`, `$AWD/sbr/facit.f90`, where `$AWD` is the user's ASTRA Working Directory.

C.2 Passing ASTRA transport coefficients to STRAHL

Another typical situation in the ASTRA-STRAHL modelling framework of this thesis is that STRAHL is called from ASTRA to evolve the impurity densities and calculate their radiation, passing to STRAHL the transport coefficients which were already in the ASTRA grid. Then, before going to STRAHL, the coefficients must be transformed as

$$D_s^* = D_a \left(\frac{\mathrm{d}r_{\mathrm{vol}}}{\mathrm{d}r_{\mathrm{tor}}}\right)^2 \left\langle |\nabla r_{\mathrm{tor}}|^2 \right\rangle = D_a \, \frac{\mathtt{G11\ VRS}}{8\pi^2\ \mathtt{RTOR\ VOLUM}}, \tag{C.10}$$

$$v_s^* = v_a \left(\frac{\mathrm{d}r_{\mathrm{vol}}}{\mathrm{d}r_{\mathrm{tor}}}\right) \left\langle |\nabla r_{\mathrm{tor}}|^2 \right\rangle = v_a \, \frac{\mathtt{G11}}{\sqrt{8\pi^2\ \mathtt{RTOR\ VOLUM}}}, \tag{C.11}$$

which follows from equations (C.2), (C.4) and (C.5), where we recall that in ASTRA notation `VRS` = d(`VOLUM`)/d(`RHO`).

For reference, this transformation is implemented in `$AWD/sbr/a2strahl.f90`

C.3 Passing GACODE transport coefficients to STRAHL

Although in the modelling workflow of this thesis the transport coefficients calculated by the transport models are not passed directly to STRAHL, always going through ASTRA first, the corresponding transformation is given for completeness:

$$D_s^* = D_g \left(\frac{\mathrm{d}r_{\mathrm{vol}}}{\mathrm{d}r_{\mathrm{min}}}\right)^2, \qquad v_s^* = v_g \left(\frac{\mathrm{d}r_{\mathrm{vol}}}{\mathrm{d}r_{\mathrm{min}}}\right). \tag{C.12}$$

We note that the transformations (C.10–C.12) are the same when going to the Aurora impurity transport code as when going to STRAHL.

Acknowledgements

First and foremost I would like to extend my heartfelt gratitude to Clemente Angioni. His kindness towards me, the generosity with his time and knowledge, and his continuous support over the past three years of my PhD (plus one year of my master thesis) cannot be overstated. I truly believe he is the best supervisor a PhD student could have.

I also want to warmly thank Hartmut Zohm for welcoming me into his department and giving me the opportunity to pursue my research at the Max Planck Institute for Plasma Physics (IPP). Knowing that I could always count on a friendly advice from him has helped a lot in this journey.

Several colleagues at IPP have played an important part of my PhD, and I want to acknowledge Giovanni Tardini and Emiliano Fable for all of their help.

All who have met me know how much I like football, and I thank all of the people that take part in the bi-weekly SV Plasma games.

Sharing my office with such wonderful people as Oleg Samoylov, Tabea Gleiter, Teobaldo Luda and Marco Muraca has helped me enjoy work much more. I want to thank them for creating a happy, funny and warm space where I spent my day to day for three years.

Among the great people that have made these years better are Nina Schwarz, Pilar Cano, Dominik Brida, Davide Silvagni, Maxi Reisner, Michael Bergmann, Andrés Cathey, Andrew Moreau, Brando Rettino, and all of the friends with whom we have marched to the Mensa so many times.

Mis papás y mi hermano siempre me brindaron su apoyo, desde las llamadas diarias cuando volvía a casa en bicicleta, hasta las visitas inolvidables que cada uno hizo a Munich. Estar lejos de ellos no ha sido para nada fácil, y entre los momentos más felices de cada año están nuestros reencuentros decembrinos. Gracias por interesarse en mi trabajo, y gracias por hacerme saber constantemente cuánto me quieren.

Faltan las palabras para agradecerle a Laura, mi novia y ahora prometida, por su cariño constante, por hacerme reír y acompañarme todos los días, incluso desde la distancia. La vida junto a ella ha sido y será siempre más feliz.

Quiero dedicar este logro especialmente a mi abuela Merce, cuya partida durante el primer año de mi doctorado ha sido el momento más difícil de mi vida, por su amor que siento aún conmigo y su ejemplo que sigue marcando para mí el norte de cómo ser una buena persona.